Beam Dynamics Design of the FAIR Proton-Linac RFQ and Design Study of a Compact 325 MHz RFQ

Dissertation
zur Erlangung des Doktorgrades
der Naturwissenschaften

vorgelegt am Fachbereich Physik
der Johann Wolfgang Goethe-Universität
in Frankfurt am Main

von
Marc Syha
aus Bad Soden am Taunus

Frankfurt am Main 2021
(D30)

vom Fachbereich Physik der
Johann Wolfgang Goethe-Universität als Dissertation angenommen.

Dekan:
Prof. Dr. Harald Appelshäuser

Gutachter:
Prof. Dr. Ulrich Ratzinger
Prof. Dr. Holger Podlech

Datum der Disputation:

There are no solutions.
There are only trade-offs.

Thomas Sowell

Contents

Zusammenfassung I

Ausblick XXII

[1] Introduction 1

1.1 The FAIR Project of GSI 1

1.2 The FAIR Proton-Linac 6

1.2.1 Conceptional Design of the Proton-Linac 7

[2] Radio Frequency Quadrupoles and their Beam Dynamics 11

2.1 The Benefits of RFQs 12

2.2 A Brief History of RFQs 14

2.3 RFQ Resonator Types 16

2.4 RFQ Beam Dynamics 17

2.5 The Two-Term Potential Approximation 17

2.6 Kapchinsky-Teplyakov Potential and Eight-Term Potential 23

2.7 Alternating Gradient Focusing Principle 24

2.8 RF-Defocusing and Acceleration Efficiency 26

2.9 Space-Charge Effects 27

2.9.1 Typical Space-Charge Electric Fields in RFQ Beam Bunches 27

2.10 RFQ Design Procedures 28

2.10.1 The LANL Four Section RFQ Design Procedure (LANL FSP) 29

2.10.2 Influence of Cell Length and Aperture 33

2.10.3 The New Four Section Procedure (NFSP) of IAP Frankfurt 33

2.11 Beam Dynamics Design of the Linac4 RFQ 37

[3]	**The p-Linac RFQ Beam Dynamics Design and Simulations**		39
	3.1	Alternative Design with the LANL-Four Section Procedure	50
	3.2	Transversal Entrance Twiss Parameter Studies with RFQGen	52
	3.3	TraceWin and RFQGen Simulations based on LEBT measurements	54
	3.4	Comparison of the RFQGen and TOUTATIS simulation results	59
	3.5	Particle loss profile along the RFQ	62
	3.6	Investigation of the Effects of Image-Charges and Neighboring Bunches	66
	3.7	Compensation of Longitudinal Entrance and Exit Gap Field Effects	74
		3.7.1 Entrance Gap Field	76
		3.7.2 Exit Gap Field	81
		3.7.3 Beam Dynamics Simulations with Entrance Gap Field Effects	84
	3.8	Entrance Beam Current Studies with RFQGen and TOUTATIS	86
	3.9	Effects of the Voltage Inhomogeneity on the Beam Dynamics	107
[4]	**Beam Dynamics Design of a New Compact RFQ**		119
	4.1	The Role of Compact RFQs in Nuclear Medicine	119
	4.2	CERN's Compact PIXE and COMPASS RFQs	121
	4.3	First Beam Dynamics Design Draft for a New Compact RFQ	122
		4.3.1 Particle Loss Profiles	126
		4.3.2 Intersection of the Phase Advance Curves	128
	4.4	Current Studies with the New Compact RFQ	130
	4.5	Further Steps	131
[5]	**Conclusions and Outlook**		133
Bibliography			139
Appendices			149
A	**The Synchronous Particle and the Separatrix**		151
	A.1	Opening of the Bucket Under Acceleration	155

B Space-Charge Compensation in the LEBT of the FAIR p-Linac 157

C The Bravery Factor 159

D Beam Emittances 161

D.1 Transverse Emittances 161

D.2 Equation of an Ellipse and Percentage Emittances 162

D.3 The Twiss Parameters 163

D.4 RMS-Emittance 167

D.4.1 RMS-Emittance Conventions 168

D.5 A Brief Remark on Emittance Definition 169

D.6 Normalized Beam Emittances 170

E Two RFQ Beam Dynamics Codes 173

E.1 The LANL RFQ Design Codes and RFQGen 173

E.1.1 PARMTEQ(M) and RFQGen 174

E.1.2 PARMTEQ's Equation of Motion Algorithm 175

E.1.3 Space-Charge Force Considerations in PARMTEQ(M) 177

E.1.4 Image-Charge Effects in PARMTEQ(M) 180

E.1.5 Input Macro-Particle Distributions for PARMTEQ(M) 182

E.1.6 Longitudinal Particle Losses in PARMTEQ(M) 183

E.2 The TOUTATIS-Code 185

E.2.1 The TOUTATIS Algorithm 186

E.2.2 The Finite Difference Method 187

E.2.3 TOUTATIS' Multigrid Method 188

E.2.4 Adaptive Mesh Refinement in TOUTATIS 189

F Lists of Figures and Tables 191

G List of Abbreviations and Acronyms 197

Danksagungen 201

Curriculum Vitae 205

Zusammenfassung

Die vorliegende Dissertation stellt die Strahldynamikdesigns zweier Hochfrequenzquadrupol-Linearbeschleuniger bzw. **R**adio **F**requency **Q**uadrupoles (RFQs) vor: das für den RFQ des Protonen-Linearbeschleunigers (p-Linac[1]) des FAIR[2]-Projekts an der GSI[3] Darmstadt sowie einen ersten Designentwurf für einen kompakten RFQ, der u.a. zur Erzeugung von Radioisotopen für medizinische Zwecke genutzt werden könnte. Der Schwerpunkt liegt auf dem ersten Design.

Wie in Kapitel [1] (der Einleitung) der vorliegenden Arbeit erläutert, werden im Zuge des 2007 ins Leben gerufenen FAIR-Projekts, das die Erforschung von Antiprotonen und Ionen zum Ziel hat, die Anlangen der GSI um mehrere Speicherringe, darunter das Synchrotron SIS100[4], erweitert (siehe Abbildung 0.1). Dem momentan betriebenen Linearbeschleuniger UNILAC[5] ist es nicht möglich, eine hinreichende Anzahl an Antiprotonen zu erzeugen, weswegen das FAIR-Projekt auch einen Linac zur Protonen-Beschleunigung umfasst (siehe Abbildung 0.2), der diese anschließend in das Synchrotron SIS18[6] injizieren soll. Die Beschleunigungskavitäten sowie die MEBT[7]-Sektion, die sich zwischen dem RFQ und diesen befindet, wurden am IAP[8] Frankfurt entwickelt. Im insgesamt ca. 30 m langen p-Linac werden zukünftig Protonen bei einem Tastverhältnis von 0.08 %[9] und einem Strahlstrom von bis zu 110 mA von 95 kV auf 68 MeV beschleunigt, um anschließend in das Synchrotron SIS18 injiziert zu werden. Die Betriebsfrequenz des p-Linacs von 325.224 MHz ergibt sich aus der Wahl der Klystren (bei einer Leistung von 2 MW pro Klystron).

[1] **lin**ear **ac**celerator

[2] **F**acility for **A**ntiproton and **I**on **R**esearch (Deutsch: Internationale Beschleuniger-Anlage zur Forschung mit Antiprotonen und Ionen; `https://www.gsi.de/forschungbeschleuniger/fair`)

[3] GSI Helmholtzzentrum für Schwerionenforschung; ehemals **G**esellschaft für **S**chwer**i**onenforschung (`https://www.gsi.de`)

[4] Das Akronym SIS in SIS100 sowie in SIS18 (siehe unten) steht für **S**chwer**i**onen-**S**ynchrotron (`https://www.gsi.de/work/gesamtprojektleitung_fair/sis100sis18_sis`).

[5] **Uni**versal **L**inear **Ac**celerator (`https://www.gsi.de/forschungbeschleuniger/beschleunigeranlage/linearbeschleuniger`)

[6] Vgl. Fußnote 4

[7] **M**edium **E**nergy **B**eam **T**ransport; Deutsch: Mittelenergiestrahl-Transport

[8] Das **I**nstitut für **A**ngewandte **P**hysik ist eines von sechs Instituten des Fachbereichs Physik der Johann Wolfgang Goethe Universität Frankfurt am Main (`https://www.uni-frankfurt.de/49311579/IAP`).

[9] Für dieses Dokument wird gemäß der angelsächsischen Konvention durchgehend ein Punkt als Dezimaltrennzeichen verwendet. Dies gilt auch für dieses, auf Deutsch verfasste, Kapitel.

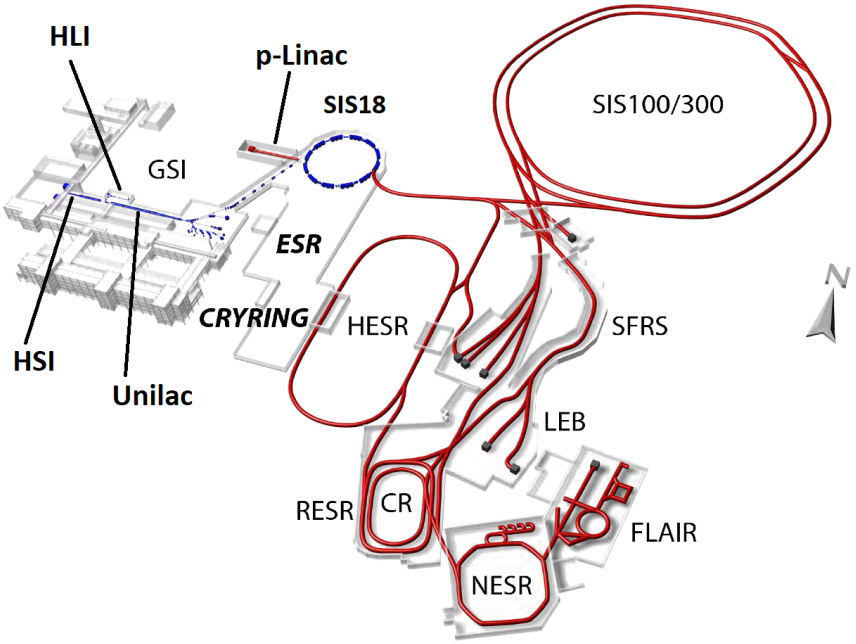

Abbildung 0.1: Übersicht über die GSI-Anlagen und jene des FAIR-Projekts: Die bereits bestehenden GSI-Anlagen UNILAC (Linearbeschleuniger), SIS18 (Synchrotron), ESR und CRYRING (Speicherringe) sind blau dargestellt. (Eine Übersicht über diese und weitere Anlagen der GSI findet sich unter `https://www.gsi.de/work/forschung/appamml/atomphysik/anlagen_und_experimente`.) Die sich zurzeit noch im Bau befindlichen FAIR-Einrichtungen sind rot dargestellt. (Abbildung basierend auf Abbildung 1 aus Referenz [1]).

Teil dieses Beschleunigungssystems ist auch der 2018 gefertigte p-Linac Leiter[10]-RFQ, dessen Elektroden kaum 3.3 m lang sind. Obwohl dieser RFQ den Hochstrom-RFQs zuzurechnen ist, können auch deutlich niedrigere Eingangsströme von noch ca. 35 mA von ihm problemlos von 95 keV, vorgegeben durch die am CEA Saclay[11] gefertigte Protonen-Quelle, auf die Endenergie von 3 MeV beschleunigt werden.

[10] Im Tank des FAIR p-Linac-RFQ befindet sich eine Leiterstruktur aus Kupfer. Damit hebt sich sein Design von dem der meisten RFQs deutlich ab. Ferner geht es mit deutlich verringerten Dipol-Feldanteilen einher, womit es sich besonders für Frequenzen jenseits von 300 MHz eignet. Das mechanische und das Hochfrequenz-Design des p-Linac Leiter-RFQ sowie deren Auswirkungen auf den Betrieb dieses RFQ werden ausführlich in Referenz [3] beschrieben. Referenzen [4] und [5] geben die vielversprechenden Ergebnisse der ersten Frequenz-Messungen und Tuningschritte an diesem RFQ wieder.

[11] Das Forschungszentrum in Saclay (bei Paris, Frankreich) ist eines von neun Zentren des **c**ommissariat à l'**é**nergie **a**tomique (CEA; Deutsch: Kommissariat für Atomenergie und alternative Energien). Es beherbergt auch den Verwaltungssitz des CEA (`https://www.cea.fr/english`).

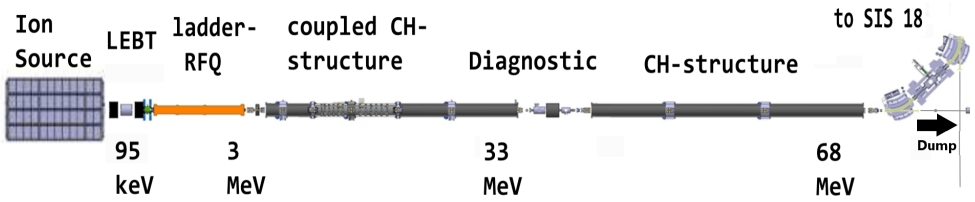

Abbildung 0.2: Layout des FAIR Protonen-Linacs [2]. Die einzelnen Elemente des Linacs sind von links nach rechts: Ionenquelle, LEBT-Sektion, Leiter-RFQ, gekoppelte CH-Struktur, Diagnostik-Sektion, CH-Struktur.

Kapitel [2] widmet sich dem für das Verständnis dieser Dissertation notwendigen Vorwissen. Am Anfang steht hier das RFQ-Konzept, welches von Kapchinskiy und Tepliakov in den 1960er-Jahren am Institut für Theoretische und Experimentelle Physik[12] in Moskau erdacht wurde [6].

Den ersten auf dem RFQ-Prinzip fußenden Versuchsaufbau lieferte das Institut für Hochenergiephysik[13] in Protvino (Russland). Nach ersten Tests konnte hier 1974 auch der erste durch einen RFQ beschleunigte Strahl erzielt werden [7, 8]. Erst 1977 wurde die westliche Beschleunigerphysik-Gemeinde durch einen tschechischen Flüchtling über das RFQ-Konzept in Kenntnis gesetzt [3]. Daraufhin erwachte vor allem am **L**os **A**lamos **N**ational **L**aboratory[14] (LANL) ein reges Interesse für diesen Linearbeschleuniger-Typ und man begann dort darauf hinzuarbeiten, das RFQ-Prinzip an Hochstrom-Strahlen niedriger Emittanz[15] testen zu können. Zeitgleich wurden am LANL Computer-Codes zur Entwicklung von RFQ-Designs auf Grundlage der parallel entwickelten LANL **F**our **S**ection **P**rocedure (FSP) geschrieben. Hierbei handelt es sich um ein Design-Schema mit dem sich systematisch effiziente und tatsächlich realisierbare RFQ-Strahldynamiken konzipieren lassen, wobei der RFQ in vier unterschiedliche Abschnitte unterteilt wird [9], denen verschiedene Funktionen bzgl. der Strahlentwicklung zukommen. Sichtbar ist dies auch am Verlauf der Kurven der Design-Schlüsselparameter entlang des RFQ. Die FSP sowie das für sie zentrale adiabatische Bunchen[16] werden in Unterabschnitt 2.10.1 detailliert dargelegt. Adiabatisches Bunchen erlaubt es, kompakte Strahlpakete zu erzeugen, ohne dass größere Teilchenverluste und Strahlaufweitungen auftreten. Die LANL FSP sowie sich eng an ihr orientierende Abwandlungen dienen bis heute

[12] Englisch: **I**nstitute for **T**heoretical and **E**xperimental **P**hysics (ITEP) (http://www.itep.ru)
[13] Englisch: **I**nstitute for **H**igh **E**nergy **P**hysics (IHEP) (http://www.ihep.ru)
[14] `www.lanl.gov`
[15] Die Strahlemittanz ist ein Maß für die Fläche, die von den Strahlteilchen im jeweiligen Phasenunterraum eingenommen wird. Eine tiefere Diskussion zu den verschieden Definitionen dieser Größe findet sich in Anhang D.
[16] Aus dem Englischen; to bunch: bündeln

als Grundlage zahlreicher RFQ-Designs. Dies trifft neben dem FAIR p-Linac RFQ auch für den Linac4-RFQ am CERN[17] zu (vgl. Unterabschnitt 2.10.1).

All diese Bestrebungen des LANLs mündeten im Frühjahr 1980 schließlich im ersten Experiment, das einen Machbarkeitsbeweis liefern konnte. Hierbei wurde ein 100 keV Protonenstrahl durch einen 425 MHz RFQ auf 100 keV beschleunigt. Die am RFQ-Ausgang bestimmte Transmission von 90% war von den Codes korrekt vorausberechnet worden. Der Startschuss für die rasche weltweite Verbreitung der RFQs war gegeben; gegenwärtig sind weltweit hunderte RFQs in Betrieb und fast jede größere Beschleunigereinrichtung hat ihre Vorbeschleuniger älteren Typs durch kompakte und effiziente RFQs ersetzt [8].

An dieser Stelle sei auch der Beitrag des IAP Frankfurts hierzu genannt: Schempp et al. begannen noch im selben Jahrzehnt nicht nur die Gattung der sog. 4-Rod[18]-RFQs beizusteuern, sondern auch erste Modifikationen an der LANL FSP vorzunehmen, um auf eine sanftere, natürlichere Strahlentwicklung in RFQs hinzuarbeiten [10, 11, 12, 13, 14, 15]. Hierdurch ergaben sich deutlich kürzere und kompaktere RFQs als es ceteris paribus gemäß der LANL FSP möglich wäre. A. Schempp und C. Zhang fassten die im Laufe der Zeit etablierten Modifikationen u.a. in der sogenannten **N**ew **F**our **S**ection **P**rocedure (NFSP) zusammen [16, 17, 18], auf die in Unterabschnitt 2.10.3 näher eingegangen wird. In jüngerer Vergangenheit widmeten sich C. Zhang und H. Podlech u.a. Überlegungen zur Vermeidung bzw. Verringerung des Emittanz-Transfers in RFQs [19].

RFQs stellen heute nicht zuletzt auch wesentlich platzsparendere Alternativen zu großen Vorbeschleunigern wie z.B. Cockcroft-Walton-Beschleunigern dar. Zudem gewährt eine starke transversale Fokussierung von Teilchenstrahlen in RFQs eine gute Kontrolle der transversalen Emittanzen. Ferner können sie CW[19]-Strahlen „bunchen“, d.h. diese in diskrete Strahlpakete (Englisch: beam bunches) unterteilen bzw. die Bunchlänge eines eingehenden bereits gebunchten Strahls verkürzen. Dies ermöglicht es nachfolgenden Linearbeschleunigern den RFQ-Ausgangsstrahl einzufangen und zu transportieren. Im Gegensatz zu anderen Beschleunigerstrukturen sind beim RFQ die longitudinalen und transversalen Teilchenbewegung gekoppelt, was bei der Entwicklung

[17] Hier: Forschungseinrichtung der gleichnamigen Europäischen Organisation für Kernforschung bei Genf in der Schweiz (`https://home.cern`). Das Akronym CERN leitet sich vom Europäischen Rat für Kernforschung ab, der mit der Gründung einer solchen Organisation beauftragt war (Französisch: **c**onseil **e**uropéen pour la **r**echerche **n**ucléaire).

[18] Diese sind mit Lecherleitungs-Resonatoren und stabförmigen Elektroden ausgestattet, während die älteren 4-Vane-RFQs mit Hohlraum-Resonatoren und propellerförmigen Elektroden ausgestattet sind.

[19] Bei Teilchenbeschleunigern wird vom continuous wave(CW)- oder auch Dauerstrichbetrieb gesprochen, wenn der beschleunigte Teilchenstrahl kontinuierlich ist, d.h. keine makroskopische Pulsung aufweist [20].

eines geeigneten Strahldynamik-Designs zwar viele Vorteile bergen, den Design-Prozess aber auch komplex gestalten kann.

Eine umfassende theoretische Beschreibung der beschleunigenden und fokussierenden elektrischen[20] Felder im RFQ ist ebenfalls unerlässlich für ein tieferes Verständnis der Strahldynamik. Das elektrische Potential der RFQ-Elektroden kann durch die sog. quasistatische Näherung als Lösung der Laplace-Gleichung formuliert werden. Dieser Ansatz ist für gewöhnlich dann gerechtfertigt, wenn die Strukturabmessungen nahe der Strahlachse klein gegenüber der Vakuum-Wellenlänge (der elektromagnetischen Schwingung) ist [21] (vgl. Abschnitt 2.5 und 2.6). Das sich hier als Lösung ergebende Kapchinsky-Teplyakov-Potential wird zumeist durch zwei bzw. acht seiner (unendlich vielen) Terme angenähert. Auf dieser Basis erfolgt die Beschreibung der Alternierenden Gradientenfokussierung sowie der longitudinalen Fokussierung und Beschleunigung in RFQs. Aus dem fein aufeinander abgestimmten Zusammenspiel dieser Phänomene ergeben sich die unterschiedlichen Funktionen des RFQ als bunchende und transversal fokussierende Beschleunigerstruktur.

In den Anhängen der Dissertation finden sich Definitionen und Erläuterungen zu folgenden grundlegenden Konzepten der Beschleunigerphysik bzw. der Strahldynamik: Synchronphase, Separatrix (Anhang A), Raumladungskompensation (Anhang B), Bravery- bzw. Kilpatrick-Faktor (Anhang C) und die verschiedenen Klassifikationen von Strahlemittanzen (Anhang D). Besonders die Klassifikation und Notation der Emittanzen wird in der Fachliteratur leider nicht immer einheitlich behandelt, was zumeist unnötige, an sich leicht vermeidbare Verwirrung erzeugen kann.

Beide im Rahmen dieser Dissertation entwickelten Strahldynamik-Designs wurden mit dem RFQGen-Code[21] erzeugt. RFQGen und TOUTATIS, ein weiterer für diese Dissertation relevanter RFQ-Strahldynamik-Code, werden in Anhang E detailliert beschrieben. Die meisten in dieser Dissertation vorgestellten Strahldynamik-Simulationen wurden mit RFQGen durchgeführt. Der Name „RFQGen“ leitet sich von „**RFQ-Gen**erator“ ab. Bei diesem Code handelt es sich um den Nachfolger des 1979 am Los Alamos National Laboratory entwickelten Codes PARMTEQ[22]. PARMTEQ wurde geschrieben zur Erzeugung von RFQ-Strahldynamik-Designs sowie zur Simulation der Bewegung von Teilchenstrahlen durch diese und wurde fortlaufend weiterentwickelt [22, 21]. Er

[20] Aufgrund der geringen Teilchen-Geschwindigkeiten in RFQs sowie des geringen magnetischen Flusses nahe der Strahlachse, kann die Lorentzkraft für die Beschreibung der Teilchenstrahl-Dynamik vernachlässigt werden.

[21] Das zugehörige Software-Paket wird von LMY Technology vertrieben und beinhaltet drei weitere Codes (`https://lmytechnology.com`).

[22] **P**hase **a**nd **R**adial **M**otion in **T**ransverse **E**lectric **Q**uadrupoles

ist möglicherweise der relevanteste und populärste aus mehreren von der **L**os **A**lamos **A**ccelerator **C**ode **G**roup (LAACG) stammenden Codes[23].

Ein weiterer fest etablierter RFQ-Strahlydynamik-Code ist TOUTATIS[24] (siehe Anhang E.2). Er wurde vor über 20 Jahren von R. Duperrier geschrieben, um den Transport von Teilchenstrahlen durch Hochstrom-RFQs zu simulieren [23]. Auch TOUTATIS verwendet ein vereinfachtes Strahldynamik-Konzept, verzichtet allerdings auf einige Näherungen aus PARMTEQ(-M)[25], um u.a. genauere Vorhersagen bzgl. der Aktivierung des RFQ treffen zu können.

Das Strahldynamik-Design des FAIR p-Linac RFQ sowie diverse an diesem durchgeführten Test-Simulationen bezüglich Eingangsparametern wie Strahlstrom und transversalen Twiss-Parametern werden in Kapitel [3], dem „zentralen“ Kapitel der Dissertation, vorgestellt: Das Design weist eine hohe Toleranz hinsichtlich Abweichungen von den Designwerten der transversalen Twiss-Parametern (vgl. Abschnitt D.3) und des Strahlstroms (vgl. Abschnitt 3.8) am RFQ-Eingang auf.

Als die Arbeit am Design für die Strahldynamik des FAIR Protonen-Linac RFQ im Februar 2017 begann, standen die mechanischen und HF-Entwürfe des RFQ (IAP) sowie die Entwürfe der Quelle und der LEBT[26]-Sektion (GSI und CEA Saclay) bereits kurz vor dem Abschluss. Dieser und weitere Umstände führten zu folgenden, nicht-trivialen Anforderungen an das Strahldynamik-Design des RFQ:

- Aus den bereits festgelegten mechanischen Abmessungen des RFQ-Tanks ergab sich eine Elektrodenlänge, die auf Werte zwischen 3324 und 3335 mm beschränkt war, so dass nur ein Spielraum von 11 mm blieb.
- Die Energie der Protonen bei ihrem Austritt aus der Quelle wurde vom CEA Saclay auf einen ungewöhnlich hohen Wert von 95 keV festgelegt, obwohl eine deutlich niedrigere Energie[27] vorzuziehen gewesen wäre. Man beachte, dass die Eingangsenergie des Linac4-RFQ, dessen Parameter denen des vorliegenden RFQ recht ähnlich sind, mit 45 keV weniger als 50 %

[23] `https://laacg.lanl.gov/laacg/services/serv_codes.phtml`
[24] `http://irfu.cea.fr/en/Phocea/Page/index.php?id=781`
[25] PARMTEQ-M ist das jüngste direkte PARMTEQ-Upgrade. Das „M“ in diesem Akronym weist auf die (bis zu sechs) zusätzlichen Multipole des für die Berechnungen verwendeten Elektroden-Potentials hin.
[26] **L**ow **E**nergy **B**eam **T**ransport (Deutsch: Niederenergiestrahl-Transport)
[27] Da die RFQ-Zellenlängen proportional zur (synchronen) Teilchengeschwindigkeit sind ($l_c = \beta_s \lambda$), führt eine höhere RFQ-Eintrittsenergie ceteris paribus zu längeren RFQ-Zellen auf der Eintrittsseite als eine niedrigere Eintrittsenergie. Es hat sich gezeigt, dass eine niedrige Eingangssynchrongeschwindigkeit und damit kürzere RFQ-Zellen am Anfang die Gesamtlänge des RFQ im Vergleich zum ersten Fall reduzieren. Darüber können hieraus auch weitere Optimierungen erfolgen, z.B. die Reduzierung der Elektrodenspannung.

der hier vorliegenden beträgt (vgl. Abschnitt 2.11). Es ist jedoch zu bedenken, dass diese Energie ursprünglich im Hinblick auf die Optimierung für einen Auslegungsstrom von 30 mA anstelle von 70 mA gewählt wurde.

- Die transversale normierte RMS-Emittanz[28] wurde auf $0.3\,\pi$ mm mrad festgelegt.
- Im Februar 2017 lag der Designwert des RFQ-Eingangsstroms noch bei lediglich 70 mA, auch wenn bereits damals absehbar war, dass er sich noch bis auf 100 mA erhöhen sollte, u.a. um mögliche Verluste besser kompensieren zu können. Schließlich fiel die Wahl auf 100 mA; für die Eingangsstromstudien in RFQGen betrug der Höchstwert sogar 110 mA.
- Um die Verlustleistung (und die hiermit verbundenen Kosten) möglichst gering zu halten und um ferner keinen Spannungsdurchschlag („RF electric break down"; vgl. Anhang C) zu riskieren, wurde als oberere Grenze für die Elektrodenspannung der Wert von 95 kV ausgegeben.
- Die Simulationen zum Hochfrequenz-Tuning [3, 4] mit der Software CST[29] Microwave Studio[30] (CST MWS) waren quasi auf einen nahezu konstanten Elektrodenradius entlang des gesamten RFQ angewiesen.

Da auch die Designs des MEBT-Abschnitts hinter dem RFQ und der nachfolgenden CH-Kavitäten weitestgehend abgeschlossen waren, lagen auch die RFQ-Austrittsenergie von 3 MeV sowie die angestrebten Werte der transversalen und longitudinalen Emittanzen am RFQ-Ausgang bereits fest [24]. Die Design-Parameter des FAIR p-Linac RFQ finden sich in Tabellen 0.1 und 0.3. Die Parameter des Designstrahls[31] am RFQ-Ausgang sind in Tabelle 0.2 aufgeführt.

Abbildung 0.3 zeigt die Verläufe der Schüssel-Parameter Apertur a, Modulation m und Synchronphase ϕ. Sie weisen Ähnlichkeit zu denen des Linac4-RFQ am CERN auf. Bis auf die nicht

[28] Sofern nicht anders angegeben, sind alle in dieser Arbeit angegebenen Emittanzen normierte RMS-Emittanzen. Die transversalen Emittanzen werden (normalerweise) in Einheiten von π mm mrad angegeben, die longitudinalen in Einheiten von π MeV deg. In Anhang D.5 findet sich eine kurze Diskussion über die Sinnhaftigkeit der Hinzunahme des Faktors π in die Einheiten, da dies im Widerspruch zur Definition der Strahlemittanz ε als von den Teilchen belegte Fläche A im jeweiligen Teilphasenraum geteilt durch π zu stehen scheint: $\varepsilon = A\,/\,\pi$ (vgl. Gleichung D.1).

[29] **C**omputer **S**imulations **T**echnology

[30] `https://www.mathworks.com/products/connections/product_detail/cst-microwave-studio.html`

[31] Hiermit ist der Protonenstrahl gemeint, der von RFQGen für die Simulation gemäß bestimmter vom Anwender vorgegeben Eingangsparameter (u.a. Energie, Strom, Emittanzen, Anzahl der Makro-Teilchen etc.) erstellt wurde und mit dem das Strahldynamikdesign gewonnen wurde. RFQGen erfordert bereits für die das Design generierende Simulation einen Eingangsstrahl. Zudem beinhaltet die Arbeit des Strahldynamikers, einzelne Designs im Hinblick auf die Strahlausgangsparameter auszuwerten um sie ggf. zu verwerfen bzw. zu modifizieren bis die Ausgangsparameter den Vorgaben (hinreichend gut) entsprechen.

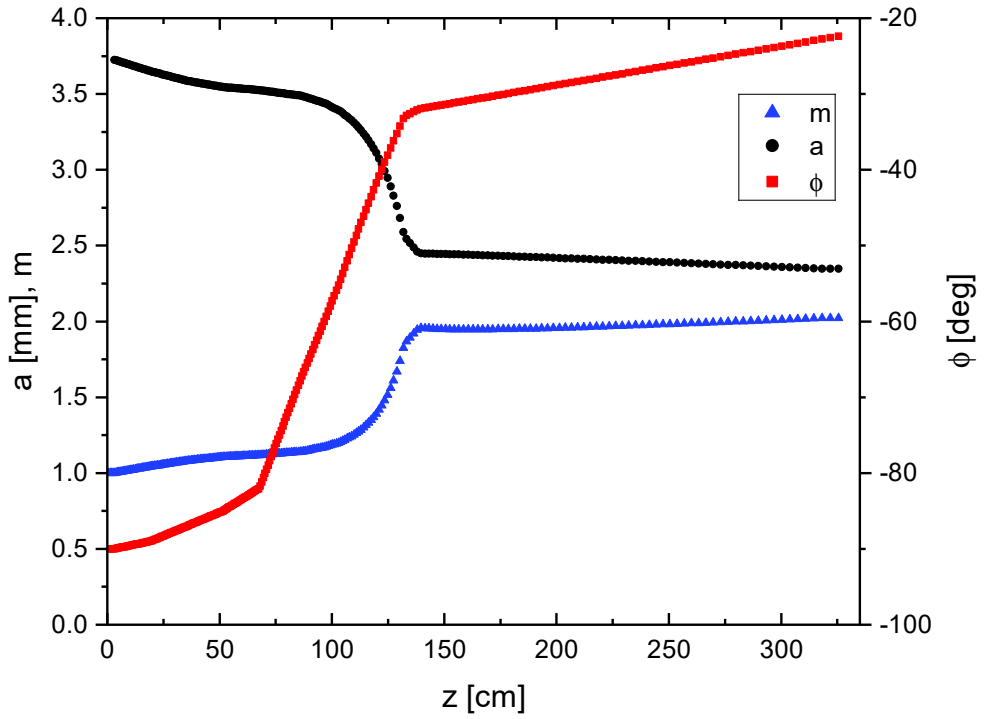

Abbildung 0.3: Strahldynamik-Design des FAIR Protonen-Linac RFQ: Verläufe des Modulationsparameters m, der radialen Apertur a und der Synchronphase ϕ entlang des RFQ.

konstanten, aber immer noch linearen Verläufe[32] der Parameterkurven innerhalb der letzten Sektion (der sog. Beschleunigungssektion, in der der Großteil des gesamten Energiegewinns entlang des RFQ erzielt wird), entspricht diese einem klassischen RFQ-Strahldynamik-Design gemäß der LANL FSP. Diese leichte Abwandlung kann aber bereits eine signifikante Kürzung des RFQ und/oder eine Absenkung der Elektrodenspannung bewirken (vgl. Abschnitt 2.11 und 3.1).

In Abschnitt 3.1 wird ein alternatives (nicht verbautes) Elektroden-Design für den FAIR p-Linac RFQ präsentiert, das einem klassischen LANL Design gemäß der FSP entspricht. Die Schlüsselparameter wie die Elektrodenspannung V_{el}, die minimale Apertur a_{min}, die maximale Modulation m_{max} und die Fokussierstärke B_{max} sind denen des Original-Designs sehr ähnlich.

Auch die Teilchenverteilung am RFQ-Ausgang des (strahldynamisch) angepassten Falls („matched case“; vgl. Abschnitt 3.2) ähneln sich stark, wobei das alternative Design zu einer leicht

[32] Man beachte die Gegenläufigkeit der Verläufe von a und m.

Parameter	**Wert**
RFQ-Eingangsstrom $I_{in}\,[mA]$	100
Verteilungsfunktion der Makro-Teilchen am RFQ-Eingang	4D-Waterbag
Anzahl der Eingangs-Macro-Teilchen	100.000
Synchron-Energie am RFQ-Eingang $W_{syn,in}\,[keV]$	95
$\varepsilon_{x/y,in,rms}\,[\pi\,mm\,mrad]$	0.29
Transversaler RFQ-Eingangs-Twiss-Parameter α_{in}	0.7
Transversaler RFQ-Eingangs-Twiss-Parameter $\beta_{in}\,[mm/\pi\,mrad]$	0.04
Energieweite am RFQ-Eingang $\Delta W_{in}\,[keV]$	0.0

Tabelle 0.1: Parameter des Designstrahls am Eingang des FAIR p-Linac RFQ. (Die entsprechenden Ausgangsparameter finden sich in Tabelle 0.2).

Parameter	**Wert**
$\varepsilon_{x,out,n,rms}$	$0.34\,\pi\,mm\,mrad$
$\varepsilon_{y,out,n,rms}$	$0.33\,\pi\,mm\,mrad$
$\varepsilon_{z,out,n,rms}$	$0.21\,\pi\,MeV\,deg$
Synch. Ausgangsenergie $W_{syn,out}$	$3.015\,MeV$
Durchschnittsausgangsenergie $W_{ave,out}$	$3.011\,MeV$
Transmission	84.3 %

Tabelle 0.2: Parameter des Designstrahls am Ausgang des FAIR p-Linac RFQ (4.88 mm hinter dem Ende der Elektroden). (Die Eingangsparameter dieses Strahls finden sich in Tabelle 0.1.) Mit 3.015 MeV wurde die tatsächliche synchrone Austrittsenergie geringfügig (0.5%) höher als der geforderte Wert von 3 MeV gesetzt. Dies geschah, um eine Sicherheitsmarge zu schaffen, damit sowohl die durchschnittliche Teilchenenergie als auch die Energien einer kritischen Anzahl von Teilchen am RFQ-Ausgang nicht niedriger als 3 MeV ausfallen würden. Dies liegt nicht zuletzt daran, dass der MEBT-Abschnitt mit diesem „Überschießen“ wesentlich besser umgehen kann als mit einem „Unterschießen“. Diese Strategie ging auf, da die durchschnittliche Ausgangsenergie bei 3.011 MeV lag. Durch optimale Wahl der transversalen Twiss-Parameter am Eingang (strahldynamisch angepasster Fall / „matched case“) lassen sich die Ausgangsemittanzen noch etwas verringern und die Transmission etwas erhöhen.

Parameter	Wert
$\rho\,[mm]$	3.17 mm
$r_0\,[mm]$	3.73 mm
$\rho\,/\,r_0$	0.85
Bravery-Faktor	1.77

Tabelle 0.3: Werte des transversalen Elektrodenradius ρ, des Radius der RFQ-Zellenmitte (mittlere Apertur) r_0 und ihr Verhältnis $\rho\,/\,r_0$ für den FAIR p-Linac RFQ. Letzteres wird vom Anwender angegeben, wohingegen sich die beiden oberen Größen aus den Einstellungen in RFQGen ergeben. Der unterste Eintrag ist der sog. Bravery-Faktor, der ein Maß für das Auftreten von Spannungsdurchschlägen darstellt und u.a. von der Frequenz f der Feldschwingung abhängt (siehe Anhang C). Mit 1.77 liegt dieser hier im für RFQs üblichen Rahmen.

abgesenkten Transmission führt. Jedoch überschreitet die Elektrodenlänge des klassischen Designs den maximal zulässigen Wert von 3335 mm um fast 190 mm, womit dieses Design eine notwendige Anforderung nicht erfüllt. Anderseits würde man mit der NFSP, mit der sich besonders kurze, kompakte RFQs designen lassen, ebenfalls kein (ohne weiteres) brauchbares Alternativ-Design für den FAIR p-Linac RFQ generieren können. Gerade dessen effiziente Parameterführung und die aus ihr resultierende Kürzung der Elektroden wäre nicht (oder nur sehr schwer und in Kaufnahme anderer Schwierigkeiten/Nachteile) mit der geforderten Elektrodenmindestlänge von 3324 mm kompatibel.

Ferner werden in diesem Kapitel Simulationsreihen, die auf von der Ionenquellen-Gruppe der GSI zur Verfügung gestellten Messungen im LEBT-Abschnitt am CEA Saclay fußen [25], beschrieben und deren Ergebnisse mit den Simulationsergebnissen verglichen, die auf generischen RFQ-Eingangsverteilungen[33] basieren. Hierzu war es auch erforderlich, die in der LEBT-Sektion von R. Berezov et al. gemessen Verteilungen in den TraceWin-Code[34] einzulesen. Aus den nachfolgenden RFQGen-Simulationen ließ sich der ideale Abstand zwischen dem zweiten Solenoiden und dem RFQ auf $\leq$ 260 mm bestimmen. Hierdurch gestalten sich Entwurf und Konstruktion ei-

[33] Im Rahmen dieser Dissertation handelte es sich bei diesen ausschließlich um sog. 4D Waterbag-Verteilungen, die sich durch eine einheitliche Phasen- und eine zufällige Energieverteilung auszeichnet. Die Wahl der Verteilungsfunktion hat u.a. auch Auswirkungen auf das Verhältnis m der totalen zur sog. RMS-Emittanz. Dieses ist im Falle einer 4D Waterbag-Verteilung $m = n + 2 = 6$ [26] (vgl. Unterabschnitt D.4.1).

[34] Die in Abschnitt 3.3 und 3.7 präsentierten LEBT-Simulationen in TraceWin wurden von M. Schütt angefertigt. Die end-to-end-Simulationen mit TraceWin für den gesamten p-Linac [27] (d.h. vom Eingang des RFQ bis zum Ende der CH-Sektion), auf die in Abschnitt 3.5 verwiesen wird, wurden von H. Hähnel durchgeführt. (Andres als „Hähnel“, wird „Schütt“ außerhalb der deutschen Zusammenfassung durch die internationale Schreibweise ohne Umlaut, d.h. „Schuett“, ersetzt. Dies geschah in Absprache mit beiden Kollegen sowie im Einklang mit der Schreibweise ihrer Namen in wissenschaftlichen Veröffentlichungen, Konferenzteilnehmerlisten etc.)

nes neuen, hierauf angepassten Konus am RFQ-Eingang als sehr herausfordernd, aber machbar. Tatsächlich sind die Arbeiten am Design zum Zeitpunkt der Fertigstellung dieser Dissertation im September 2021 nahezu abgeschlossen.

Nachdem das Design des FAIR p-Linac RFQ erfolgreich in TOUTATIS eingelesen werden konnte[35], erfolgten verschiedene Simulationen mit diesem Model. Diese hatten folgende Zielsetzungen:

- Ermittlung der idealen transversalen Eingangs-Twissparameter (angepasster Fall / „machted case“); auch die Ergebnisse dieser Untersuchung decken sich mit denen der entsprechenden RFQGen-Simulationsstudien zur Ermittlung der optimalen Twiss-Parameter am RFQ-Eingang (vgl. Abschnitt 3.2).
- Reproduktionscheck der Strahldynamik-Simulation mit den für die Erzeugung des Designs in RFQGen verwendeten Eingangsstrahl-Parametern (100 mA Eingangsstrom etc.); dieser Check fiel positiv aus, d.h. die Ähnlichkeit der Teilchenverteilungen am RFQ-Ausgang im Hinblick auf Schlüssel-Parameter wie Transmission, Emittanzen, Energien etc. war erfreulich hoch (vgl. Abschnitt3.4).
- Eingangsstromstudien (mit den optimalen Twiss-Parametern), deren Ergebnisse ebenfalls ähnlich zu denen in RFQGen-Simulationen ausfielen (vgl. Abschnitt3.8).

Die hohe Reproduzierbarkeit der RFQGen-Simulationen in TOUTATIS stimmt sehr zuversichtlich auf die Robustheit des Strahldynamik-Designs.

Des Weiteren werden in diesem zentralen Kapitel der Dissertation auch noch die Ergebnisse von diversen anderen Simulationsreihen präsentiert. Diese Simulationen dienen dazu, die Auswirkungen folgender Faktoren auf die Strahldynamik zu untersuchen:

- Schwellenwert für die Energiedifferenz zwischen Teilchen- und Synchronenergie, für die RFQGen Teilchen als verloren wertet: Dieser nahezu beliebig frei wählbare Parameter hat kaum Einfluss auf die Verteilung am RFQ-Ausgang, beeinflusst aber das Teilchenverlust-Profil des RFQ. Letzteres gibt Aufschluss darüber, wo (d.h. für welche z-Werte und damit bei welchen Teilchenenergien) in welchem Maße mit Verlusten zu rechnen ist. Diese Einschätzung ist essentiell um der Aktivierung der verkupferten Struktur durch Einschläge von Protonen mit Energien über 2 MeV vorzubeugen. Gemäß der Simulationsergebnisse steht eine solche nicht zu befürchten (vgl. Abschnitt 3.5).

[35] Das Übertragen des Designs von RFQGen nach TOUTATIS sowie alle in dieser Dissertation präsentierten TOUTATIS-Simulationen wurden von H. Hähnel vorgenommen.

- Raumladungskräfte zwischen benachbarten Strahlpaketen („beam bunches“): Diese sollten keinesfalls vernachlässigt werden (wie zu erwarten für den hohen Eingangsstrom) (vgl. Abschnitt 3.6).
- Spiegelladungen: Diese scheinen sich trotz des hohen Stroms nur relativ gering auszuwirken. Die Ursachen hierfür konnten noch nicht ausgemacht werden, sodass es weiterer Nachforschungen bedarf, die möglicherweise auch Nachbesserungen an RFQGen nach sich ziehen könnten (vgl. Abschnitt 3.6).
- Wert der initialen Energiebreite: Die Strahldynamik erwies sich auch bei deutlich höheren Energieaufweitungen am RFQ-Eingang als der zu erwartenden als vergleichsweise stabil und effizient (vgl. Abschnitt 3.8).

Bereits im Juni 2019 erschien in *Nuclear Inst. and Methods in Physics Research A* ein Artikel zur Auswirkung der longitudinalen elektrischen Felder am Eingangs- und Ausgangsspalt des FAIR p-Linac RFQ auf dessen Strahldynamik [28]. Abschnitt 3.7 fasst diesen zusammen. Die in ihm präsentierten Simulationsergebnisse zeigen, dass diese Felder unbedingt während der Entwurfsphase von 4-Rod[36]-RFQs berücksichtigt werden sollten. Erste vergleichbare Untersuchungen an 4-Rod-RFQs wurden vor nahezu einem Jahrzehnt vom IAP Frankfurt (A. Schempp et al.), dem LANL (S. S. Kurennoy et al.) und dem **F**ermi **N**ational **A**ccelerator **L**aboratory[37] (FNAL) (C. Y. Tan et al.) unternommen [29, 30, 31]. Jedoch beschränkten sich diese Studien ausschließlich auf den Einfluss der longitudinalen elektrischen Felder des RFQ-Ausgangsspalts. Man kam zu dem Schluss, dass abhängig vom konkret vorliegenden Fall durch diese Felder mithin schwere Störungen der Strahldynamik auftreten können, welche sich aber durch entsprechende Sorgfalt beim HF-Design sowie unter Zuhilfenahme moderner Simulationssoftware voraussehen und abmildern lassen. Auf diese Weise lassen sich trotzdem immer noch gut funktionierende, effiziente 4-Rod-RFQs designen und fertigen [31].

Es stand jedoch zu vermuten, dass die longitudinalen elektrischen Felder des Eingangsspalts den dort noch relativ langsamen Strahl deutlich stärker beeinflussen sollten. Die aktuellen Studien

[36] Die Klassifikation des FAIR p-Linac Leiter-RFQ als 4-Rod-RFQ bezieht sich hierbei primär auf die Aufhängung seiner Elektroden, die wie bei „tatsächlichen“ 4-Rod-RFQs für ein signifikantes oszillierendes elektrisches Potential entlang der Strahlachse und somit zu nicht vernachlässigbaren longitudinalen Feldkomponenten zwischen den Elektrodenenden und den (inneren) RFQ-Tankwänden sorgen.

[37] Das Fermi National Accelerator Laboratory (kurz: Fermilab) ist ein vom U.S. Department of Energy betriebenes Teilchenphysik-Forschungszentrum in Batavia, Illinois. 2012 wurde der dortige Cockcroft-Walton-Injektor nach vierzig Betriebsjahren durch eine neue Strahlführung ersetzt, die auch einen 750 keV 4-Rod-RFQ beinhaltet, welcher von A. Schempp et al. am IAP Frankfurt entwickelt wurde (`https://news.fnal.gov/2012/08/so-long-cockcroft-walton`).

hierzu bestätigen dies: Die Eingangsfelder können sich besonders fatal, im Idealfall allerdings auch deutlich vorteilig auf die Strahldynamik eines 4-Rod-RFQ auswirken. Wird die Länge des Eingangsspalts in Hinblick auf die Phase des Synchronteilchens bei Eintritt in den Spalt und auf das durch die Raumladungskräfte bedingte Emittanzwachstum besonders günstig bzw. sogar optimal gewählt, kann der Eingangspalt als eine Art Vor-Buncher fungieren, d.h. die Raumladungsdichte des Strahls bereits entlang der z-Achse modulieren und somit den späteren, eigentlichen Bunchvorgang sanfter und effizienter gestalten. Aus diesen Gründen sollten die Auswirkungen der longitudinalen elektrischen Felder in beiden Spalten für jeden 4-Rod-RFQ vor Finalisierung seines Designs untersucht werden. Wünschenswert wäre zudem die Erweiterung von RFQ-Strahldynamik-Codes wie RFQGen dahingehend, dass diese Felder bzw. ihre Auswirkungen auf die Strahldynamik in den Simulationsprozess integriert werden[38].

Im letzten Abschnitt dieses Kapitels werden die Spannungsstudien präsentiert: Im April 2019 folgte der letzte Bearbeitungsschritt hinsichtlich der Frequenzeinstellung und der Ebenheit der elektrischen Feldverteilung[39] entlang des FAIR p-Linac RFQ. An diesen schlossen sich unmittelbar entsprechende Messungen an [5]. Abbildung 0.4 zeigt die inhomogene Verteilung des elektrischen Feldes entlang des RFQ vor (rote Kurve) und nach dem Tuning (schwarze Kurve). Leider bietet RFQGen für seine Strahldynamiksimulationen keine Möglichkeit die relativ komplexe, tatsächlich vorhandene Spannungsverteilung entlang des RFQ einzustellen bzw. zu simulieren. Allerdings ist RFQGen in der Lage, einfachere Spannungsverteilungen entlang des RFQ zu generieren, so dass man sich nicht darauf beschränken muss, die Strahldynamik mit einer konstanten, der Designspannung entsprechenden Spannung, entlang des RFQ zu simulieren.So war es de facto möglich, die gemessene Spannungsverteilung durch eine hinreichend feine Stufenfunktion anzunähern[40]. Im Zuge dessen wurde der RFQ in mehrere z-Intervalle mit jeweils konstanter Spannung entsprechend dem jeweiligem Intervall-Mittelwert[41] unterteilt (vgl. blaue Kurve in Abbildung 0.4).

[38] Komplexere Behelfslösungen, die zwei oder mehr verschiedene Strahldynamik-Codes umfassen, könnten (und sollten) aber weiterhin zur Gegenkontrolle herangezogen werden.

[39] Hierfür haben sich auch innerhalb der deutschen Beschleuniger-Gemeinde die Begriffe „Field-Flatness“ bzw. „Flatness“ etabliert.

[40] Dies trifft streng genommen nicht zu, da eine solche Option in RFQGen nicht existiert. Allerdings wurde ein äquivalentes Vorgehen gewählt. Hierzu wurde der RFQ zunächst in mehrere Intervalle aufgeteilt. Die Spannungswerte wurden in jedem Intervall gemittelt und je Intervall wurde eine Strahldynamiksimulation mit einer dem jeweiligen Mittelwert entsprechenden, über das Intervall konstanten Spannung durchgeführt (RFQGen erlaubt die freie Auswahl der Start- und Endzellen der Simulation). Die Ausgangsverteilung eines Intervalls wurde hierbei als Eingangsverteilung für das jeweils nachfolgende eingelesen. Solche vergleichsweise aufwändige, langwierige und fehleranfällige Behelfslösungen ließen sich nach möglichen Modifikationen der RFQ-Strahldynamik-Codes durch eine einzelne Simulation ersetzen. Hierzu müsste es diesen Codes ermöglicht werden, komplexere Spannungsverteilungen entlang der Strahlachse zu generieren und/oder einzulesen.

[41] Die einzige Ausnahme bildet hier das lange mittlere Intervall, dem die Design-Elektrodenspannung von 88.43 keV zugeordnet wurde. Dies geschah u. a. in Hinblick auf eine Maximalfehler-Abschätzung.

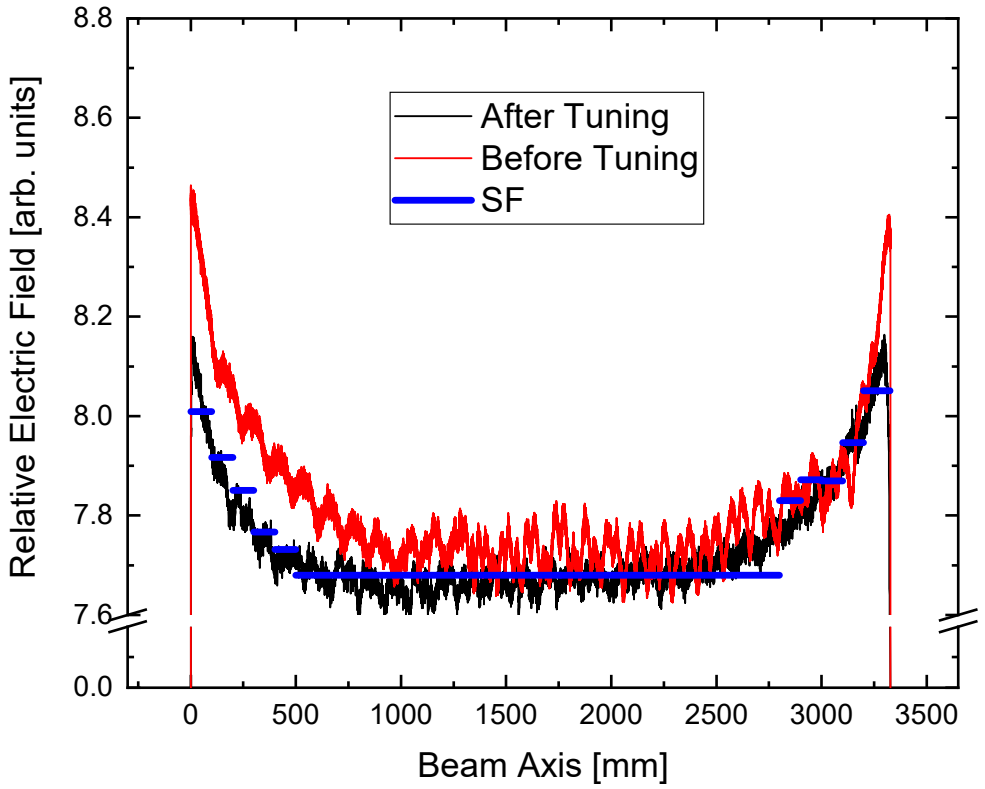

Abbildung 0.4: Feldebenheit des FAIR p-Linac RFQ, d.h. das elektrische Feld (willkürliche Einheit) entlang der Strahlachse des FAIR p-Linac RFQ, vor (rot) und nach (schwarz) dem Tuning (mit freundlicher Genehmigung vom M. Schütt; vgl. Abbildung 4 in Ref. [4]). Die blaue Kurve zeigt die Durchschnittswerte in den jeweiligen Intervallen. Die einzige Ausnahme stellt das lange mittlere Intervall dar: Das hier eingezeichnete Feld ergibt sich direkt aus der Design-Elektrodenspannung von 88.43 keV.

Die Unterschiede zur originalen Simulation mit konstanter Designspannung entlang des RFQ, d.h. mit homogener Feldverteilung, waren hier marginal. Die Strahldynamik schien diese Abweichungen zur Designspannung gut verkraften zu können. Daher wurde die Stufenfunktion im Rahmen weiterer Simulationsreihen dahingehend angepasst, dass sich hier jeweils ein vielfaches f der gemessen Spannungsabweichung entlang des RFQ ergab[42]: $f = \frac{V_f - V_{des}}{V_{mess} - V_{des}}$, wobei V_f die entsprechend erhöhte, zur Strahldynamiksimulation verwendete Spannung und V_{mess} die gemessene (bzw. aus den Messwerten für das jeweilige Intervall der Stufenfunktion gemittelte) Spannung darstellt. Erst bei ungefähr der fünffachen gemessenen Abweichung ergaben sich erste signifikante

[42] f steht hier schlicht für „Faktor“ und ist nicht mit der Frequenz zu verwechseln.

Änderungen in einigen Parametern der Ausgangsverteilungen. Für $f = 7.5$ und $f = 10.0$ sind alle Parameter in beachtlichem Ausmaß unterschiedlich zu ihren Originalwerten (d.h. mit homogener Spannungsverteilung entlang des RFQ). Man beachte, dass sich für $f = 10$ Abweichungen von der Designspannung von bis zu $+50\%$ ergaben. Die Grenze zum Spannungsüberschlag wird bereits deutlich vorher überschritten. Während also die Simulationen mit $f = 2$ noch eine pessimistische Fehlerabschätzung liefern, dienten die Simulationen mit höheren f-Werten lediglich der isolierten Untersuchung der Auswirkungen der Abweichungen auf die Strahldynamik. Die Simulationsreihen waren jedoch insofern konsistent, als dass die Parameterkurven bereits für kleine f-Werte gewisse Auffälligkeiten aufwiesen, von den die meisten sich in zunehmendem Maße mit wachsendem f verstärkten.

Der FAIR p-Linac RFQ traf Anfang 2020 in der Experimentierhalle des IAP ein. Aufgrund des kurz darauf folgenden COVID19-Lockdowns mussten die geplanten Messungen und Tests verschoben werden. Die nächsten Schritte umfassen:

- weiteres Tuning der Frequenz und zur Verbesserung der Flatness mit Dummykolben aus Aluminium (vgl. Ref. [5])
- Fertigung und Montage der eigentlichen, wassergekühlten Kupfer- oder Edelstahlkolben, deren Design sich aus den vorangegangenen Messungen ergibt
- Konditionierung bei Niederleistung
- Fertigstellung des Eingangskonus
- Transport des RFQ zum Klystron HF-Teststand der GSI für den Betrieb am Leistungspegel des HF-Designs.

Die ersten Strahltests sind für frühestens 2023 geplant und werden vermutlich erst im p-Linac-Gebäude auf dem FAIR-Gelände erfolgen bzw. nach Installation der Quelle, der LEBT-Sektion und des RFQ in dieses. Zum Zeitpunkt der Fertigstellung dieser Dissertation im September 2021 ist die erfolgreiche Inbetriebnahme der Ionenquelle bereits erfolgt: Die gemessenen Parameter passen zu den bei der Auslegung des RFQ getätigten Annahmen[43].

Kapitel [4] widmet sich einer Studie zum Strahldynamik-Design eines kompakten RFQ, ebenfalls mit einer Betriebsfrequenz von 325.224 MHz, der mit knapp 1.6 m Elektrodenlänge Protonen von 25 keV auf 2 MeV beschleunigen würde. Neben diversen industriellen und kunsthistorischen Anwendungen, wäre vor allem ein Einsatz dieses RFQ in der Nuklearmedizin, aber auch in der

[43] Korrespondenz mit C. Kleffner (GSI)

Strahlentherapie denkbar. So kommen offene radioaktive Quellen bei medizinischen Anwendungen jährlich über 30 Millionen mal zum Einsatz. Dies umfasst sowohl die Diagnose verschiedenster Krankheiten als auch die gezielte Behandlung befallener Körperregionen unter möglichst umfassender Schonung gesunden Zellgewebes. Radionuklide sind von essentieller Bedeutung für die Nuklearmedizin und müssen bis auf wenige Ausnahmen durch künstliche Transmutation gewonnen werden, die entweder durch Kernreaktoren oder Teilchenbeschleuniger getrieben werden. In diesem Kapitel wird zur Einleitung detailliert auf die möglichen Anwendungsgebiete eines solchen RFQ eingegangen. Hierzu werden u. a. auch kurz bereits existente Niederenergie-Kompakt-RFQs wie der PIXE[44] / COMPASS[45]-RFQ [32, 33] des CERN sowie die am IAP entwickelten HIT[46]- und MedAustron[47]-RFQs [34, 35] beschrieben.

Es besteht noch Bedarf an einem neuen kompakten Niederenergie-RFQ mit geringem Tastverhältnis, der Protonen von ca. 20 keV auf ca. 2.0 MeV beschleunigt und dabei für Eingangströme zwischen 5 und 10 mA Transmissionswerte von etwa 70% erreicht. Tabelle 0.4 zeigt die vorläufigen Schlüsselparameter (der Strahldynamik) eines solchen RFQ im Vergleich zu denen des FAIR p-Linac RFQ (die Betriebsfrequenz beider RFQs beträgt 325.224 MHz). Mit einer Elektrodenlänge von 1561.2 mm und einer Spannung zwischen diesen von 88.00 kV sowie einem erwartbaren Ausgangsstrom von mindestens 3.75 mA wäre dieser RFQ gut geeignet für eine Vielzahl verschiedener medizinischer und nicht-medizinischer Anwendungen.

[44] **P**roton **I**nduced **X**-ray **E**mission

[45] **CO**mmon **M**uon and **P**roton **A**pparatus for **S**tructure and **S**pectroscopy

[46] Das **H**eidelberger **I**onenstrahl-**T**herapiezentrum (HIT) ist ein deutsches Zentrum für die Teilchenstrahltherapie von Krebspatienten mit beschleunigten Protonen und Kohlenstoff-Ionen auf dem Gelände des dortigen Universitätsklinikums. Das HIT war die erste europäische Therapieeinrichtung, bei der auch Schwerionen zum Einsatz kommen, und weltweit die erste mit Gantry, d.h. einer beweglichen Strahlführungsanlage, die eine 360°-Rotation des Strahls um den Patienten ermöglicht (`https://www.klinikum.uni-heidelberg.de/interdisziplinaere-zentren/heidelberger-ionenstrahl-therapiezentrum-hit`).

[47] Das MedAustron-Zentrum für Ionentherapie und Forschung befindet sich in Wiener Neustadt in Niederösterreich (`https://www.medaustron.at/de`).

Parameter	**p-Linac RFQ**	**Kompakter RFQ**
Eingangsenergie $W_{syn}\,[keV]$	95	25
Eingangsstrahlstrom $I_{in}\,[mA]$	100	5
Elektrodenlänge [mm]	3329.8	1561.2
Long. Elektrodenprofil	sinusoidal	sinusoidal
Elektrodenspannung [kV]	88.43	88.00
Anzahl der RFQ-Zellen	245	124
ρ/r_0	0.85	0.85
$\rho\,[mm]$	3.2	3.2
$r_0\,[mm]$	3.8	3.8
$a_{min}\,[mm]$	2.4	2.3
m_{max}	2.02	1.98
Anzahl der RM-Zellen	5	5
Ausgangssynchronph. $\phi_{syn,out}$ [deg]	-22.40	-30.03
$\varepsilon_{x/y,in,rms}\,[\pi\,mm\,mrad]$	0.30	0.15
$\Delta W_{in}\,[keV]$	0.0	0.1
$\varepsilon_{x,out,rms}\,[\pi\,mm\,mrad]$	0.32	0.22
$\varepsilon_{y,out,rms}\,[\pi\,mm\,mrad]$	0.32	0.22
$\varepsilon_{z,out,rms}\,[\pi\,MeV\,deg]$	0.20	0.13
Synchrone Ausgangsenergie $W_s\,[MeV]$	3.015	2.043
Mittlere Ausgangsenergie $W_{ave}\,[MeV]$	3.011	2.045
Transmission [%]	88.470	74.381

Tabelle 0.4: Vergleich der Schlüsselparameter zwischen dem FAIR p-Linac RFQ und dem neuen kompakten RFQ. Die Strahlparameter an den RFQ-Ausgängen beziehen sich bei ersterem auf die Werte 4.88 mm und bei letzterem auf die 4.81 mm hinter dem Ende der Elektroden.

Abbildung 0.5 zeigt die Strahlendynamik-Designs des neuen kompakten RFQ, d.h. die Kurven von m, a und ϕ gegen die Zellennummer (oben) und z-Achse (unten).

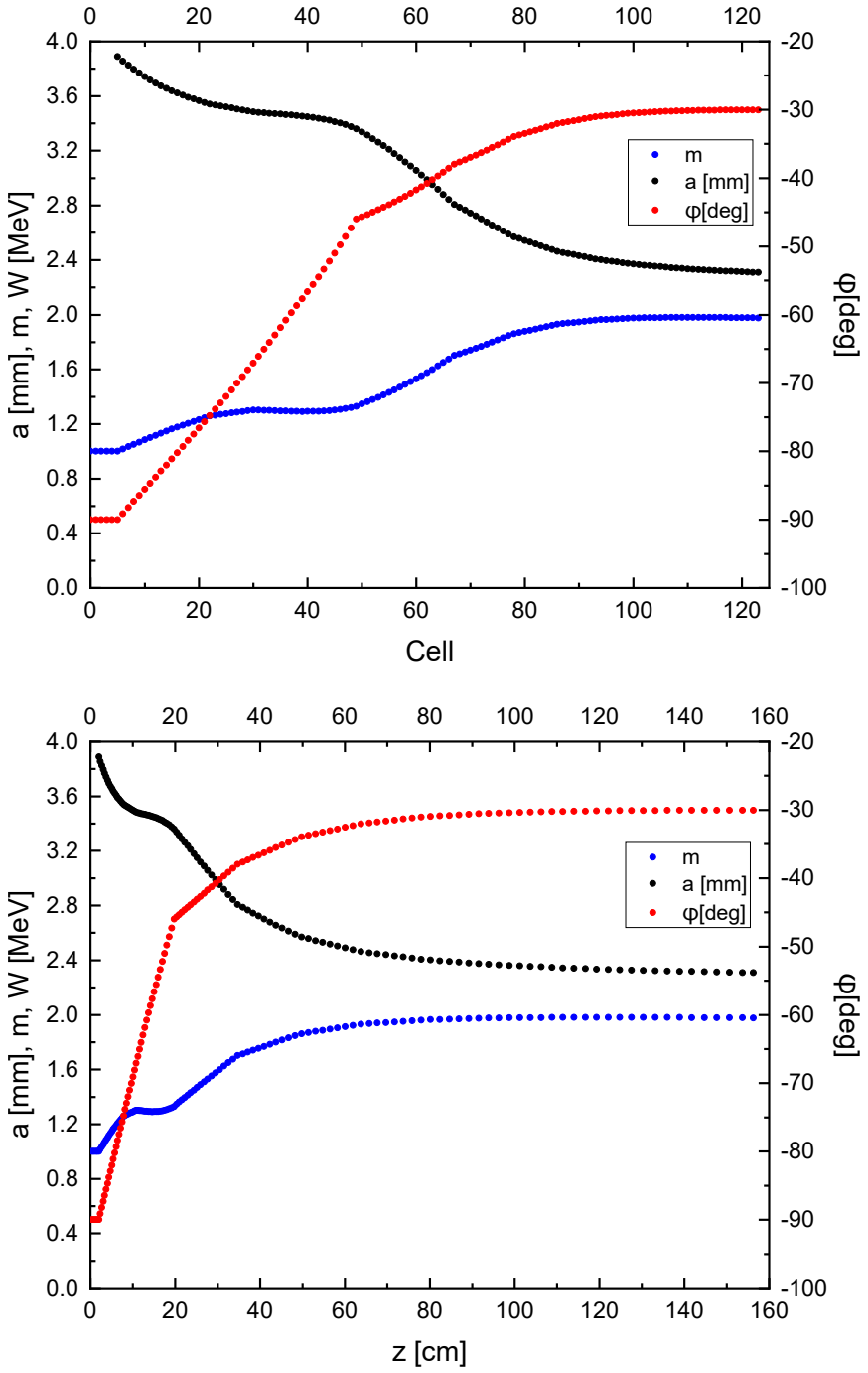

Abbildung 0.5: Strahldynamik-Design des neuen kompakten RFQ: Parameterkurven gegen die Zellennummer (oben) und z-Achse (unten) aufgetragen.

Die Phasenraumplots am Ausgang des neuen kompakten RFQ, d.h. 4.81 mm hinter dem Ende der Elektroden (vgl. Tabelle 0.4), sind in Abbildung 0.6 zu sehen. Die Verteilung im longitudinalen

Unterraum weist eine gewisse Spiralförmigkeit auf (analog zu denen, die sich für Simulationen mit niedrigem Eingangsstrom in den FAIR p-Linac RFQ ergeben (vgl. Abschnitt 4.4)). Das Fehlen von potenziell schädlichen Auffälligkeiten wie der Ausbildung mehrerer Bunchzentren gibt Anlass zu Optimismus.

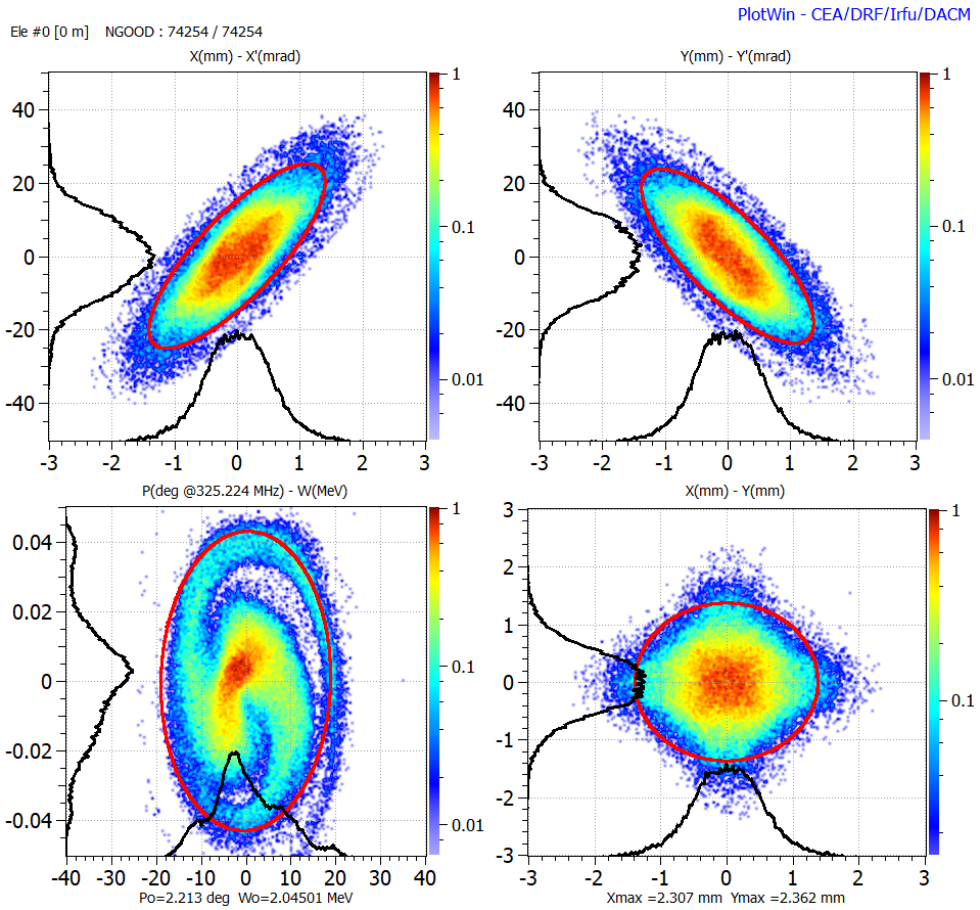

Abbildung 0.6: Phasenraumplots und die Projektionen der Verteilungen (schwarze Kurven) am Ausgang des neuen, kompakten RFQ, d.h. 4.81 mm hinter den Elektrodenenden (vgl. Tabelle 0.4). Der Eingangsstrom betrug 5 mA, die Anzahl der Makro-Teilchen am Eingang war 10^5. Die Färbung der Punktdiagramme bezieht sich auf die normierte Makro-Teilchendichte (vgl. Skalen an den rechten Rändern der Diagramme), die roten Ellipsen beziehen sich auf die normierten 95%-Emittanzen.

Abbildung 0.7 zeigt die Kurven der longitudinalen und transversalen Nullstrom-Phasenvorschübe $\sigma_{0l/t}$ gegen die Zellennummer für den FAIR p-Linac RFQ (links) und den neuen kompakten RFQ (rechts). Eine innerhalb weiter Teile der RFQ-Gemeinschaft Zuspruch findende „Faustregel“ besagt, dass sich beide Kurven (zumindest innerhalb der Gentle Bunching- und der Beschleunigungs-

sektion) möglichst nicht schneiden sollten, da dies den sogenannten Emittanztransfer, oder auch: austauschsbedingte Resonanzen, während des Bunches/Beschleunigens begünstigen könnte. Solche Resonanzen wurden innerhalb der Strahldynamik-Gemeinde über Jahrzehnte hinweg durchgehend untersucht, woran neben anderen auch I. Hofmann einen großen Anteil hatte [36, 37]. Jüngere Veröffentlichungen zu diesen Resonanzen in RFQs stammen u.a. von R. A. Jameson [38] sowie C. Zhang und H. Podlech [19].

Während die $\sigma_{0l/t}$-Kurven des p-Linac-RFQ sich nicht schneiden, ist dies für den neuen kompakten RFQ an zwei Stellen der Fall. Jedoch weisen u. a. auch der Linac2-RFQ[48] am CERN sowie der HIT/MedAustron-RFQ jeweils mindestens eine solche Überschneidung auf [34, 35], ohne dass diese für den Betrieb dieser RFQs Probleme verursachen.
Ob sich also durch solche Überschneidungen der Nullstrom-Phasenvorschubkurven Probleme ergeben bzw. worin genau diese sich äußern und in welchem Maße, sollte falls möglich für jeden RFQ individuell untersucht werden. Überlegungen, diesen Sachverhalt für das vorliegende Design möglichst zeitnah abschließend zu klären (sowie die Durchführung der dann evtl. notwendigen Modifikationen am Design), wird Gegenstand zukünftiger Anstrengungen sein.

Zusammenfassend lässt sich festhalten, dass dieses erste Strahldynamik-Design für einen möglichen zukünftigen, kompakten Niederenergie-RFQ mit geringem Tastverhältnis sich bisher als sehr vielversprechend erwiesen hat. Die Ergebnisse der Eingangsstudien geben weitere Zuversicht, dass ein praktikables Strahldynamik-Design bereits gefunden (oder zumindest grob umrissen) wurde. Auch die Verlustprofile entlang des RFQ geben keinen Anlass, die Verlässlichkeit des Designs anzuzweifeln[49].

Neben Studien zur Auswirkung der Wahl des Verhältnisses ρ/r_0 sollte auch die die Optimierung der RFQ-Enden, besonders des Hochenergie-Endes in Hinblick auf die longitudinalen elektrischen Felder erfolgen (wie für den FAIR p-Linac RFQ bereits geschehen (vgl. Abschnitt 3.7)). Trotz der glatten Ränder des von RFQGen generierten Strahlprofils entlang des RFQ, die auf bereits (hinreichend) passend gewählte transversale Twiss-Parameter am Eingang schließen lassen, sind dezidierte Studien zu diesen in RFQGen mit anschließender Gegenprobe in TOUTATIS auch

[48] Persönliche Korrespondenz mit A. M. Lombardi.
[49] Die (Haupt-)Motivation für die entsprechenden Studien war hier eine andere als im Falle des FAIR p-Linac RFQ: Da die Ausgangsenergie von 2 MeV nahezu identisch mit der Schwellenenergie für die Aktivierung von Kupfer ist, war hier von Anfang an mit Aktivierung (innerhalb des RFQ) nicht oder schlimmstenfalls nur sehr vereinzelt zu rechnen. Ziel dieser Studien war vielmehr, mögliche kritische Positionen entlang des RFQ auszumachen, um ggf. eine Optimierung der Strahlführung bzgl. dieser vornehmen zu können sowie generell die Verlässlichkeit und Aussagekraft der Strahldynamiksimulationen zu überprüfen.

hier durchzuführen, sobald das eigentliche Design feststeht (vgl. Abschnitte 3.2 und 3.4). Nachdem der strahldynamisch angepasste Fall ermittelt und bestätigt ist, sind auch für dieses Design Eingangsstromstudien durchzuführen – der angestrebte Eingangsstrahlstrom dürfte in Hinblick auf das Emittanzwachstum sowie den für die möglichen Anwendungen optimalen Strahlstrom am RFQ-Ausgang wohl nach wie vor bei ca. 5 mA liegen. Weitere Untersuchungen sollten auch eine erste Toleranzstudie bzgl. Spannungsabweichungen beinhalten. Sobald die Entwicklungsstadien des mechanischen und des HF-Designs es zulassen, sollten auch Flatness-Simulationen in die Strahldynamikrechnungen einfließen. In einem deutlich später zu erfolgenden Schritt – der erst nach Fertigstellung des RFQ bzw. nach den ersten Messungen und Tuningarbeiten erfolgen kann – wäre dann die gemessene Feldverteilung in die Strahldynamiksimulationen einzubauen bzw. für diese abzubilden (vgl. Abschnitt 3.9).

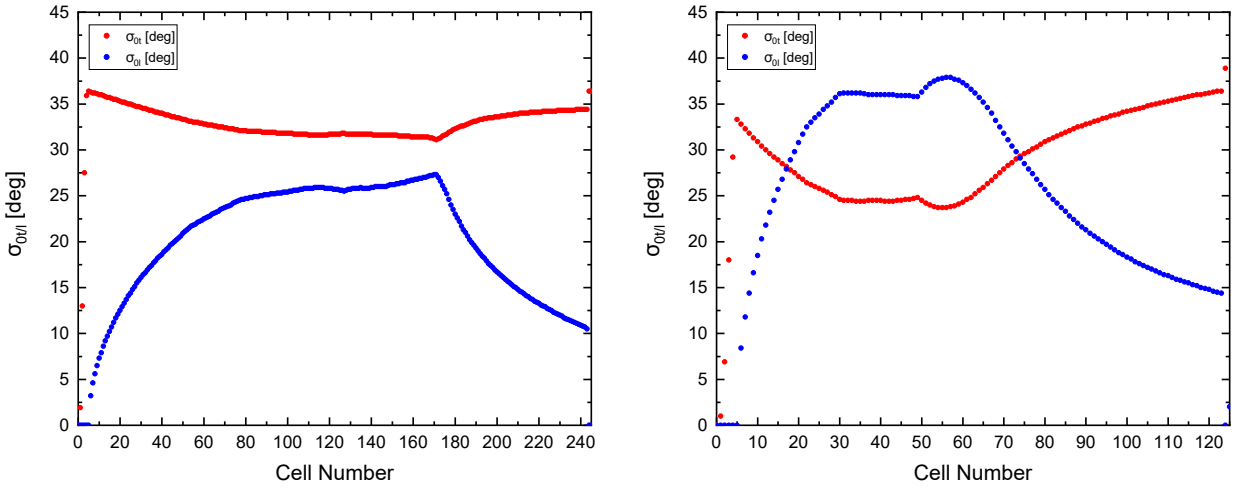

Abbildung 0.7: Kurven der longitudinalen und transversalen Nullstrom-Phasenvorschübe $\sigma_{0l/t}$ gegen die Zellennummer für den FAIR p-Linac RFQ (links) und den neuen kompakten RFQ (rechts).

Ausblick

Von nicht unerheblichem Interesse für zukünftige Forschungsarbeiten wäre möglicherweise auch die Entwicklung alternativer Elektrodendesigns für die beiden in dieser Dissertation präsentierten RFQs. Hierbei könnte neben RFQGen auch weitere Software zur Entwicklung von RFQ-Strahldynamik-Designs zum Einsatz kommen. So veröffentlichte das CEA erst in jüngerer Vergangenheit seinen „RFQ Designer“-Code[50]; Strahldynamik-Simulationen an den mit diesem erzeugten Designs können ebenfalls mit TOUTATIS durchgeführt werden. Prinzipiell wären diese Alternativ-Designs den gleichen Design- und Fehlerstudien zu unterziehen, die auch die in dieser Arbeit vorgestellten Designs bereits durchlaufen haben bzw. noch werden. Sofern möglich sollte jede Simulation dieser Studien jeweils mit mindestens einem weiteren RFQ-Strahldynamik-Code wiederholt werden. Die Aussicht beim Vergleich der Ergebnisse der verschieden Codes auf unerwünschte und/oder voneinander abweichende Ergebnisse zu stoßen, sollte keinesfalls abschrecken, da ihnen potentiell tiefere Erkenntnisse innewohnen könnten. Im Idealfall ließen sich durch sie nicht nur vor Fertigung der RFQs (bzw. ihrer Elektroden) potentiell fatale Design-Fehler aufspüren und beheben, sondern auch wichtige Hinweise auf mögliche Lücken und Fehler in den Codes gewinnen. Sollten diese nicht (allein) in den Algorithmen der Codes begründet liegen, wäre wohl auch eine (partielle) Re-Evaluierung der den Codes zu Grunde liegenden Näherungen und Formeln in Betracht zu ziehen. Ein reger Austausch zwischen Anwendern und Autoren[51] von RFQ-Strahldynamik Codes ist und bleibt unerlässlich für die in Hinblick auf Ressourcenverbrauch und Zeitaufwand optimierte Entwicklung immer leistungsfähigerer, anspruchsvollerer, spezialisierterer und effizienterer RFQ-Designs[52].

[50] `http://irfu.cea.fr/en/Phocea/Page/index.php?id=932`

[51] Natürlich sind auch die Autoren solcher Codes Mitglieder der RFQ-Strahldynamik-Gemeinschaft und zählen somit auch zur Gruppe der Anwender. Die Unterscheidung sollte also zwischen jenen Mitgliedern der RFQ-Strahldynamik-Gemeinschaft getroffen werden, die RFQ-Strahldynamik-Software entwickeln und anwenden, und jenen, die zwar solche Software anwenden, aber nicht direkt an ihrer Entwicklung mitwirken. (Es ließe sich ihnen jedoch durchaus ein indirekter Beitrag zur Entwicklung der Codes zuschreiben, da ihr Feedback für die Autoren im Hinblick auf die Wartung und Weiterentwicklung ihrer Software von großem Wert ist.)

[52] Ein fruchtbarer Austausch zwischen den Designern der RFQ-Strahldynamiken und solchen der mechanischen und HF-Designs ist ebenfalls unerlässlich. Auch wenn sich ein Trend zur Spezialisierung ausmachen lässt, existieren auch zwischen diesen Personenkreisen nicht unerhebliche Überlappungen.

[1] Introduction

Accelerator facilities and components are indispensable for basic research in areas such as nuclear physics, particle physics and astrophysics, as well as for a variety of applications in medicine and industry. They offer unique methods to reproduce states of matter and energy that otherwise only exist in far away regions of our universe. Particle accelerators can be classified regarding the following four categories:

- electron and ion accelerators
- circular and linear accelerators.

Linear accelerators can function both as stand-alone machines/systems and as particle beam injectors for circular accelerators. There exist two categories of linear accelerators: electrostatic linear accelerators and radio frequency or RF **lin**ear **ac**celerators, which can be abbreviated as "RF linacs" or simply "linacs". The term "linac" nowadays almost exclusively refers to RF linacs, whereas electrostatic linear accelerators are usually referred according to their type directly: e.g. the van de Graaff-accelerator.

A linac system usually consists of three main parts: an ion source, a **R**adio **F**requency **Q**uadrupole (RFQ) linac followed by a **D**rift **T**ube **L**inac (DTL). A **L**ow **E**nergy **B**eam **T**ransport (LEBT) line is placed between the source and the RFQ, and a **M**edium **E**nergy **B**eam **T**ransport (MEBT) line is placed between the RFQ and the succeeding structures to match the beam between the respective sections.

1.1 The FAIR Project of GSI

GSI[1] was founded in 1969 to perform research on heavy ion acceleration, atomic and nuclear physics. A further pillar of GSI is the application of research results to solve scientific or engineering problems in these fields. The synthesis of heavy elements and accelerator driven tumor

[1] GSI Helmholtzzentrum für Schwerionenforschung (GSI Helmholtz Centre for Heavy Ion Research), formerly **G**esellschaft für **S**chwer**i**onenforschung (German: Society for Heavy Ion Research); `https://www.gsi.de/en/start/news`.

therapy have been main topics so far, although the fields of atomic physics, spectroscopy, material sciences and biophysics are also of high relevance. Commissioning of the **Uni**versal **L**inear **Ac**celerator (UNILAC[2]) in its first version took place in 1975. This 120 m long linac can accelerate ions as light as hydrogen and such as heavy as uranium to 11.4 MeV. The chemical elements Z = 107 to 112 were discovered in the following two decades. In 1990, GSI's first heavy ion synchrotron SIS18 (German: **S**chwer**i**onen-**S**ynchrotron) with a rigidity of up to 18 Tm went online. In the same year the ESR[3] was launched. Besides other features electron- and laser-cooling enable the ESR to store high brilliant ion beams with energies up to 560 MeV/u. In 1997 the first successful tumor treatment of a patient using carbon ions at an energy range of $200 - 400$ MeV/u was carried out. The PHELIX[4] laser paved the way for a whole array of new areas of research in 2008. This versatile Nd:glass laser system delivers intense laser beams for both pico-second pulses at $2 \cdot 10^{21}\, W/cm^2$ or nano-second pulses at $10^{16}\, W/cm^2$.

In 1991 the high charge-state injector (German: **H**och**l**adungs**i**njektor (HLI[5])) was commissioned, which comprises the first RFQ IH[6]-DTL combination ever built [39, 40, 41]. Developed at IAP[7] Frankfurt by U. Ratzinger, A. Schempp et al. and GSI Darmstadt, it mainly serves the super heavy element research (SHIP[8], TASCA[9]), one of GSI's outstanding projects. After initial problems with the RFQ could be overcome, it worked reliably for many years. Since the original RFQ was designed only for 25 % duty cycle and plans to build a new superconducting linac to provide 100% duty cycle operation became increasingly specific, it was decided to launch a front-end upgrade program for the HLI. Commissioning of the new RFQ, which was developed at IAP, Frankfurt, as well, took place in 2010.

[2] More information is given at `https://www.gsi.de/en/researchaccelerators/accelerator_facility/linear_accelerator`.

[3] **E**xperimental **S**torage **R**ing (`https://www.gsi.de/en/researchaccelerators/accelerator_facility/storage_ring`)

[4] (**P**etawatt **H**igh-**E**nergy **L**aser for Heavy **I**on E**X**periments (`https://www.gsi.de/en/work/research/appamml/plasma_physicsphelix/phelix`)

[5] `https://www.gsi.de/en/work/beschleunigerbetrieb/beschleuniger/unilac/unilac/high_charge_state_injector`

[6] Two different kinds of H-mode structures have been developed in recent decades: the interdigital H-mode (IH) structure and the crossbar H-mode (CH) structure. The IH mode might be considered as similar to a TE_{110}-like mode of a pillbox cavity, whereas the CH mode resembles a TE_{210} pillbox cavity mode [26].

[7] The Institute for Applied Physics is one of six institutes of the physics faculty of Goethe University at Frankfurt am Main, Germany (`https://www.uni-frankfurt.de/49311579/IAP`).

[8] **S**eparator for **H**eavy **I**on Reaction **P**roducts (`https://www.gsi.de/en/researchaccelerators/research_an_overview/new_elements/production`)

[9] **T**rans **A**ctinide **S**eparator and **C**hemistry **A**pparatus (`https://www.gsi.de/en/researchaccelerators/research_an_overview/new_elements/production`)

The High Current Injector (German: **H**och**s**trom**i**njektor (HSI[10])) provides an increase of beam intensities and thus for all ions – including Uranium [2] – charges the synchrotron up to its space-charge limit[11]. Accelerating ion species with A/q-values[12] of up to 65 ($^{130}Xe^{2+}$) within the given length of the former Wideröe injector of UNILAC required an increase of the acceleration gain by a factor of 2.5. A 15 mA $^{238}U^{4+}$ beam coming out of the HSI should result in $4 \cdot 10^{10}\, U^{73+}$ particles being accepted in the SIS18 during 100 µs.

The 36 MHz HSI is fed by two ion source terminals. The ion beam is accelerated from 2.2 keV/u up to 120 keV/u within the RFQ. The IH1-cavity accelerates the ion beam up to 0.743 MeV/u, while the IH2-cavity accelerates it to its final HSI energy of 1.4 MeV/u. The ions then get stripped (for example from U^{4+} to U^{28+}) and separated by their charge-state before one charge-state can be matched to the Alvarez-DTL. Here, acceleration takes place up to 11.4 MeV/u without any significant particle loss.

The FAIR (**F**acility for **A**ntiproton and **I**on **R**esearch) project[13] was officially started in 2007. FAIR extends the existing UNILAC and SIS18 by a synchrotron SIS100 as a main accelerator[14] The already existing GSI accelerators will function as its injector. SIS100, with a circumference of 1100 m, a rigidity of up to 100 Tm and a fast ramping of 4 T/s, will accelerate high intensity heavy ion beams with A/q-values as low as 8.5 up to 1 GeV/u at a repetition rate of 0.5 Hz. For shielding reasons, the tunnel will be installed 20 m below surface, which causes minimum impact of this facility on the environment. The tunnel design also took into account a possible upgrade by an additional SIS300 [42].

Also included in FAIR will be additional rings like a **C**ooler **R**ing (CR) and the **H**igh-**E**nergy **S**torage **R**ing (HESR). The new**Super**conducting **Fr**agment **S**eparator (Super-FRS[15]) will be a powerful in-flight separator for relativistic radioactive beams and exotic nuclei. The CR is isochronously operated and offers stochastic cooling as well as mass analysis for short-lived radioactive ions and anti-protons and will provide secondary particle beams. The HESR is optimized

[10] `https://www.gsi.de/en/work/beschleunigerbetrieb/beschleuniger/unilac/unilac/high_current_injector`

[11] If this upper current limit is surpassed, the space-charge interactions within the beam can no longer be counterbalanced by the present focusing forces and rapid emittance growth occurs.

[12] A is the (atomic) mass number or nucleon number of the ion-species, q is its charge-state.

[13] `https://www.gsi.de/en/researchaccelerators/fair`

[14] Analogous to SIS18, "100" refers to the synchrotron's maximum rigidity in Tm. More information on the Subproject SIS100/SIS18 (SIS) of FAIR is provided at: `https://www.gsi.de/en/work/project_management_fair/sis100sis18_sis`.

[15] `https://www.gsi.de/work/forschung/nustarenna/nustarenna_divisions/frs_super_frs/super_frs`

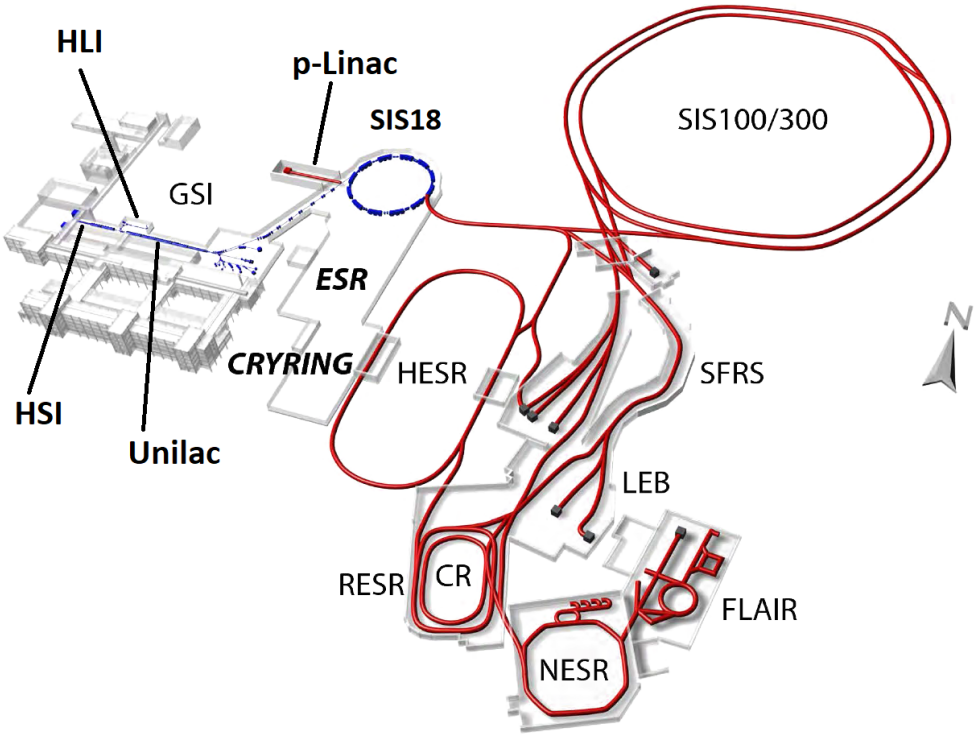

Figure 1.1: Overview of the GSI and FAIR project: The already existing GSI facilities UNILAC, SIS18, ESR and CRYRING are shown in blue. (An overview of these and further facilities is provided at `https://www.gsi.de/en/work/research/appamml/atomic_physics/experimental_facilities`.) The upcoming FAIR facilities are colored red. (Figure modified from Fig. 1 of Ref. [1]).

for storing and cooling anti-protons of energies as high as 14 GeV. Besides an internal fixed target, it will also contain the PANDA (see below) detector, which combines two spectrometers for 4π-detection around the interaction region as well as for forward direction. This Anti-proton experimental program needs high intensity proton beams as a starting point. These will be delivered by a new high current proton-linac (see Fig. 1.2), where the RFQ described in this thesis is the first element of the RF accelerator.

The protons will be injected into SIS18 from the the new p-linac at an energy of 68 MeV to be further accelerated to 4 GeV [1]. In SIS100 four proton bunches of SIS18 are united into a single bunch, that subsequently is compressed into a 50 ns pulse to be accelerated up to 29 GeV. In that way a single bunch of up to $2 \cdot 10^{13}$ protons will be extracted and sent to the anti-proton target. For fixed target experiments, the proton beam can alternatively be slowly extracted from the SIS100.

Although not directly relevant to this thesis, besides accelerating protons, SIS18 and SIS100 are also capable of accelerating Uranium-ions, whereby the following two operation modes are planned:

1. Low charge-state, high current $^{238}Uranium^{28+}$ beams at a fixed energy of 11.4 MeV/u are injected from the upgraded UNILAC into SIS18 for further acceleration up to 200 MeV/u Four SIS18 bunches with up to $1.25 \cdot 10^{11}$ particles each will be delivered to the SIS100 at an energy of 200 MeV/u. Subsequently, SIS100 will accelerate the ions up to 1.5 GeV/u. Extraction can either take place by fast extraction (50 ns pulses) or slowly, i.e. during about 2 s.

2. High charge-state, high energy U^{73+}/U^{92+} beams at energies up to 11 GeV/u: U^{73+} beams are injected from the UNILAC into the SIS18 (with intensities of $\leq 2 \cdot 10^{10}$ ions), where they will be accelerated to about 1 GeV/u. After being stripped to U^{92+}-ions, four batches of these ions will be delivered to SIS100 and will be accelerated to 11 GeV/u and subsequently extracted slowly. Alternatively, SIS18 can also provide U^{73+} beams at energies between 0.1 and 1 GeV/u into the ESR or the GSI target hall, whereby both slow and fast extraction are possible.

FAIR comprises the following four sub-programs[16], which will be operated in parallel. All of them require beam intensities and brilliances, that so far have not been reached at GSI:

[16] `https://www.gsi.de/en/researchaccelerators/fair/research`

- APPA[17] (**A**tomics, **P**lasma **P**hysics and **A**pplications)
- PANDA[18] (**A**ntiproton **An**nihilation at **Da**rmstadt experiment)
- CBM[19] (**C**ompressed **B**aryonic **M**atter)
- NUSTAR[20] (**Nu**clear **St**ructure, **A**strophysics and **R**eactions).

In the PANDA experiment at the HESR, a central part of FAIR, anti-protons will be used for fixed target collisions, in order to study strong interaction physics via proton-anti-proton annihilation. Particularly, the anti-proton programs require a high intensity proton driver beam.

1.2 The FAIR Proton-Linac

The anti-proton program at FAIR requests $7 \cdot 10^{10}$ cooled anti-protons per hour for multiple experiments. With respect to the anti-proton production and cooling rate – the $\bar{p}$ generation rate being approximately $1 : 10,000$ – this number is equivalent to $2 \cdot 10^{16}$ protons per hour in the primary beam, which have to be provided after extraction from SIS100 at an energy of 29 GeV. Additionally, the transversal acceptance of SIS18 demands a normalized linac beam brilliance of no less than $16.5\,mA/\mu m$ at a maximum momentum spread of 0.1 % [43]. The UNILAC can only offer currents up to $0.25\,\text{mA}\cdot A/q$, i.e. a maximum beam current of 0.25 mA at 18 MeV in the case of proton beams. Even though undergoing significant enhancements and being exposed to efforts like using beams composed of hydrocarbon-ions[21], 3 mA of protons is considered as a hard upper

[17] https://www.gsi.de/en/researchaccelerators/fair/research/appa_from_atoms_and_planets_to_cancer_treatment
[18] https://www.gsi.de/en/researchaccelerators/fair/research/panda_particle_magic_with_antimatter
[19] https://www.gsi.de/en/researchaccelerators/fair/research/cbm_inside_a_neutron_star
[20] https://www.gsi.de/en/researchaccelerators/fair/research/nustar_stars_and_nuclei
[21] A detailed overview about the specific hydrocarbon species is given in Ref. [44].

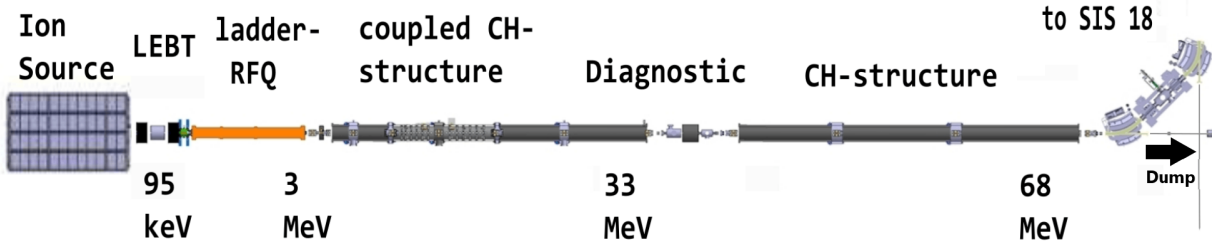

Figure 1.2: Layout of the FAIR Proton-Linac [2].

limit for the UNILAC [45], which definitely is not sufficient to fill SIS18 up to the space-charge limit. SIS18 is filled by horizontal multi-turn injection. The maximum possible number of ions in a synchrotron depends on their velocity via the factor[22] $\beta^2\,\gamma^3$ [46]:

$$N_{max} \propto \beta^2\,\gamma^3\,\frac{A}{q^2}. \tag{1.1}$$

The incoherent tune shift limits the maximum number of protons per single-turn injection (also referred to as "spill") into SIS18 to $5 \cdot 10^{12}$. This synchrotron will get protons of 68 MeV from the Proton-Linac. These will then be accelerated to 4 GeV in SIS18. Subsequently, four proton bunches from SIS18 are merged into a single bunch in SIS100, whereby acceleration to 29 GeV takes place and the bunch is compressed into a 50 ns pulse of up to $2 \cdot 10^{13}$ protons, which will be subsequently transported to the anti-proton target. The proton beam can alternatively also be slowly extracted from the SIS100 in order to perform fixed target experiments [1].

The stochastic cooling capability of the CR additionally restricts the rate of cooled anti-protons. From an economic point of view, the ideal injection energy[23] into SIS18 is about 70 MeV [46]. Smaller energies would lead to higher space-charge forces and to a reduction of the number of protons per spill. Higher driver energies would lead to the cooling time for the anti-protons in the CR exceeding SIS100's cycle time. This would require a longer waiting time for SIS100 and thus be inefficient.

1.2.1 Conceptional Design of the Proton-Linac

The decision was made for a dedicated Proton-Linac to deliver a beam of up to 70 mA at 68 MeV, which will be directly injected into SIS18 (see Fig. 1.2). Not only will a dedicated and separated proton driver provide beams with the required parameters, it will also enable the parallel operation of SIS100 for the acceleration of further ion species injected from the UNILAC during the cooling times of the anti-protons, which raises FAIR's efficiency. The beam is generated by a 2.45 GHz ECR[24] source, that extracts up to 110 mA of 95 keV protons. Source and LEBT (see

[22] $\beta = v/c$ is the relative particle velocity, and $\gamma = 1/\sqrt{1-\beta^2}$ is the relativistic Lorentz-factor.
[23] The decision to reduce the final energy from 70 MeV to 68 MeV due to limited klystron power was made in early 2017.
[24] **E**lectron **C**yclotron **R**esonance

Figure 1.3: Digital mock-up of the p-linac building viewed at from south (courtesy of K. Knie, GSI).

Fig. 1.4) are in-kind contributions by CEA Saclay[25], France. The source has a five electrode extraction system. The electric field does not exceed 96 kV/cm to keep sparking risks low. The LEBT entails two magnetic focusing solenoids used for beam transport and for matching into the RFQ. An aperture separates H^{2+}- and H^{3+}-ions from the proton beam. The diagnostics are contributed in joint responsibility by GSI and CEA. As initially planned [47] an Allison scanner for beam emittance[26] measurements, a beam stopper and two **AC**[27] **C**urrent **T**ransformers (ACCTs) for the measurement of beam currents and intensities have been integrated to the LEBT. One ACCT is positioned after the extraction system, the other after the second solenoid. The beam will be structured into four bunches per second and with a length of typically 50 µs defined by a chopper. The chopped beam will be dumped at a water cooled tungsten cone. On-axis particles enter the RFQ, where they will be bunched, transversally focused and accelerated to 3 MeV by electric RF-fields.

In the succeeding MEBT section the beam emittances will be matched into the **C**ross-Bar **H**-type (CH) drift tube linac by a steerer, two quadrupole triplets and a rebuncher [48, 49]. Three

[25] The Saclay Nuclear Research Center is one of nine laboratories belonging to the Commissariat à l'énergie atomique (CEA) (English: French Alternative Energies and Atomic Energy Commission). It also hosts the administrative headquarters of the CEA (`https://www.cea.fr/english`). CEA's **D**épartement des **A**ccélérateurs, de **C**ryogénie et de **M**agnétisme (DACM; English: Department of Accelerators, Cryogenics and Magnetism) furthermore provides many well established codes (`http://irfu.cea.fr/dacm/logiciels`), some of which (i.e. PlotWin, TOUTATIS and TraceWin) are of relevance to this thesis. (They will be introduced individually further on in this work.)

[26] The beam emittance is a measure for the area of the respective phase-(sub)-space occupied by beam particles. Appendix D provides a definition of this crucial beam parameter and introduces the many criteria used to classify and specify beam emittances.

[27] **A**lternating **C**urrent

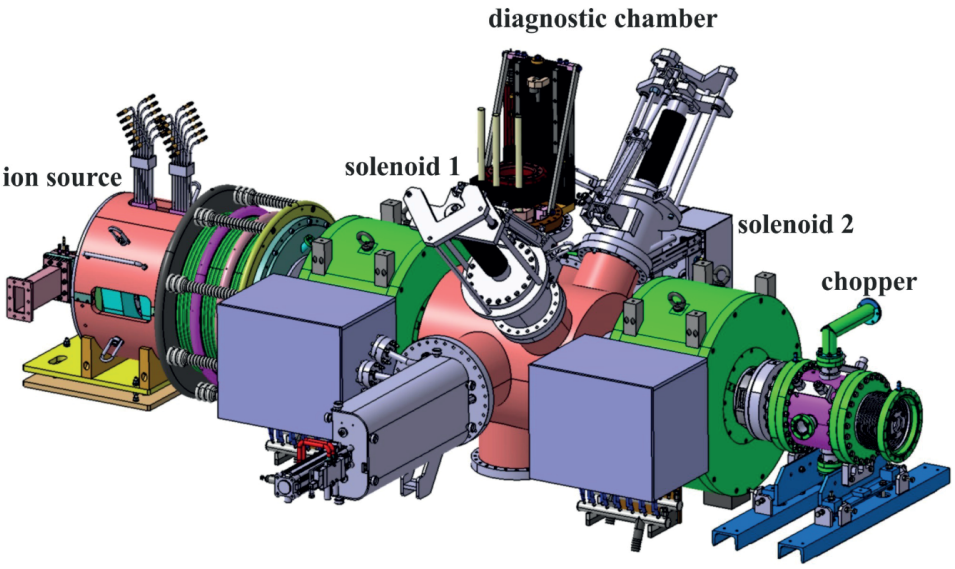

Figure 1.4: Isometric view of the LEBT for the FAIR p-Linac RFQ ([3]; design by CEA Saclay).

coupled CH-cavities make up the 33 MeV section. Each of them entails two drift tube structures RF-coupled by a single cell resonator, that oscillates in the Alvarez mode. A quadrupole triplet for transversal focusing is placed within this cell. The CH-cavities are operated in the H21(0)-mode – in contrast to **I**nterdigital **H**-type (IH) drift tube structures, which are operated in the H11(0)-mode. CH-structures can be operated at about twice the RF-frequency of IH-structures with similar cavity diameters.

The energy is then boosted to 68 MeV by another three CH-structures prior to beam transport and injection into SIS18. Seven 3 MW class klystron amplifiers power the cavities and the RFQ. 12 quadrupole triplets will provide transversal focusing along the Proton-Linac. A variety of different beam diagnostic elements will be employed, such as three Faraday cups as beam dump, nine ACCT's (in addition to two in the LEBT), four **S**econdary-**E**lectron emission **M**onitors (SEMs) grids for emittance measurement, an iris for halo scraping, 14 **B**eam **P**osition **M**onitors (BPMs) [50] as well as a Feschenko monitor for measuring the bunch lengths.

A typical beam current for operation is around 35 mA, whereas the design current is chosen 70 mA. This allows for an experimental optimization of the multi-turn injection into SIS18. The p-linac building (see Fig. 1.3) is not expected to be completed before 2024. At possible further delays it is important to find a testing hall for beam development up to the 3 MeV injection point

into the CH-DTL. Otherwise further delays are expected until high $\bar{p}$-production rates can be achieved.

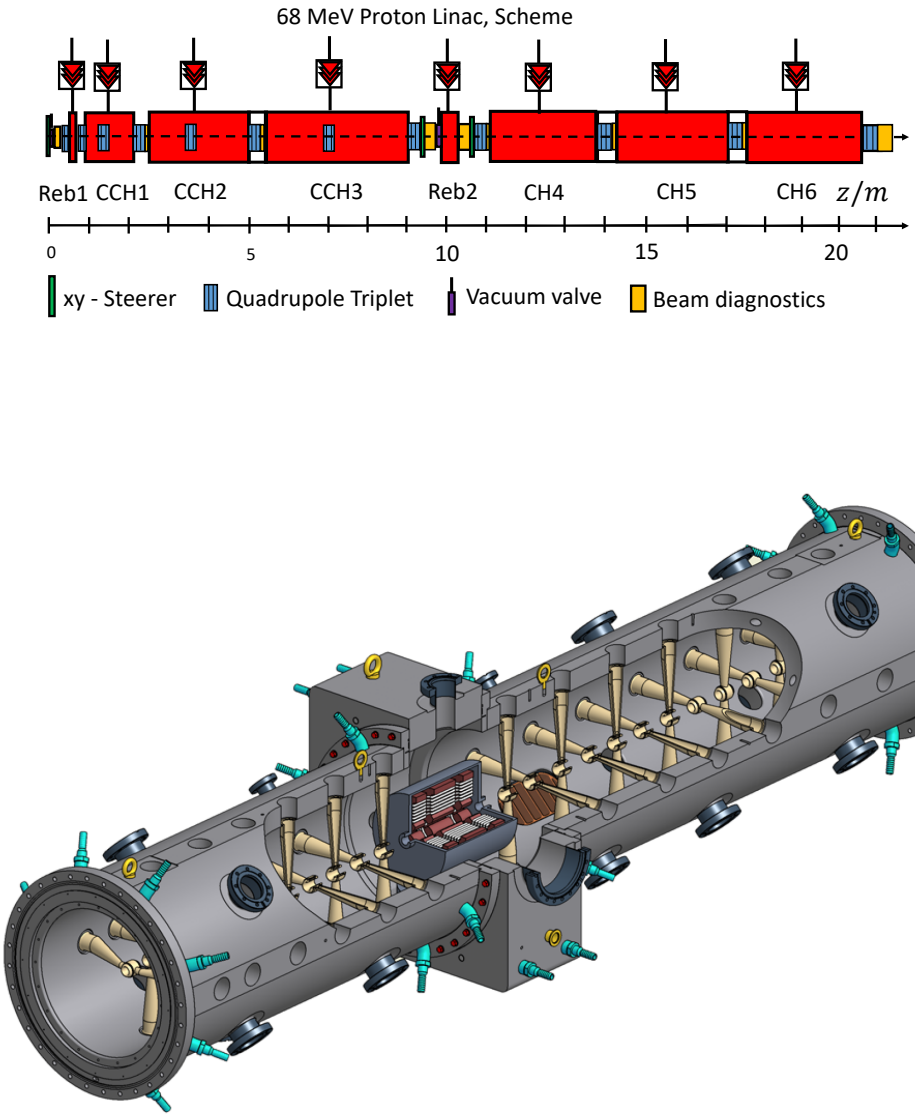

Figure 1.5: **Top:** Schematic layout of the p-linac (courtesy of U. Ratzinger). **Bottom:** Isometric view of the coupled CH prototype of the p-linac [51]. A coupling cell of the lengths of $2\,\beta\lambda$ connects both drift tube sections. This cell hosts the quadrupole triplet lens and the coupler flange.

[2] Radio Frequency Quadrupoles and their Beam Dynamics

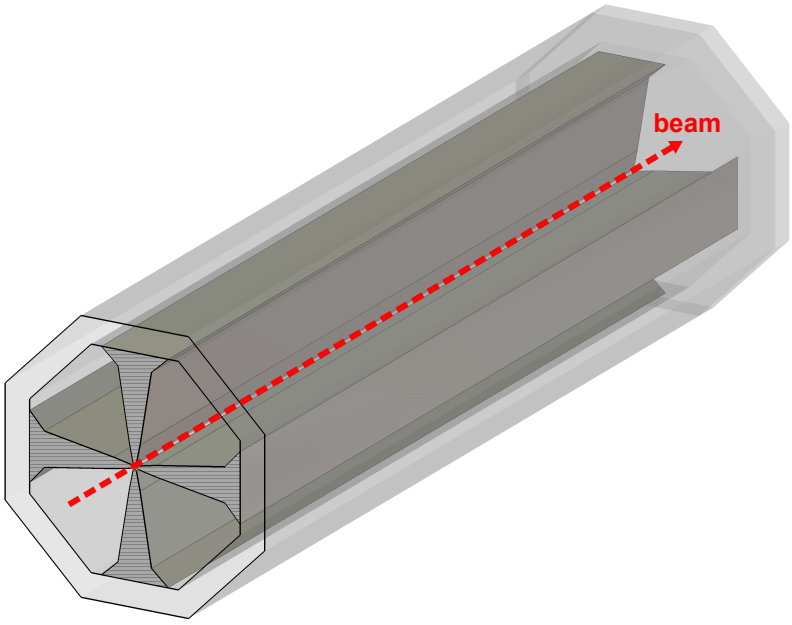

Figure 2.1: Basic structure of a 4-vane RFQ [52]: the electric quadrupole channel is placed in an octagonal resonator cavity. (Cylindrical resonator cavities are much more common, but the planar sectors of the cavity surface may be better suited for planting flanges. CERN's PIXE-RFQ is such a case (cf. Sec. 4.2).) The electrode surfaces are modulated along the beam axis (z-axis) depicted as dashed red line.

The radio frequency quadrupole linac (RFQ) is a rather new type of linear accelerator, that poses a major innovation. Since it is especially suited to accelerate particle beams up to a relative velocity $\beta = v/c$ between 1 % and 10 % of the speed of light. Higher particle velocities would result in impractically long cell lengths. Furthermore, this would lead to small acceleration rates, unless the frequency would be increased to about 1 GHz. For protons, $\beta = 0.05$ is equivalent to a kinetic energy W of 1.2 MeV.

RFQs are not applied in electron acceleration (as electrons already are emitted from a typical electron-gun source with velocities $v \approx 0.5\,c$), but widely used for ion acceleration. That is also due to the fact that high-energy beams also start out with low velocities, and the acceleration method used on the beam at these low velocities contributes substantially to the overall performance of an accelerator system. As will be shown in the following RFQs provide their succeeding structures with beams of high quality that more often than not cannot be reached by other means.

2.1 The Benefits of RFQs

As will be elaborated on later, RFQs have not least gained popularity within the linac community due to their favored beam bunching propensities, which make them irreplaceable for many projects. In order to establish the specific reasons for this, the bunching process in linac-systems absent RFQs shall be presented first.

Any RF accelerator requires the beam to be longitudinally bunched so that (ideally) all beam particles will undergo acceleration and (ideally) none will be decelerated. For "conventional" linacs, e.g. drift tube linacs (DTLs), this bunching is performed prior to the injection into the linac by one or more RF cavities placed in front of the linac. The RF electric field distribution in these so-called buncher cavities or simply bunchers, is such that they impose a velocity modulation on the unbunched input beam: particles faster than the so-called synchronous particle are decelerated, whereas particles slower than it are accelerated (cf. Chap. A). After a suitable drift length, the beam becomes bunched, and can subsequently be injected into the linac. This bunching usually is rather inefficient and results in quite poor beam qualities, especially for high-intensity beams. As bunching (locally) increases the beam density, the (local) space-charge forces also grow and thus often blow up the transverse beam emittances [26]. These problems fundamentally restrict the performance of "conventional" linac-systems, especially if beam currents are high. Appropriately designed RFQs are able to adiabatically bunch the input DC beam, whereby these problems can be (almost) completely avoided.

The three main tasks of an RFQ are as follows:

- Transversal focusing: the beam leaving the ion source usually exhibits transversal emittances and a cross-section in the x-y-plane that are much too high for the small aperture of the RFQ. Furthermore, since the particles within a given ion beam are either all pos-

itively or all negatively charged, they exert repulsive forces on each other, which might require compensation to avoid (too much) emittance growth. Transversal focusing in RFQs is accomplished via the **A**lternating-**G**radient **F**ocusing (AGF) principle (see Sub-Sec. 2.7), which ensures that despite the presence of an alternating voltage a net transversal focusing takes place.

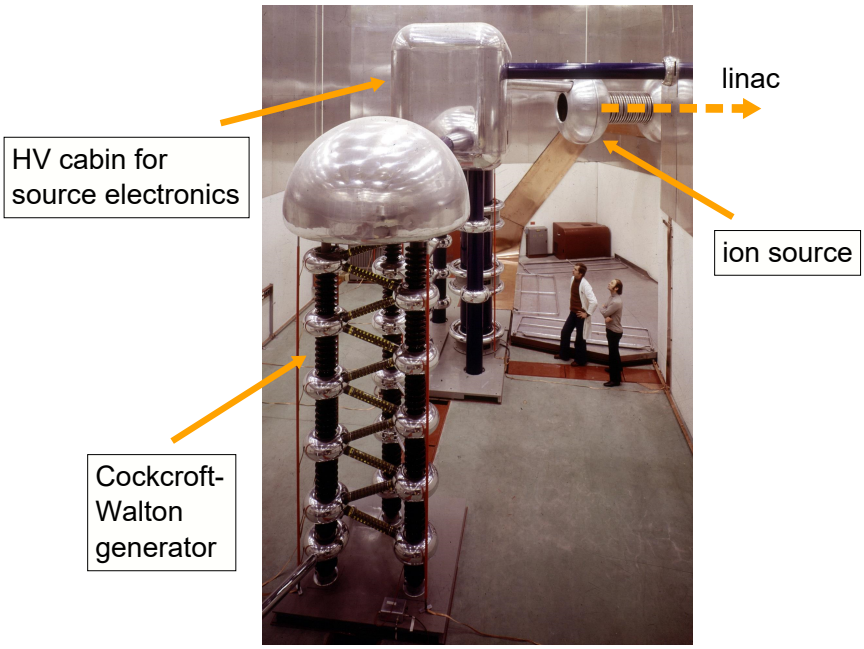

Figure 2.2: The 750 kV Cockcroft-Walton generator for CERN's Linac2, which was replaced in 1993 by a 90 kV pre-injector and a 1.8 m long 750 keV RFQ [53]. Note the huge discrepancy of both setups' dimensions. ([52]; photo from `https://cerncourier.com/a/the-tale-of-a-billion-trillion-protons/`, CERN-AC-7602012.)

- Bunching: as the electric extraction field of the ion source has to be static, the extraction beam is a DC-beam, optimally with a scaled macro-pulse structure with pulse lengths from the ion source typically being between 10 µs and 10 ms. As discussed above, RF linacs require bunched beams for their operation with RF voltages. Typical radio frequencies applied reach from ca. 10 MHz to 1 GHz. RFQs are capable of quasi-adiabatic bunching, resulting in almost no particle losses. This poses another advantage over the above mentioned larger pre-accelerators, which had to be supported by an additional buncher cavity.

- (Pre-)Acceleration of the source beam: for considerations concerning mechanical stability, avoidance of sparking and limitations in manufacturing processes, the gap length, which is proportional to the particle velocity, in many cases can not be manufactured as short as

required for the slow source particles to enter the first drift tube right after being emitted from the source. Therefore, RFQs offer potent and efficient particle pre-acceleration resulting in particle velocities corresponding to feasible gap length in the succeeding DTLs. RFQs today are the pre-accelerators of choice and even have replaced nearly all of the much lager pre-accelerators such as Cockcroft-Walton[1] generators used in long existing facilities (cf. Fig. 2.2).

2.2 A Brief History of RFQs

The birth of the RFQ as a theoretical concept dates back to 1967, when I. M. Kapchinskiy and A. V. Teplyakov proposed to modify the fields of a radio frequency quadrupole channel inserted into a cylindrical cavity (see Fig. 2.1) in order to efficiently accelerate high current beams of low energy ions [6].

Alternating gradient focusing (also referred to as strong focusing) with electrical quadrupoles was first discovered 1950 by N. C. Christofilos and shortly afterward and (independently from the former) by E. D. Courant, M. S. Livingston and H. S. Snyder [55]. J. P. Blewett and L. C. Teng were the first to (independently from each other) made use of such quadrupoles for particle acceleration in 1952 [56] and 1953 [57], respectively. As shown in Figure 2.3, RFQs are related to these ordinary quadrupole channels: four electrodes with opposite electric potential on adjacent electrodes and the same potential on opposing electrodes generate a quadrupole field. In order for acceleration and bunching – also referred to as longitudinal focusing – to occur, a longitudinal component of the electric field (i.e. a field component along beam direction) is required. In RFQs, this component stems from a surface profile of the electrodes modulated along the beam axis (see Figure 2.3).

The first experimental model of a linac based on the RFQ principle was constructed at IHEP[3]. In 1974, initial testing had been achieved, and the first accelerated beam was obtained with a 148.5 MHz RFQ accelerating 100 keV protons to 620 keV with an exit transmission of 50% [7, 8]. It took until 1977 for the RFQ concept to be made known among the western world. The moment it was, it immediately raised strong interest in **L**os **A**lamos **N**ational **L**aboratory[4] (LANL). Here then, efforts were made to test the RFQ principle regarding possible high-current beams of low emittance.

[1] The Cockcroft-Walton generator is named after the British and Irish physicists John Douglas Cockcroft and Ernest Thomas Sinton Walton, who in 1932 used this circuit design to power their particle accelerator, performing the first artificial nuclear disintegration in history [54].

[3] **I**nstitute for **H**igh **E**nergy **P**hysics, Protvino/Russia (http://www.ihep.ru)

[4] `https://www.lanl.gov`

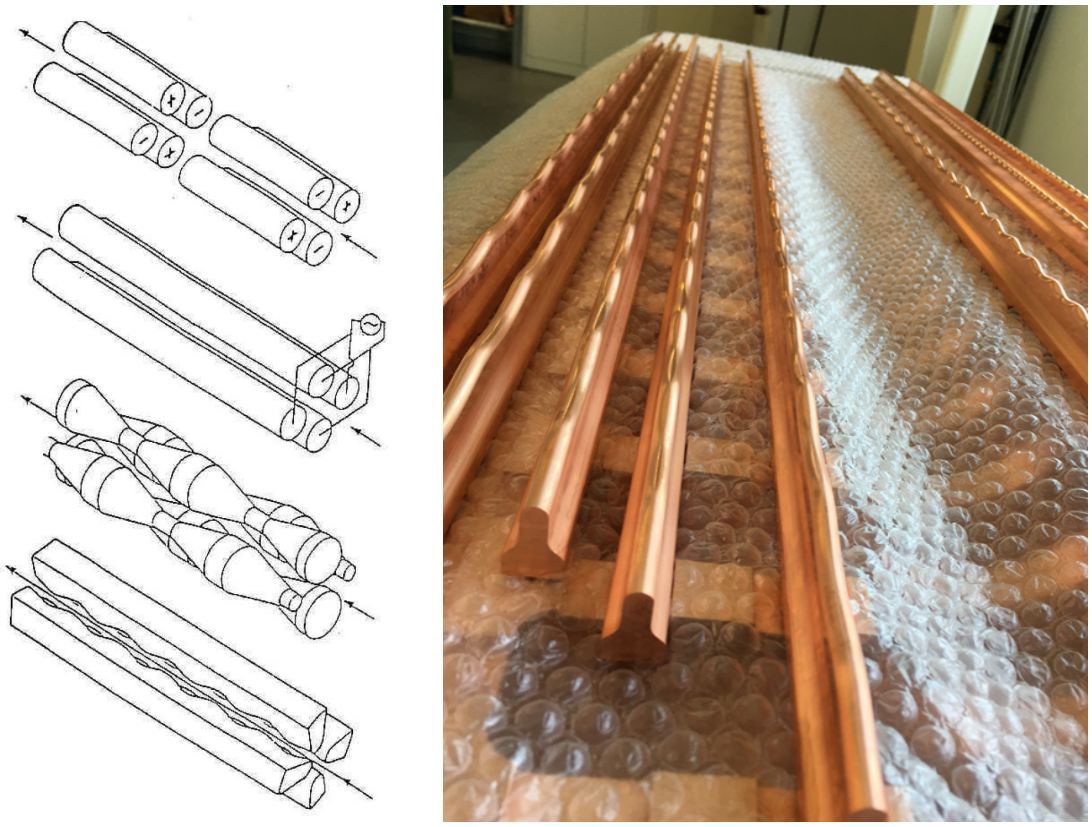

Figure 2.3: **Left:** Geometric development of quadrupole/RFQ electrodes [58]. First Blewett and Teng used single magnetic and electric quadrupoles in series in 1952 and 1953, respectively [56, 57]. Paul and Raether applied an RF-driven quadrupole a few years later [59]. Finally, Kapchinskiy and Teplyakov from the Institute for Theoretical and Experimental Physics[2] (ITEP) in Moscow made use of a simple triangular shaped modulation [6]. However, both the process of manufacturing and the lack of simulation methods posed limitations on this approach. The picture at the bottom shows the classic electrode profile for 4-vane RFQs, the second to last picture depicts the classic 4-rod RFQ electrode profile.
Right: Shown are the electrodes of the p-Linac RFQ, which fall into the modern mini-vane category, placed on the lower RFQ half. Air cushion foil is placed between the components to prevent scratches (courtesy of M. Schuett; photo taken at facility of Fa. Kress GmbH, Biebergemünd/Germany).

Simultaneously, computer codes for RFQ design were developed at LANL. These codes are based on the in parallel developed LANL **F**our **S**ection **P**rocedure (FSP), a systematic strategy for gaining efficient and feasible RFQ beam dynamics, which sub-segments the RFQ into four sections [9]. These sections differ in regard to their functions for beam transport and in their characteristic design and beam parameter behaviors. Furthermore, this scheme includes the concept of (quasi-)adiabatic bunching, a method of transforming a DC beam leaving the ion source into several bunches without (significant) particle losses. Adiabatic bunching causes highly compact beam bunches with minimal expansion in longitudinal phase space[5].

All these efforts of LANL eventually led to the first **P**roof-**o**f-**P**rinciple (POP) experiment in February of 1980, in which a 425 MHz RFQ accelerated a 100 keV proton beam to an exit energy of 640 keV. As predicted by the codes, the exit transmission turned out to be 90%. This success initiated a fast world-wide spread of RFQs. By now, almost every "old style" pre-injector of the major laboratories got replaced by a much more compact and efficient RFQ. The number of currently operating RFQs is in the hundreds [8].

2.3 RFQ Resonator Types

The resonator geometry determines the resonant frequency of an RFQ. RFQs can be (apart from very few exceptions[6]) divided into two different types: 4-vane-RFQs and 4-rod-RFQs. The former are equipped with cavity resonators and vane-shaped electrodes, whereas the latter are equipped with with transmission-line (or Lecher) type resonators and rod-shaped electrodes. Developed at IAP Frankfurt in the mid-eighties by A. Schempp et al. [10], the 4-rod-RFQ marked a massive innovation in the field of RFQs and has since then undergone contentious improvement. It is dominantly used in the lower-frequency range, ca. below 250 MHz, and is the most commonly used RFQ structure for heavy ions of very low velocities [26].

For all RFQ types, beam dynamics are defined by the electrode geometry (cf. Section 2.4). Ladder RFQs enjoy the benefits of all RFQ types. An up-to-date overview of ladder-like RFQ structures can be found in Ref. [3]. Further RFQ designs are given in Refs. [60, 13]. References [15, 12] also provide a good overview over the different RFQ (sub-)types and their applications.

[5] The FSP and the concept of Adiabatic Bunching will be further discussed in Sub-Sec. 2.10.1).
[6] Further RFQ-types are Described in Refs. [60, 13] and [60, 13].

2.4 RFQ Beam Dynamics

As the particle velocities within RFQs are quite low ($v \leq 0.1\,c$) and the magnetic fields are of sufficiently low magnitude near the beam axis, the Lorentz-force $\vec{F} = q\,e\,\vec{v} \times \vec{B}$ on the beam particles can be neglected. This leaves only the electric forces emerging from the RFQ electrodes on the beam particles as well as space- and image-charge effects to determine the beam dynamics. Especially in case of high-current/intensity beams the latter two forces have to be considered (cf. Sec. 2.9 as well as Sub-Secs. E.1.3 and E.1.4). For RFQs, the electric potential stemming from the RFQ electrodes and thus the associated electric field components can be derived from a scalar potential that satisfies Laplace equation [21] (cf. Secs. 2.5 and 2.6). This approach is also referred to as the quasi-static approximation and is usually valid in case of the geometrical dimensions around the beam axis being small in comparison to the free-space wavelength.

In the following a closer look shall be taken at a simple, but relevant approach for the electric potential within RFQs, i.e. the so-called two-term potential, as well as a more expansive and accurate approach in form of the Kapchinsky-Teplyakov potential and also the eight-term potential (cf. Secs. 2.5 and 2.6). It will further be discussed how the resulting electric field components or rather their specific behavior along the beam axis enable the RFQ to perform its three main tasks: transversal beam focusing, acceleration and longitudinal beam focusing (i.e. the formation of stable beam bunches via (quasi-)adiabatic bunching). Therefore, different RFQ beam dynamics design schemes – including the LANL Four Section Procedure (LANL FSP) and several schemes conceptualized at IAP Frankfurt by Schempp et al. – will be presented and explained. A further focus will be laid on the functions distinct RFQ sections provide in regard to the beam dynamics within these different schemes.

2.5 The Two-Term Potential Approximation

In RFQs the (radial) aperture $a(z)$, i.e. the distance from the beam axis to the electrode tips, modulates (approximately) sinusoidally in z. It can be seen in Fig. 2.4 that whereas $a(z)$ is modulated "in phase" for opposing electrodes, a 90°-shift occurs for adjacent ones. The mechanical modulation period l of the longitudinal electrode tip profile comprises two RFQ unit cells: $l = 2\,l_c = \beta_s\,\lambda$. As the synchronous velocity β_s (i.e. the velocity of the synchronous particle) increases along the beam axis, so does the cell length $l_c = \beta_s\,\lambda/2$. This constitutes the synchronism condition (cf. Chap. A). Therefore, actually not one, but multiple modulation period lengths exist within a given RFQ. However, the assumption of a periodic modulation is both convenient and justified, if the acceleration rate is small in regard to the distance the

particle traverses during one RF period.

The mechanical modulation is quantified by the modulation parameter or simply modulation m as quotient of maximum over minimum radial aperture within a given RFQ unit cell: $m = \frac{a_{max}}{a_{min}}$. Per convention, the minimal radial aperture[7] a_{min} is often simply referred to as aperture a. Within this nomenclature the maximal radial aperture is given by $m\,a$ instead of $m\,a_{min}$ (see Fig. 2.4). The modulation amplitude within a given RFQ-cell is half the difference between the extremal aperture values $(ma - a)/2$.

The two-term potential basically is the shortest simplification possible of the Kapchinsky-Teplyakov potential (cf. Sec. 2.6) that constitutes a solution to the Laplace equation given in cylindrical coordinates by

$$\frac{\partial^2 V}{\partial r^2} + \frac{1}{r}\frac{\partial V}{\partial r} + \frac{1}{r^2}\frac{\partial^2 V}{\partial \theta^2} + \frac{\partial^2 V}{\partial z^2} = 0. \tag{2.1}$$

Also introduced early on by Kapchinsky and Teplyakov [6] it still serves as basis for RFQ beam dynamics designs. The two-term potential only takes into consideration two of the numerous multipole potential terms of the Kapchinsky-Teplyakov potential (hence its name), namely the z-independent quadrupole term and the θ-independent monopole term:

$$V_{TT}(r,\theta,z) = \underbrace{A_0 r^2 \cos(2\theta)}_{quadrupole\,term} + \underbrace{A_{10}\, I_0(k_l r)\cos(k_l z)}_{monopole\,term}, \tag{2.2}$$

with r, θ, and z being the cylindrical coordinates. k_l is the wave number of the mechanical modulation[8]: $k_l = \frac{2\pi}{l} = \frac{2\pi}{\beta_s \lambda} = \frac{\pi}{l_c}$. In order to simplify the following formulas the variable $u = k_l\, r$ is introduced. In case of $\frac{r}{a} \ll 1$ (i.e. near the beam axis), the modified Bessel function of 0-th order $I_0(u)$ can be simplified to $I_0(u) \cong 1 + \frac{u^2}{4}$. A Modified Bessel function of order s is described by

$$I_s(u) = \sum_{l=0}^{\infty} \frac{\left(\frac{u}{2}\right)^{2l+s}}{l!\,\Gamma\big(l+s+1\big)}. \tag{2.3}$$

As a first step to arrive at a new RFQ beam dynamics design, the required electrode geometry can be derived from the two-term potential: in a very first approximation the profiles of the

[7] However, at some instances a_{min} refers to the minimal minimum aperture per cell along the RFQ, i.e. to the minimum of a_{min} along the RFQ (cf. Tab. 3.1 of Chap. [3]). What quantity exactly is referred to by the symbols a_{min} and a is mostly made clear by the context.

[8] Not to be confused with the wave number $k = \frac{2\pi}{\lambda}$ of the electromagnetic wave.

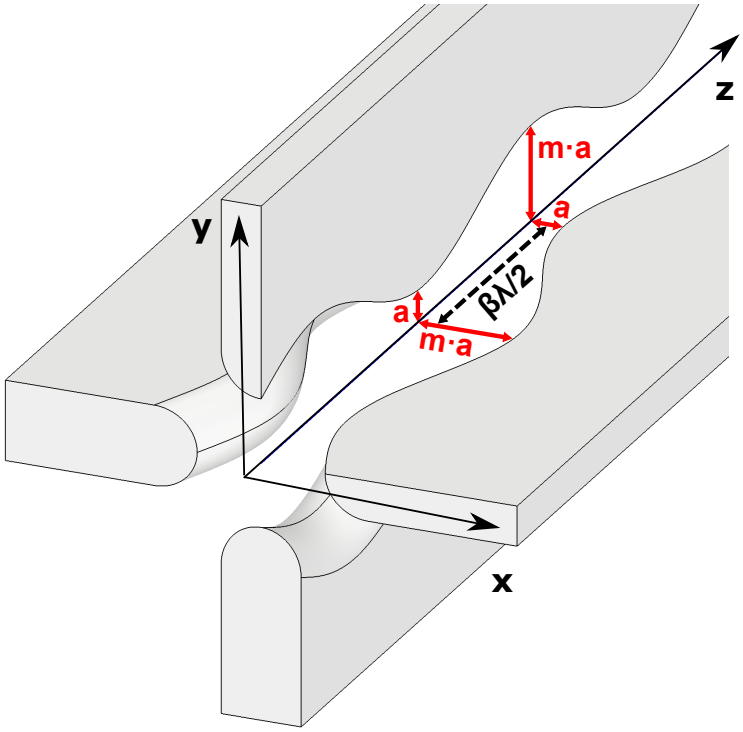

Figure 2.4: RFQ-electrodes (adjusted from Ref. [52]; originally based on Fig. 7 of Ref. [8]); the upper and the right electrode are depicted "halved" to exhibit their longitudinal cross sections for better illustration. The radial aperture $a(z)$ is modulated "in phase" for opposing electrodes and with a 90°-shift for adjacent ones. Note the nomenclature in this figure, which is common among the RFQ community: a does not refer to the radial aperture $a(z)$ in general, but specifically to the minimal radial aperture a_{min} within the respective cell (cf. Fn. [7]). $m\,a$ is the maximum radial aperture within this RFQ-cell. Furthermore, in this figure β specifically refers to the synchronous relative velocity β_s in this RFQ-cell. Thus, in this figure $\beta\,\lambda$ refers to the respective RFQ-cell length l_c, which is half the respective modulation period length l of the longitudinal electrode profile: $l_c = \frac{l}{2} = \frac{\beta_s\,\lambda}{2}$ (synchronism condition).

electrode should match the equipotential surfaces. The boundary conditions depending on the specific electrode geometry are reflected in the constants A_0 and A_{10}. They are defined as [61]:

$$A_0 = \frac{V_0}{2a^2} \frac{I_0(k_l a) + I_0(k_l m a)}{m^2 I_0(k_l a) + I_0(k_l m a)} \tag{2.4}$$

and

$$A_{10} = \frac{V_0}{2} \frac{m^2 - 1}{m^2 I_0(k_l a) + I_0(k_l m a)}. \tag{2.5}$$

It can easily be seen that the units of A_0 are $\frac{Volt}{m^2}$ and that the unit of A_{10} is Volt. ($[V_0]$ = Volt, $[a] = m$; modulation m and I_0 are dimensionless.) For convenience, both constants A_0 and A_{10} are replaced with equivalent but dimensionless coefficients X and A:

$$X = \frac{I_0(k_l a) + I_0(k_l m a)}{m^2 I_0(k_l a) + I_0(k_l m a)} \tag{2.6}$$

$$A = \frac{m^2 - 1}{m^2 I_0(k_l a) + I_0(k_l m a)}, \tag{2.7}$$

with $A_0 = \frac{V_0}{2\,a^2} X$ and $A_{10} = \frac{V_0}{2} A$. In terms of these new coefficients and using cylindrical coordinates the time-dependent two-term potential becomes [61]:

$$V(r, \theta, z, t) = \frac{V_0}{2} \left[X \left(\frac{r}{a}\right)^2 \cos(2\theta) + A\, I_0(k_l r) \cos(k_l z) \right] \cos(\omega t + \phi). \tag{2.8}$$

With the trigonometric relation $\cos 2\theta = \cos^2 \theta - \sin^2 \theta$ and the relations between cylindrical coordinate r and Cartesian coordinates x and y, i.e. $x = r\cos\theta$ and $y = r\sin\theta$,[9] the time-dependent two-term potential in Cartesian coordinates[10] can now be derived from Eq. 2.8 as [61]:

$$\Phi(x, y, z, t) = \frac{V_0}{2} \left[\frac{X}{a^2} (x^2 - y^2) + A\, I_0(k_l r) \cos(k_l z) \right] \cos(\omega t + \phi). \tag{2.9}$$

The transversal cross sections of the electrodes (i.e. the cross sections parallel to the x-y-plane) are assumed to be hyperbolic (see Fig. 2.5). At the center of an RFQ unit cell, i.e. at $z = \frac{\beta_s \lambda}{4} + n\, l_c$ (with $n = 0, 1, 2, 3, ...$), the arrangement of the electrodes is equal to that of a non-modulated electric quadrupole (cf. Fig. 2.4). Here, perfect quadrupole symmetry exists: for all four electrodes the radial apertures are identical and take on the value of the average cell radius or mid-cell

[9] All these relations lead to $r^2 \cos 2\theta = r^2 (\cos^2 \theta - \sin^2 \theta) = x^2 - y^2$.

[10] In the following, the zero order Bessel function I_0 remains a function of cylindrical coordinate r, although r could in principle be substituted via $r = \sqrt{x^2 + y^2}$. However, this would be highly counter-intuitive and rather inconvenient.

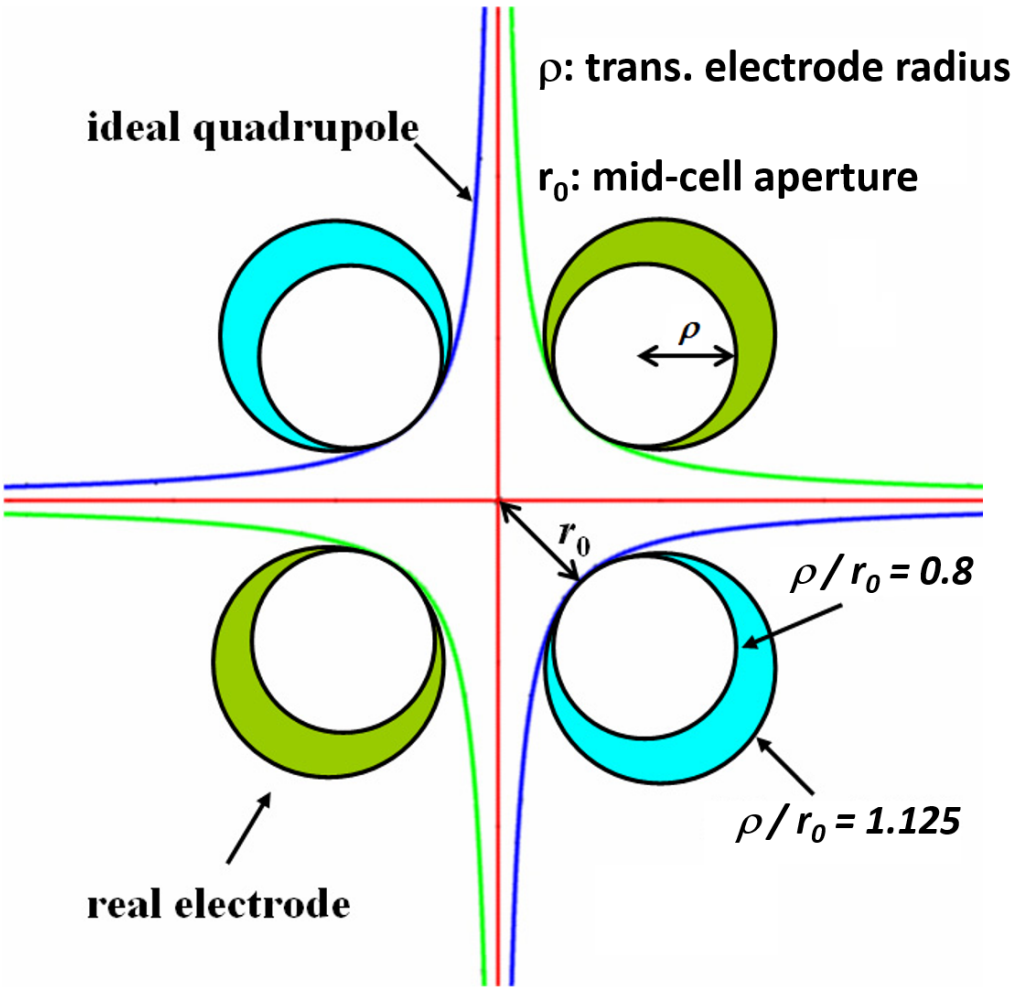

Figure 2.5: Ideal, i.e. hyperbole-shaped, vs. real transversal RFQ-electrode profiles in case of rod-shaped electrodes with $\rho/r_0 = 0.8$ and $\rho/r_0 = 1.125$, respectively (modified from Fig. 3.1.1-2 of Ref. [18]). Shown are the x-y-cross sections through the center of an RFQ cell, where the aperture gets the mid-cell radius $r_0 = \frac{a}{\sqrt{X}}$ (see Eq. 2.11).

radius[11] $r_0 = \frac{m\,a+a}{2} = \frac{(m+1)\,a}{2}$ [26] (see Fig. 2.5). It can also be expressed by a and X as the following considerations reveal.

For $t = \frac{(2\,n-1)\,\pi}{\omega}$, i.e. for $\cos(\omega t + \phi) = 1$, the two-term potential at the right horizontal electrode-tip, i.e. at $x = r_0$ and $y = 0$, at the (longitudinal) center of an RFQ-cell, i.e. at $z = n\,l_c + \frac{l_c}{2}$ and thus for $\cos(k_l z) = 1$, gets $\frac{V_0}{2}$ and can be expressed according to Eq. 2.9 as:

$$\Phi(x = r_0, y = 0, z = n\,l_c + \frac{l_c}{2}, t = \frac{(2\,n-1)\,\pi}{\omega}) = \frac{V_0}{2}\,(\frac{X}{a^2}\,r_0^2). \tag{2.10}$$

Hence, $\frac{X}{a^2}\,r_0^2 = 1$ holds true, which leads to the following relation:

$$r_0 = \frac{a}{\sqrt{X}}. \tag{2.11}$$

The ratio ρ/r_0 of the transversal electrode radius ρ to the average aperture r_0 is an important design factor as the minimum distance between two adjacent electrode tips d_{min} amounts to (see Fig. 2.5):

$$d_{min} = \sqrt{2}\,(\rho + r_0) - 2\,\rho. \tag{2.12}$$

By differentiating the right-hand side of Eq. 2.9 with respect to the three Cartesian coordinates the following expressions for the amplitudes of the three Cartesian electric field components are obtained [26]:

$$E_{x,0} = -\,\frac{\partial V(x,y,z)}{\partial x} = -\,\frac{X\,V_0}{a^2}\,x\;-\;\frac{k_l\,A\,V_0}{2}\,I_1(k_l r)\,\frac{x}{r}\,\cos(k_l z), \tag{2.13}$$

$$E_{y,0} = -\,\frac{\partial V(x,y,z)}{\partial y} = \frac{X\,V_0}{a^2}\,y\;-\;\frac{k_l\,A\,V_0}{2}\,I_1(k_l r)\,\frac{y}{r}\,\cos(k_l z), \tag{2.14}$$

and

$$E_{z,0} = -\,\frac{\partial V(x,y,z)}{\partial z} = \frac{k_l\,V_0\,A}{2}\,I_0(k_l r)\,\sin(k_l z), \tag{2.15}$$

with $I_1(k_l r)$ being the modified Bessel function of the first kind. Close to the beam axis it can be approximated as $I_1(k_l r) \approx \frac{k_l\,r}{2}$ [61]. The $E_{z,0}$-component is proportional to A, enables acceleration and longitudinal focusing of the beam. The contributions $-\,\frac{X\,V_0}{a^2}\,x$ and $+\,\frac{X\,V_0}{a^2}\,y$ of the transversal components $E_{x,0}$ and $E_{y,0}$ allow for transversal net focusing through **A**lternating **G**radient **F**ocusing (AGF) (cf. Subsection 2.7). (This kind of focusing is more

[11] In literature r_0 is sometimes also referred to as average radial aperture a_0.

widely known as Strong Focusing, but as the former term is more descriptive, it shall be used.) Therefore, they control, respectively limit, space-charge induced transversal emittance growth, which might lead to a low-density beam halo surrounding the beam's core. This poses a risk of beam loss and subsequent radioactivation of the accelerator [26] (cf. Sec. 3.5 and Sub-Sec. 4.3.1).

Consequently X is referred to as focusing efficiency, and accordingly the first right-hand side terms in Eq. 2.13 and Eq. 2.14 are referred to as focusing terms [26]. In literature, instead of focusing efficiency X the focusing strength B_f or B (not to be confused with the magnetic flux density) is often quoted[12]:

$$B_f = \frac{qeV_0\lambda^2}{mc^2 r_0^2} = \frac{qeV_0\lambda^2}{mc^2}\,\frac{X}{a^2}. \tag{2.16}$$

Multiplication of above expressions for the field amplitudes with[13] $\cos(\omega t + \phi)$ gets the time-dependent field components: e.g. $E_x(x,r,z,t) = E_{x,0}(x,r,z)\,\cos(\omega t + \phi)$.

2.6 Kapchinsky-Teplyakov Potential and Eight-Term Potential

A more complex solution to the Laplace equation (cf. 2.1) is the Kapchinsky-Teplyakov potential or short: K-T potential [6]. For structures without z-profile only $2D$-solutions are of interest. In case of a z-profile – and thus for RFQs – $3D$-solutions of the Laplace equation also have to be taken into account. The general solution is arrived at by solving the 2D- and the 3D-problems with a separation approach and then superimposing the two solutions. This leads to the K-T potential $V_{K-T}(r,\theta,z)$:

$$V_{K-T}(r,\theta,z) = \underbrace{\sum_{s=0}^{\infty} A_s r^{2(2s+1)}\,\cos(2(2s+1)\theta)}_{general\,2D-solution} + \underbrace{\sum_{n=1}^{\infty}\sum_{s=0}^{\infty} A_{ns}\,I_{2s}(k_l n r)\,\cos(2s\theta)\,\cos(k_l n z)}_{general\,3D-solution}. \tag{2.17}$$

The components A_s and A_{ns} are defined by the boundary conditions of the specific problem; I_{2s} is the modified Bessel function of the second kind (cf. Eq. 2.3).

An improved solution of the Laplace equation when compared to the two-term potential results

[12] PARMTEQ(M) and RFQGen also require this quantity to be specified on several occasions.

[13] Via $r = \sqrt{x^2+y^2}$ cylindrical coordinate r in Eq. 2.13 – Eq. 2.15 could be substituted, so that $E_{x,0}(x,r,z)$, $E_{y,0}(y,r,z)$ and $E_{z,0}(r,z)$ could be expressed as functions solely of the three Cartesian coordinates. This would be rather inconvenient, though (cf. Fn. [10]).

in the eight-term potential. Whereas the former only consists of one $2D$-term and one $3D$-term of the K-T potential, i.e. the two lowest order terms (quadrupole term ($s = 0$) and monopole term ($s = 0$; $n = 1$)), the eight-term potential in addition also comprises one further $2D$-term and six further $3D$-terms [61]:

$$V_{8-term}(r,\theta,z) = \begin{array}{c} \frac{V_0}{2}\,[A_0\big(\frac{r}{r_0}\big)^2\cos(2\theta) \;+\; A_1\big(\frac{r}{r_0}\big)^6\cos(6\theta) \\ +A_{10}I_0(kr)\cos(kz) \;+\; A_{12}I_4(kr)\cos(4\theta)\cos(kz) \\ +A_{21}I_2(2kr)\cos(2\theta)\cos(2kz) \;+\; A_{23}I_6(2kr)\cos(6\theta)\cos(2kz) \\ +A_{30}I_0(3kr)\cos(3kz) \;+\; A_{32}I_4(3kr)\cos(4\theta)\cos(3kz)]. \end{array} \tag{2.18}$$

The RFQ beam dynamics design and simulation codes PARMTEQM and RFQGen offer to include these six additional terms. The eight-term potential constitutes a much more realistic approach to the actual potential within RFQs since actual RFQ electrode geometries differ quite significantly from those of the idealized electrodes, that the two-term potential function originally was derived for.

2.7 Alternating Gradient Focusing Principle

In order to better conceptualize transversal focusing in RFQs, first taking a look at this phenomenon in DTLs can be of help. Since the electric fields in the gaps of a DTL vary during the time it takes a particle to cross the gap and the field magnitude changes with the particle's radial displacement which again varies along the gap, the particle bunches actually undergo transversal defocusing within the gaps [26]. Additionally, noticeable space-charge forces might contribute to the transversal defocusing of the beam (and even dominate this defocusing for low-energy/high-current beams). A large variety of transversal focusing elements such as electric and magnetic quadrupoles are placed at crucial positions along the beam line to counteract transversal beam spreading. (In the ideal representation of a DTL each transversal focusing element exerts strictly transversal forces on the beam. Due to the non-ideal nature of actual setups this is not valid in a strict sense, but often times serves as a sufficient approximation when developing a DTL's beam dynamics design. However, successive error studies considering misalignment of these transversal elements etc. should be performed.)

One common transversal beam focusing scheme is the Alternating Gradient Focusing (AGF), where the particle beam traverses a so-called FODO-lattice. Such a lattice is depicted in Fig. 2.6: the green convergent lenses represent arbitrary transversally focusing elements (F), whilst the red diffusion lenses represent arbitrary transversally defocusing (D) elements. Each element is followed by a drift (O) to an element with opposite focusing properties, hence the name

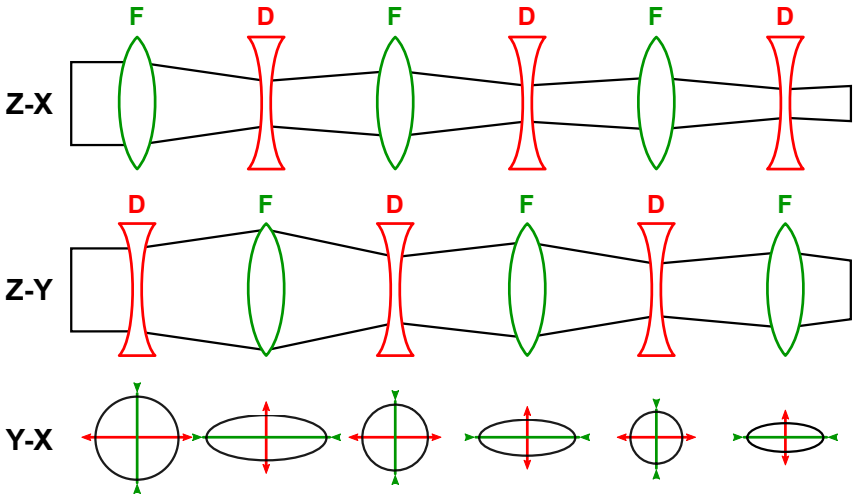

Figure 2.6: Alternating gradient focusing of an ion beam in a FODO-channel [52]. Whenever the beam is focused (F) in the x-z-plane it is simultaneously defocused (D) in the y-z-plane and vice versa. Over time net focusing occurs in both planes due to AGF and hence the x- and y-dimensions of the beam cross section decrease.

FODO-lattice. Note that a focusing element in the x-z-plane is equivalent to a defocusing element in the y-z-plane and vice versa. The actual elements used depend on the type of linac (or beam line) and ion species, among others.

As an ion bunch traverses the FODO-lattice shown in Fig. 2.6, it will first be transversally focused in the x-z-plane whilst being transversally defocused in the y-z-plane. afterward it will be defocused in the x-z-plane whilst being focused in the y-z-plane. The direct proportionality of $|\vec{E}_x|$ to $|x|$ and of $|\vec{E}_y|$ to $|y|$, respectively, guarantees a net focusing effect in both planes along the beam line as every defocusing element is followed by a focusing one overcompensating its defocusing.

The RFQ can also be viewed as a FODO-lattice[14], whereby its electrodes with their oscillating polarity [62] serve as focusing and defocusing elements. AGF occurs in RFQs, if the second terms in Eq. 2.13 and Eq. 2.14, which originate from the distortion from the ideal quadrupole symmetry, are sufficiently small, i.e. in case the influence of the first terms on the transversal beam dynamics dominates. For this, the ratio of coefficients X and A (see. Sub-Sec. 2.8) has to be sufficiently

[14] Of course representation as a FODO-lattice does not include the longitudinal beam dynamics for neither RFQs nor DTLs, but is sufficient for the illustration of the AGF-principle in both types of linacs.

high.

2.8 RF-Defocusing and Acceleration Efficiency

In the following the influence of the second terms in Eq. 2.13 and Eq. 2.14 on the RFQ beam dynamics shall be investigated in detail. These terms are the products of coordinates x and y, respectively, with $\frac{-k_l A V_0}{2} \frac{I_1(k_l r)}{r} \cos(k_l z)$. Other than the focusing terms they therefore show a dependency on z. Whereas the focusing terms are proportional to X, the defocusing terms are proportional to A.

As the electric field component E_z, responsible for acceleration (and longitudinal focusing), also exhibits a proportionality to A (cf. Eq. 2.15), A is referred to as acceleration efficiency. Between both efficiencies the following relation holds true[15]:

$$\begin{aligned} & X + I_0(k_l a)\, A \\ &= \frac{I_0(k_l a) + I_0(k_l m a) + I_0(k_l a)\,(m^2 - 1)}{m^2 I_0(k_l a) + I_0(k_l m a)} \\ &= \frac{I_0(k_l a) + I_0(k_l m a) + m^2\, I_0(k_l a) - I_0(k_l a)}{m^2 I_0(k_l a) + I_0(k_l m a))} \\ &= \frac{m^2\, I_0(k_l a) + I_0(k_l m a)}{m^2 I_0(k_l a) + I_0(k_l m a)} = 1. \end{aligned} \tag{2.19}$$

As a perfect electric quadrupole shows no longitudinal modulation, i.e. $m = 1$, these efficiencies would amount to $X = 1$ and $A = 0$ via Eq. 2.6 and Eq. 2.7. In a perfect quadrupole channel transversal focusing is more efficient than in an "equivalent" RFQ ($m > 1 \Rightarrow X < 1$), since the focusing terms are maximal and the defocusing terms disappear. However, according to Eq. 2.15 $E_{z,0}$ also disappears for $A = 0$. This is congruent with the fact, that an ion beam in a longitudinally unmodulated quadrupole experiences neither longitudinal acceleration nor longitudinal focusing. Thus A has to be chosen in regard to keeping transversal RF-defocusing of the beam sufficiently small, whilst still achieving efficient acceleration and longitudinal focusing.

In conclusion, along an RFQ acceleration and longitudinal focusing have to be balanced efficiently and proficiently with transversal focusing.

[15] Valid in the two-term approximation.

2.9 Space-Charge Effects

The K-T potential was formulated disregarding space-charge effects (cf. Eq. 2.1). (Thus, these are also ignored in case of the two-term and the eight-term potential). However, an ion beam within an RFQ is not only subject to externally applied electric fields, but also to internal space-charge interactions, which increasingly influence beam dynamics in dependence of the beam current/intensity and particle velocities. Especially in case of a high current/intensity and low energy/velocity beam they can not be neglected.

For RFQs, basically two different space-charge effects are of interest:

1. interference of the electric fields of single particles leads to a space-charge field, which in turn acts on the single particles and exhibits variation only over distances that are large compared to the average separation between the particles, i.e. a space-charge field which constitutes a smoothed field distribution
2. Coulomb impacts: particles colliding and thereby exerting impact forces on each other.

For beam bunches consisting of more than 10^8 particles – i.e. for most beam bunches within RFQs – the effect of Coulomb impacts is negligible compared to the contributions of the space-charge field [26]. As space-charge effects affect beam emittances and as the geometric dimensions of an RFQ have to be compatible with the desired emittance values, space-charge effects most of the time have to be considered for RFQ beam dynamics simulations. (Subsections E.1.3 and E.2.1 describe how the RFQ beam dynamics codes PRAMTEQ(M)/RFQGen and TOUTATIS, respectively, process space-charge effects.)

2.9.1 Typical Space-Charge Electric Fields in RFQ Beam Bunches

Envelope equations for continuous beams with arbitrary density profiles that exhibit elliptical symmetry in the x-y space were independently derived at by Sacherer and Lapostolle [26]. The electric-field components for the uniform-density distribution are given by [63]:

$$E_{sx} = \frac{I}{\pi\varepsilon_0\nu(r_x + r_y)}\,\frac{x}{r_x}, \tag{2.20}$$

and analogously

$$E_{sy} = \frac{I}{\pi\varepsilon_0\nu(r_x + r_y)}\,\frac{y}{r_y}, \tag{2.21}$$

with r_x and r_y being the semi-axes of the ellipse in the laboratory frame. $r_x = 2\,a_x$ and $r_y = 2\,a_y$, where a_x and a_y are the rms-beam sizes in x and y, respectively.

Although a linac beam is bunched, above results for a continuous beam can still serve as an approximate description of the transverse electric fields of a long bunch.

However, the electric-field components for a three-dimensional uniform ellipsoid are much more suited to describe a typical linac bunch, for which the three semi-axes are of comparable length. They are

$$E_{sx} = \frac{3\,I\,\lambda\,(1-f)}{4\pi\varepsilon_0 c(r_x + r_y)r_z}\,\frac{x}{r_x}, \tag{2.22}$$

$$E_{sy} = \frac{3\,I\,\lambda\,(1-f)}{4\pi\varepsilon_0 c(r_x + r_y)r_z}\,\frac{y}{r_y} \tag{2.23}$$

and

$$E_{sz} = \frac{3\,I\,\lambda\,(1-f)}{4\pi\varepsilon_0 c(r_x + r_y)r_z}\,\frac{z}{r_z}. \tag{2.24}$$

I is the average beam current over one RF period, and λ is the wavelength. The semi-axes r_i relate to the rms-beam sizes via $r_i = \sqrt{5}\,a_i$, i.e. $r_x = \sqrt{5}\,a_x$ with $a_x \equiv \sqrt{x^2}$. Coordinates x, y and z refer to the centroid of the bunch. The ellipsoid form factor f is a function of parameter $p = \gamma\,r_z\,/\,\sqrt{r_x\,r_y}$. A nearly spherical bunch where $0.8 < p < 5$ is best approximated with[16] $f = 1\,/\,3p$.

By making use of the uniform three-dimensional ellipsoid model an approximation for the longitudinal current limit can be derived [64, 26]. These considerations play a decisive role for the CURLI-code [21] (see Sec. E.1).

2.10 RFQ Design Procedures

In order to get the optimum beam dynamics design for a specific RFQ several objectives have to be balanced out, e.g. :

- highest possible transmission,

[16] Figure 9.4 in Ref. [26] shows the values of f for $p \in [0, 1]$ and $\frac{1}{p} \in (0, 1)$, i.e. for all f-values for $p \geq 0$.

- lowest possible emittance growth,
- shortest possible (electrode) lengths,
- sufficiently low surface fields (and hence bravery factor[17] (cf. Tab. 3.1)) to prevent field breakdown,
- lowest possible power losses.

Some of these features are of course intertwined: for example increasing the electrode voltage also increases the RF power and – ceteris paribus – leads to a shorter RFQ, but also raises the risk of field breakdown [61].

The actual search for a suitable RFQ beam dynamics design can begin once certain requirements have been agreed upon. To this end (most of) the following parameters should have been defined (at least roughly, e.g. in the context of feasible parameter intervals):

- the ion species (and therefore the charge-to-mass ratio(s) $\frac{q}{A}$),
- the entrance current,
- the desired transmission,
- operation frequency f and electrode voltage V_{elec},
- the initial and final (synchronous) energies W_{in} and W_{out},
- and the expected entrance and the desired exit emittances.

With knowledge of these parameters the profiles of the cell length $l_c(z)$[18], focusing strength $B_f(z)$ (cf. Sec. 2.5; Eq. 2.16), modulation $m(z)$, minimum radial aperture $a(z)$ and synchronous energy $W_s(z)$ [62] can be derived.

2.10.1 The LANL Four Section RFQ Design Procedure (LANL FSP)

Although the Los Alamos National Laboratory (LANL) RFQ Design Codes including RFQGen and its predecessor PARMTEQm allow for a variety of different RFQ beam dynamics design approaches, they were originally developed in the context of the Four Section Procedure

[17] Appendix C covers the so-called Kilpatrick or bravery factor, which is associated with the risk of electric field breakdown. A detailed discussion on the FAIR p-Linac RFQ's bravery factor is given in Ref. [3].
[18] $l_c(z)$ is often replaced by synchronous phase[19] $\phi_s(z)$ [61].

(FSP), that also originates from LANL. This design strategy has been adopted and successfully applied for many RFQ projects around the world [65]. Here, the RFQ is segmented into four sections. Each of them performs different tasks with regard to beam transport and evolution. In accordance to this the parameters ϕ_s, W_s, m, a and B_f exhibit a certain behavior along the beam axis (see Fig. 2.7).

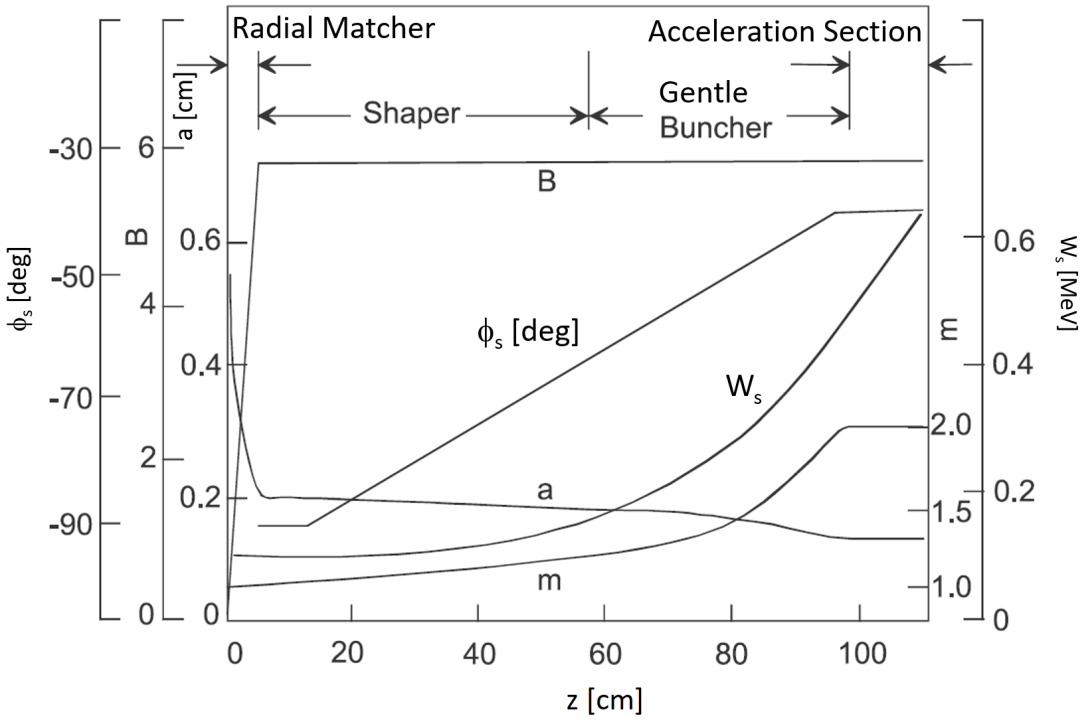

Figure 2.7: Shown are the curves of parameters m, a, W_s, ϕ_s and B along the four different sections as determined by the LANL FSP for a 425-MHz test design published by Crandall et al. in Ref. [9] (modified from Fig. 3.6 of Ref. [62]).

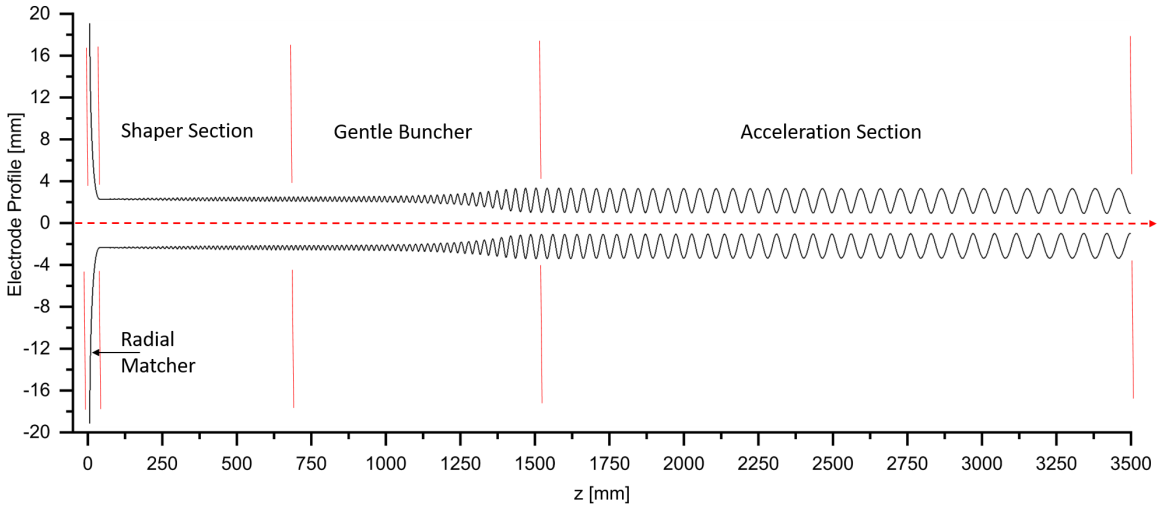

Figure 2.8: Sketch of the electrode tip profile along an arbitrarily chosen hypothetical RFQ (figure based on Fig. 8.7 of Ref. [26]). Shown are the four classic RFQ sections from left to right, i.e. along the beam axis (cf. red dashed horizontal line): the radial-matching section, the shaper section, the gentle-bunching section and the accelerator section. While bunching already begins in the shaper section, adiabatic bunching specifically sets on and is completed in the gentle buncher. (Note that m rises linearly in the acceleration section, whereas a declines linearly, which is not in accordance to the classic LANL 4 Section Procedure, where both m and remain constant within this section, but resembles the beam dynamics designs of CERN's Linac4 and the FAIR p-Linac RFQ (see Fig. 3.3 in Chap. [3]).)

Figure 2.8 shows the electrode tip profile along these four RFQ sections. They are from left to right (i.e. along the beam axis) [62]:

1. Radial Matching Section (RMS; also: Radial Matcher (RM)): in this very short segment right at the RFQ entrance the source DC beam must be matched into the RFQ without particle losses. As the electric field is time-depended so is the acceptance of the beam into the RFQ. This section usually consists of 2 to 8, but most commonly 4 or 5 unmodulated ($m = 1$) RFQ unit cells. Note the steep decline of the (minimal) radial aperture a within this section that leads one to overestimate the longitudinal field components influence on beam dynamics within this section. Due to the non-existent modulation within the RM cells, the E_z-contribution can be neglected near the beam axis. Thus, the beam experiences this section de facto as a channel of almost ideal quadrupole-symmetry and therefore ϕ_s keeps its value of $-90°$. B_f is increased rapidly up to its final value.

2. Shaper Section (also: Shaper): for a beam within a linac to be accelerated according to the

synchronism condition $l_c = \frac{\beta_s \lambda}{2}$, it must be made up of bunches. In the Shaper Section the DC beam form the LEBT is very gently distorted along the z-axis, so it can be shaped almost adiabatically into (ideally) equal bunches in the subsequent Gentle Bunching Section. Therefore, this first shaping process occasionally also is referred to as prebunching; the ions start to accumulate at "pre-bunches". To this end, the Shaper Section provides a smooth transition from a purely transversal electric field distribution within the RM to one with a comparatively strong longitudinal field contribution E_z. For this purpose, modulation m is successively increased from initially small values about 1. $\phi_s(z)$ has shifted from $-90°$ to ca. $-70°$ by the end of this section, which results in some coupling between transversal and longitudinal dynamics. This beginning longitudinal focusing is usually accompanied by moderate transversal emittance growth.

3. Gentle Bunching Section (GBS; also: Gentle Buncher (GB)): here, the previously pre-bunched beam gets properly bunched in a quasi-adiabatic[20] process, i.e. it is gently shaped into (ideally) equal, symmetrical bunches by the E_z-component without (greater) particle losses. While the initial acceleration continues, the synchronous phase is moved toward the crest of the accelerating waveform, where the acceleration is more efficient: ϕ_s is shifted to a value between ca. $-40°$ and ca. $-20°$ by appropriately increasing the center-to-center spacing between successive RFQ-cells. The spacings between the bunch centers also grow and the bunch phase width decreases as the beam is accelerated[21]. As the modulation parameter m increases so do the acceleration efficiency A and subsequently the synchronous particle energy W_s. W_s at the end of this section will be about ten times the entrance energy [22].

4. Accelerator Section: the now formed beam bunches are accelerated in accordance to the synchronism condition so that most of the energy gain $W_{out} - W_{in}$ in the RFQ is obtained within this section. ϕ_s, m and a exhibit nearly constant behaviors and thus the geometric bunch length remains almost constant during the (main) acceleration process (cf. Chap. A). This keeps the bunch from being spatially compressed, which would lead to large space-charge forces accompanied by correspondingly serve emittance growth and particle losses.

Within the FSP the design of these sections is not performed in above order, i.e. in the order of the beam transport trough the RFQ. The FSP actually starts by designing the gentle buncher or rather the end of the gentle bunching section. Here, the Kapchinskiy-Teplyakov conditions have to be satisfied, namely the changing rates of the parameters being sufficiently low in order

[20] Since adiabatic processes are ideal processes, a GBS of infinite length would be required in order to perform actual adiabatic bunching.

[21] The geometric bunch length relates to the length of the so-called bucket, i.e. the region of stable particle motion in the ΔW-$\Delta\phi$ sub-space (see App. A).

to enable adiabatic bunching [26]. Since acceleration efficiency A is still relatively low within the GB, the design algorithm then introduces the prebunching shaper section to reduce the overall RFQ length. afterward the Shaper is designed followed by the Radial Matcher and finally the accelerator section [16].

2.10.2 Influence of Cell Length and Aperture

It can be seen from Eq. 2.3 in Sec. 2.5 that for small arguments $u = k_l\, r$, the modified Bessel function of the 0-th order can be approximated as $I_0(u) \cong 1 + \frac{u^2}{4}$. In the long cells regime, i.e. for $l_c \gg a$, the second term of this approximation can be neglected. Hence, the acceleration efficiency gets $A \approx \frac{m^2-1}{m^2+1}$ (cf. Eq. 2.7 in Sec. 2.5) and thus A increases with growing m in this regime [21]. (For the sake of completion it shall be mentioned that for a regime of large m-values and short cells above approximations of $I_0(u)$ and thus A break down. Thus, in such a case increasing m does not enhance acceleration. Fortunately, the implementation of such a regime is almost never required [21].)

2.10.3 The New Four Section Procedure (NFSP) of IAP Frankfurt

One noticeable characteristic of the LANL FSP is that the mid-cell electrode aperture r_0 and (hence) the transversal focusing strength B are held constant after the RM section. This guaranties a rather undemanding manufacturing of RFQ electrodes and straightforward RFQ tuning, especially at the backdrop of the technological limitations of the seventies and eighties. Although still very common and highly advantageous, this property is no longer imperative for electrode manufacturing due to present-day ball milling.

Despite serving as a feasible and well thought through design scheme for many RFQs, the Four Section Procedure is not optimal with regard to the natural beam developing process within RFQs, precisely because of its constant B-value, which might result in the longitudinal and transversal forces acting on the beam being unbalanced and thus might lead to unstable bunches [16]. After the RM the forces exerted on the beam will undergo the following changes: the beam is gradually bunched whilst acceleration is still low. The decreasing bunch size increases the space-charge forces within the single beams. This effect is most pronounced at the end of the gentle buncher. At the subsequent beginning of the main acceleration process the transversal defocusing forces will be weakened due to the rapidly increasing beam velocity [18].

It should furthermore be considered, that bunching a high velocity beam is more difficult than bunching a slow one[22] [17]. This can be seen from the following equation [66]:

$$\frac{d\,\Delta\phi}{dz} = -\frac{\omega\,\Delta W}{mc^3\,\beta_s^3\,\gamma_s^3} = q\,E_0\,T\,(cos\phi\,-\,cos\phi_s). \tag{2.25}$$

Thus, for a given value of $\frac{d\,\Delta\phi}{dz}$ is inversely proportional to $\beta_s^3\,\gamma_s^3$. This results in longer Shaper and Buncher sections for higher energetic beams, but also in a larger phase width of the "bucket", i.e. the region of stable particle motion in the ΔW-$\Delta\phi$ sub-space (see Appx. A). This reduces beam losses in case of high space-charges.

Since the 1980-ties the LANL Four Section Procedure has been modified at the Institute of Applied Physics (IAP) of Goethe University Frankfurt by Schempp et al. These modifications allow greater variation of the parameters to gain shorter RFQs and decrease emittance growth. For instance, a smoother and varied behavior of $B(z)$ can result in more compact RFQs with high transmission, in case the geometric bunch length is kept constant [14] (cf. Chap. A). This principle was applied – among others – for RFQs at GSI, DESY[23], **B**rookhaven **N**ational **L**aboratory (BNL; New York) and the **F**ermi **N**ational **A**ccelerator **L**aboratory[24] (FNAL).

It eventually gave rise to the so-called **N**ew **F**our **S**ection **P**rocedure (NFSP)[25] developed by A. Schempp and C. Zhang at IAP Frankfurt [16]. Its main features are [67]:

- variation of focusing strength B in accordance with the changes in the space-charge forces along the RFQ and an according retuning of the synchronous phases' evolution speed for an improved bunching process [16].
- replacement of the more "forced" prebunching of the LANL FSP by a smooth and symmetric prebunching accompanied by more stable particle motion
- a shortened bunching process compared to that of the LANL FSP, leading to a more compact structure.

During bunching, the transversal and longitudinal forces are always balanced in order to achieve a

[22] Higher injection energies/velocities also lead to longer Shaper and Buncher sections.
[23] **D**eutsches **E**lektronen-**Sy**nchrotron (English: German Electron Synchrotron) in Hamburg, Germany
[24] The Fermi National Accelerator Laboratory (also known as Fermilab) is a particle physics research center operated by the U.S. Department of Energy. It is located about 50 kilometers west of Chicago, Illinois, in the community of Batavia. In 2012, its Cockcroft-Walton based injector was replaced after 40 years of operation by a new beam line including a 750 keV 4-rod RFQ developed by A. Schempp et al. at IAP Frankfurt: `https://news.fnal.gov/2012/08/so-long-cockcroft-walton` (cf. Sec. 3.7).
[25] Also known as BABBLE: **B**alanced and **A**ccelerated **B**eam **B**unching at **L**ow **E**nergy [18]

high quality beam. B increases with growing space-charge forces until the transversal defocusing effects have been sufficiently weakened by the increase in beam energy and bucket length. The focusing strength then declines accordingly in order to keep the longitudinal and transversal forces acting on the beam balanced.

Figure 2.9 shows the exemplary curves of B and further design parameters along the beam axis of an RFQ, for whose beam dynamics design the NFSP was partly applied (it differs in that it shows no maximum-seperatrix section (see below)).

Like the LANL FSP, the NFSP also divides an RFQ into four sections, whereby different partitioning rules are applied and the transitions between the sections are much smoother [16, 17, 18, 19]:

- Maximum-Separatrix[26] (MS) Section is characterized by $\phi_s \approx -90°$; ϕ_s increases only at an almost marginal rate. Besides its function as a Radial Matcher, the MS Section also performs symmetrical and soft bunching at a wide phase acceptance. The B-curve exhibits a discontinuity: after a short and steep increase – similar to the one this parameter undergoes in the RM section of a FSP design, but to an about 40% lower interim final value – B continues to grow in a (quasi-)linear fashion. m undergoes a slight increase, and analogously a undergoes a slight decrease.
- Main Bunching (MB) Section: in this section B is further increased in order to balance the stronger growing transversal defocusing forces due to the decreasing bunch size. This allows for a strong, yet safe speeding-up of the bunching process. In the MB section B reaches its maximum value, which is higher than the one of the corresponding FSP design would be. As the bunches are stabilized by the high B-values, the growth rates of ϕ_s and m rise significantly.
- Mixed Bunching-Accelerating (MBA) Section: A rapidly increasing beam velocity results in weakened transversal defocusing effects. B is accordingly decreased in order to avoid longitudinal emittance growth and to allow for (slightly) larger apertures whereby the bunches are still kept stable. Thus, ϕ_s and m eventually rise much more rapidly than they would in the GB of the corresponding FSP design. Hence, the length increase due to the preceding slowed down bunching can at least be compensated, if not even over-compensated for (which is the case pleasingly often).
- Main Accelerating (MA) Section: In order to achieve stable acceleration ϕ_s and m are held

[26] The so-called Separatrix is the trajectory in the $\Delta\phi$-ΔW sub-space, that encloses the area of stable particle motion around the so-called stable fixed point. This area is also referred to as RF "bucket". Further information is given in Appx. A.

(nearly) constant or preferably rise linearly until the desired final energy is reached – like they would in the acceleration section of an RFQ of the classic or modified FSP design. Ideally, B continues its smooth decline.

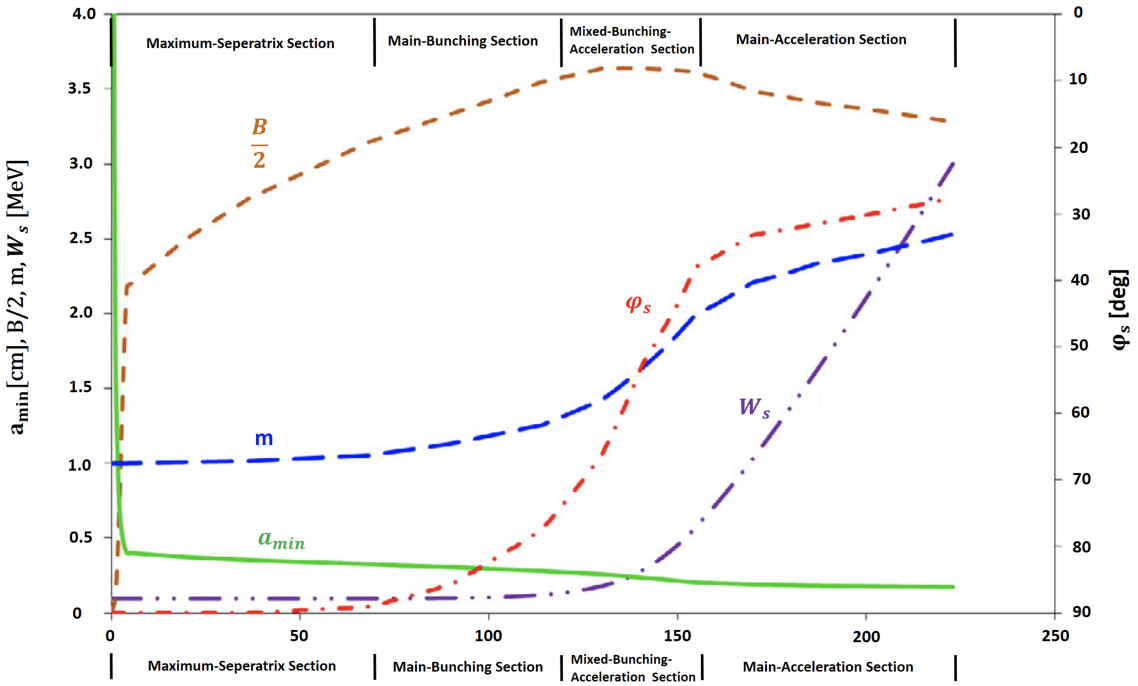

Figure 2.9: Curves of parameters m, a_{min}, ϕ_s, W_s and B (actually depicted is $B/2$) along the beam axis in the four different RFQ sections of a NFSP design. (Figure modified from Fig. 2 of Ref. [19].)

For a given NFSP design, acceleration starts later than for the corresponding LANL FSP design. Once it set in, however, it increases more rapidly than for the associated LANL FSP design. This allows for a significant net-reduction in RFQ length by application of the NFSP. (Rather recently, the beam dynamics design of the new MYRRHA-RFQ was also generated according to the NFSP [68, 67].)

2.11 Beam Dynamics Design of the Linac4 RFQ

Besides the designs discussed above, there also exist many further approaches. One noticeable concept was laid out by A. Lombardi for the beam dynamics design of the Linac4 RFQ at CERN[27] [69, 70].

Parameter	**CERN's Linac4 RFQ**
Ion Species	H^-
Operation Frequency f $[MHz]$	352.2
Des. In. Current I $[mA]$	70
Input Energy W_{in} $[keV]$	45
Output Energy W_{out} $[keV]$	3.0
Trans. In. Emittance, norm., rms $[\pi\, mm\, mrad]$*	0.20 - 0.35

Table 2.1: Key design and beam parameters of the Linac4 RFQ at CERN [69, 70]. (*An explanation for the (at first glance perhaps inconsistent) presence of factor π in this expression (and all further emittance expressions within this thesis) is given in Sec. D.5 of App. D.)

The beam dynamics design of the Linac4 RFQ is not too dissimilar from one generated by the classic LANL FSP, in that focusing strength B almost exactly behaves as it would in the latter throughout all sections: along the $16.7\,mm$ long radial matcher (consisting of four cells) B undergoes a very steep increases to its maximum value of 5.77 [70] to only drop by about 6% by the RFQ exit. Also in almost complete accordance with the LANL FSP are the behaviors of parameters a, m and ϕ (see Fig. 2.10). However, in the acceleration section a, m and ϕ still show linear, but non-constant behavior. Whereas m and ϕ increase linearly from 1.9 to 2.4 and from $-30°$ to $-22°$, respectively, a decreases linearly from 2.0 mm to 1.8 mm. These parameter progressions allow for a more rapid acceleration. In that way the RFQ length could be kept at ca. 3 m, despite a desired exit energy of 3.0 MeV [70]. (Values such as the RFQ length as well as the extreme values of a, B, ϕ and m along the beam axis are compared for the CERN Linac4 RFQ and the FAIR p-Linac RFQ in Tab. 3.1 of Chap. [3].)

[27] Here: research facility of the equally named European Organization for Nuclear Research at Geneva, Switzerland (`https://home.cern`). The acronym CERN derives from the European Council for Nuclear Research, which was charged with establishing such an organization (French: **c**onseil **e**uropéen pour la **r**echerche **n**ucléaire).

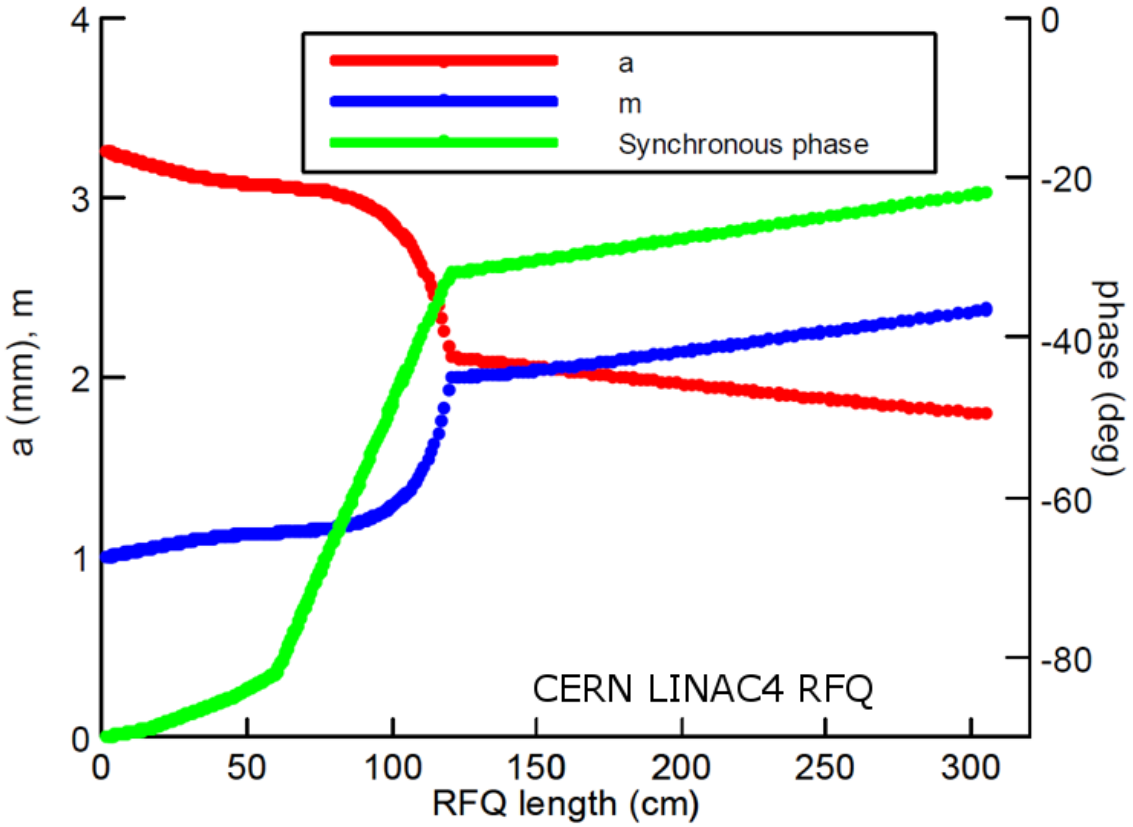

Figure 2.10: Beam dynamics design of CERN's Linac4 RFQ by A. Lombardi. Shown are the curves of (minimum) aperture a, modulation parameter m and synchronous phase ϕ_s against the RFQ length (modified from Fig. 1 of Ref. [70]). The not depicted curve for focusing strength B exhibits an (almost) classical FSP-course: along four RM cells of (in total) 16.7 mm length, B rapidly rises to its maximum value of 5.77, which it (nearly) keeps for the rest of the RFQ length. (At the high-energy end, B has declined by about 6%.)

[3] The p-Linac RFQ Beam Dynamics Design and Simulations

When design work of the FAIR Proton-Linac RFQ's beam dynamics began in February 2017, the RFQ's mechanical and RF designs by IAP as well as the source and LEBT designs by GSI's and CEA Saclay's Ion Source Groups were already close to finish. This and further factors led to the following rather challenging requirements regarding the beam dynamics design:

- as the mechanical dimensions of the RFQ tank had already been specified, the electrode length was restricted to a value between 3324 and 3335 mm, leaving just 11 mm of margin
- the energy of the source protons was chosen to an unusually high value of 95 keV by CEA Saclay, France, albeit a considerable lower energy would have been preferable[1]. Note that the entrance energy of the Linac4 RFQ, whose parameters are quite similar to these of the RFQ at hand, with 45 keV is less than 50 % of the given one (cf. Sec. 2.11). It has, however, to be kept in mind, that this energy was originally chosen in regard to optimize for a design current of 30 mA instead of 70 mA.
- the transversal normalized rms-entrance emittance was decided to be $0.3\,\pi$ mm mrad[2]
- in February 2017 the RFQ exit design current was chosen to be 70 mA, although it was foreseeable that the RFQ injection current would be selected to a value between 70 mA and 100 mA

[1] As the RFQ cell lengths are proportional to the (synchronous) particle velocity ($l_c = \beta_s \lambda$) a higher RFQ entrance energy results in longer RFQ cells on the entrance side than a lower entrance energy ceteris paribus would. Starting out with a low entrance synchronous velocity and hence short RFQ cells has proven to reduce the overall RFQ length compared to the former case. In addition, it might also allow for further optimization, e.g. the reduction of the electrode voltage.

[2] Note, that unless stated otherwise all emittances presented in this thesis are normalized rms-emittances. The transversal emittances are (usually) given in units of π mm mrad, the longitudinal in units of π MeV deg. Section D.5 in App. D provides a brief discussion on the meaningfulness of adding the factor π as this seems to be at odds with the definition of the beam emittance ε as occupied area A in the respective sub-phase space divided by π: $\varepsilon = A / \pi$ (cf. Eq. D.1 in App. D).

- in order to keep the loss power (and the associated costs) low and to not risk voltage breakdown the electrode voltage (amplitude) had to be kept below 95 kV
- CST Microwave Studio RF tuning simulations were in favor of a constant electrode radius along the RFQ.

Since the designs of the subsequent MEBT and CH-DTL were also mostly completed the RFQ exit energy of 3 MeV as well as the desired exit values for the transversal and longitudinal emittances had already been specified, too [24].

The FAIR p-Linac RFQ's beam dynamics design was developed with the RFQGen-code, which was also used to perform several simulation studies to investigate the influence certain parameters exert on the RFQ beam dynamics and beam at the RFQ exit. The beam dynamics design was completed in May 2018. Among others, the RFQGen-output data also contain milling lists for the RFQ electrodes. These were handed over to the manufacturer[3] that built the RFQ in close cooperation with IAP. The manufacturing and first assembly of the RFQ including the electrodes was completed in September 2018. (Manufacturing of the tank components, consisting of the upper and lower tank shells as well as the middle frame, had began in September 2017 and had been completed in April 2018.) The final machining steps for flatness and frequency took place in April 2019 [5]. In February 2020, the RFQ was delivered to IAP. Not least due to the COVID-19 outbreak and the successive shut-down, tests of all kinds are still suspended so far (September 2021). Thus, as of yet the RFQ is also not set up with the source and LEBT-line and has not been operated with a beam. This will probably take place in the completed p-Linac building near Darmstadt and thus is not expected before 2023[4].

Therefore, all associated beam parameters and particle distributions presented in this chapter stem from simulations. If not stated otherwise these simulations were performed with RFQGen. (Section 3.4 presents the reproducibility check of the beam dynamics design within TOUTATIS, whereas sections 3.3 and 3.7 also include TraceWin-simulations.) As mentioned in Sec. 2.11 the beam dynamics of the FAIR Proton-Linac RFQ exhibits resemblance of CERN's Linac4 RFQ, in that both represent a specific modification of the classic LANL FSP (cf. Sub-Sec. 2.10.1). Figure 3.1 shows the curves of modulation parameter m, (minimum) radial aperture a and of synchronous phase ϕ_s for the FAIR p-Linac RFQ against the cell number and the RFQ length, respectively. Tab. 3.1 offers a direct comparison of the key parameters for both designs (cf. Tab. 2.1).

[3] Fa. Kress Sondermaschinenbau GmbH (`https://www.kress-gmbh.de/en`
[4] Personal correspondence with C. Kleffner (GSI)

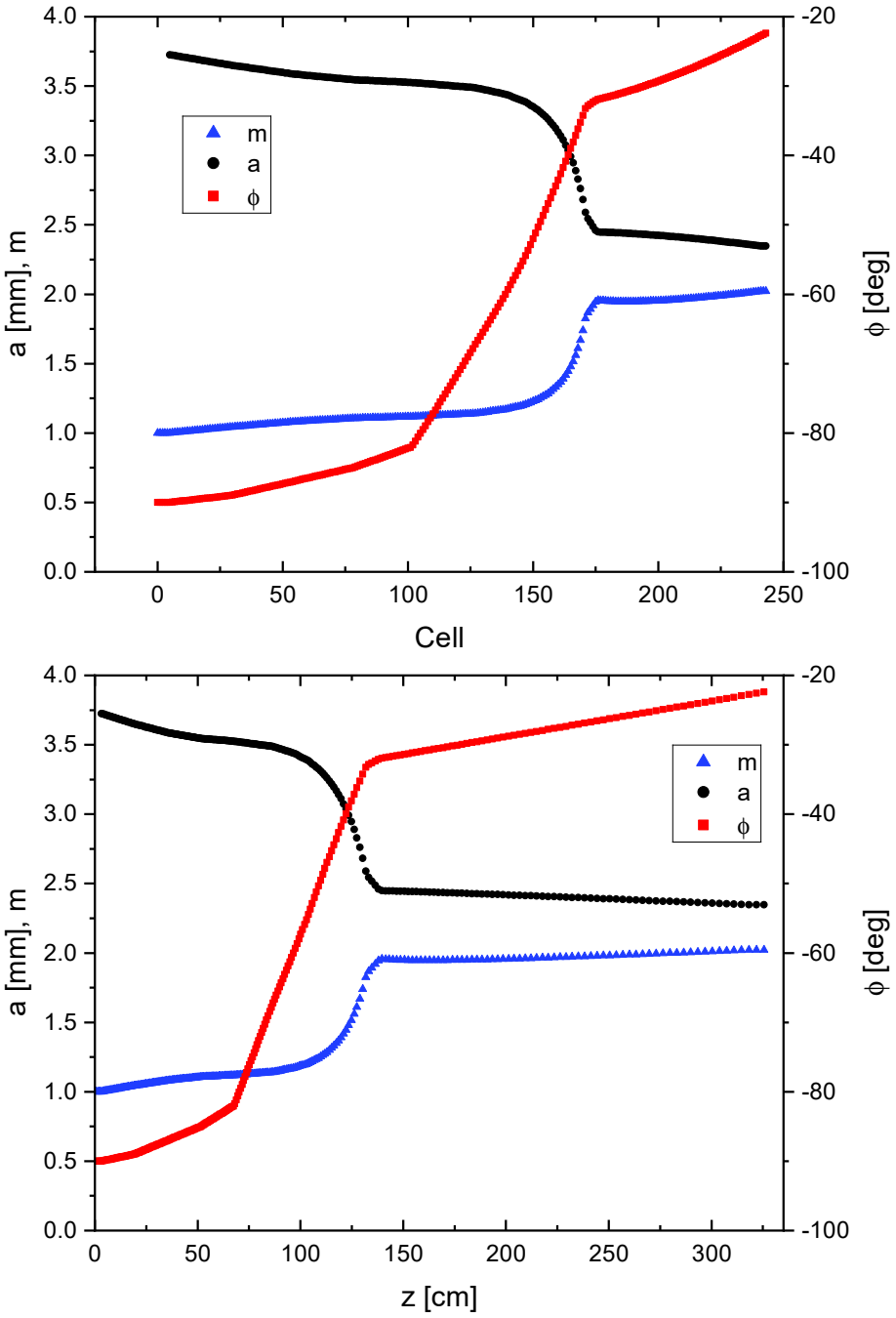

Figure 3.1: Beam dynamics design of the FAIR Proton-Linac RFQ. Shown are the behaviors of modulation parameter m, (minimum) radial aperture a and of synchronous phase ϕ against the RFQ cell number (top) and against the RFQ length (bottom), respectively.

The linear and non-constant behaviors of parameters a, m and synchronous phase ϕ_{syn} within the acceleration section differ from the LANL Four Section Design Scheme and also enable more efficient acceleration as well as shorter RFQs (cf. Sec. 2.11). The opposing behavior of modulation parameter m and minimal radial aperture a is of high importance in this regard.

As will be shown in Sec. 3.1 an alternative design adhering to the original FSP with otherwise similar key parameters such as electrode voltage V_{el}, minimum aperture a_{min}, maximum modulation m_{max} and focusing parameter B_{max} would produce a similar RFQ exit distribution (with a slightly reduced transmission in the matched case) for the matched case (cf. Sec. 3.2) – albeit with a slightly reduced transmission. However, the alternative electrode length surpasses the allowed maximum of 3335 mm by almost 19 cm, making this approach unsuitable. As the NFSP on the other hand was introduced to generate particularity compact/short RFQs it presents no feasible alternative either: such a design could not be realized with electrodes not shorter then the minimum requirement of 3324 mm without otherwise impractical choices for the other key parameters.

Figure 3.3 shows the usual parameter curves against the RFQ length for both the FAIR p-Linac RFQ and the CERN Linac4 RFQ. Note how the a-curves almost appear to be horizontal mirror images of the m-curves for both beam dynamics designs. Despite the rather strong resemblance of the respective parameter curves for both RFQs the a- and the m-curves run steeper in case of the CERN Linac4 RFQ. The Gentle Bunching Section of the Linac4 RFQ ends at cell 227, i.e. 120.3 cm behind the RFQ entrance, where the synchronous energy is $W_s = 449.8$ keV. Thus, its acceleration section extends from cell 228, $z = 121.7\,cm$ and $W_s = 477.2$ keV to cell 303, $z = 307.0$ cm and $W_s = 3.024$ MeV. Within this section, m rises from 2.04 to 2.37, whereas the (minimum) aperture a drops from 2.11 mm to 1.82 mm.

In contrast, due to the higher synchronous entrance energy in case of the FAIR p-Linac RFQ the synchronous energy has reached a slightly higher value at the start of the acceleration section, i.e. at cell 172 or 133.3 cm behind the RFQ entrance ($W_{syn} = 512.4$ keV (cf. Sec. 3.8)). Hence, its acceleration section extends from cell 173, $z = 134.8$ cm and $W_{syn} = 541.1$ keV to cell 243, $z = 325.5$ cm and $W_{syn} = 3.001$ MeV. In this section m is increased from 1.89 to 2.02, whereas a drops from 2.52 mm to 2.35 mm.

Parameter	CERN Linac4 RFQ	FAIR p-Linac RFQ
Ion Species	H^-	proton
Operation Frequency f $[MHz]$	352.2	325.224
Electrode Length L_{el} $[cm]$	306	333
Des. In. Current I $[mA]$	70	100
Electrode Voltage V_{el} $[kV]$	78.27	88.43
Input Energy W_{in} $[keV]$	45	95
Output Energy W_{out} $[MeV]$	3.024	3.015
Trans. In. Emit. $[\pi\, mm\, mrad]$	0.20 - 0.35	0.30
Max. Modulation Parameter m_{max}	2.38	2.02
Max. Focusing Parameter B_{max}	5.77	5.70
Minimum Radial Aperture* a_{min} $[mm]$	1.8	2.4
Final Synchronous Phase ϕ_f $[deg]$	-22.0 deg	-22.4 deg
Trans. Electrode Radius ρ $[mm]$	2.8	3.2
Long. Electrode Profile	sinusoidal	sinusoidal
Average Aperture r_0 $[mm]$	3.3	3.3
ρ / r_0	0.85	0.85
Bravery Factor**	1.84	1.77
Number of RFQ Cells	303	246
Number of Radial Matching Cells	4	5

Table 3.1: Parameter comparison between the Linac4 RFQ and the FAIR p-Linac RFQ. (Further and more detailed information on the FAIR p-Linac RFQ's mechanical and RF design are found in Ref. [3].) (*Expressed precisely, this value specifically refers to the minimum of the minimum aperture per cell along the RFQ (cf. Fn. [7] in Sec. 2.5). **The so-called bravery or Kilpatrick factor b is a measure for the risk of electric field breakdown. It is the quotient of the actually present maximum surface field $E_{S,max}$ along the RFQ and its so-called Kilpatrick field limit E_K: $b = E_{S,max} \,/\, E_K$. In case of the FAIR p-Linac $E_{S,max} = 31.5\, MV \,/\, m$ and $E_K = 17.8\, MV \,/\, m$. Further information on this limit and on electric field breakdown in linacs is given in Appx. C.)

Table 3.6 shows the direct comparison[5] between the two RFQs' acceleration sections. It can be seen that for both RFQs about 80.7% of the total energy gain takes place in the acceleration

[5] The presented parameters for the Linac4 RFQ were gained from a reconstruction of its design based on RFQGen/PARMTEQ(M) input files (courtesy of A. Lombardi); their actual values might slightly differ. The geometry file used for this reconstruction was VSINE.txt (cf. Tab. E.1 in Sub-Sec. E.1.4 of App. E).

sections, which are almost equally long and thus make up roughly the same percentage of their respective overall RFQ length. The same holds true in regard to the number of cells in these sections. A look at the ϕ_{syn}-curves reveals their great similarity for both beam dynamics designs. The strongest difference between them concerns the m- and a-curves. Despite the stronger rise and decline, respectively, of m and a in case of the CERN Linac4 RFQ's acceleration section its ratio of acceleration section length to overall RFQ length is raised by 3.7 % compared to the p-Linac RFQ (cf. Tab. 3.6). Nonetheless, the overall RFQ length of the p-Linac RFQ exceeds the Linac4 RFQ's by 10.9 % not least because of its much larger entrance energy. This also contributes to a and m exhibiting lower and higher values, respectively, at the beginning of the acceleration section in case of the Linac4 RFQ. Although the z-coordinates of the acceleration section's first cell are very similar for both RFQs, the numbers of these cells deviate quite strongly. Whereas cell 228 marks the beginning of this section for the Linac4 RFQ, cell 173 is the first cell of the p-Linac RFQ's acceleration section. Here, the lower ion source energy results in shorter cells for the Linac4 RFQ and hence an increased number of cells in the first three RFQ-sections (+ 32 % to FAIR's RFQ) in order to reach approximately the same energy as in case of the FAIR p-Linac RFQ. This higher number of cells in these three sections in turn allows for a steeper rise in m and fall in a within them as $|\Delta m|$ and $|\Delta a|$ for two consecutive cells can be lower and thus the transition from one cell to its neighbor can be smoother. In this regard again a lower entrance energy proves as a great advantage which also manifests in the Linac4 RFQ's electrode voltage of 78.27 keV equaling only 88.5 % of the p-Linac RFQ's. Not least due to the higher RFQ entrance energy in combination with the restrictions given above the transmission at the exit of the p-Linac-RFQ is ca. 6 % lower than for the Linac4 RFQ (see also Sec. 3.5).

Table 3.2 provides an overview of the lengths of the different sections and regions of the FAIR Proton-Linac RFQ. Tables 3.3 and 3.4 show the electrode parameters and the design beam parameters at the RFQ entrance, respectively: in Summer 2017 it was decided between CEA's Source Group and IAP to settle the initial Twiss Parameters to $\alpha_{in} = 0.7$ and $\beta_{in} = 0.04\,mm/\pi\,mrad$ as they at the time were considered to constitute the optimum amongst the feasible Twiss parameter sets. The resulting phase space plots at the RFQ exit for this choice of Twiss parameters are depicted in Fig. 3.4.

A comparison between the simulation results of this case, i.e. the original design[6] case, and these

[6] "Design" as these parameters were entered in the original "input"-line of RFQGen's input-file that the FAIR p-Linac RFQ's beam dynamics design is based on. However, the choice of these entries in the "input"-line does not influence the beam dynamics design, but it determines the beam dynamics simulation and hence the RFQ exit distribution.

corresponding to the actual optimal transversal entrance Twiss parameters (cf. Fig. 3.6) are given in Tab. 3.8 of Sec. 3.2. This section furthermore provides a thorough investigation of the influence the initial transverse Twiss parameters exert on the RFQ's beam dynamics. Therefore, this set of parameters was set in RFQGen for the simulations that eventually led to the RFQ's beam dynamics design. These simulations used a 4D-Waterbag distribution consisting of 100,000 macro-particles at the RFQ entrance. The entrance emittance of $0.3\,\pi\,\mathrm{mm\,mrad}$ followed the proposal from a CEA report of 2013 [24]. With 3.015 MeV the actual synchronous exit energy was set slightly (0.5 %) higher than the required value of 3 MeV (see Sec. 3.7). This was done to establish a safety margin so that the average particle energy as well as the energies of a critical number of particles would not turn out lower than 3 MeV at the RFQ exit. This is not least due to the MEBT being able to handle this "overshooting" far better than an "undershooting". This strategy worked well as the average exit energy turned out to be 3.011 MeV (cf. Tab. 3.5).

RFQ Section/Region	**Length [mm]**
Radial Matching Section	32.79
RM Gap d	8.28
Electrode Length	3329.84
Δm-transition cell	2.84
$m = 1$-transition cell	4.99
Exit Gap	4.88
Exit-Fringe-Field Region	10.00

Table 3.2: Lengths of various RFQ sections and regions given by the RFQGen-output files; the gap lengths are preliminary, not as built. Further information on the transition cells and the actual gap lengths of the RFQ as built is given in Sec. 3.7; cf. Fig. 3.2.

Parameter	**Value**
$\rho\,[mm]$	3.17 mm
$r_0\,[mm]$	3.73 mm
$\rho\,/\,r_0$	0.85

Table 3.3: Values of the trans. electrode radius ρ, the mid-cell aperture / mid-cell radius r_0 and their ratio $\rho\,/\,r_0$.

Parameter	Value
RFQ Entrance Current $I_{in}\,[mA]$	100
Entrance Macro-Particle Distribution Function	4D-Waterbag
Synchronous RFQ Entrance Energy $W_{syn,in}\,[keV]$	95
$\varepsilon_{x/y,in,rms}\,[\pi\,mm\,mrad]$	0.29
Transversal RFQ Entrance Twiss Parameter α_{in}	0.7
Transversal RFQ Entrance Twiss Parameter $\beta_{in}\,[mm/\pi\,mrad]$	0.04
RFQ Entrance Energy Spread $\Delta W_{in}\,[keV]$	0.0
Number of Input Macro-Particles	100,000

Table 3.4: Design and entrance beam parameters of the FAIR p-Linac RFQ.

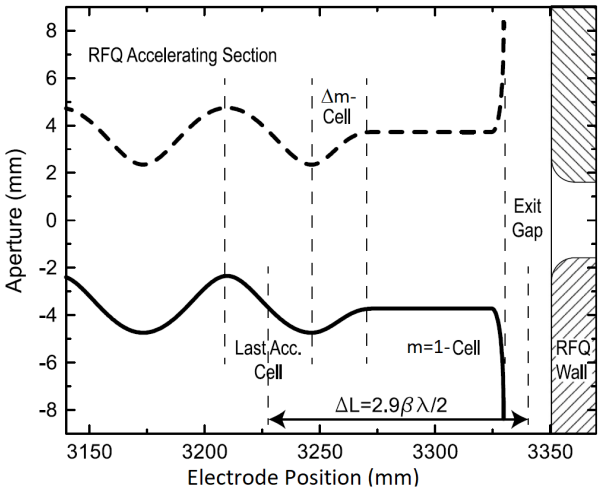

Figure 3.2: Detailed sketch of the electrode profiles at the RFQ exit [28]. Both curves represent a pair of opposing electrodes in the horizontal (dashed, top) and vertical (continuous, bottom) plane, respectively. Note that the actual exit gap length (depicted here) varies from the preliminary given in the RFQGen output data (cf. Tab. 3.2). (The same holds true regarding the entrance gap (cf. Tab. 3.2 and Tab. 3.13 in Sec. 3.7).)

Figure 3.4 provides the phase space plots at the RFQ exit, i.e. 4.88 mm behind the electrode ends, for this simulation (cf. Tab. 3.5). As all other phase space plots presented in this thesis they are plotted with PlotWin[7], a code provided by CEA DACM. All phase space plots of simulations on the FAIR p-Linac RFQ refer to the distributions 4.88 mm behind the electrode ends.

[7] `http://irfu.cea.fr/en/Phocea/Page/index.php?id=783`

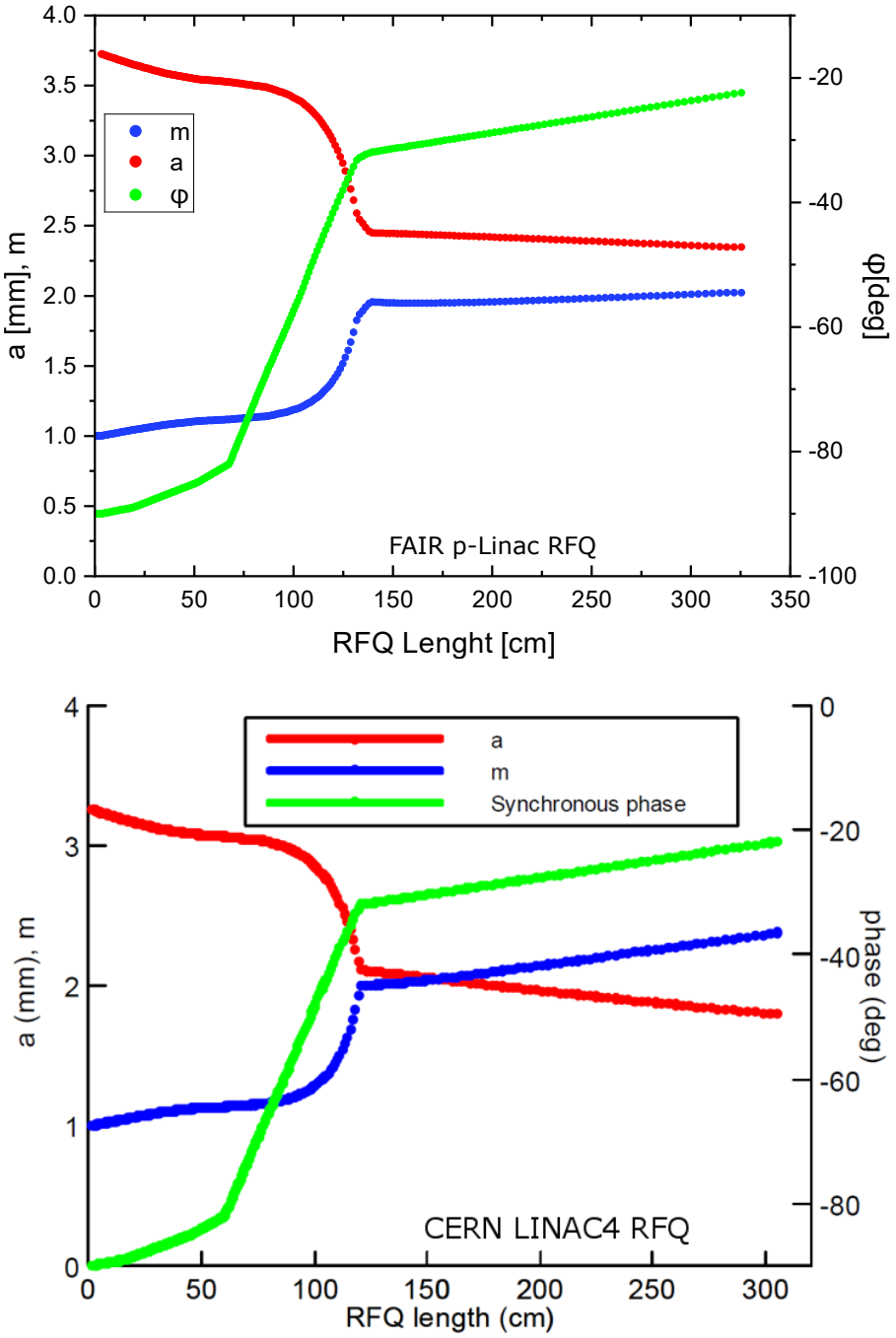

Figure 3.3: Beam dynamics design of the FAIR Proton-Linac RFQ (top) and CERN's Linac4 RFQ (bottom; modified from Fig. 1 of Ref. [70]). Shown are the curves of modulation parameter m, (minimum) radial aperture a and of synchronous phase ϕ against the RFQ length.

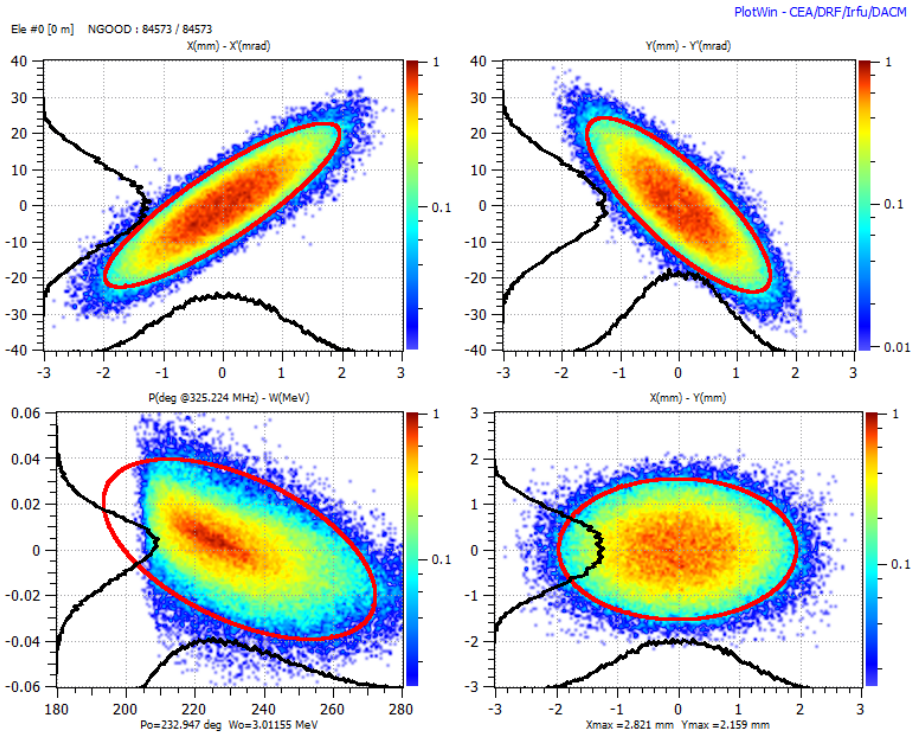

Figure 3.4: Phase space plots and distribution projections (black curves) for the design beam at the FAIR p-Linac RFQ's exit (4.88 mm behind the electrode ends). The entrance current was chosen to 100 mA represented by 100,000 macro-particles. The transversal entrance Twiss parameters were set $\alpha_{in} = 0.7$ and $\beta_{in} = 0.04\,mm/\pi\,mrad$ (cf. Sec. 3.2). The colors of the scatter plots refer to the normalized macro-particle density (cf. scales at the right frames of the plots). The red ellipses correspond to the normalized 95% emittances (cf. Tab.3.5).

Parameter	Value
$\varepsilon_{x,out,n,rms/95\%}$	$0.34/1.76\,\pi\,mm\,mrad$
$\varepsilon_{y,out,n,rms/95\%}$	$0.33/1.75\,\pi\,mm\,mrad$
$\varepsilon_{z,out,n,rms/95\%}$	$0.21/1.33\pi\,MeV\,deg$
$\varepsilon_{x-y,out,n,rms/95\%}$	$0.58/3.03\pi\,mm^2$
Synch. Exit Energy W_{syn}	$3.015\,MeV$
Ave. Exit Energy W_{syn}	$3.011\,MeV$
Transmission	84.3 %

Table 3.5: Beam parameters at the exit of the FAIR p-Linac RFQ (4.88 mm behind the end of the electrodes) for the 100 mA design proton-beam with transversal RFQ entrance Twiss Parameters $\alpha_{in} = 0.7$ and $\beta_{in} = 0.04\,mm/\pi\,mrad$ (cf. Sec. 3.2) and an RFQ entrance energy spread of $\Delta W = 0.0$ keV; 100,000 input macro-particles.

Parameter	CERN Linac4 RFQ	FAIR p-Linac RFQ
First Cell of Acc. Sec.	228	173
Begin of Acc. Sec. (z-coordinate [cm])	121.7	134.8
Last Cell of Acceleration Section	303	243
End of Acc. Sec. (z-coordinate [cm])	307.0	325.5
#Cells in Acc. Sec.	76	71
Length of Acc. Sec. [cm]	185.3	190.7
#Cells in Acc. Sec. \ #RFQ Cells [%]	25.0	28.9
Length of Acc. Sec. \ RFQ Length [%]	60.4	57.0
Acc. Sec. Entrance Energy W_{syn} [keV]	477.2	541.1
Acc. Sec. Exit Energy W_{syn} [keV]	3,024.1	3,000.5
Acc. Sec. ΔW_{syn} [keV]	2,546.9	2,459.4
Acc. Sec. $\frac{\Delta W_{syn,Acc.\,Sec.}}{\Delta W_{syn,RFQ}}$ [%]	82.7	78.8
Acc. Sec. Entrance Mod.-Parameter m	2.04	1.89
Acc. Sec. Exit Mod.-Parameter m	2.37	2.02
Acc. Sec. Δm	0.33	0.13
Acc. Sec. Entrance Aperture a [mm]	2.11	2.52
Acc. Sec. Exit Aperture a [mm]	1.82	2.35
Acc. Sec. Δa [mm]	0.29	0.17
Acc. Sec. Entrance Sync. Phase ϕ [deg]	-32.15	-32.60
Acc. Sec. Exit Sync. Phase ϕ [deg]	-21.75	-22.40
Acc. Sec. $\Delta\phi$ [deg]	10.40	10.20

Table 3.6: Comparison between the parameters of the Linac4 RFQ's and the FAIR p-Linac RFQ's acceleration sections.

3.1 Alternative Design with the LANL-Four Section Procedure

To demonstrate the advantages of the beam dynamics design with non-constant parameter-curves (a, m and ϕ) in the acceleration section compared to the standard LANL design, the p-Linac RFQ's beam dynamics design was re-modeled according to the latter. Figure 3.5 shows the parameter curves of both designs against the z-coordinate. Table 3.7 presents a direct comparison of their key parameters. The exit beam parameters are very similar for both designs, but the electrodes of the LANL design are almost 19.5 cm longer than the manufactured electrodes according to the actual design[8]. Within the LANL-scheme a sufficient shortening of the electrodes would not have been possible without either risking sparking due to a too high voltage and therefore KP factor or due to an intolerable transmission reduction and/or emittance growth. However, the slightly modified LANL-approach similar to that of the Linac4 RFQ allows for sufficiently short electrodes and even slightly improves the transmission and emittances at the RFQ exit.

Parameter	**As Built**	**LANL**
Cell Number*	243	249
Electrode Length $[mm]$	3329.84	3524.17
Electrode Voltage $[kV]$	88.43	86.00
min. aperture a_{min} $[mm]$	2.35	2.38
max. modulation m_{max}	2.02	1.99
max. Foc. Par. B_{max}	5.70	5.79
Transmission [%]	88.470	85.127
$\varepsilon_{x,rms,n,out}$ $[\pi\, mm\, mrad]$	0.323	0.325
$\varepsilon_{y,rms,n,out}$ $[\pi\, mm\, mrad]$	0.321	0.328
$\varepsilon_{z,rms,n,out}$ $[\pi\, MeV\, deg]$	0.205	0.208
Synchronous Exit Energy W_s $[MeV]$	3.015	3.0169
Average Exit Energy W_{ave} $[MeV]$	3.0115	3.0170

Table 3.7: Comparison of the design parameter for the p-Linac RFQ as built (left) and an alternative design according to the LANL scheme (right). (*Cell number refers to last cell of the acc. section).

[8] Initially, the voltage of the actual p-Linac RFQ had also been chosen to be 86.0 kV. However, this would have resulted in an electrode length of 3370.84 mm, which exceeds the actual one by 41 mm and the allowed maximum of 3335 mm by 35.85 mm. Hence, a slight adaption of the electrode voltage to 88.43 kV was required, which resulted in the desired electrode length. Hereby, the beam dynamics design itself and thus the RFQ exit distribution underwent only marginal changes.

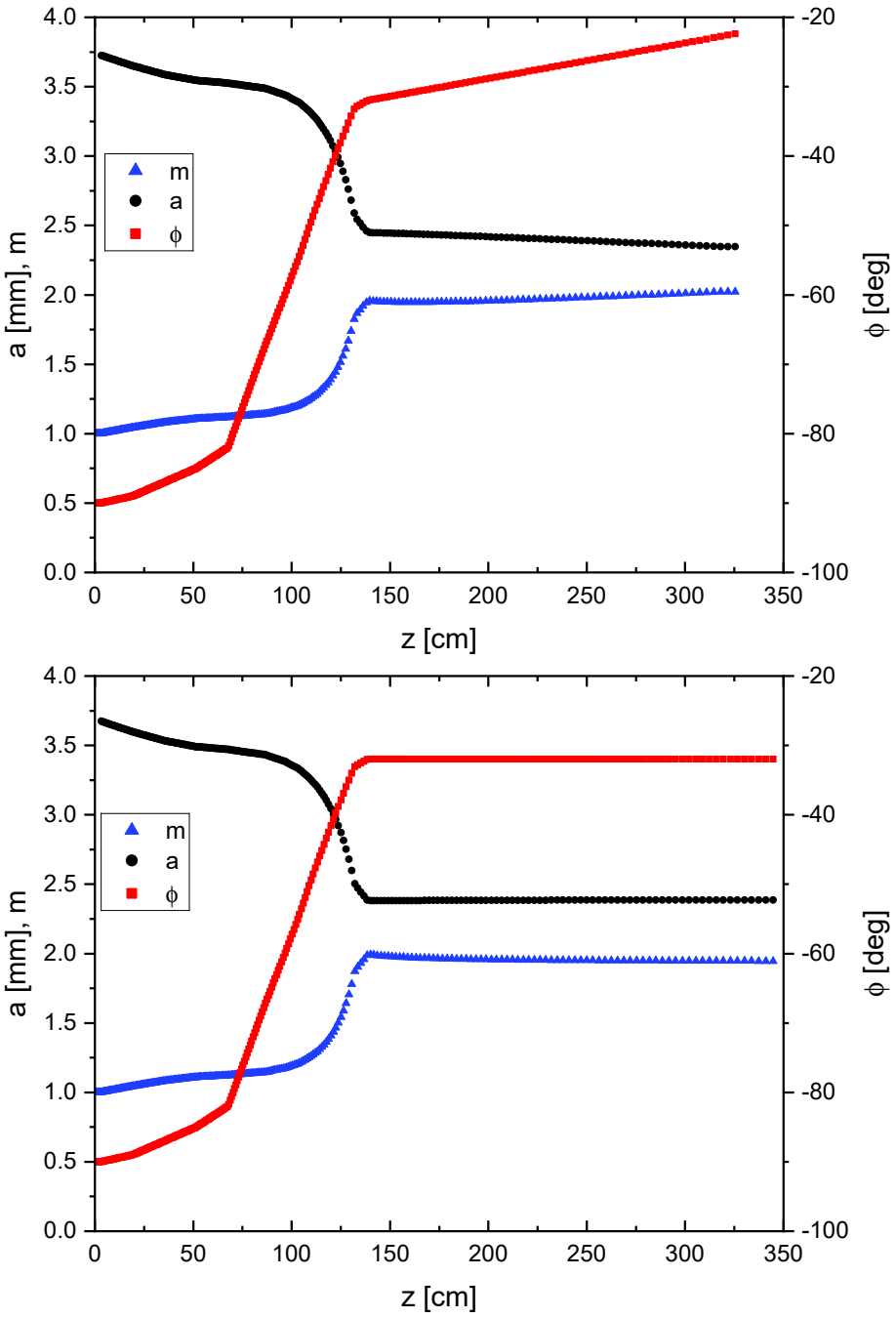

Figure 3.5: Beam dynamics design of the FAIR Proton-Linac RFQ as built (top) and the alternative design according to the LANL scheme (bottom). Shown are the curves of the modulation parameter m, (minimum) radial aperture a and of synchronous phase ϕ against the RFQ length.

3.2 Transversal Entrance Twiss Parameter Studies with RFQGen

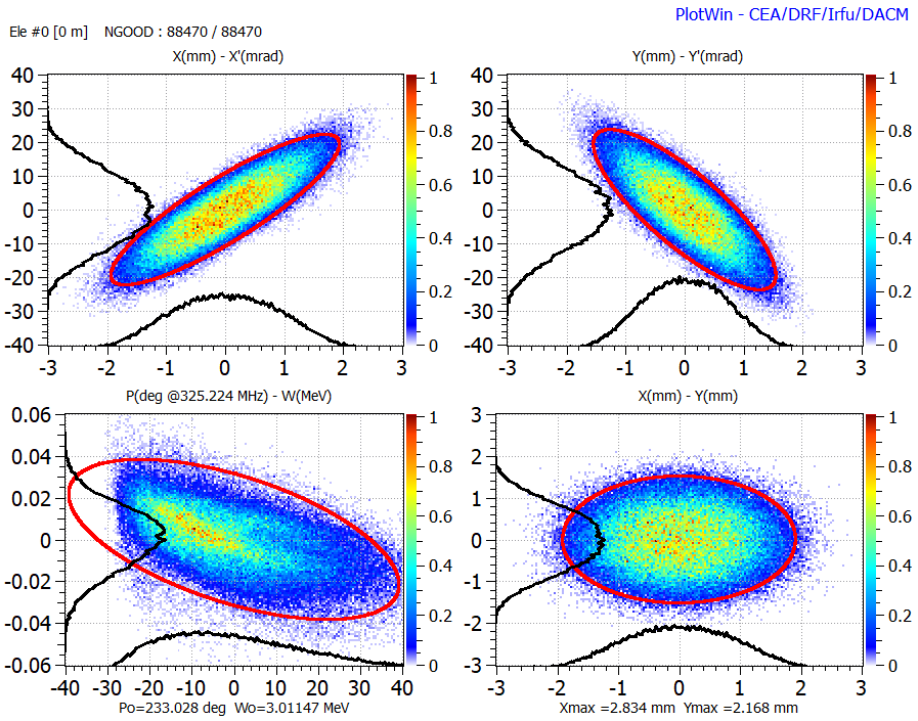

Figure 3.6: Phase space plots and distribution projections (black curves) at the RFQ exit (4.88 mm behind the electrode ends) for the optimal design set of transversal input Twiss parameters $\alpha = 1.5$ and $\beta = 0.06\,mm/\pi\,mrad$ (cf. Tab. 3.8). The entrance current was chosen to 100 mA represented by 100,000 macro-particles. The colors of the scatter plots refer to the normalized macro-particle density (cf. scales at the right frames of the plots). The red ellipses correspond to the normalized 95% emittances (cf. Tab.3.8).

In January 2018 GSI's Ion Source Group performed emittance measurements in the LEBT at CEA Saclay. The emittance measurement device was placed behind the first solenoid (see Fig. 3.10). Successive TraceWin simulations based on these measurements suggested that the entrance Twiss parameters α_{in} and β_{in} might deviate from their design values mentioned above. In order to investigate how far the RFQ beam dynamics design could cope with these deviations, initial Twiss parameter studies were performed with RFQGen. α_{in} was run from 0.1 to 2.5 with a step width of 0.1, whereas β_{in} was varied from $0.01\,mm/\pi\,mrad$ to $0.14\,mm/\pi\,mrad$ with a step width of $0.01\,mm/\pi\,mrad$ (see Fig. 3.7). This amounted to 375 combinations of α_{in} and β_{in}. As the RFQGen-code itself unfortunately does not include a sweep-function, a short workaround routine was coded with Python to automate the variation of the initial Twiss parameters.

β [mm/π mrad] α	0.01	0.02	0.03	0.04	0.05	0.06	0.07	0.08	0.09	0.10	0.11	0.12	0.13	0.14	0.15	
2.5	14.59%	30.16%	47.95%	64.40%	74.32%	79.91%	83.57%	85.33%	85.11%	83.90%	81.75%	79.68%	77.75%	75.61%	73.20%	**2.5**
2.4	15.48%	32.27%	50.95%	66.81%	76.34%	81.58%	84.40%	85.83%	85.68%	83.68%	81.83%	79.54%	77.46%	74.82%	72.54%	**2.4**
2.3	16.64%	34.34%	53.90%	69.02%	77.90%	82.65%	85.93%	86.46%	85.29%	83.66%	81.77%	78.95%	76.94%	74.58%	71.80%	**2.3**
2.2	17.75%	36.90%	57.02%	71.58%	79.30%	83.89%	86.69%	86.92%	85.44%	83.48%	81.36%	78.47%	76.09%	73.63%	70.61%	**2.2**
2.1	19.24%	38.81%	60.05%	73.68%	80.68%	85.34%	87.28%	87.00%	85.47%	83.35%	80.77%	78.34%	75.65%	72.56%	70.41%	**2.1**
2.0	20.50%	41.81%	62.95%	75.46%	82.13%	86.51%	88.07%	86.93%	85.19%	82.85%	79.97%	77.41%	74.90%	71.91%	69.38%	**2.0**
1.9	22.33%	44.90%	66.01%	77.38%	83.58%	87.18%	**88.00%**	87.10%	84.93%	82.11%	79.32%	76.86%	74.55%	71.67%	68.62%	**1.9**
1.8	23.47%	47.90%	68.43%	78.79%	84.69%	87.62%	88.23%	86.87%	84.19%	81.38%	***79.05%***	76.33%	73.37%	70.57%	67.79%	**1.8**
1.7	25.12%	50.72%	70.91%	80.81%	86.24%	88.52%	88.01%	86.31%	83.38%	80.57%	78.17%	75.60%	72.54%	69.93%	66.89%	**1.7**
1.6	26.79%	54.07%	73.17%	81.91%	86.71%	**88.70%**	87.79%	85.59%	83.14%	79.98%	77.29%	74.74%	71.84%	68.60%	65.61%	**1.6**
1.5	28.94%	57.33%	74.81%	83.14%	87.66%	**88.57%**	87.14%	85.14%	82.16%	79.49%	76.54%	73.76%	70.73%	68.05%	65.01%	**1.5**
1.4	30.89%	60.87%	76.51%	84.15%	88.16%	88.45%	87.26%	83.98%	81.27%	78.41%	75.71%	72.64%	70.22%	66.95%	63.82%	**1.4**
1.3	33.28%	63.41%	78.30%	**85.03%**	88.36%	88.34%	85.99%	83.29%	80.68%	77.61%	75.01%	72.18%	69.06%	65.83%	62.84%	**1.3**
1.2	35.62%	66.14%	79.62%	85.71%	88.14%	87.43%	85.34%	82.34%	79.28%	76.48%	***73.81%***	***70.68%***	67.94%	64.89%	62.31%	**1.2**
1.1	38.70%	68.25%	80.27%	85.96%	87.73%	86.78%	84.68%	81.28%	78.57%	75.77%	72.74%	69.84%	66.75%	63.92%	60.69%	**1.1**
1.0	41.51%	70.16%	80.96%	85.83%	87.08%	85.95%	83.37%	80.28%	77.74%	74.61%	71.66%	68.79%	65.60%	62.88%	60.02%	**1.0**
0.9	43.99%	71.78%	81.45%	85.69%	86.33%	84.50%	82.05%	79.13%	76.38%	73.60%	70.49%	67.85%	64.71%	61.41%	58.74%	**0.9**
0.8	46.35%	73.01%	82.14%	85.16%	84.84%	83.38%	80.92%	77.99%	74.97%	72.38%	69.53%	66.79%	63.16%	60.10%	57.42%	**0.8**
0.7	48.73%	73.80%	81.31%	84.52%	83.79%	82.04%	79.21%	77.00%	74.52%	71.38%	68.33%	65.18%	62.04%	59.19%	56.47%	**0.7**
0.6	50.62%	74.21%	81.48%	83.40%	82.49%	80.40%	78.06%	75.70%	72.80%	70.23%	66.89%	63.98%	60.98%	57.98%	55.28%	**0.6**
0.5	52.04%	74.27%	80.44%	81.96%	81.03%	78.92%	77.26%	74.36%	71.67%	68.67%	65.69%	62.18%	59.51%	56.78%	53.69%	**0.5**
0.4	53.26%	73.79%	79.42%	80.67%	79.53%	77.64%	75.70%	73.21%	70.30%	66.90%	63.93%	61.19%	58.08%	55.74%	52.97%	**0.4**
0.3	53.51%	72.78%	77.97%	78.92%	78.11%	76.37%	73.99%	71.62%	68.61%	65.63%	62.48%	59.27%	57.18%	54.01%	51.49%	**0.3**
0.2	53.47%	71.64%	76.78%	77.58%	76.41%	74.68%	72.33%	69.83%	67.03%	63.88%	61.09%	58.52%	55.02%	52.60%	50.46%	**0.2**
0.1	52.20%	70.30%	75.07%	75.64%	74.76%	72.92%	71.07%	68.39%	65.22%	62.59%	59.83%	56.68%	53.91%	51.39%	49.49%	**0.1**
	0.01	**0.02**	**0.03**	**0.04**	**0.05**	**0.06**	**0.07**	**0.08**	**0.09**	**0.10**	**0.11**	**0.12**	**0.13**	**0.14**	**0.15**	

Figure 3.7: This Matrix provides an overview over the combinations of the initial Twiss parameters α_{in} and β_{in} deviating from the original design Twiss parameter set $\alpha = 0.7$ and $\beta = 0.04\,mm/\pi\,mrad$. For each parameter pair the transmission is given in percent. The transmission is also color-coded by a red-blue-spectrum with dark-red indicating transmissions $\geq$85% and dark-blue indicating transmissions $\leq$30%. The size of the total area within this plot covered in either dark-red, light-red or rose indicates that transmission remains sufficiently high, i.e. $T \geq 80\%$, even for Twiss parameter combinations deviating rather much from the optimal set $\alpha = 1.5$ and $\beta = 0.06\,mm/\pi\,mrad$, which results in $T = 88.70\,\%$.

Parameter	Original Design Case*	Opt. Matched Case
α_{in}	0.7	1.5
$\beta_{in}\,[mm/\pi\,mrad]$	0.04	0.06
Transmission [%]	84.322	88.470
$\varepsilon_{x,n,out,rms/95\%}\,[\pi\,mm\,mrad]$	0.337/1.7893	0.323/1.686
$\varepsilon_{y,n,out,rms/95\%}\,[\pi\,mm\,mrad]$	0.329/1.759	0.321/1.694
$\varepsilon_{z,n,out,rms/95\%}\,[\pi\,MeV\,deg]$	0.214/1.349	0.205/1.2403
$\varepsilon_{x-y,n,out,rms/95\%}\,[\pi\,mm^2]$	0.583/3.029	0.570/2.905
Average Exit Energy $W_{ave}\,[MeV]$	3.0113	3.0115
Average Exit Energy $W_{syn} - W_{ave}\,[keV]$	3.7	3.5
Long. Losses / Radial Losses [%]	58	68

Table 3.8: Comparison of the RFQGen simulations run with the original design transversal entrance Twiss parameters (i.e. the preliminary Twiss parameters agreed on by CEA Saclay and IAP in summer 2017) and the matched ones (cf. Fig. 3.6). For both cases the entrance current was 100 mA, the RFQ entrance energy spread was $\Delta W = 0.0\,\mathrm{keV}$ and 100,000 input macro-particles were chosen.

It turned out that setting $\alpha = 1.5$ and $\beta = 0.06\,mm/\pi\,mrad$ results in the optimum RFQ exit distribution, not only in terms of transmission (88.7%), but also regarding the emittances at the RFQ exit (cf. Fig. 3.7 and Tab. 3.8). This finding was confirmed by TOUTATIS simulations by H. Hähnel [27] (cf. 3.12). The size of the total area within this plot covered in either dark-red, light-red or rose indicates that transmission remains sufficiently high, i.e. $T \geq 80\%$, even for Twiss parameter combinations deviating rather much from this optimal set.

3.3 TraceWin and RFQGen Simulations based on LEBT measurements

New emittance measurements were performed by the GSI Ion Source Group at CEA Saclay in April 2019. They were carried out about 240 mm behind the second solenoid of the LEBT and constituted the basis for LEBT simulations with CEA's TraceWin-Code performed by M. Schuett. With this code, the measured distributions were tracked through a drift of 700 mm – whereby the degree of **s**pace-**c**harge **c**ompensation (SSC)[9] was set to 90% – in order to determine the respective position of the beam waist, i.e. the focus. The RFQ entrance should be placed at this position,

[9] Note, that the space-charge compensation degree of the proton beam as it enters the RFQ is 0%. The causes for this space-charge compensation and its sudden drop are briefly outlined in Appx. B.

which turned out to be placed ca. 260 mm behind the measuring device (see Fig. 3.8 and Tab. 3.9).

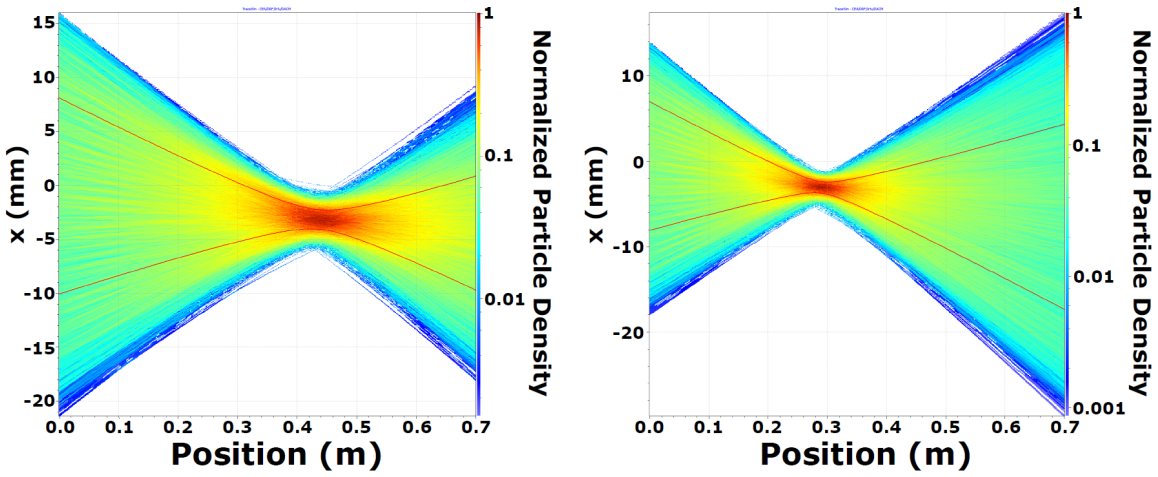

Figure 3.9: TraceWin simulated beam density plots in the LEBT-line of the FAIR p-Linac RFQ: in order to determine the likely resulting RFQ entrance distributions both measured distributions were converted to TraceWin distributions consisting of 10,201 macro-particles each. These were than tracked in order to determine their beam waist/focal position, which is where the RFQ entrance should be placed. (TraceWin simulations performed and beam density plots provided by M. Schuett.) The foci of the distributions are located ca. 450 mm (left) and ca. 260 mm (right) behind the measurement position (see Tab. 3.9).

Two promising RFQ entrance distributions were measured behind the second solenoid (each of them determined by the solenoid currents). Note that their transversal normalized rms emittances were significantly lower than $0.3\,\pi$ mm mrad: $\varepsilon_{n,rms,x/y} = 0.22\,\pi\,mm\,mrad$ (see Tab. 3.9). These distributions were converted into TraceWin distributions consisting of 10,201 macro-particles each, which were then traced trough the remaining LEBT-line to the RFQ entrance. However, the optimal Twiss parameters for the RFQ entrance could not been reached with either of them. The set of RFQ entrance Twiss parameters closest to the optimum were $\alpha_{in} = 1.0$ and $\beta_{in} = 0.06\,mm/\pi\,mrad$ (see Tab. 3.9 and Fig. 3.8). So, while the value for β_{in} was matched, that for α_{in} was off by a value of 0.5 (i.e. ca. 33 %). In order to reach the highest possible RFQ exit current and furthermore to test the RFQ beam dynamics design's tolerance of currents higher than the nominal one of 100 mA the source current was set to 110 mA, a value that could be reached by the source according to GSI's Ion Source Group. (Furthermore, the MEBT as well as the following cavities will should be able to transport and/or accelerate

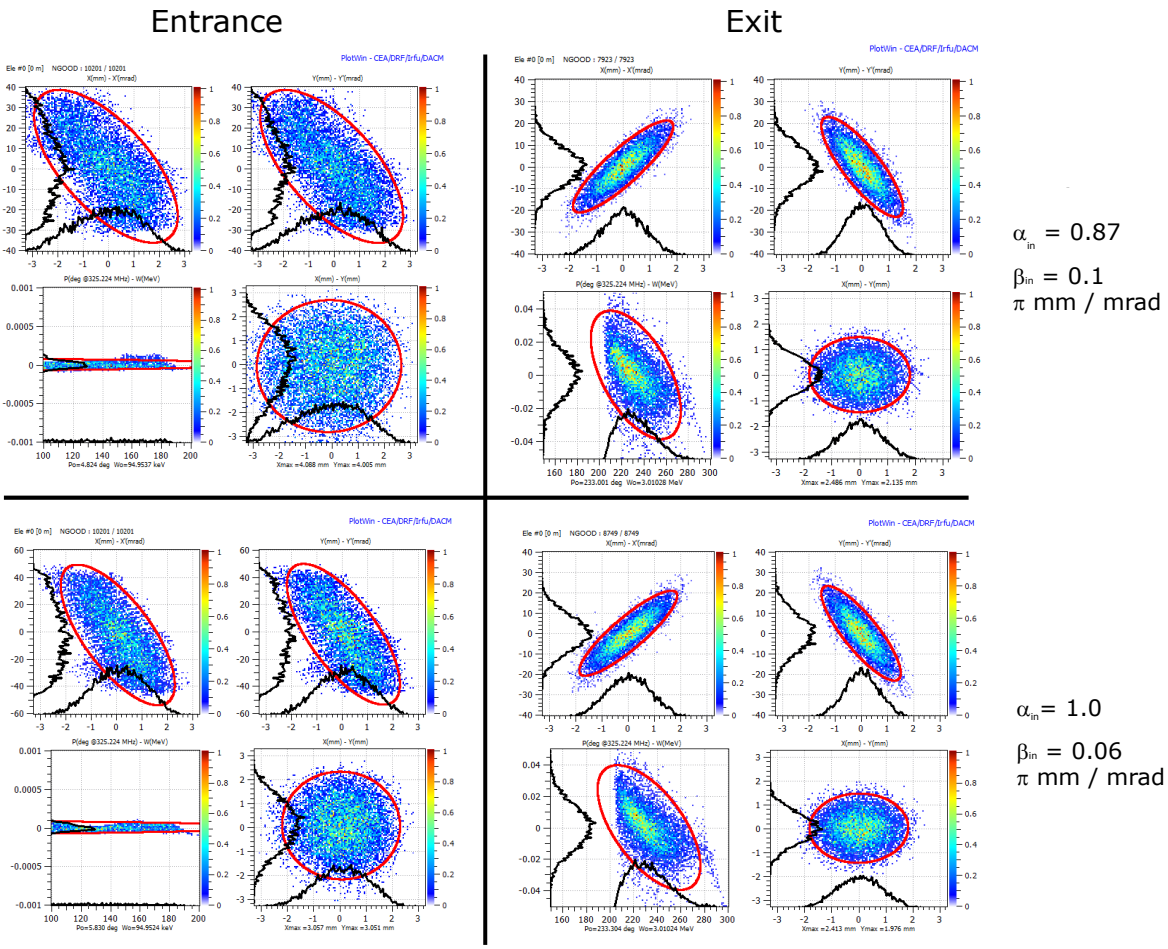

Figure 3.8: Phase space plots and distribution projections (black curves) at the RFQ entrance (left-hand column) and the RFQ exit (4.88 mm behind the electrode ends) (right-hand column). The top row shows the distributions for $\alpha = 0.87$ and $\beta = 0.1\,mm/\pi\,mrad$ (first measured distribution), the bottom row these for $\alpha = 1.0$ and $\beta = 0.06\,mm/\pi\,mrad$ (second measured distribution). The entrance current was chosen to 110 mA represented by 100,000 macro-particles in both cases. This higher current value was agreed upon in accordance with GSI's Ion Source Group as they stated the source might be able to provide such a high current beam. As the MEBT as well as the following cavities will also be able to handle currents ≥ 100 mA there was hope for a higher source current leading to an RFQ exit current closer to 100 mA. The colors of the scatter plots refer to the normalized macro-particle density (cf. scales at the right frames of the plots). The red ellipses correspond to the 95% emittances. For $\alpha_{in} = 0.87$ and $\beta_{in} = 0.1\,mm/\pi\,mrad$ (left values) and $\alpha = 1.0$ and $\beta = 0.06\,mm/\pi\,mrad$ (right values) these are $\varepsilon_{x,n,95\%} = 1.55/1.49\,\pi\,mm\,mrad$, $\varepsilon_{y,n,95\%} = 1.57/1.53\,\pi\,mm\,mrad$, $\varepsilon_{z,n,95\%} = 1.29/1.37\,\pi\,MeV\,deg$, and $\varepsilon_{x-y,n,95\%} = 2.67/2.65\,\pi\,mm^2$ at the RFQ exit. The values of the entrance distributions are listed in Tab. 3.9. Note, that the number of RFQ entrance macro-particles was 10,201. Hence, the transmissions at the RFQ exit are $7,890/10,201 = 77.669\,\%$ and $8,727/10,201 = 85.766\,\%$, respectively.

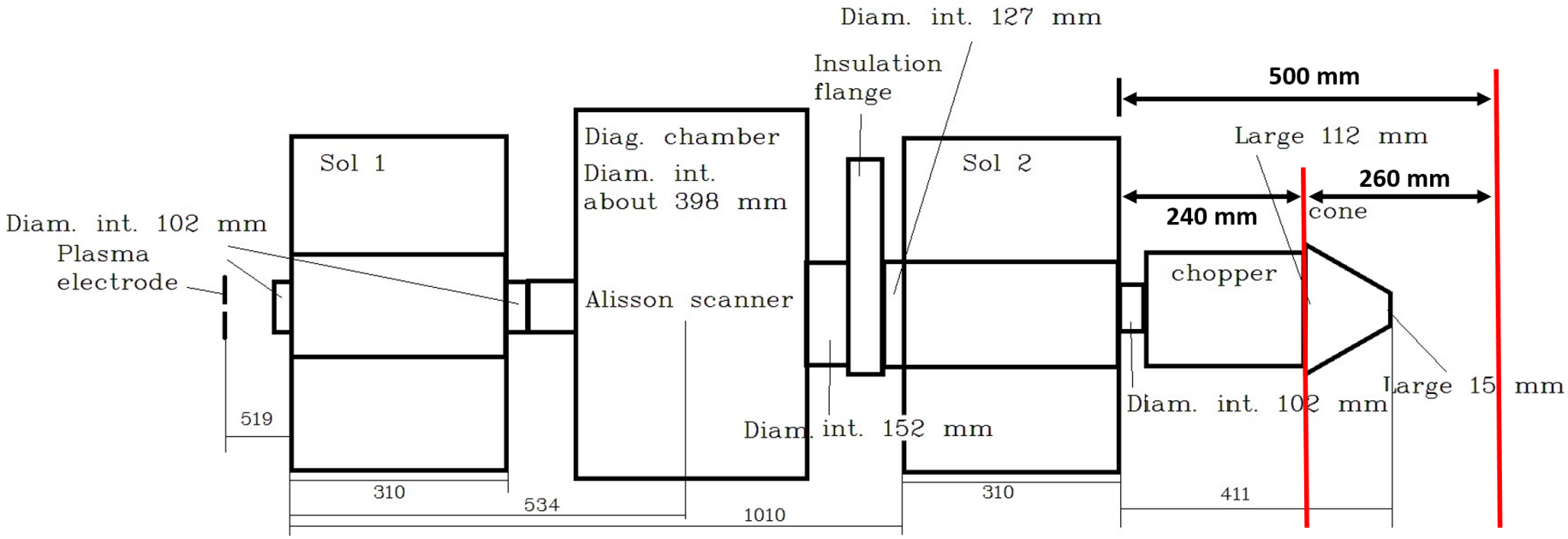

Figure 3.10: Sketch of the LEBT-line for the FAIR p-Linac RFQ (courtesy of R. Berezov). The left red line marks the position of the emittance measuring device. For the measurements of April 2019 it was placed ca. 240 mm behind the second solenoid, i.e. at the end of the chopper (cf. Tab. 3.9). The right red line marks the preferred position of the RFQ entrance, ca. 260 mm behind the measuring device (i.e. ca. 500 mm behind the second solenoid).

currents ≥100 mA.) As the current losses in the LEBT-line are negligible, this setting results in an RFQ entrance current of 110 mA.

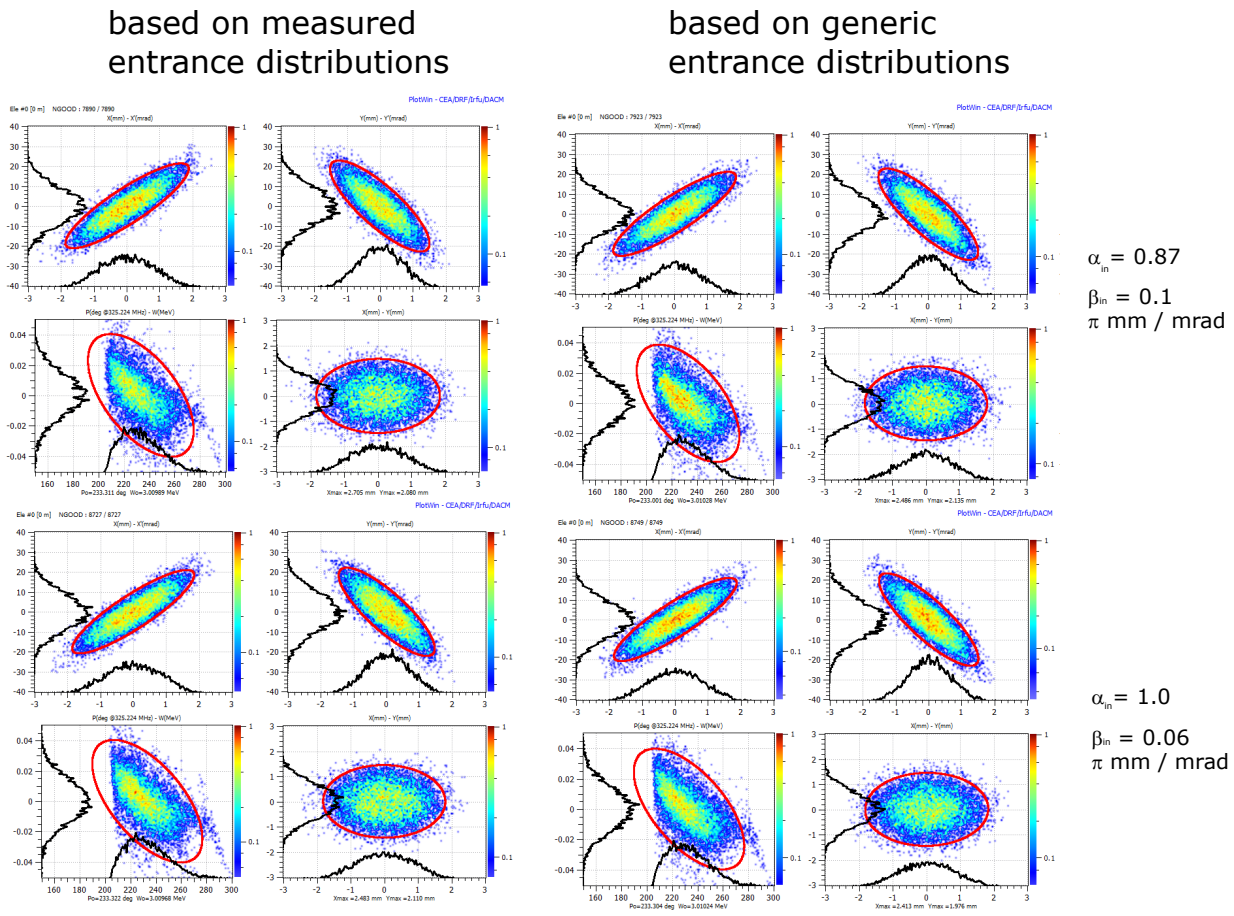

Figure 3.11: Comparison of the RFQ exit distributions resulting from simulations using the measured distributions (left column; 10,201 input macro-particles) and generic 4D-water bag entrance distributions (right column; 10,000 input macro-particles) whose emittances and Twiss parameters were set to those of the measured distributions. The upper row is associated to the first measurement ($\alpha_{in} = 0.87$ and $\beta_{in} = 0.1\,mm/\pi\,mrad$), the bottom row to the second measurement ($\alpha_{in} = 1$ and $\beta_{in} = 0.06\,mm/\pi\,mrad$). The colors of the scatter plots refer to the normalized macro-particle density (cf. scales at the right frames of the plots). The red ellipses correspond to the normalized 95%-emittances (cf. Tab. 3.9).

Fortunately, one of the thereby derived particle distributions at the RFQ entrance exhibited Twiss parameters sufficiently close to the matched or optimal case leading to a satisfying RFQ exit distribution (see Fig. 3.8 and Tab. 3.9 (third column; second measured distribution)). The respective RFQ exit distribution generated by an RFQGen simulation was compared to that of

the corresponding case of above Twiss parameter studies (see Tab. 3.9). The RFQ entrance and exit distributions associated to the optimum measured and tracked input case are depicted in Fig. 3.8.

Particle Distribution	Measured		Gen. 4D Waterbag	
	1-th	2-th	1-th	2-th
Distance measurement to focus [mm]	450	260	n/a	n/a
α_{in}	0.87	1	0.9	1
β_{in} $[mm/\pi\, mrad]$	0.1	0.06	0.1	0.06
$\varepsilon_{x/y,in,n,rms}[\pi\, mm\, mrad]$	0.22	0.22	0.20	0.20
$\varepsilon_{x/y,in,n,95\%}[\pi\, mm\, mrad]$	1.14	1.17	0.94	0.94
$\varepsilon_{x/y,out,n,rms}[\pi\, mm\, mrad]$	0.26	0.26	0.27	0.26
$\varepsilon_{x/y,out,n,95\%}[\pi\, mm\, mrad]$	1.55/1.57	1.49/1.53	1.55/1.57	1.48/1.45
$\varepsilon_{z,out,n,rms/95\%}[\pi\, MeV\, Deg]$	0.20/1.29	0.21/1.37	0.21/1.39	0.21/1.39
$\varepsilon_{x-y,out,n,rms/95\%}[\pi\, mm^2]$	0.47/2.67	0.48/2.65	0.49/2.71	0.49/2.62
Transmission [%]	77.7	85.8	77.3	85.6

Table 3.9: The results of the TraceWin- and RFQGen-simulations based on the first and second measured distributions (distance between position of measurement and focus ca. 450 mm and ca. 260 mm, respectively) are compared to the RFQGen results performed with Generic 4D water bag RFQ entrance distributions (100,000 macro-particles), whereby the latter were set up with the same RFQ entrance emittances and Twiss parameters as the RFQ entrance distributions (10,201 macro-particles) that were derived by tracing the measured distributions to the RFQ entrance with TraceWin. The LEBT/RFQ entrance current was set to 110 mA in accordance with GSI's Ion Source Group for all four simulations. All emittances are normalized rms-emittances.

As the distance between the chopper and the RFQ entrance is required to be $\leq$ 260 mm according to above findings (see Tab. 3.9), design and construction of a new well-fitting cone at the RFQ entrance are very challenging, but still feasible. In fact, the design work is already nearing completion.

3.4 Comparison of the RFQGen and TOUTATIS simulation results

In order to check the beam dynamics design it was transferred into a TOUTATIS model by H. Hähnel in early 2019 [27]. Figure 3.12 and Table 3.10 exhibit the comparison of the results of the RFQGen simulation and the succeeding reproducibility check in TOUTATIS performed by H. Hähnel. Both simulations were run with the matched entrance beam. The resulting differences

Parameter	RFQGen Simulation	TOUTATIS Reproducibility Check
Transmission	88.470	91.454
$\varepsilon_{x,out,n,rms/95\%}[\pi\, mm\, mrad]$	0.323/1.686	0.345/1.833
$\varepsilon_{y,out,n,rms/95\%}[\pi\, mm\, mrad]$	0.321/1.694	0.338/1.794
$\varepsilon_{z,out,n,rms/95\%}[\pi\, MeV\, deg]$	0.205/1.240	0.182/1.173
$\varepsilon_{x-y,out,n,rms/95\%}[\pi\, mm^2]$	0.570/2.905	0.637/3.285
$W_{syn,fin.}\,[MeV]$	3.015	3.015
$W_{ave,fin.}\,[MeV]$	3.011	3.010
$W_{syn,fin.} - W_{ave,fin.}\,[keV]$	3.53	5.51

Table 3.10: Comparison of the exit beam parameters for the RFQGen- and TOUTATIS-simulations performed on the matched beam (i.e. with transversal RFQ entrance Twiss parameters $\alpha_{in} = 1.5$ and $\beta_{in} = 0.06\, mm/\pi\, mrad$).

are negligible and rooted in the different routines used by both codes. The reproducibility of the RFQGen results shows the reliability and solidity of the developed beam dynamics design of the FAIR Proton-Linac RFQ. Note that the transmission of 91.45 % for the TOUTATIS simulation given in Tab. 3.10 refers to the actual (properly) accelerated particles. Other than RFQGen TOUTATIS reveals how many of the particle traversing the whole RFQ fall into this category. The total transmission given by TOUTATIS is 96.81 %. Thus the difference between the total beam current at the RFQ exit and that of the accelerated protons amounts to 5.36 mA. This value is of the same order of magnitude as that derived with a workaround in RFQGen of 2.1 mA (see Sec. 3.5).

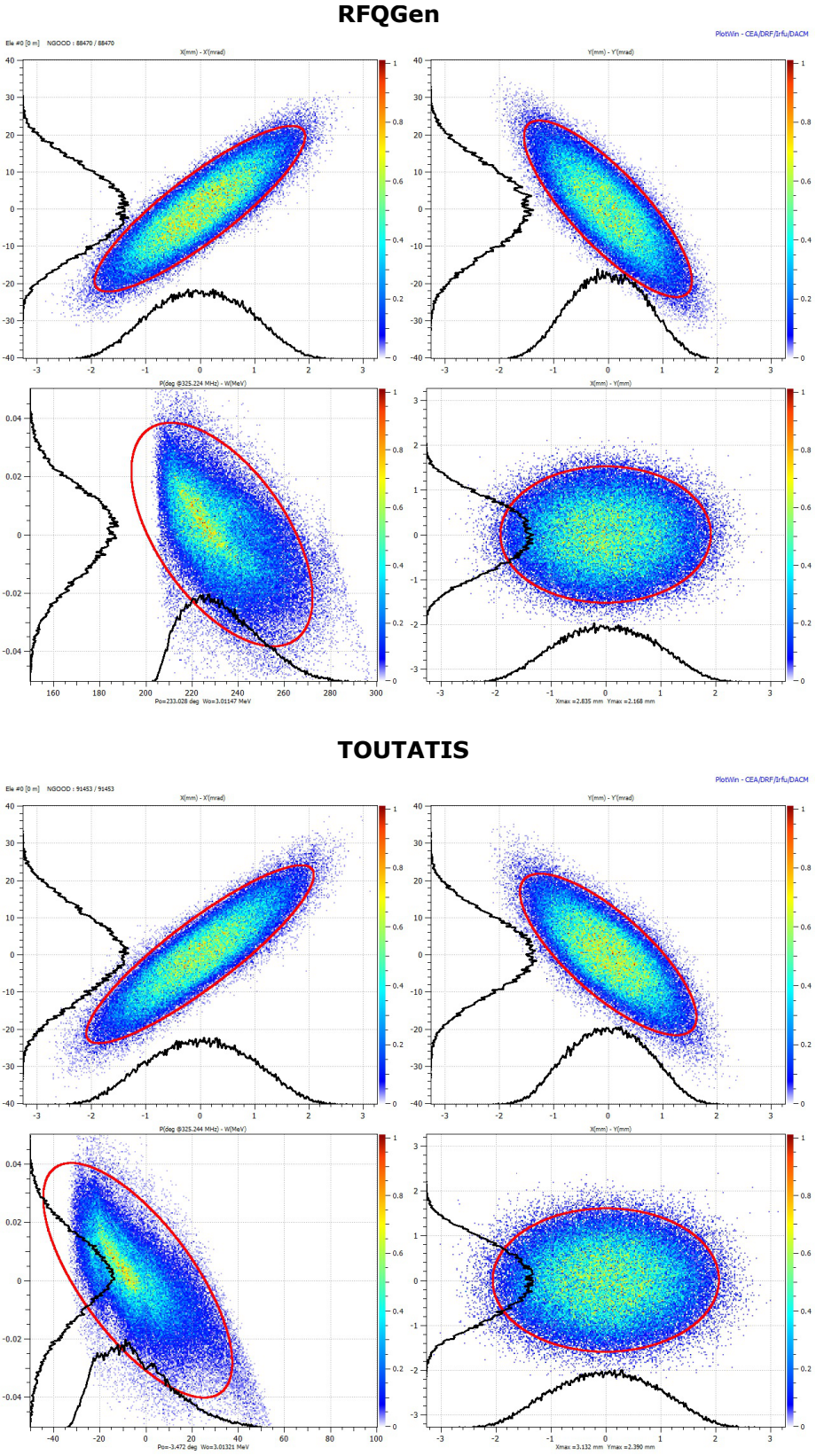

Figure 3.12: Comparison of the exit phase space plots for the RFQGen (top) and TOUTATIS (bottom) simulations performed on the 100 mA matched beam (i.e. with trans. emittances $\varepsilon_{x/y,in,rms} = 0.3\,\pi\,mm\,mrad$ and trans. entrance Twiss parameters $\alpha_{in} = 1.5$ and $\beta_{in} = 0.06\,mm/\pi\,mrad$). The colors of the scatter plots refer to the normalized macro-particle density (cf. scales at the right frames of the plots). The red ellipses correspond to the normalized 95%-emittances (cf. Tab. 3.10).

3.5 Particle loss profile along the RFQ

When investigating an RFQ's beam dynamics design, the development of the emittances along the beam axis is of high interest. Their evolution is also interrelated with that of the particle loss distribution. This becomes particularly clear at the end of the Gentle Buncher section, where a growing percentage of particles first get increasingly off-phase and thereby blow up the longitudinal (normalized rms-) emittance. Subsequently, these outliers rapidly get lost longitudinally (cf. Sub-Sec. E.1.6) along a relatively short distance, which causes a rapid decline in this emittance.

The emittance and transmission curves for the matched beam along the FAIR Proton-Linac RFQ are shown in Fig. 3.13. It can be seen how the transversal emittances are raised from 0.3 to $0.5\,\pi$ mm mrad and compressed again to almost their entrance value into the Radial Matching section. They then rise until the end of the Gentle Buncher section (whereby the curves exhibit several local extrema) followed by a fall back to almost their entrance value (again exhibiting local extrema). Note the final small step-like rise in the exit fringe-field region.

It is especially crucial to know at which z-positions or in which cells, respectively, how many particles are expected to get lost as this information of course determines the respective particle energies. Hence, predictions of cavity and electrode radioactivation can only be stated once the distribution of lost particles along the RFQ can be approximated with sufficient accuracy.

The upper graph of Fig. 3.14 shows the macro-particle losses per cell and the synchronous energy W_s against the synchronous energy as simulated by the RFQGen-Code for the matched case. The losses peak at $W_s = 0.5124\,\text{MeV}$ ($W_{ave} = 0.4931\,\text{MeV}$), i.e. cell 172. These particles make up slightly more than 5 % of the overall particle losses. The longitudinal losses around this cell lead to a decreased longitudinal emittance, that grows substantially during the earlier stages of the bunching process and goes into saturation with a value close to that at the end of the Shaper section (cf. Fig. 3.13). The losses in cells corresponding to a $W_s > 2\,\text{MeV}$ do not even make up 2 % of all losses. This attribute is important as the collisions of protons exhibiting energies above 2 MeV with the electrodes or the cavity could lead to radioactivation of the material. The ratio of overall longitudinal to overall transversal losses along the RFQ is about 68 %.

The number of all longitudinally lost particles along the RFQ would hereby amount to a current of 4.7 mA.

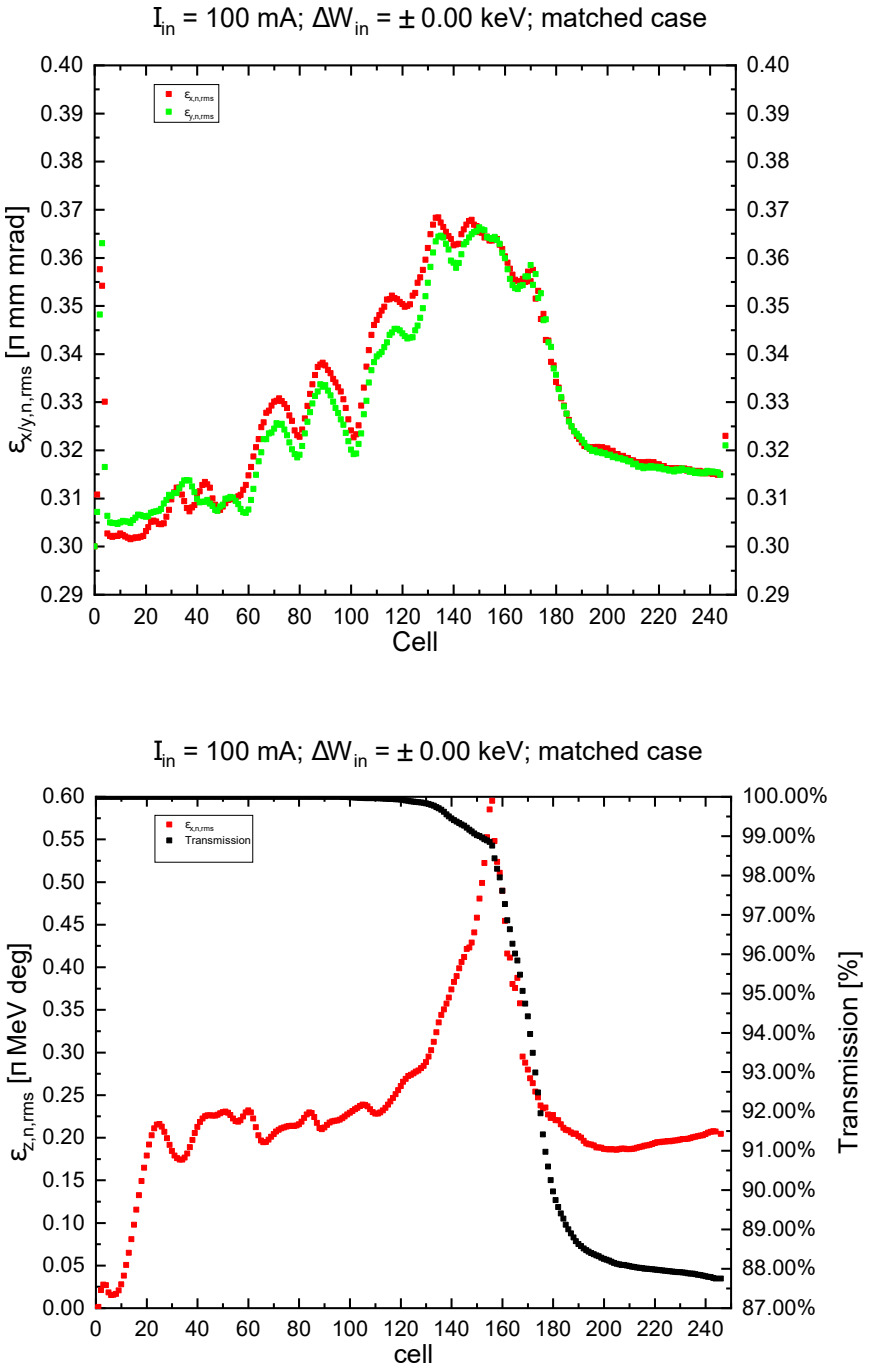

Figure 3.13: Normalized x- (red) and y- (green) rms-emittances (top) as well as longitudinal normalized rms-emittance (red) and transmission (black) (bottom) against the cell number in case of the matched beam ($I_{in} = 100\,\mathrm{mA}$; $\Delta W_{in} = \pm 0.00\,\mathrm{keV}$).

For the reference case as well as almost all other simulations presented in this thesis (regarding

the FAIR p-Linac RFQ), this amounts to $\Delta W_{thr} = 2W_{h-w} = 160\,\text{keV}$. The only exception is a simulation almost identical to the matched reference case except for this parameter. Here, it was set to $\Delta W_{thr} = 2.99\,\text{MeV}$[10], i.e. almost the RFQ exit synchronous energy (see Tab. 3.11). This disables the code to classify any particle as a longitudinal loss particle, i.e. $N_{L,total} = 0$. Naively one might assume that setting the energy threshold that unrealistically high might result in the transmission raising by about 4.7% as ca. 4,700 macro-particles were lost longitudinally along the RFQ in the reference case. However, transmission was only raised by 2.1 % as not all off-phase particles reach the RFQ exit: particles that get too much out of phase with the electric field (but are not disregarded by the code due to this adjustment) are thus exposed to improper radial fields, which cause them to hit the electrodes. Hence, for this simulation the number of radially lost particles increases and to some degree "compensates" the lowered longitudinal losses and the effective RFQ exit beam current according to RFQGen might actually amount to $88.5\,mA + 2.1\,mA = 90.6\,mA$ instead of only 88.5 mA, i.e. just the current of the (properly) accelerated protons. The successive LORASR- and TraceWin-simulations concerning the MEBT-section and the CH-DTL as well as the-end-to-end simulations in TraceWin [27][11], which all were performed by H. Hähnel, took the discrepancy of the accelerated and the effective current (88.5 mA vs. 90.6 mA according to RFQGen and 91.5 mA vs. 96.8 mA according to TOUTATIS) into account. Table 3.11 shows the total, longitudinal and transversal losses at the RFQ exit for both cases.

Parameter	**Reference Case**	$\Delta W_{thr} = 2.99\,MeV$ **case**
Transmission	88.470%	90.616%
Long. Losses	4,665	0
Radial Losses	6,865	9,384

Table 3.11: Comparison of the transmissions at the FAIR p-Linac RFQ exit and the total longitudinal and radial losses along the RFQ for the reference case (matched case) and the $\Delta W_{thr} = 2.99\,MeV$ case. As the only deviating setting for both simulations was the cut-off energy for longitudinal losses, the RFQ current and number of macro-particles at the RFQ entrance was $I_{in} = 100\,\text{mA}$ and 100, 000 in both cases, respectively. In total, 11,530 (left) and 9,384 (right), respectively, of initially 100, 000 macro-particles are lost along the RFQ.

[10] This is done in RFQGen's **e**nergy **limit**/*elimit*-line. The numerical value entered here refers to ΔW_{thr} in MeV: $\Delta W_{thr} = elimit\,MeV$ (cf. Sub-Sec. E.1.6).

[11] These simulations included the RFQ, the MEBT and the CH-linac section.

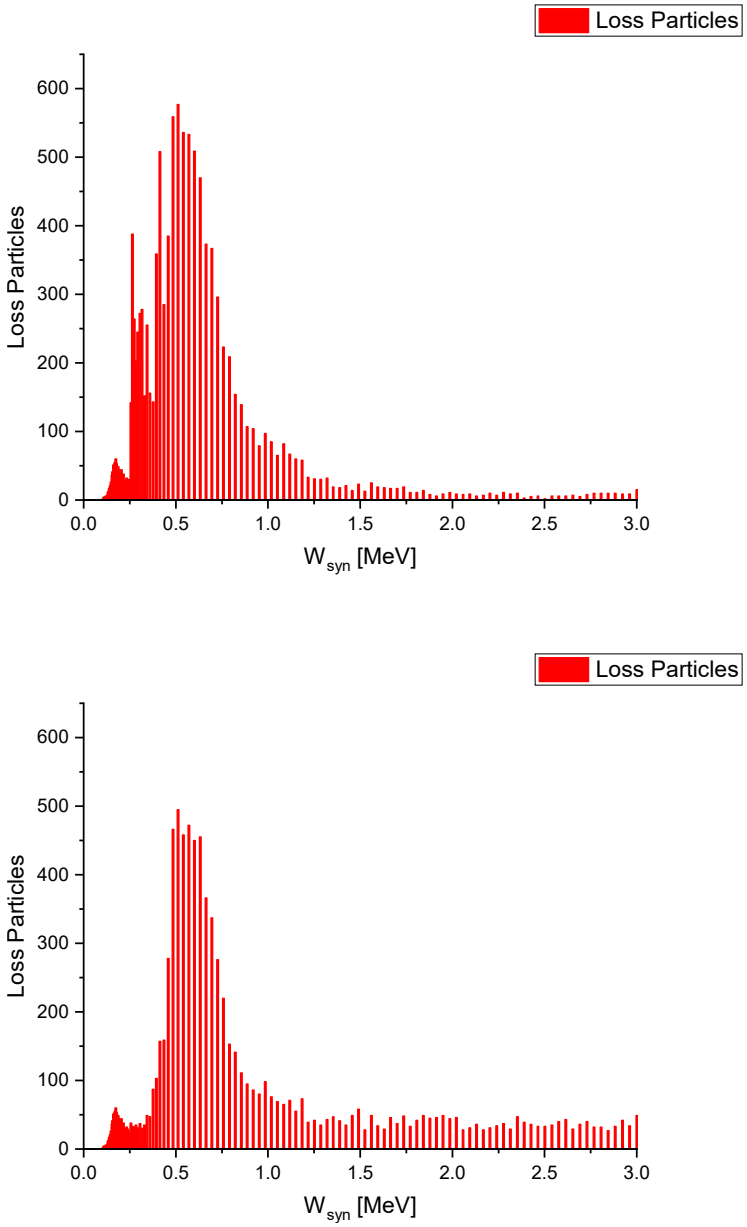

Figure 3.14: Particle losses per cell against the synchronous energy W_s in case of the matched reference case (top) and the $\Delta W_{thr} = 2.99\,MeV$ case (bottom). As the only deviating setting for both simulations was that of the cut-off energy for longitudinal losses ΔW_{thr}, the RFQ entrance current was $I_{in} = 100\,\mathrm{mA}$ in both cases. In total, 11,530 (top) and 9,384 (bottom), respectively, of initially $100,000$ macro-particles are lost along the RFQ.

3.6 Investigation of the Effects of Image-Charges and Neighboring Bunches

RFQGen permits to switch off space-charge effects in the *scheff*-line (see Sub-Sec. E.1.3 in App. E). Here, one can also adjust if or and how many of the neighbor bunches affect the considered beam bunch via space-charge interactions. Furthermore, the RFQGen input-file (IN4-file) contains the image-line, where image-charge effects of the electrodes can be turned off (see Sub-Sec. E.1.4 in App. E).

For the original simulation performed on the matched beam both image-charge and space-charge effects were switched on, whereby the number of neighboring bunches each in front and behind the bunch of interest affecting it due to space-charge interactions was set to 5. This setting for the neighboring bunches applies to almost all RFQGen simulations presented in this thesis; the only two exceptions are given within this section (cases 1 and 3; see below).

Three further simulations were run on the matched beam (cf. Tabs. 3.8 and 3.10) with the following settings:

- case 1: neighbor bunch interactions are switched off by setting the number of neighboring bunches in the *scheff*-line to 0, i.e. only intra-bunch space-charge interactions are considered; image-charge effects are switched on (this was also the case for the original simulation performed on the matched beam)
- case 2: the number of neighboring bunches each in front and behind the bunch of interest effecting it via space-charge interactions is set 5 (as in case of the original simulation run on the matched beam); image-charge effects are switched off
- case 3: neighbor bunch interactions as well as image-charge effects are switched off.

Table 3.12 shows the comparison of these simulation results with those of the original simulation performed on the matched beam (referred to as case 0). It can be seen that whereas the image-charge effects hardly influence the beam dynamics results at all, turning off the inter-bunch space-charge interactions leads to a significant fall of the transmission by 7.5 % and a rise in the exit transversal and longitudinal emittances by 7.8 % and 11.2 %, respectively. This is also reflected in the associated phase space plots shown in Fig. 3.19.

The weak effect of the image-charges may seem unexpected at first in light of the high beam current. However, it can be understood if one considers that the beam is kept rather compact

Case number	Settings	Trans-mission[%]	N_L	N_R	$\varepsilon_{x,out,n,rms/95\%}$ $[\pi\, mm\, mrad]$	$\varepsilon_{y,out,n,rms/95\%}$ $[\pi\, mm\, mrad]$	$\varepsilon_{z,out,n,rms/95\%}$ $[\pi\, MeV\, deg]$
0 (original case)	$NNB = 5$, ICE on	88.470	4665	6865	0.3230 1.6862	0.3210 1.6936	0.2046 1.2403
1	$NNB = 0$, ICE on	81.050	8203	10747	0.3482 1.6757	0.3460 1.6689	0.2466 1.4612
2	$NNB = 5$, ICE off	88.229	6999	4772	0.3285 1.8873	0.3244 1.8828	0.2071 1.2915
3	$NNB = 0$, ICE off	81.018	10130	8852	0.3427 1.8549	0.3363 1.8232	0.2276 1.3357

Table 3.12: Comparison of the RFQ exit beam parameters for cases 0-3. NNB: number of neighboring bunches each in front an behind the bunch of interest, ICE: image-charge effects. The number of input macro-particles was 100,000 for all four cases. (The top values in the emittance columns refer to the rms-emittances, and the bottom values refer to the 95%-emittances.)

in the x- and y-plane by the high transversal fields of the electrodes. Hence, the induced image-charges are rather small and too distant from the beam to influence it in any significant way despite the rather high beam current of 100 mA.

The loss particles spectra for each of the four cases 0 to 3 are shown in Fig. 3.20. It can be seen that for the two cases with switched off inter-bunch interactions, i.e. cases 1 and 3, the particle losses exhibit a sharp peak at the end of the Gentle Bunching section, i.e. cell 156, where $W_{syn} = 260$ keV. Furthermore, for these two cases the peak around cell 139, i.e. at $W_{syn} = 168.2$ keV, is more pronounced than for the original case (0) and for case (2), i.e. if $\#Bunch = 5$ in the $scheff$-line.

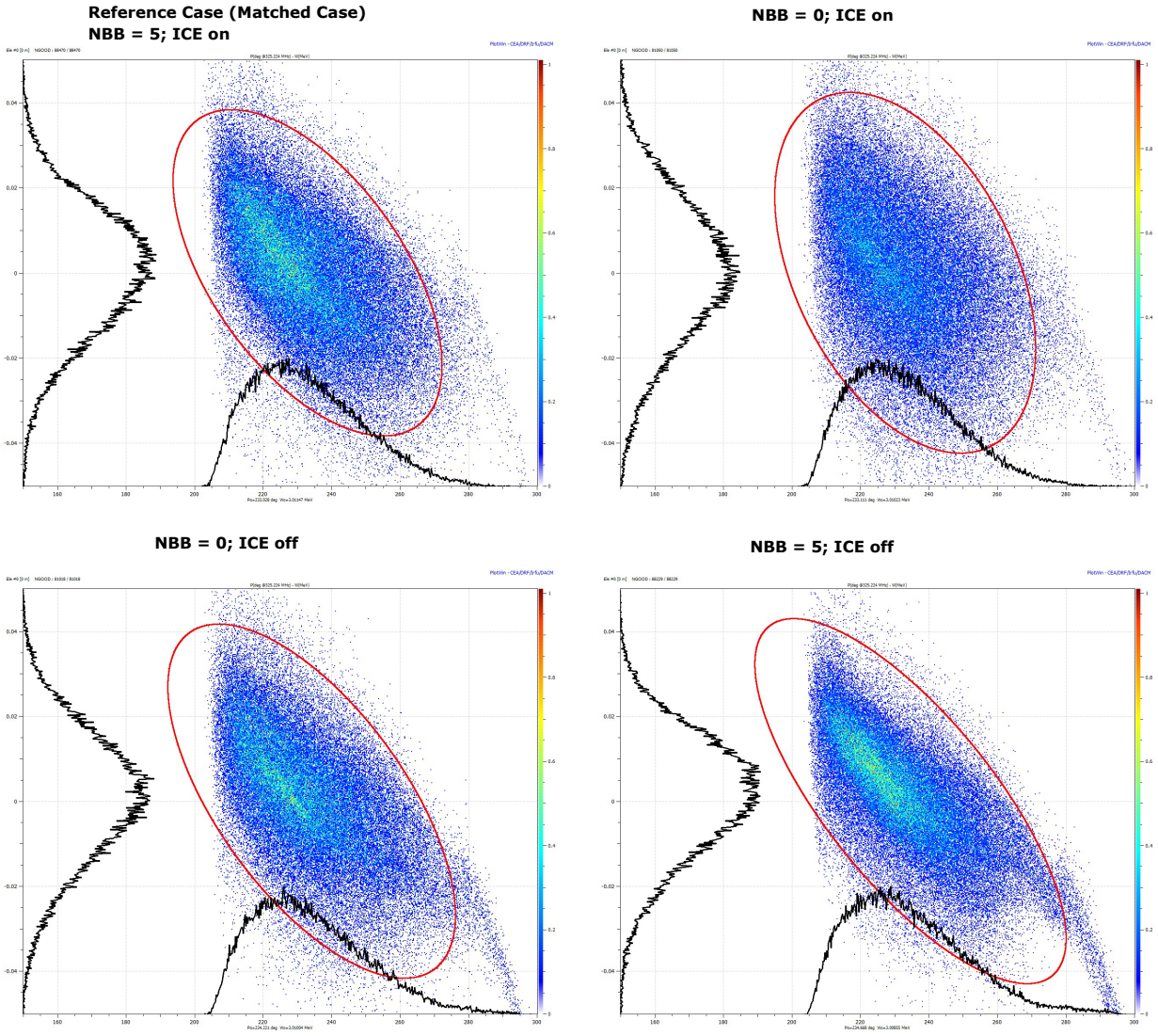

Figure 3.15: Longitudinal phase space plots and distribution curves (black curves) at the RFQ exit for different settings regarding image charge interactions and the number of "active" neighbor bunches, whereby the plots for case 0 are placed in the above left corner followed clockwise by those of cases 1-3 (cf. Tab. 3.12; NNB : next neighbor bunches, ICE: image-charge effects). All simulations were run with 100,000 input macro-particles, an entrance current of 100 mA and the matched Twiss parameters at the RFQ entrance. The red ellipse correspond to the normalized 95% emittances (see Tab. 3.12). The colors of the scatter plots refer to the normalized macro-particle density (cf. scales at the right frames of the plots).

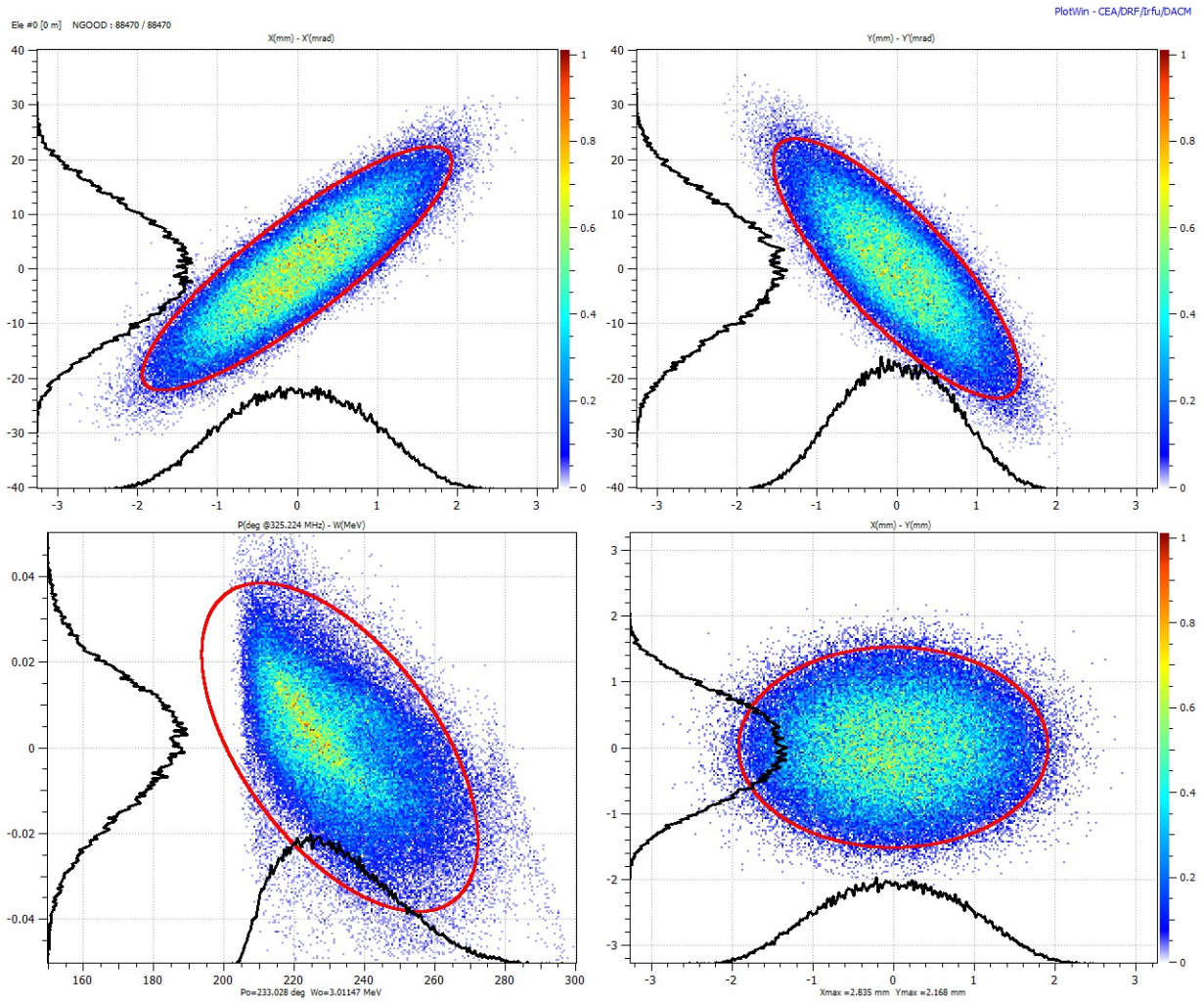

Figure 3.16: Phase space plots and distribution curves (black curves) at the RFQ exit for different settings regarding image charge interactions and the number of "active" neighbor bunches for the reference case (matched case) (cf. Tab. 3.12. The simulation was run with 100,000 input macro-particles, an entrance current of 100 mA and the matched Twiss parameters at the RFQ entrance. The red ellipse correspond to the normalized 95% emittances (cf. Tab. 3.12); $\varepsilon_{x-y,out,n,rms/95\%} = 0.5702/2.9049\,\pi\,mm^2$ (cf. Tab.3.10 and Fig. 3.6). The colors of the scatter plots refer to the normalized macro-particle density (cf. scales at the right frames of the plots).

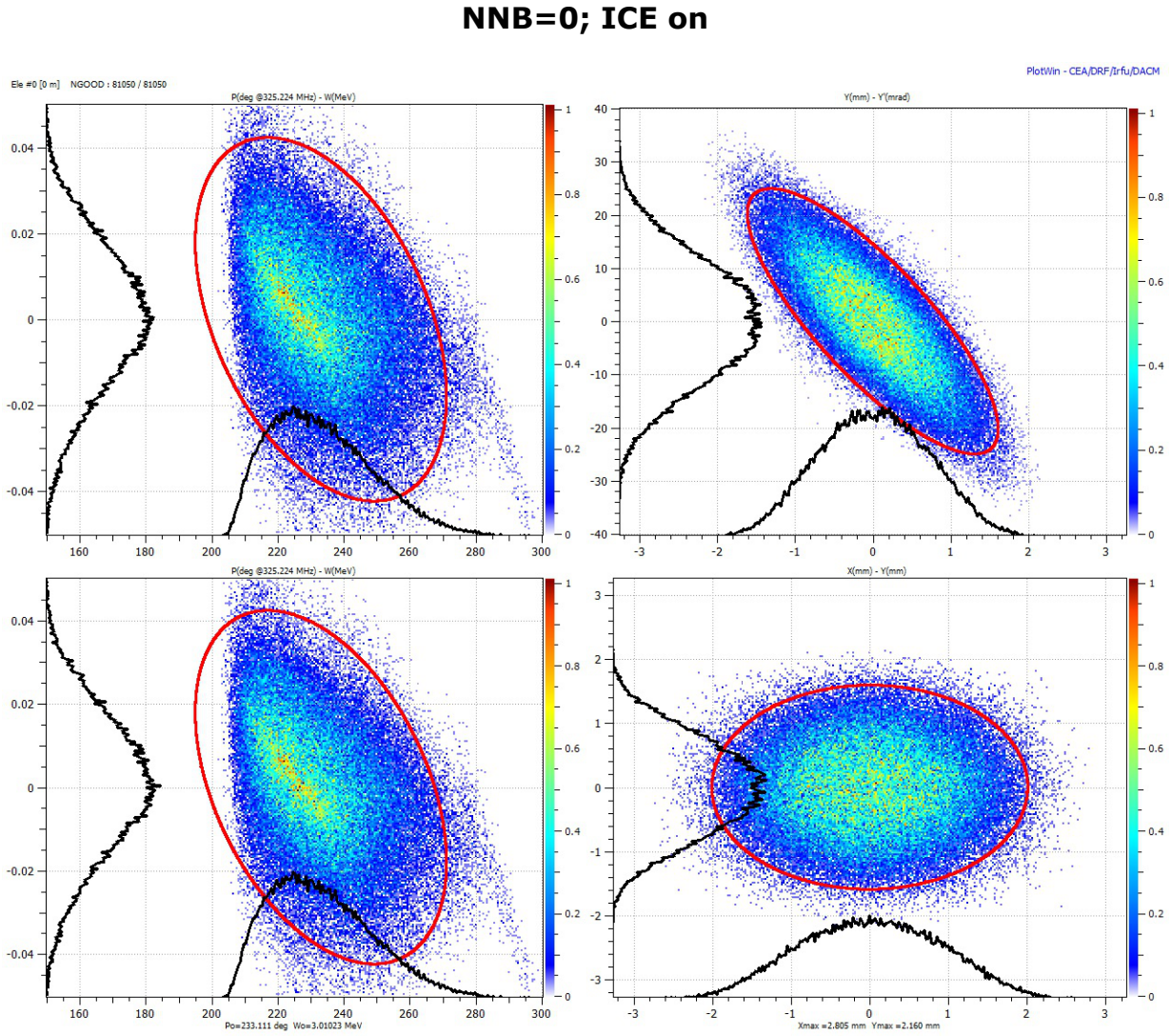

Figure 3.17: Phase space plots and distribution curves (black curves) at the RFQ exit for different settings regarding image charge interactions and the number of "active" neighbor bunches for case 1 (NNB: effects of next neighbor bunches switched off; ICE: image-charge effects switched on) (cf. Tab. 3.12). The simulation was run with 100,000 input macro-particles, an entrance current of 100 mA and the matched Twiss parameters at the RFQ entrance. The red ellipse correspond to the normalized 95% emittances (cf. Tab. 3.12); $\varepsilon_{x-y,out,n,rms/95\%} = 0.6041/3.1915\,\pi\,mm^2$. The colors of the scatter plots refer to the normalized macro-particle density (cf. scales at the right frames of the plots).

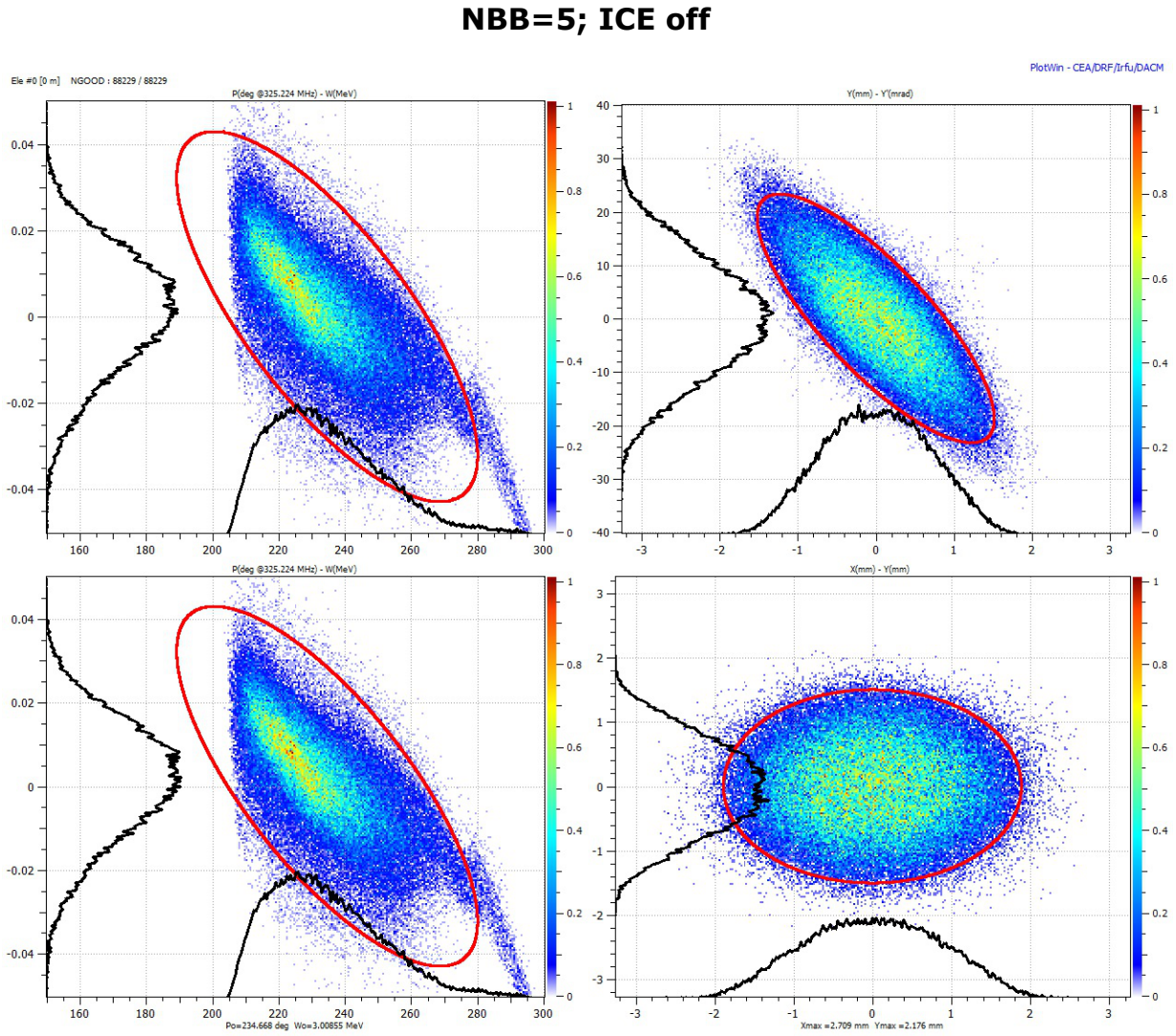

Figure 3.18: Phase space plots and distribution curves (black curves) at the RFQ exit for different settings regarding image charge interactions and the number of "active" neighbor bunches for case 2 (NNB: number of next neighbor bunches set to 5; ICE: image-charge effects switched off) (cf. Tab. 3.12). The simulation was run with 100,000 input macro-particles, an entrance current of 100 mA and the matched Twiss parameters at the RFQ entrance. The red ellipse correspond to the normalized 95% emittances (cf. Tab. 3.12); $\varepsilon_{x-y,out,n,rms/95\%} = 0.5654/2.8316\,\pi\,mm^2$. The colors of the scatter plots refer to the normalized macro-particle density (cf. scales at the right frames of the plots).

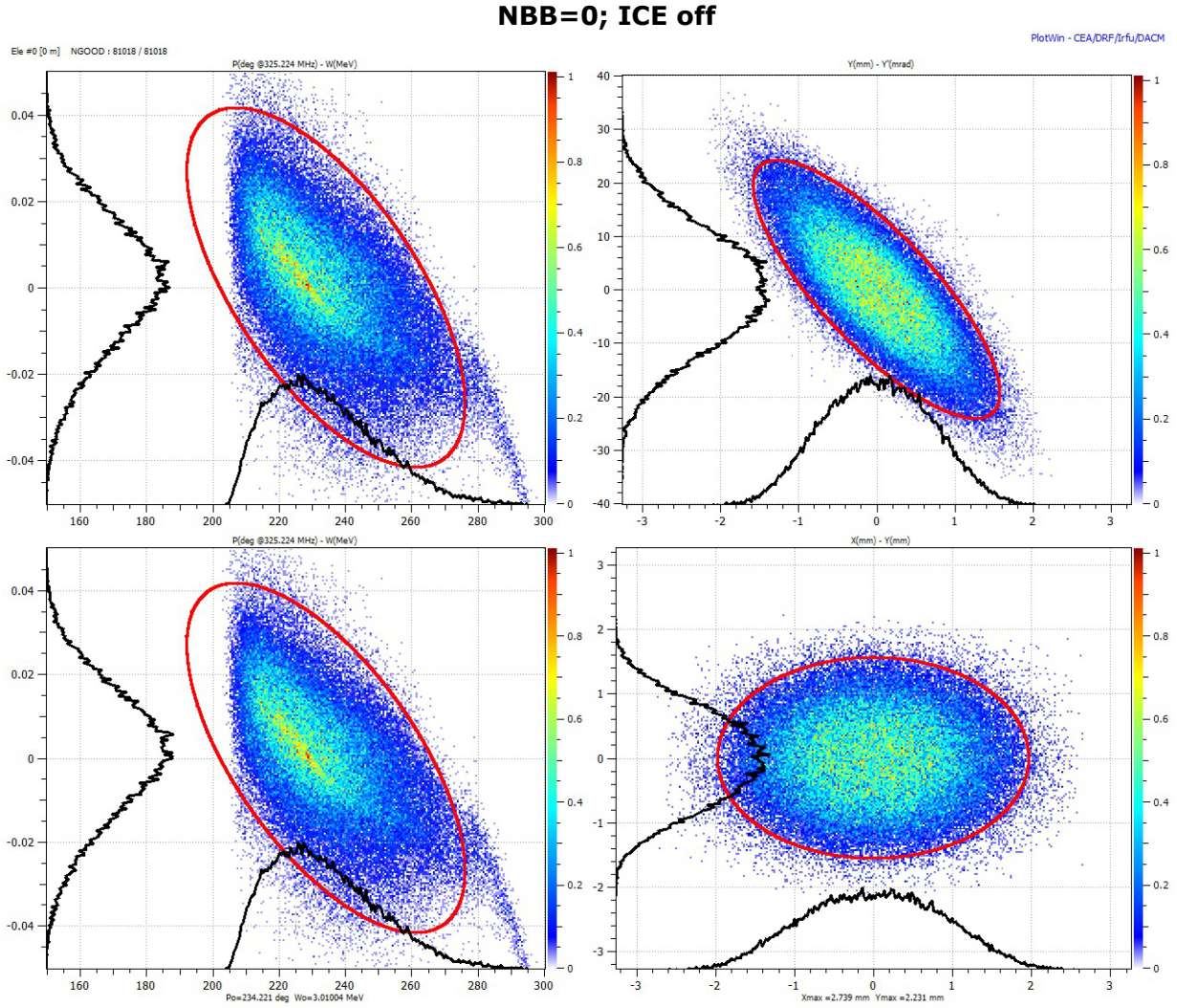

Figure 3.19: Phase space plots and distribution curves (black curves) at the RFQ exit for different settings regarding image charge interactions and the number of "active" neighbor bunches for case 3 (NNB: effects of next neighbor bunches switched off; ICE: image-charge effects switched off) (cf. Tab. 3.12). The simulation was run with 100,000 input macro-particles, an entrance current of 100 mA and the matched Twiss parameters at the RFQ entrance. The red ellipse correspond to the normalized 95% emittances (cf. Tab. 3.12); $\varepsilon_{x-y,out,n,rms/95\%} = 0.5826/3.0662\,\pi\,mm^2$. The colors of the scatter plots refer to the normalized macro-particle density (cf. scales at the right frames of the plots).

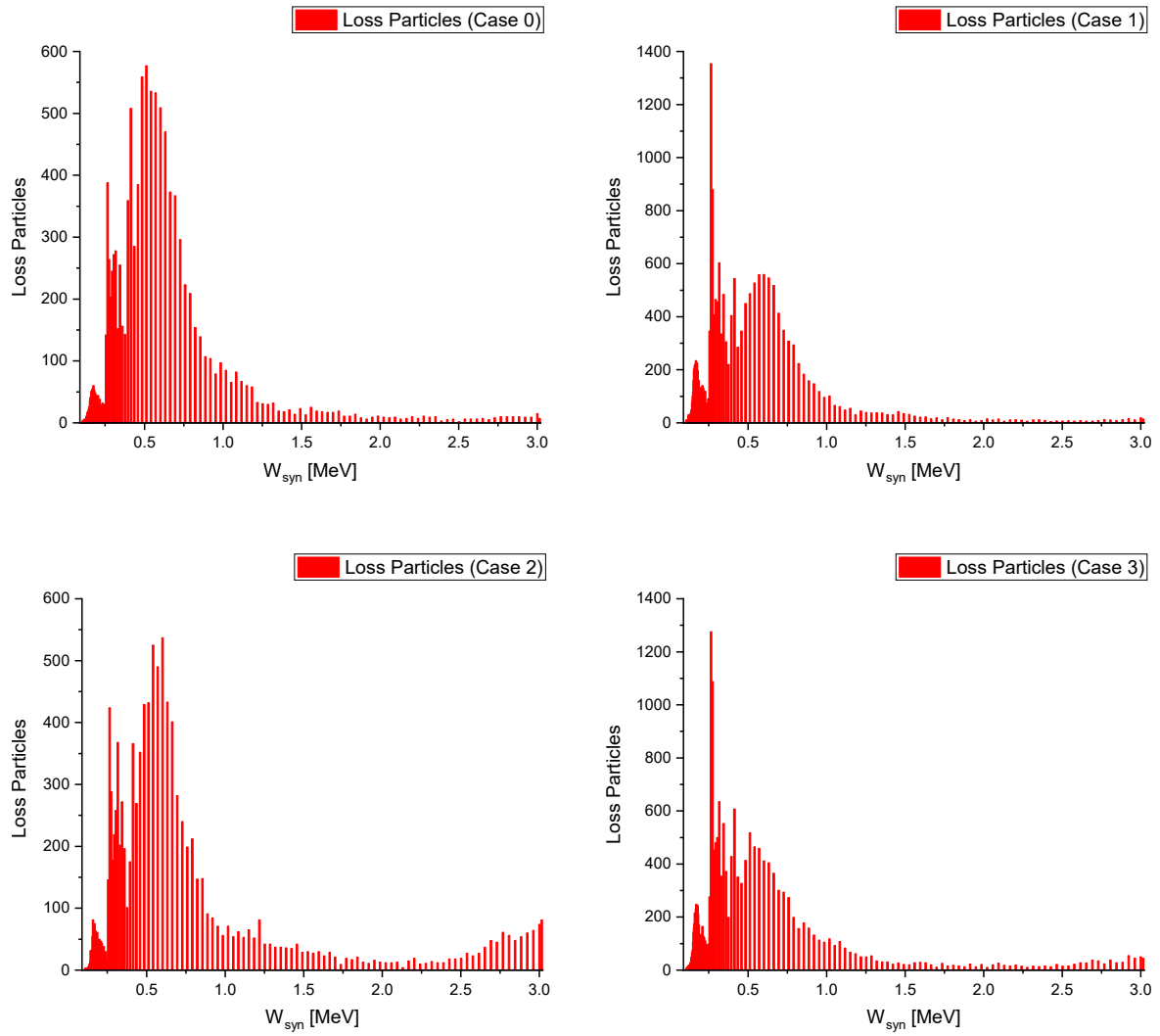

Figure 3.20: Particle losses against the synchronous energy within the cell they are lost in for cases 0-3 (cf. Tab. 3.12). All simulations were run with 100,000 input macro-particles, an entrance current of 100 mA and the matched Twiss parameters at the RFQ entrance. (NNB: next neighbor bunches; ICE: image-charge effects.)

3.7 Compensation of Longitudinal Entrance and Exit Gap Field Effects

Other than the electrodes of 4-Vane RFQs, which are equally charged to $\pm\frac{V_0}{2}$ and only feature a quadrupole on-axis field, the electrodes in 4-Rod-type RFQs are excited by a series of coupled RF oscillators. Since the contact planes between both electrode pairs differ, an oscillating electric potential along the beam axis remains and results in non-negligible longitudinal field components between the electrode ends and the RFQ tank end walls. First investigations of the influence of these types of gap fields on the beam dynamics of 4-Rod-type RFQs were undertaken by IAP Frankfurt (A. Schempp et al.), LANL (S. S. Kurennoy et al.) and FNAL (C. Y. Tan et al.) about a decade ago [29, 30, 31]. These studies were, however, limited specifically to the influence of the longitudinal fields at the exit gap. They arrived at the conclusion, that depending on the individual 4-Rod-type RFQ, these gap fields can cause severe energy distortions, but trough a careful RF design in combination with (even back then classified as) modern simulation tools, the field distributions can nonetheless be optimized to generate well-performing, reliable 4-rod RFQs [31].

It is reasonable to assume that

- such distortions are more severe at the front-end gap of 4-Rod RFQs, where the particles are still slow and hence particularly sensitive to energy modulations
- the entrance gap might also function as a prebuncher even resulting in reduced particle losses and/or shorter Shaper and Buncher sections, if the front-gap field was appropriately considered for the RFQ beam dynamics design.

Both assumptions could be verified with a series of simulations performed for the FAIR Proton-Linac RFQ. The according investigations were first[12] published in June 2019 in *Nuclear Inst. and Methods in Physics Research A* [28]. They are outlined and their results are presented also here in detail to provide a comprehensive description of the FAIR p-Linac RFQ's beam dynamics design within this thesis. Among others, they revealed that resulting energy shifts of up to $\pm\,1.1\,\mathrm{keV}$ and $\pm\,30\,\mathrm{keV}$ could be reached by the end-gaps of the p-Linac RFQ's entrance and exit, respectively.

[12] Preliminary considerations regarding this topic based on a not yet fully completed beam dynamics design can be found in the doctoral thesis of M. Schuett [3].

The associated simulations were performed with the original transversal entrance Twiss parameters $\alpha_{in} = 0.7$ and $\beta_{in} = 0.04\,mm/\pi\,mrad$ (cf. Tab. 3.8 instead of these of the matched case, i.e. $\alpha_{in} = 0.7$ and $\beta_{in} = 0.04\,mm/\pi\,mrad$ (cf. Sec. 3.2)[13].

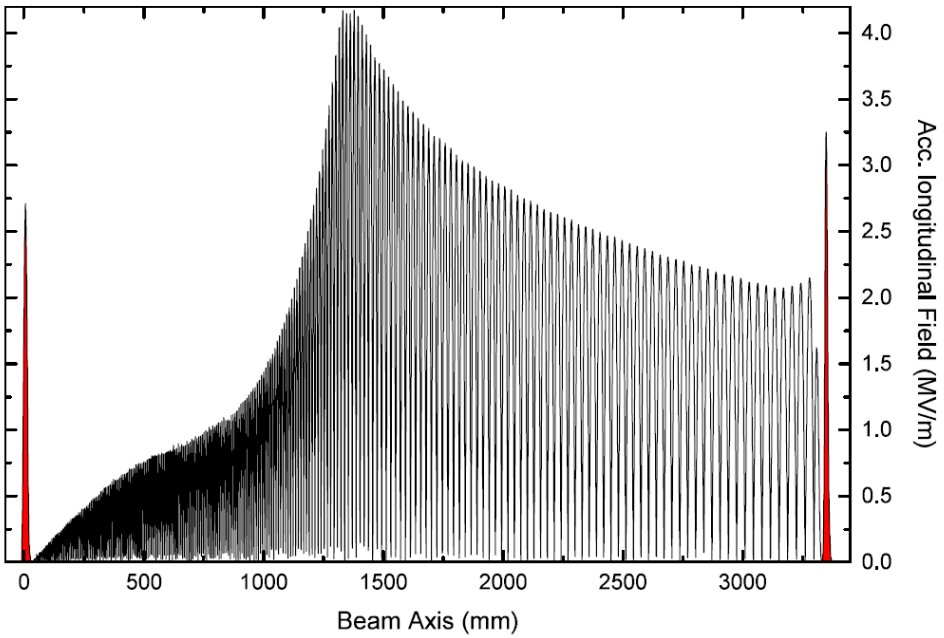

Figure 3.21: Longitudinal electric field distribution along the beam axis of the p-Linac RFQ as built [28]. The field-values at the two end gaps (first and last peak) are significantly larger than those of the single RFQ cells. This discrepancy is especially high at the RFQ entrance (for low m-values). The data were gained by 3D electrodynamic simulations involving the actual electrode profiles. They were performed in CST MWS by M. Schuett.

Figure 3.21 shows the longitudinal electric field distribution along the beam axis of the p-Linac RFQ as built. As will be demonstrated, a strong case can be made to include the evaluation of the longitudinal gap-field effects into the beam dynamics designs of all (future) 4-Rod type RFQs; in case the gap-field effects are found to be harmful, they ought to be reduced accordingly and/or – if possible – directly made use of to even improve the beam dynamics. The general steps for this field evaluation and (if needed) reduction are:

- Analyze longitudinal 3D-fields. If the initial design turns out to not be chosen optimally (or at least sufficiently reasonably) with regards to these fields, optimize the tank-to-electrode

[13] The investigations regarding the gap-field effects preceded the search for the matched case. These Twiss parameters also lead to an sufficient RFQ exit beam (cf. Tab. 3.8 in Sec. 3.2).

distance d (cf. Fig. 3.22). A compromise has to be found between low voltages and short drift lengths within the gaps.

- Evaluate the expected energy gain in dependence of the entrance phase for the drift to the first shaper cell. In order to use the entrance gap-field for prebunching, the electrodes might have to be slightly shortened or extended. The rising edge of the energy modulation[14] induced by the entrance gap should match a phase of $-90°$ at the center of the first modulated ($m \neq 1$) RFQ cell.
- Slightly vary the RFQ entrance energy to find the optimal RFQ entrance phase.
- In order to determine the energy gain or loss induced by the gap-field of the RFQ exit gap calculate the effective phase of the exit gap. The exact energy at the RFQ exit can only be determined by including the effects of the exit gap. The phase dependent energy modulation (cf. Fig. 3.28) usually can be expected to be about $\pm 1\%$ and should thus be considered for the beam dynamics designs of future 4-Rod-type RFQs.

3.7.1 Entrance Gap Field

Figure 3.22 shows the distribution of the electric longitudinal gap field E_z at the entrance of the p-Linac RFQ as built. The distance d between the tank wall and the electrode is about 10 mm. L_g is the distance between the onset position of the longitudinal gap-field and the beginning of the first modulated RFQ cell, which follows directly behind the radial matcher. The total drift length L_d is the distance between the field onset position and the center of the first Shaper cell. Note, that the values of these parameters as shown in Fig. 3.22 refer to the values of the RFQ as built instead of the ones for the optimized RFQ. Due to a tight schedule, these optimization considerations took place after machining had already progressed to a degree that did not allow to implement these findings. Instead, the design as built was tested for its tolerance of the gap field effects present in the RFQ as built. The according beam dynamics simulations and their results are presented in Sub-Sec. 3.7.3.

Minimizing the influence of the gap field on the entering DC beam requires a minimal integral of the gap field $\int E_z(r = 0)dz$ from $z = 0$ to $z = L_g$, i.e. a minimal gap voltage V_{gap}. To re-design the entrance of the p-Linac RFQ to that measure the gap field length L_{gap} or rather the gap distance d has to be re-accessed. Figure 3.23 shows the gap voltage as a function of d: V_{gap} decreases with increasing d. However, at $d \approx 20\,mm$ further increase in d only results

[14] "Energy modulation" refers to the "sinusoidal" shape in the longitudinal sub-space the particle distribution takes on here (cf. Fig. 3.28).

in minor ($< 5\%$) voltage decline. Nevertheless, the final distance cannot simply be chosen to $d \approx 20\,mm$ as on the other hand the high current beam only can pass a rather short drift within the RFQ cavity before its space-charge forces[15] result in no longer tolerable emittances growth. For the p-Linac RFQ, $d \approx 15\,mm$ would pose the optimal compromise between a sufficiently reduced gap field and tolerable space-charge effects as indicated by the marked area in Fig. 3.23[16].

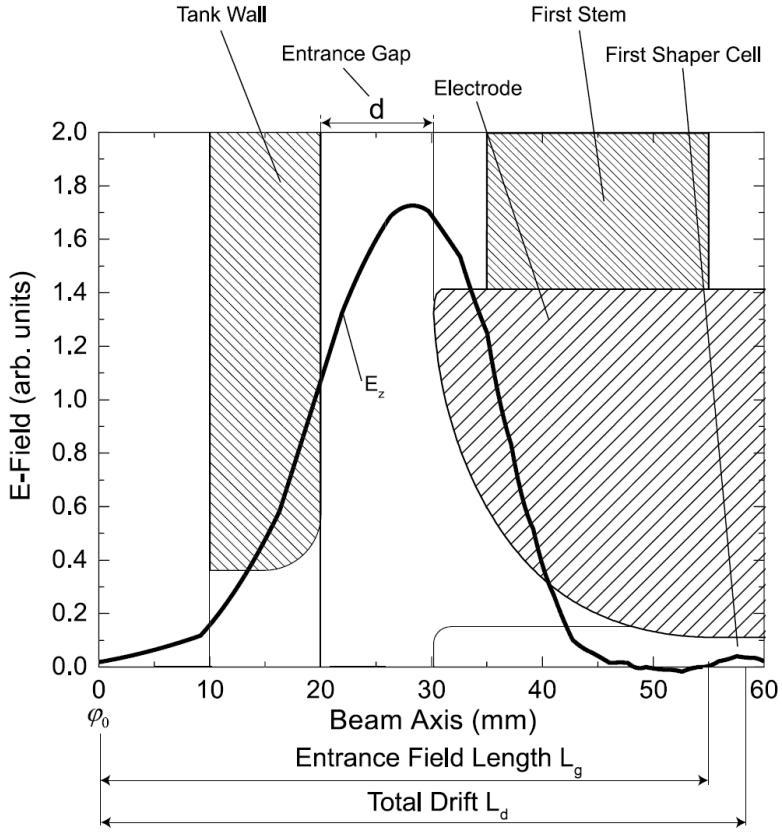

Figure 3.22: Curve of the longitudinal electric field component E_z along the beam-axis from the entrance flange in the tank to the first cell of the electrodes [28]. The first shaper cell starts at $z = L_g \approx 55\,mm$, its center is located at $z = L_d \approx 58\,mm$ (cf. 3.13).

[15] As already mentioned, the beam is considered 90% space-charge compensated in the LEBT, but not space-charge compensated at all as it enters and traverses the RFQ. More information on this is given in Appx. B.

[16] Since these studies were performed after manufacturing of the RFQ had been finished, the actual d-value of approx. 10 mm (cf. 3.22) is slightly outside this optimal range. As shown below, it is still chosen close enough to this range to not lead to significant distortions of the beam dynamics, though.

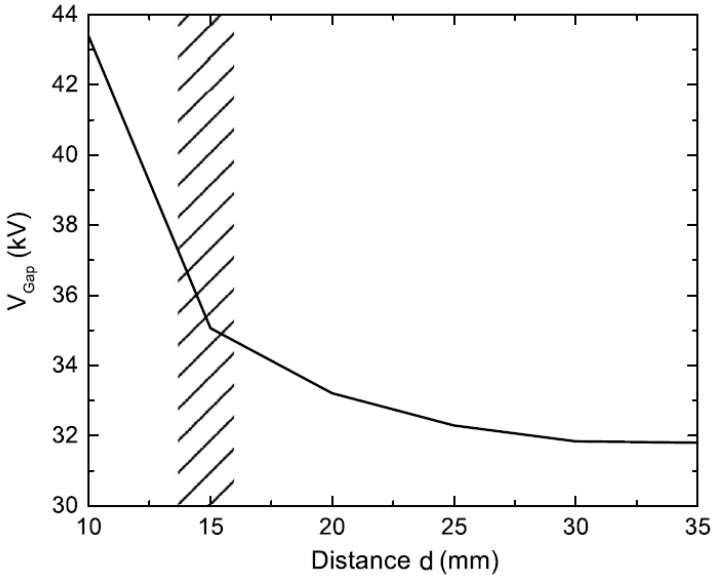

Figure 3.23: Voltage amplitude at the entrance of the p-Linac RFQ as a function of the gap distance d (cf. Fig. 3.22). The shaded area marks the d-range of optimal compromise between a sufficiently reduced gap field and tolerable space-charge forces along d. (As shown below, values outside this range can still lead to a reasonable, albeit sub-optimal, compromise.)

Section/Gap/Cell	**Length [mm]**
Total Drift L_d*	57.9
Entrance Field L_g*	54.6
RM Gap d*	10.08
RM-Section	34.60
RM-Cell**	6.558
First Shaper Cell	6.560

Table 3.13: Characteristic lengths at the RFQ entrance. *Cf. Fig. 3.22. **Due to the quadrupole-symmetry of the RM Section no acceleration takes place within it and thus all 5 RM cells are of the same length. (The electrodes are 3329.84 mm long.)

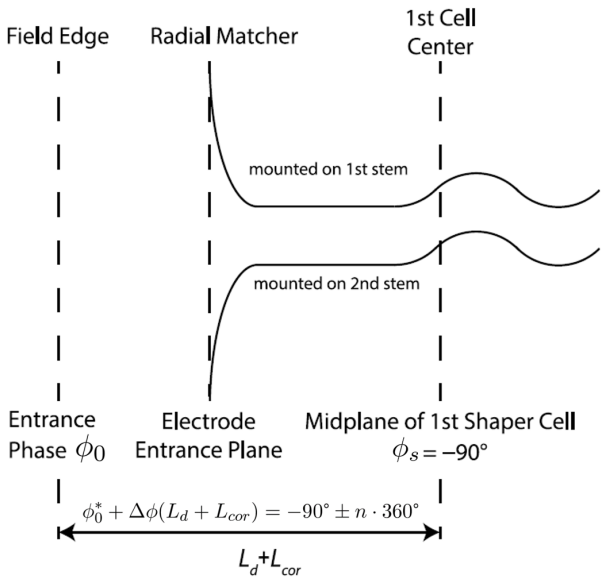

Table 3.14: Sketch of the p-Linac RFQ entrance [28]. The outlined electrode profiles each represent a vertical and a horizontal electrode pair. The top one is mounted to the first stem, whilst the bottom one is mounted to the second stem. For better visualization modulations and distances are not to scale. For the gap field to lead to optimal prebunching, the total drift L_d has to be adjusted by an additional drift L_{cor} as outlined in Eq. 3.1).

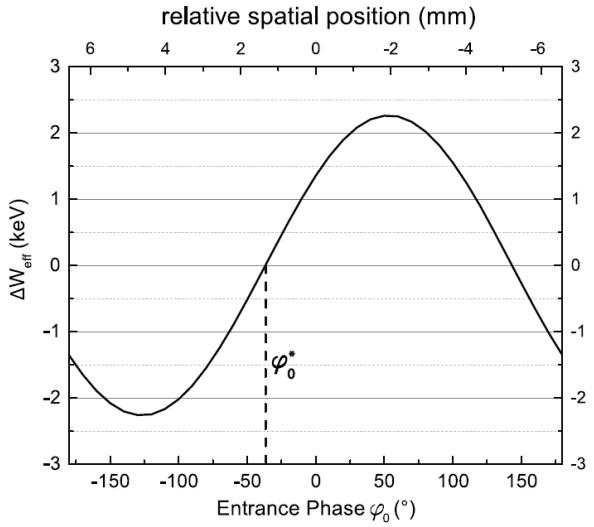

Figure 3.24: Effective energy gain ΔW_{eff} along the gap field in dependence of the entrance phase ϕ_0 and particle position, respectively [28]. $\Delta W_{eff} = 0$ for $\phi_0 = \phi_0^*$.

By design the synchronous phase at the center of the first shaper cell is $-90°$. The gap field leads to optimal prebunching, if the particles passing the gap field without an energy gain on the

rising edge of the energy modulation at ϕ_0^* arrive at the center of the first shaper cell at a phase of $\phi_0 = -90°$ (cf. Fig. 3.24). To fulfill that condition the total drift $L_d = 57.9\,mm$ (cf. 3.13) from the entrance flange to the center of the first shaper cell has to be adjusted by an additional drift L_{cor}:

$$\phi_0^* + \Delta\phi(L_d + L_{cor}) = -90° \pm n \cdot 360°. \tag{3.1}$$

Equation 3.1 holds true for the geometry plotted in Fig. 3.14 as here the gap field is in parallel with the field within the first shaper cell. However, if the stem connections are exchanged between rod pairs, or if the modulation starts in opposite direction at the first shaper cell, the additional drift L_{cor} is determined by

$$\phi_0^* + \Delta\phi(L_d + L_{cor}) = +90° \pm n \cdot 360° \tag{3.2}$$

instead. This is the case for the p-Linac RFQ, where with $L_d = 57.9\,mm$, $\phi_0^* = -37°$ and $n = 4$ the re-adjusted total drift $L_d + L_{cor}$ between the entrance and the first shaper cell would have to amount to 57.0 mm. Hence, the total drift length would have to be shortened by $L_{cor} = -0.9\,mm$: In case that the electrode geometry shall be kept, the gap distance could be adjusted by changing the inner tank length. Otherwise, the electrodes should be modified directly. Both measures lead to a changed entrance phase, which requires an iterative process for re-adjustment (cf. Fig. 3.25). The electrode length adjustment has to be realized within the radial matcher. For sufficiently small values of $L_{cor} < 2\,mm$ the radial matching section could be shortened by a steeper decrease of the aperture.

A third solution consists in shifting the electrodes longitudinally against the cavity mid plane. Should this result in mechanically impractical values, the electrodes could be extended within the radial matching section according to Eq. 3.1; the mountings of the electrode pairs would then have to be re-designed accordingly. For the FAIR Proton-Linac RFQ, this solution would require to insert a quadrupole focusing channel of length $L_{cor} = 5.7\,mm$ and constant mean aperture a_0. However, simply shortening the electrodes by $L_{cor} = -0.9\,mm$ is the clearly preferable solution in case of the FAIR Proton-Linac RFQ.

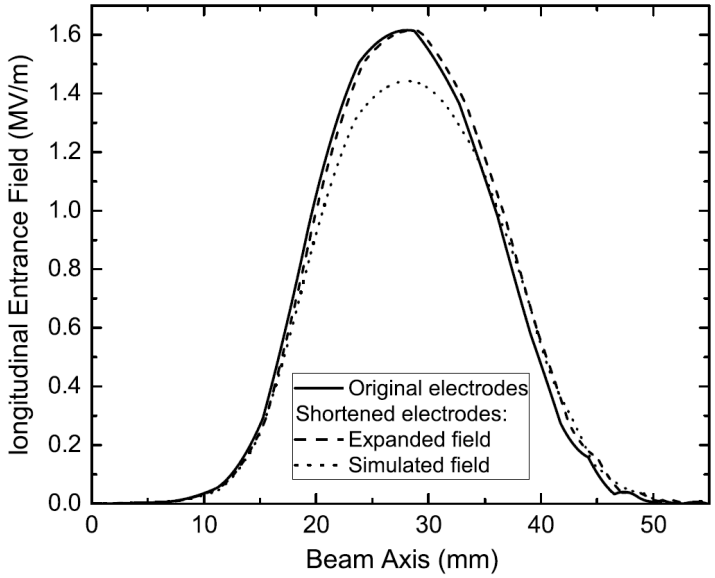

Figure 3.25: On-axis gap fields at the p-Linac RFQ entrance [28]. The solid curve refers to the original gap geometry, whereas the dashed curve shows the same curve symmetrically stretched by 2.5 mm. The dotted curve refers to a 3D electrodynamic field simulation based on the re-adjusted gap geometry.

Adjusting L_{cor} by modifying the gap distance at the RFQ entrance and exit changes the effective gap field lengths. Consequently the zero crossing entrance phase ϕ_0^* also requires re-evaluation. For the p-Linac RFQ this phase change could be predicted by a symmetrical longitudinal expansion of the original field. This expansion leads to nearly the same ϕ_0^*-value as a 3D electrodynamic field simulation based on the re-adjusted gap geometry (see Fig. 3.25). However, both approaches yield different energy shifts: The simulated field leads to a smaller shift. Knowledge of the stable ϕ_0^* allows for an iterative determination of the final length correction without the need to simulate each single length deviation.

3.7.2 Exit Gap Field

Whereas the length of the radial matcher has to remain an integer multiple of $\beta_{in}\,\lambda$, the high energy end of the electrodes can be continuously adjusted in length and phase. The last "cell" or rather region of the RFQ is the so-called exit fringe-field region. It stretches from the end of the last actual RFQ cell, i.e. from the end of the transition region (see below), to the end plane of the beam dynamics simulation. Its default value in RFQGen is 10 mm, which was also chosen for all simulations presented in this thesis. Including an "exitff"-line in the RFQGen input-file ensures that the code takes into account the transversal RF focusing fields, referred to as

fringe-fields[17], that exist within this region. Omitting this line leads RFQGen to implicitly and incorrectly assume the transversal fields abruptly end at the end of the RFQ electrodes. In case of the p-Linac-RFQ the end plane of the beam dynamics simulation is located 4.88 mm behind the end of the electrodes, i.e. roughly in the center of the exit gap (cf. Tab. 3.15; "Simulation Surplus"). In 1994 Crandall purposed today's standard scheme for designing the last RFQ cells by introducing a transition region connecting the last accelerating cell, i.e. the last cell of the acceleration section, to the exit fringe-field region \"cell" [71]. If a transition region is included into an RFQ's beam dynamics design, all four electrodes are of equal length (regardless of whether a fringe-field region follows).

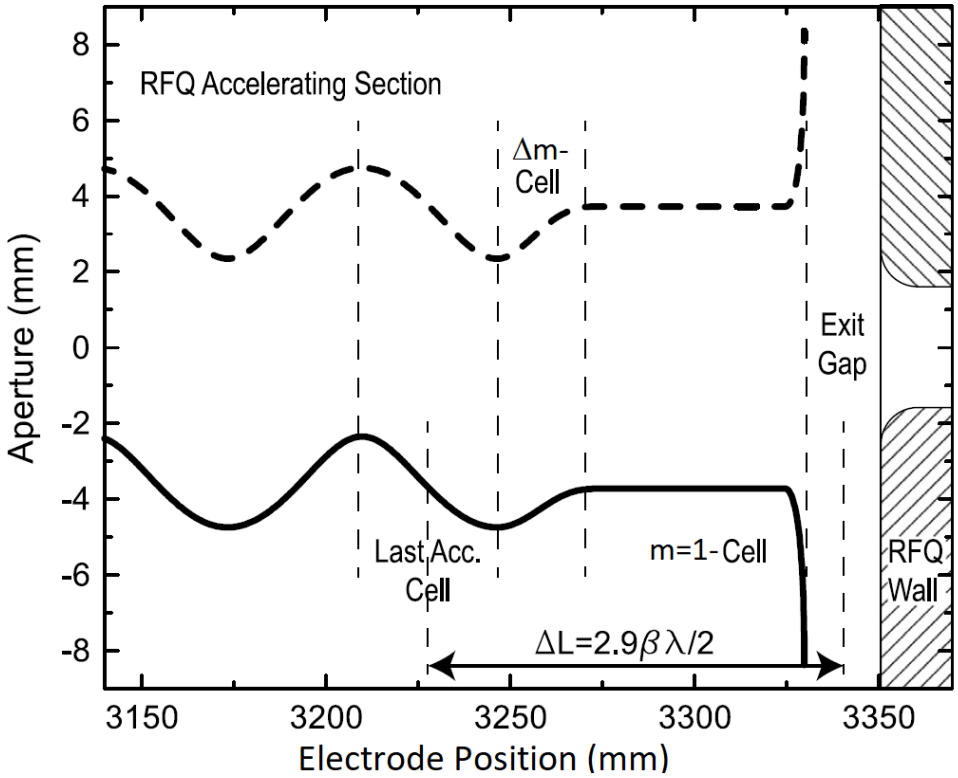

Figure 3.26: Detailed sketch of the electrode profiles at the p-Linac RFQ exit [28]. Both curves represent a pair of opposing electrodes in the horizontal (dashed, top) and vertical (continuous, bottom) plane, respectively.

The transition region can be thought of as a radial matching section at the RFQ exit [71] and consists of a $\Delta\, m$-cell and optionally a $m = 1$-cell. The first transition cell smoothly transits the

[17] They ought not to be confused with the longitudinal gap fields (also simply referred to as gap fields).

modulation parameter $m > 1$ of the last cell of the acceleration section to $m = 1$. Due to this quadrupole symmetry the on-axis field at the end of the transition cell, which is derived from a three-term potential, vanishes. The $\Delta\, m$-cell (or Crandall cell) is slightly to moderately shorter than a succeeding default RFQ cell of length $\frac{\beta\lambda}{2}$ would have been. In case of the p-Linac RFQ cell 243, i.e. the last cell of the acceleration section, is 36.7 mm long, followed by the $\Delta\, m$-cell of only 28.4 mm length[18] The second transition cell, the so-called $m = 1$-cell, can be thought of as a quadrupole focusing transport channel. Its length is given by $l_{\Delta m} = (\phi_{m=1} - \phi_{\Delta m})\, \frac{\beta_{m=1}\lambda}{2\pi}$, with $\phi_{\Delta m}$ and $\phi_{m=1}$ the phases at the end of the $\Delta\, m$- and the $m = 1$-cell, respectively, and $\beta_{m=1}$ the relative synchronous velocity within the $m = 1$-cell. RFQGen enables adjusting the length of the second transition cell through the value of $\phi_{\Delta m}$. This parameter has to be entered in the "trans"-line of the RFQGen input file and refers to the value in degree and sine(!)-convention [21, 22]. If this entry is omitted in the "trans"-line, the transition region will only consist of the $\Delta\, m$-cell.

By re-adjusting the length of the $m = 1$-cell the Twiss parameters of the beam ellipse in both transversal planes can be re-modeled. This allows for a maximal reduction of the detrimental influence of the exit-gap field. The energy shift along the exit gap field is minimal for a synchronous particle phase of $\phi_0 = \pm 90°$ at the effective gap center between the electrode ends and the tank wall of the RFQ, i.e. the plane of the end of the simulation.

Cell/Region/Gap	**Length [mm]**
Last Cell of Acc. Sec.	3.67
Δm-Cell (Crandall Cell)	2.84
$m = 1$-Cell	4.99
Exit Fringe-Field Region	10.0
Exit Gap*	10.08
Simulation Surplus**	4.88
Electrode Surpass	5.12

Table 3.15: Characteristic lengths at the p-Linac RFQ exit. *Both end gaps are of equal length. **Distance from end of electrode end plane to simulation end plane. (The electrodes are 3329.84 mm long.)

[18] For comparison, cell 242, the second to last cell of the acceleration section, is 36.4 mm long.

3.7.3 Beam Dynamics Simulations with Entrance Gap Field Effects

The following simulations exhibit the significance the entrance gap-field effects can have for the beam dynamics design of a 4-Rod-type RFQ. As these effects cannot be included in the RFQGen simulations directly (as of now) a workaround was needed. In RFQGen, the default starting plane of the beam dynamics simulation is located between the tank wall and the beginning of the electrodes[19], more precisely 8.28 mm in front of the beginning at the electrodes. In a first step, the distribution at this plane is transported backwards towards the LEBT-line in TraceWin. This simulation was performed by M. Schuett and included space-charge effects. The transversal input Twiss parameters were $\alpha_{in} = -0.7$ and $\beta_{in} = 0.04\,mm\,/\,\pi\,mrad$, i.e. the original design Twiss parameters apart from a sign switch in α_{in} (cf. Sec. 3.2). (The backward tracked beam is divergent as the actual beam is convergent.) For the aperture shaped entrance flange with a diameter increase from 18 mm to 28 mm towards the inner side of the cavity, even the diameter of the 100% beam envelope remained well below the aperture (see Fig. 3.27).

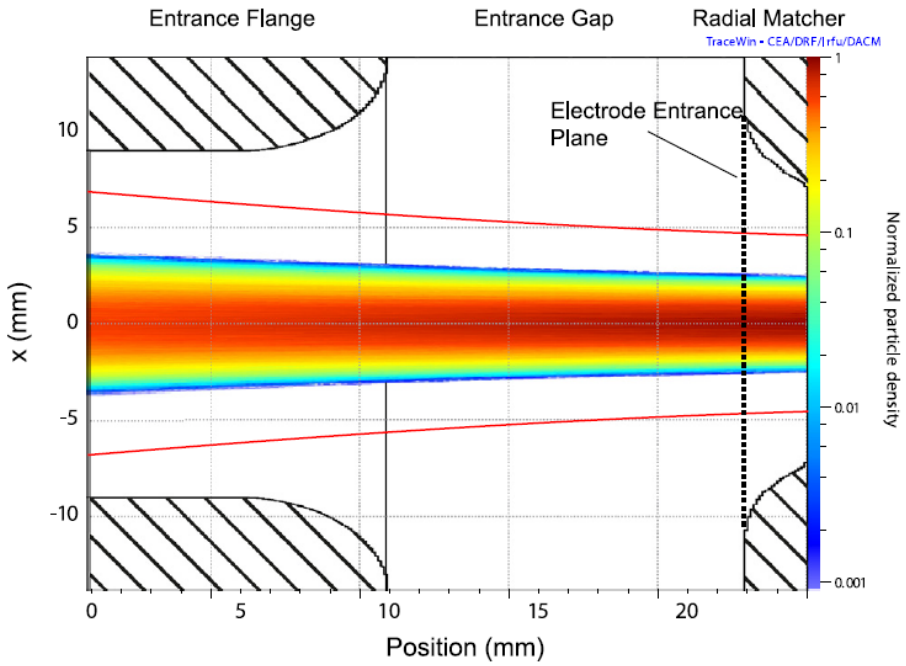

Figure 3.27: Normalized particle density plot along the drift between the entrance flange and the radial matcher as given by the reverse TraceWin beam dynamics simulation. A total drift of 25 mm and an aperture of 18 mm at the entrance flange are suited to avoid any particle losses. The red curves show the 100% beam envelope [28].

[19] Default starting cell 0 equivalent to cell 1 in RFQGen's "start"-line.

Two RFQGen input distributions were generated this way. One distribution refers to the optimal case, for which the rising edge of the energy modulation arrives at a synchronous phase of $\phi_0 = -90°$ at the center of the first shaper cell. For the other one ϕ_0 is shifted by 180° to $\phi_0 = +90°$, which constitutes the most detrimental phase, i.e. the worst case scenario. The amplitude of the energy modulation at the RFQ entrance was $\Delta W_{in} = \pm 3.8 keV$, the beam current was 100 mA. Figure 3.28 shows the longitudinal phase space plots of both distributions. The beam parameters at the RFQ exit for the associated RFQGen-simulations and are presented in Tab. 3.16.

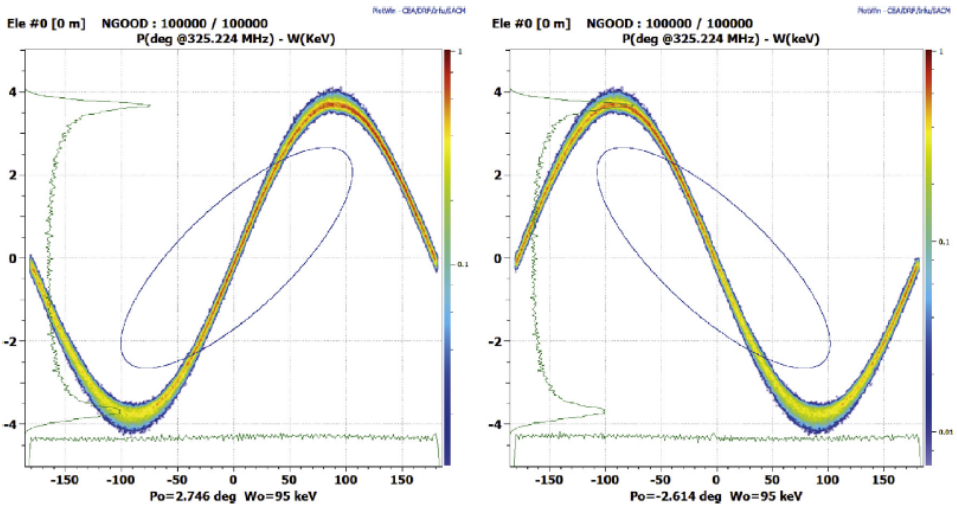

Figure 3.28: Two RFQ entrance distributions in longitudinal phase space (logarithmically scaled right ordinates); the green curves refer to the ΔW_{in}- and ϕ-distributions. The left plot refers to the optimal case, for which the rising edge of the energy modulation passes the center of the first Shaper cell at $\phi_0 = -90°$ and the right one to the most mismatched (i.e. the "worst") case with $\phi_0 = +90°$.

This table also shows these parameters for the reference case, where the entering continuous wave (CW) beam is not exposed to the gap field thus exhibits no energy modulation[20]. The optimal phase $\phi_0 = -90°$ leads to an increased transmission and reduced emittances due to the beneficial prebunching effect of the entrance gap. Accordingly, a ϕ_0 of +90° maximally deteriorates these beam parameters. This deterioration is increased significantly for values of $\frac{\Delta W_{in}}{W_{in}}$ above ±5%. (However, as stated in Sec. 3.8, in case of the FAIR p-Linac RFQ even $\Delta W_{in} = \pm 3.8\,\mathrm{keV}$, i.e. $\frac{\Delta W_{in}}{W_{in}} = \pm 2.0\%$, constitutes an unrealistically pessimistic assumption.)

[20] Note that this case is not identical to the original case in Tab. 3.8 of Sec. 3.2, which refers to a generic 4D Waterbag distribution generated by RFQGen.

For entrance energy spreads above that threshold not even a ϕ_0 of $-90°$ leads to any improvement.

These findings stress that performing such investigations (at least regarding the entrance gap) is crucial for each 4-Rod-type RFQ as its (entrance) gap field could "make or break" its beam dynamics.

Table 3.16 shows the transmission, emittances and the transversal emittance growth at the RFQ exit. (Note, that the less crucial effects of the exit gap-fields were not yet included in the beam dynamics simulations.)

Beam Parameter	Optimal Case	Ref. Case	Worst Case
	$\phi_0 = -90°$	w/o gap-field	$\phi_0 = +90°$
Transmission [%]	87	86	73
$\varepsilon_{x,out,n,rms}\,[\pi\, mm\, mrad]$	0.31	0.33	0.34
$\varepsilon_{y,out,n,rms}\,[\pi\, mm\, mrad]$	0.31	0.32	0.34
$\varepsilon_{z,out,n,rms}\,[\pi\, MeV\, deg]$	0.20	0.21	0.27
Trans. Emit. Growth [%]	3	10	13

Table 3.16: Transmissions and normalized rms-emittances at the p-Linac RFQ exit for the three cases of interest. The transversal normalized rms-emittances at the RFQ entrance were $0.3\,\pi$ mm mrad for all three cases.

3.8 Entrance Beam Current Studies with RFQGen and TOUTATIS

At the beginning of its conditioning process the RFQ is not operated with a beam of the design current. The source, LEBT, RFQ and MEBT have to be put into operation with great care, whereby the source beam initially carries a current of only several μA, i.e. close to the zero-current case. This very early phase of beam commissioning is also referred to as the beam "running-in". Here, reaching sufficient matching into the RM section is critical. However, in case of insufficient matching and the resulting collision of beam and RFQ the damage done by multipacting and similar undesirable effects might likely be tolerable due to the very low current at that stage. The high design current can only be reached after a time consuming, properly executed and monitored commissioning process.

These beam dynamics studies were performed for currents from 0 mA to 110 mA in steps of 1 mA, whereby 3 different values for the entrance energy spread ΔW were set: $\Delta W_{in} = \pm 0.00$ keV ($\frac{\Delta W_{in}}{W_{in}} = \pm 0\%$), $\Delta W_{in} = \pm 1.9$ keV ($\frac{\Delta W_{in}}{W_{in}} = \pm 2.0\%$) and $\Delta W_{in} = \pm 3.8$ keV ($\frac{\Delta W_{in}}{W_{in}} = \pm 4.0\%$).

All other RFQGen settings remained the same as for the matched case simulation (cf. Sec. 3.2). Hence, $111 \times 3 = 333$ simulations were run within the scope of these current studies. Figure 3.29 summarizes the results for selected RFQ entrance currents at the RFQ exit.

Note: as the beam can be expected to leave the source exhibiting almost no energy spread, setting $\Delta W_{in} = \pm 0.00\,\mathrm{keV}$ in RFQGen's input-line is justified, whereas $\Delta W_{in} = \pm 1.9\,\mathrm{keV}$ and especially $\Delta W_{in} = \pm 3.8\,\mathrm{keV}$ are much too pessimistic assumptions. The purpose of choosing these high values was to investigate the effect of this parameter on the beam dynamics in general rather than to test the beam dynamics design's tolerance for such high energy spreads. However, the p-Linac RFQ's beam dynamics proved quite stable even for such large entrance energy spreads.

Furthermore, the comparison of RFQGen and TOUTATIS current studies under the reasonable assumption of an RFQ entrance energy spread of $\Delta W_{in} = \pm 0.00\,\mathrm{keV}$ is presented in Fig. 3.30. The corresponding TOUTATIS simulations were performed by H. Hähnel: for I_{in} between 10 mA and 100 mA the step width was set to 10 mA, whereby the interval $(30\,mA, 40\,mA)$ was investigated more thoroughly with a step width of 1 mA. Furthermore, a TOUTATIS simulation for $I_{in} = 75\,\mathrm{mA}$ was also run. For better comparison, the graphs of the RFQGen simulations in Fig. 3.30 only contain the data-points for the 19 current values that correspond to TOUTATIS simulations.

As can be seen from Fig. 3.29 the parameter curves run similarly for all three ΔW-values[21]. For all ΔW-values, the transmission falls slowly with a growing entrance current, whereby the decline takes place more rapidly at increased ΔW-values (especially from $\Delta W = \pm 1.9\,\mathrm{keV}$ to $\Delta W = \pm 3.8\,\mathrm{keV}$).

As expected, the longitudinal exit emittance is minimal for the design entrance current of $I_{in,des} = 100\,\mathrm{mA}$. For lower currents the space-charge forces are overcompensated, for higher currents they are insufficiently compensated. The longitudinal emittance exhibits a bump between ca. 30 mA and ca. 40 mA whilst the transversal emittances show the opposite behavior. These behaviors of the emittances occur for both the RFQGen and the TOUTATIS simulations and therefore are unlikely to be the result of software bugs etc. They are less pronounced for $\Delta W_{in} = \pm 1.9\,\mathrm{keV}$ and vanish for $\Delta W_{in} = \pm 3.8\,\mathrm{keV}$. In order to understand them fully, further

[21] To allow for a better comparison, the graphs of the RFQGen-simulations in Fig. 3.30 only contain the data points for the same 19 values that are also available from the TOUTATIS simulation series. However, to provide more information, for the curves of Fig. 3.29 the general step-width is reduced to 5 mA; the step-width in the interval $(30\,mA, 40\,mA)$ remains 1 mA. Furthermore, the data points for $I_{in} = 1\,\mathrm{mA}$, 2 mA and 3 mA are included.

studies, ideally also performed with further beam dynamics codes, might be required.

At all entrance currents, the longitudinal exit emittances are raised for higher values of ΔW_{in} since these correspond to a higher longitudinal entrance emittance. Also, for all entrance currents the longitudinal normalized rms-emittances peak at about cell 156 (cf. Fig. 3.31), i.e. the foot of the peak in losses per cell (cf. Fig. 3.32). This peak exhibits a maximum at about cell 172, the last GB cell[22]. As expected the magnitude of the peak increases with higher entrance currents, whereas its position and width remain nearly constant.

The peak in loss particles per cell is reflected in the transmission curves, which undergo a rapid decline at its position. This still rather minor, acceptable decline at the end of the GB section is an intended feature of this RFQ design (cf. Sec. 3.5) as it results in a desired significant reduction of the longitudinal and transversal emittances (see Figs.3.33 - 3.35). The peak in the transversal emittances at the end of the GB becomes much more pronounced for higher currents[23].

This trade-off between a sufficiently high transmission and sufficiently low RFQ exit emittances is also illustrated in Fig. 3.29. This figure shows, among others, the curves of the total longitudinal and radial particle losses along the RFQ against the entrance currents. For RFQ entrance currents I_{in} up to values between 80 mA and 90 mA the longitudinal losses dominate the total losses along the RFQ, then the situation is reversed (see Fig. 3.29). Furthermore, the crossing point of both curves shifts for growing values of ΔW_{in} to higher values of I_{in}, i.e. from 80 mA for $\Delta W_{in} = \pm 0.0$ keV to 82 mA for $\Delta W_{in} = \pm 1.9$ keV and to 90 mA for $\Delta W_{in} = \pm 3.8$ keV, respectively. This behavior was to be expected since higher ΔW_{in}-values should correspond with higher longitudinal losses at the end of the GB section. Hence, for increasing initial energy spreads the radial losses require higher space-charge forces and hence beam currents to "catch up" with the longitudinal losses.

Figures 3.42 - 3.45 show the longitudinal phase space plots at the RFQ exit for entrance currents of 0 mA, 2 mA, 10 mA, 25 mA, 35 mA, 50 mA, 70 mA and 110 mA[24]. If space-charge effects are switched off completely (zero-current case), the beam is exposed to the external sinusoidal fields

[22] Here, the curves of a, m and ϕ_s exhibit their characteristic kinks (cf. Fig. 3.1), which mark the transition from the GB to the acceleration section.

[23] The local minima around cell 70 and their decline with increasing I_{in}- and decreasing ΔW_{in}-values might be subjects of further investigations.

[24] The corresponding transversal and the x-y-phase space plots closely resemble these of the 100 mA matched case (cf. Fig. 3.6 in Sec. 3.2) and would offer no information that is not also provided by Figs. 3.29, 3.30 and 3.33 - 3.35.

only and a spiral-like pattern emerges in the longitudinal phase space. This leads to a high effective emittance whilst the actual area occupied by particles is rather small. With growing RFQ entrance current this spiral pattern blurs evermore until it vanishes at about 25 mA. As would be expected, these patterns are more pronounced for the lower initial energy spreads. Furthermore, the longitudinal 95%-ellipses exhibit a divergence, i.e. α_z becomes increasingly positive; cf. Fig. D.4[25]. This divergence increases with I_{in} and decreases with ΔW_{in}. The lower the current, the more sensitive α_z becomes regarding ΔW_{in}.

The curves of the transversal phase-advances $\sigma_{x/y}$ (see Figs. 3.36 - 3.38) exhibit an expected kink at cell 172, i.e. at the transition from GB to acceleration section. Up to this cell $\sigma_{x/y}$ declines, from then on it increases. However, super-positioned on this general behavior are oscillations. With rising I_{in}-values, the $\sigma_{x/y}$-values of each RFQ cell (generally) decline and the minimum at cell 172 becomes more pronounced, both in absolute terms and relatively to $\sigma_{x/y}$ at the RFQ ends. Furthermore, the curves oscillate stronger for higher values of I_{in} and weaker for higher ΔW_{in}-values.

The curves of the longitudinal phase-advance σ_z (see Figs. 3.39 - 3.41) also exhibit oscillations, which increase for higher currents and for lower energy spreads. Unlike the $\sigma_{x/y}$-curves, they also exhibit blanks: along an interval at the end of the GB section no σ_z-values can be defined due to too high currents. The length of this interval increases with rising entrance current and decreases for growing entrance energy spreads.

It thus might be worth considering to attempt damping the oscillations of the phase advances during "running-in" by imposing a larger energy spread on the RFQ entrance distribution.

[25] Note that the associated ellipses in z-z',-phase space would actually be tilted to the right (since higher z-coordinates correspond to lower ϕ-coordinates).

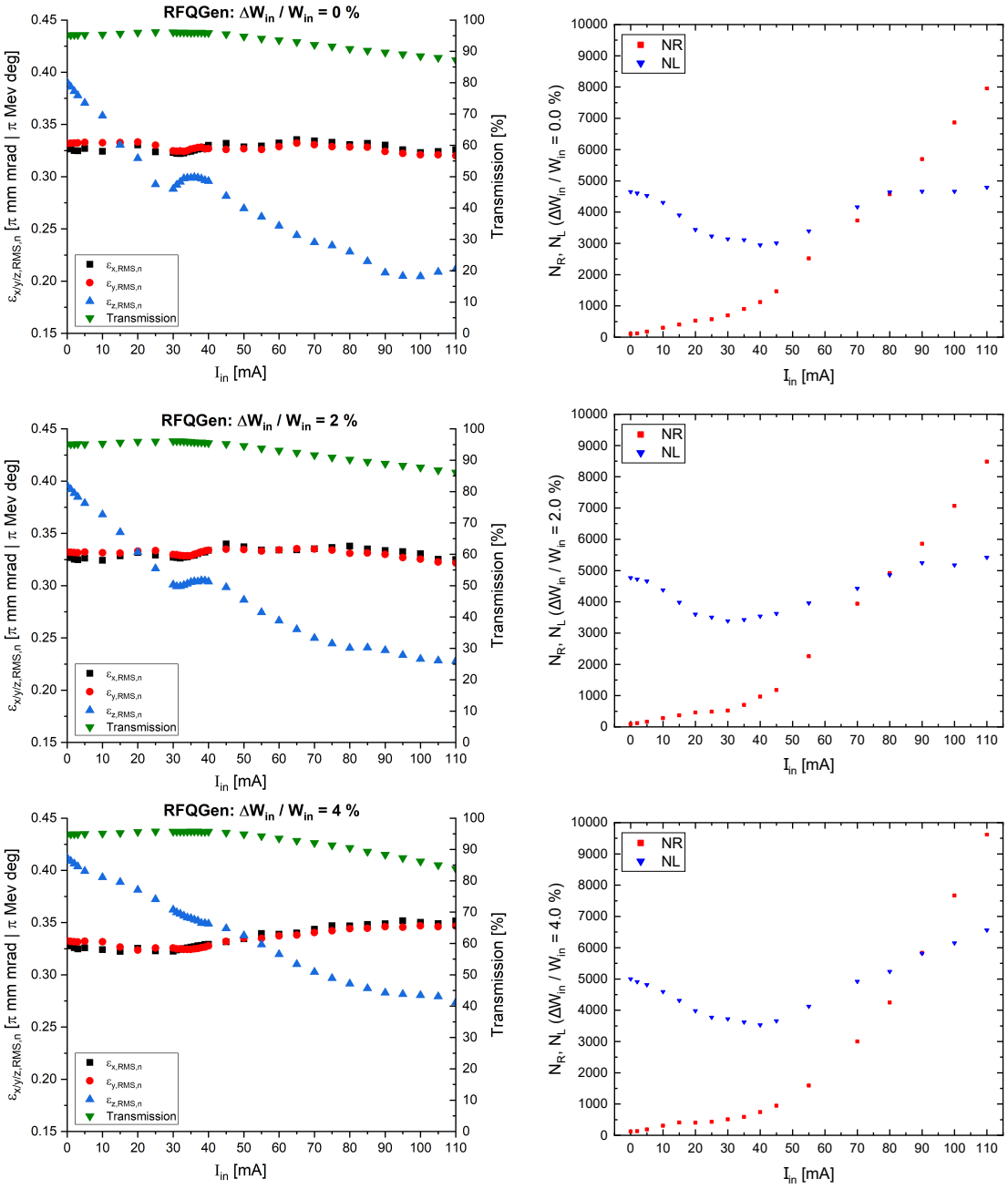

Figure 3.29: **Left:** Beam parameters at the RFQ exit for the RFQGen entrance current studies with different entrance energy spreads of $\Delta W_{in} = \pm 0.00\,\text{keV}$, $\Delta W_{in} = \pm 1.90\,\text{keV}$ and $\Delta W_{in} = \pm 3.80\,\text{keV}$ (from top to bottom).
Right: Total number of radially N_R and longitudinally N_L lost macro-particles along the RFQ in dependence of the entrance current value for the entrance energy spreads of $\Delta W_{in} = \pm 0.00\,\text{keV}$ ($\frac{\Delta W_{in}}{W_{in}} = \pm 0.0\,\%$), $\Delta W_{in} = \pm 1.90\,\text{keV}$ ($\frac{\Delta W_{in}}{W_{in}} = \pm 2.0\,\%$) and $\Delta W_{in} = \pm 3.80\,\text{keV}$ ($\frac{\Delta W_{in}}{W_{in}} = \pm 4.0\,\%$) (from top to bottom).

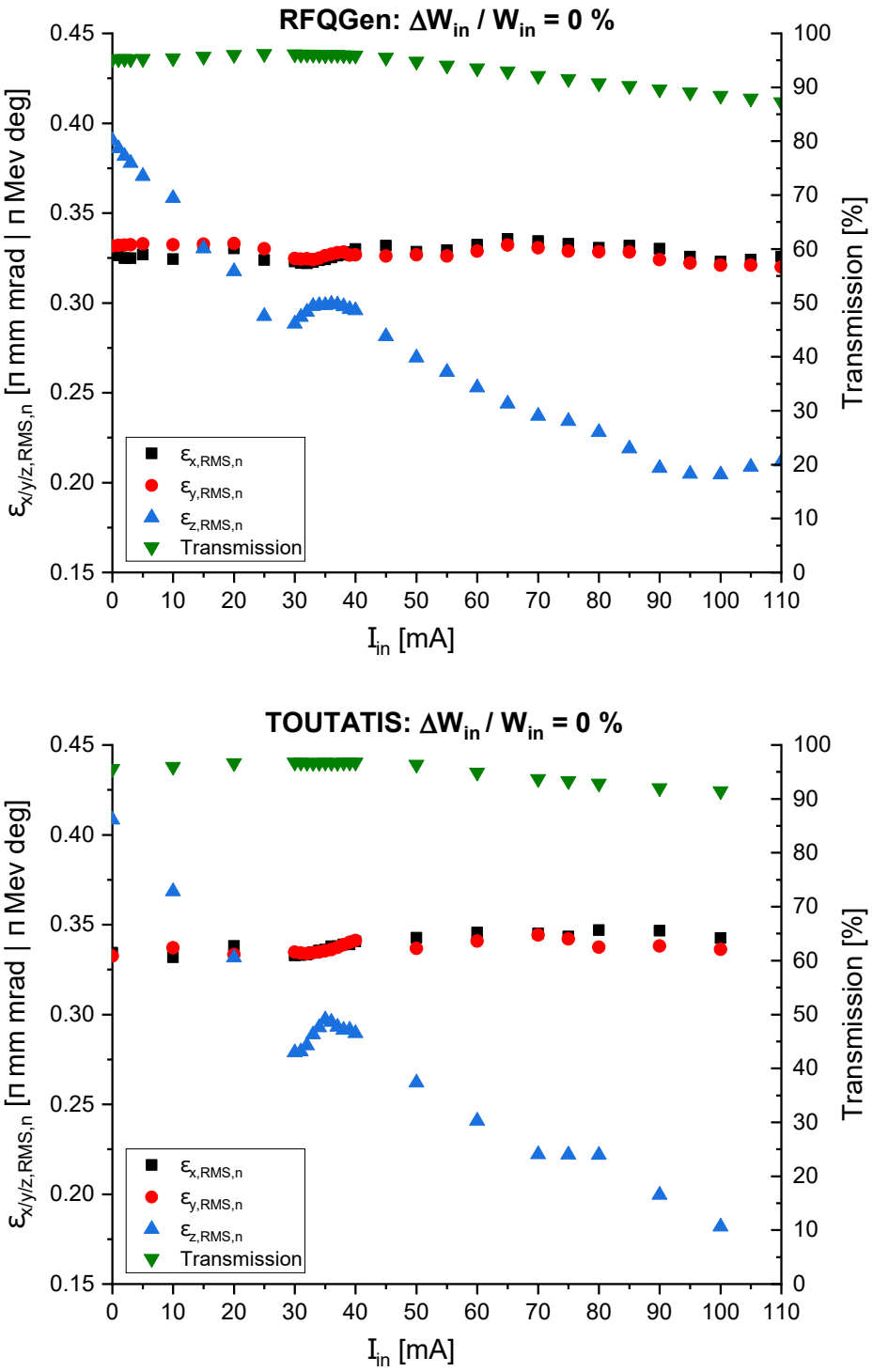

Figure 3.30: Beam parameters at the p-Linac RFQ exit for the RFQGen (top) and TOUTATIS (bottom) current studies with a reasonable energy spread of $\Delta W_{in} = \pm 0.00\,\mathrm{keV}$ at injection.

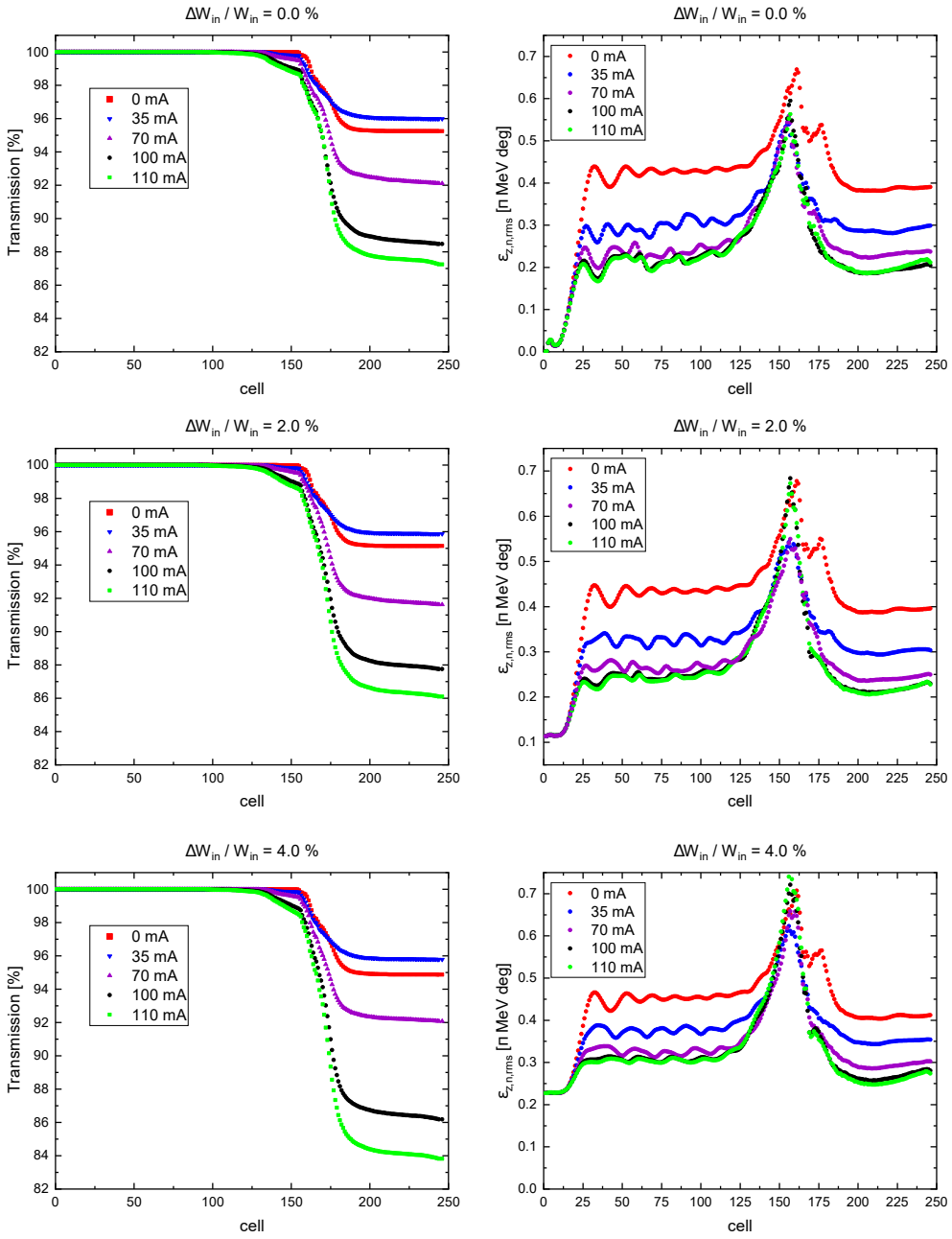

Figure 3.31: Transmissions (left) and the normalized longitudinal rms-emittances (right) along the p-Linac RFQ for selected entrance current values between 0 and 100 mA and different entrance energy spreads of $\Delta W_{in} = \pm 0.00\,\mathrm{keV}$ ($\frac{\Delta W_{in}}{W_{in}} = \pm 0.0\,\%$), $\Delta W_{in} = \pm 1.90\,\mathrm{keV}$ ($\frac{\Delta W_{in}}{W_{in}} = \pm 2.0\,\%$) and $\Delta W_{in} = \pm 3.80\,\mathrm{keV}$ ($\frac{\Delta W_{in}}{W_{in}} = \pm 4.0\,\%$) (from top to bottom). In all three cases, the entrance distributions consisted of 100,000 macro-particles.

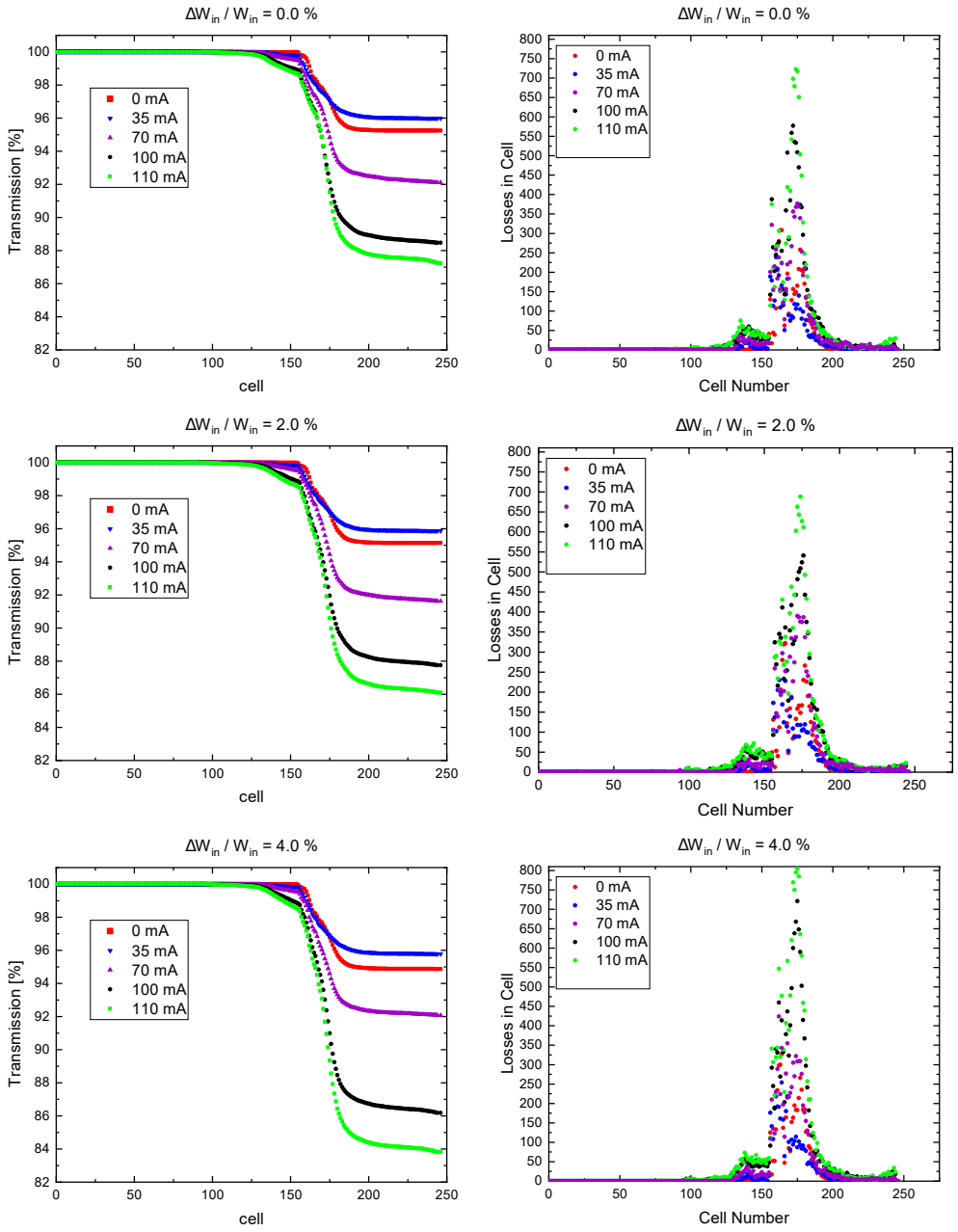

Figure 3.32: Transmissions (left) and the number of loss particles per RFQ cell (right) along the p-Linac RFQ for selected entrance current values between 0 and 100 mA and different entrance energy spreads of $\Delta W_{in} = \pm 0.00\,\mathrm{keV}$ ($\frac{\Delta W_{in}}{W_{in}} = \pm 0.0\,\%$), $\Delta W_{in} = \pm 1.90\,\mathrm{keV}$ ($\frac{\Delta W_{in}}{W_{in}} = \pm 2.0\,\%$) and $\Delta W_{in} = \pm 3.80\,\mathrm{keV}$ ($\frac{\Delta W_{in}}{W_{in}} = \pm 4.0\,\%$) (from top to bottom). In all three cases, the entrance distributions consisted of 100,000 macro-particles.

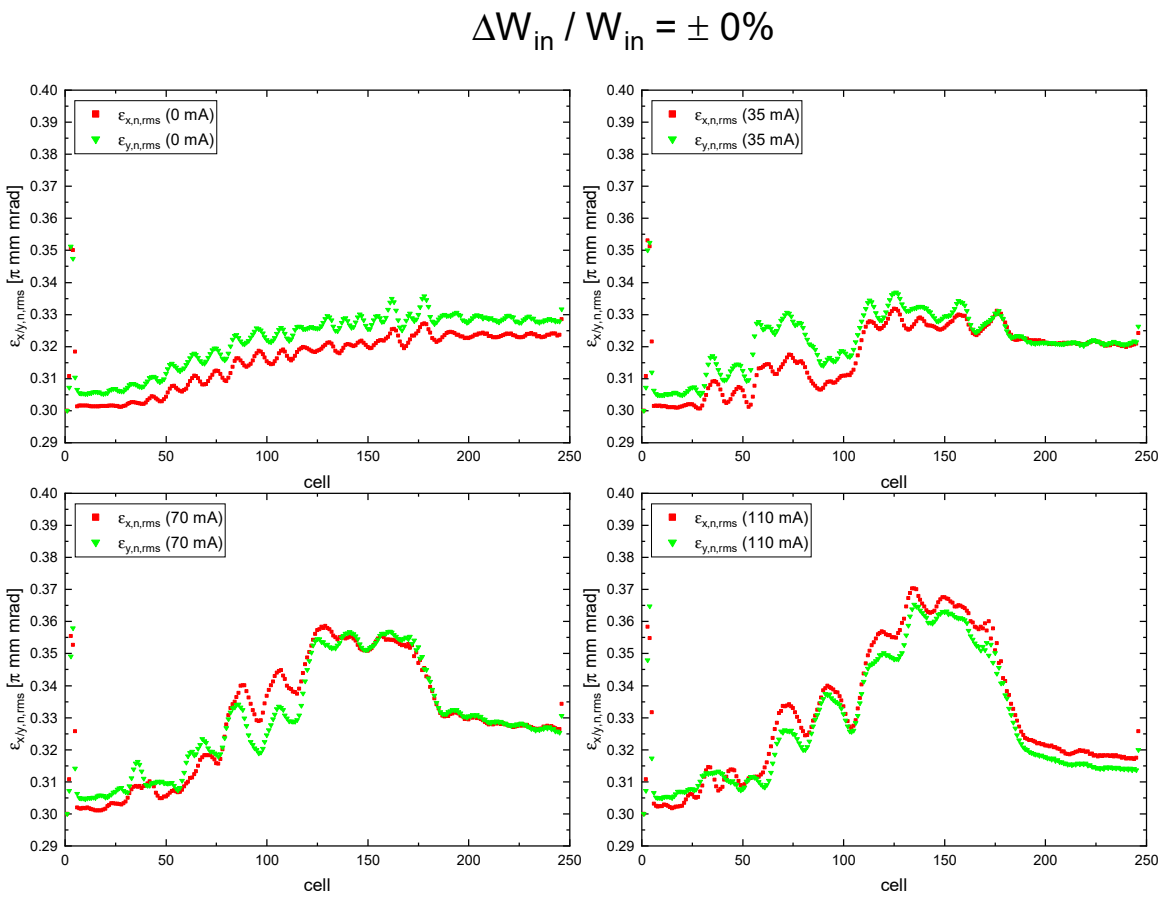

Figure 3.33: Curves of the normalized transversal rms-emittances along the p-Linac RFQ for selected entrance current values between 0 and 100 mA with an entrance energy spread of $\Delta W_{in} = \pm 0.00\,\mathrm{keV}$ ($\frac{\Delta W_{in}}{W_{in}} = \pm 0.0\,\%$).

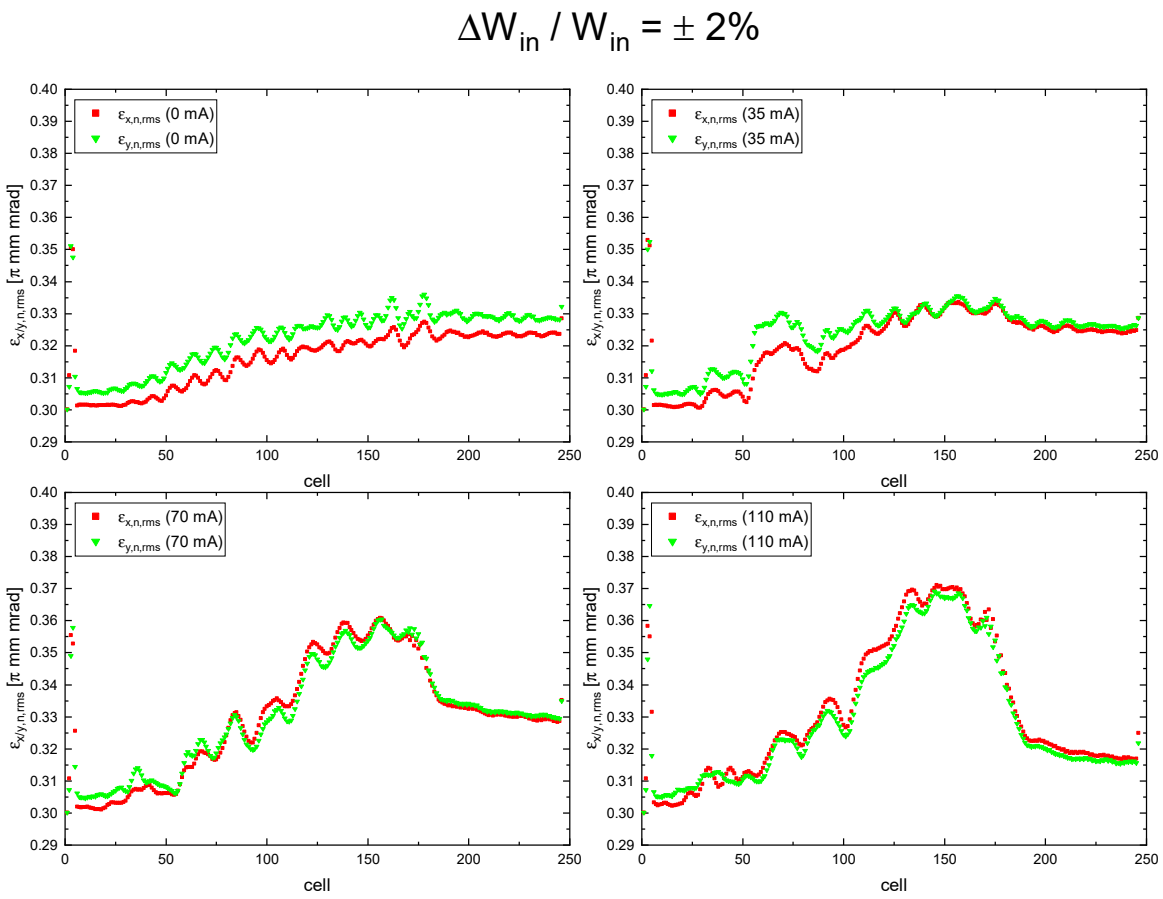

Figure 3.34: Curves of the normalized transversal rms-emittances along the p-Linac RFQ for selected entrance current values between 0 and 100 mA with an entrance energy spread of $\Delta W_{in} = \pm 1.90\,\mathrm{keV}$ ($\frac{\Delta W_{in}}{W_{in}} = \pm 2.0\,\%$).

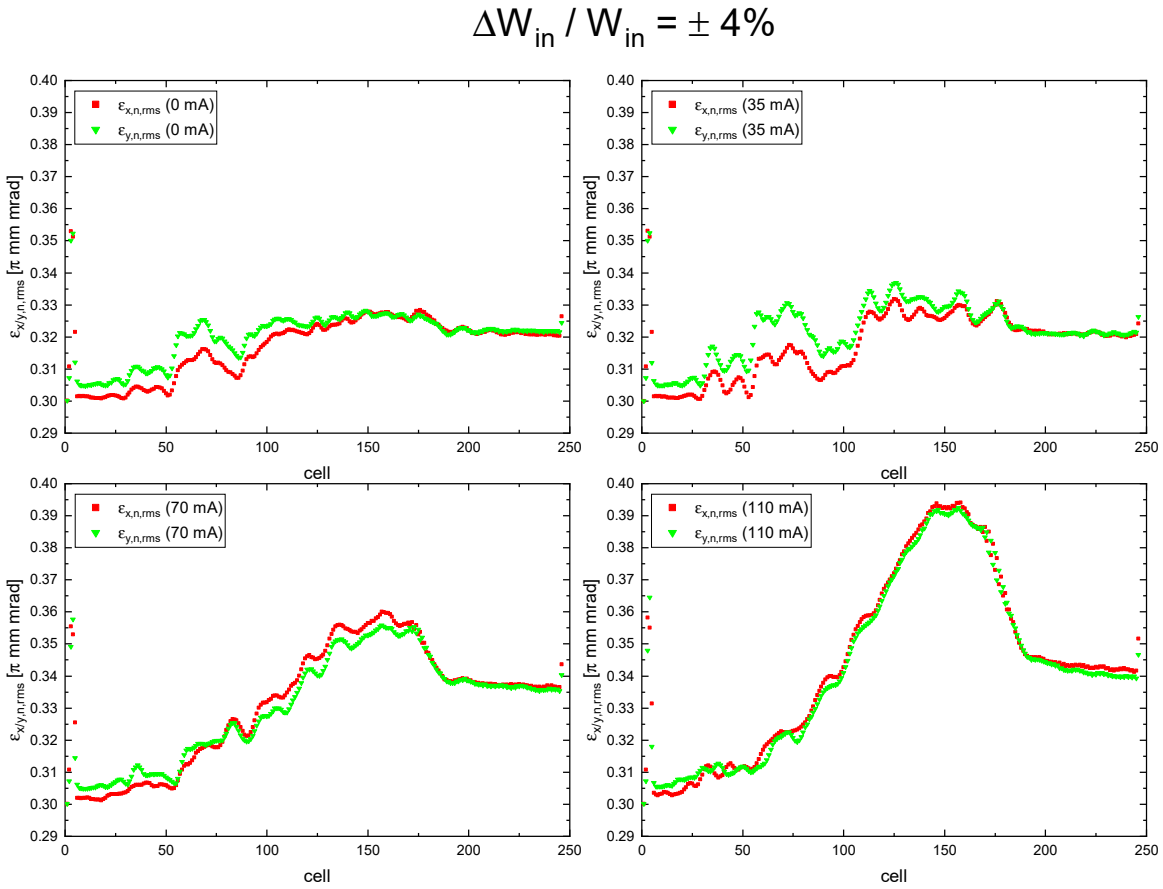

Figure 3.35: Curves of the normalized transversal rms-emittances along the p-Linac RFQ for selected entrance current values between 0 and 100 mA with an entrance energy spread of $\Delta W_{in} = \pm 3.80\,\mathrm{keV}$ ($\frac{\Delta W_{in}}{W_{in}} = \pm 4.0\,\%$).

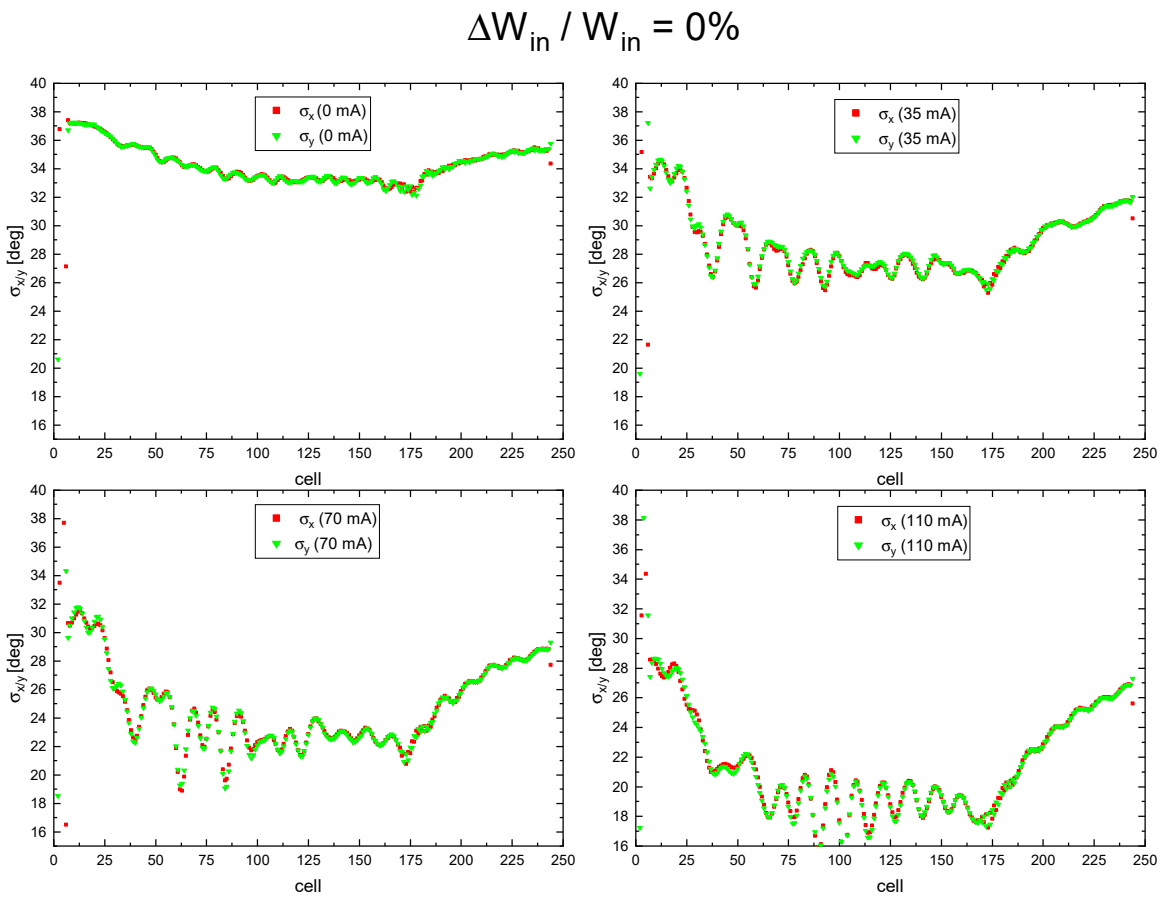

Figure 3.36: Curves of the transversal phase-advances along the p-Linac RFQ for selected entrance current values between 0 and 100 mA with an entrance energy spread of $\Delta W_{in} = \pm 0.00\,\mathrm{keV}$ ($\frac{\Delta W_{in}}{W_{in}} = \pm 0.0\,\%$).

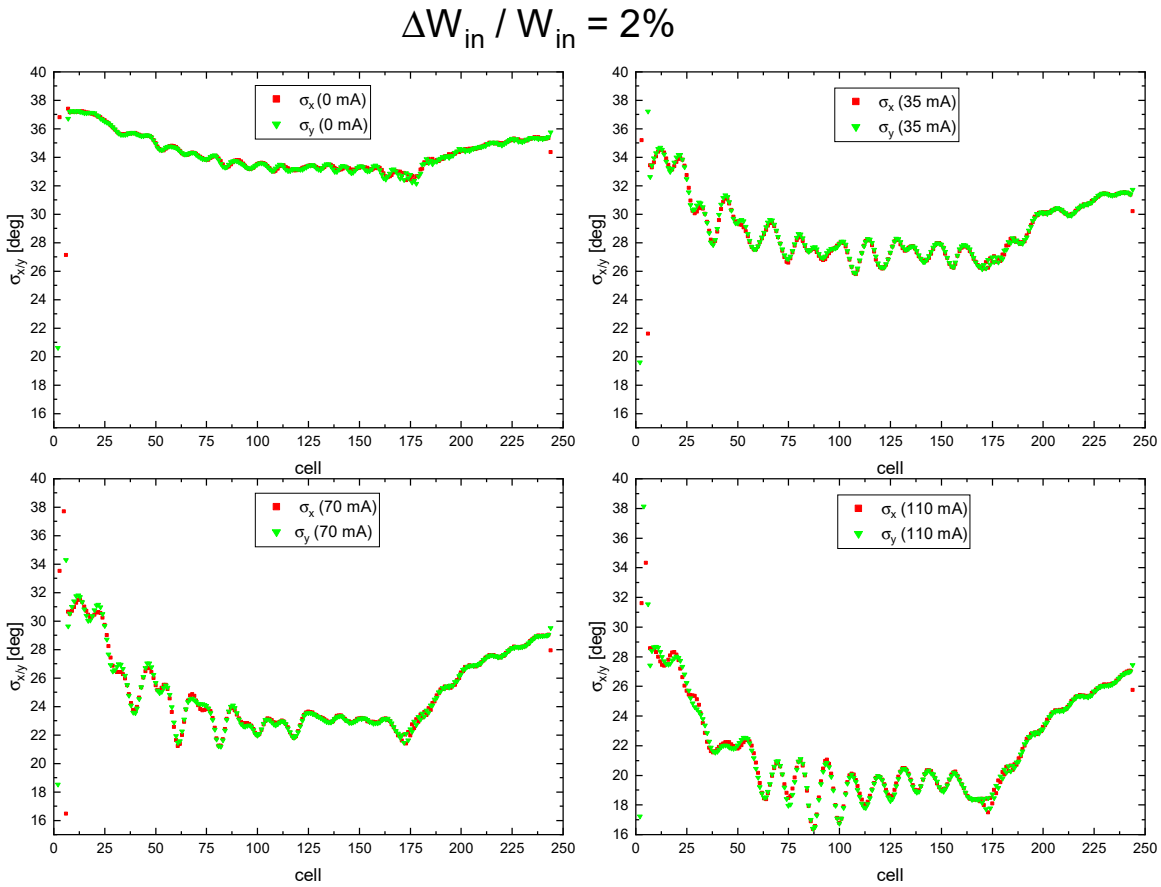

Figure 3.37: Curves of the transversal phase-advances along the RFQ for selected entrance current values between 0 and 100 mA with an entrance energy spread of $\Delta W_{in} = \pm 1.90\,\mathrm{keV}$ ($\frac{\Delta W_{in}}{W_{in}} = \pm 2.0\,\%$).

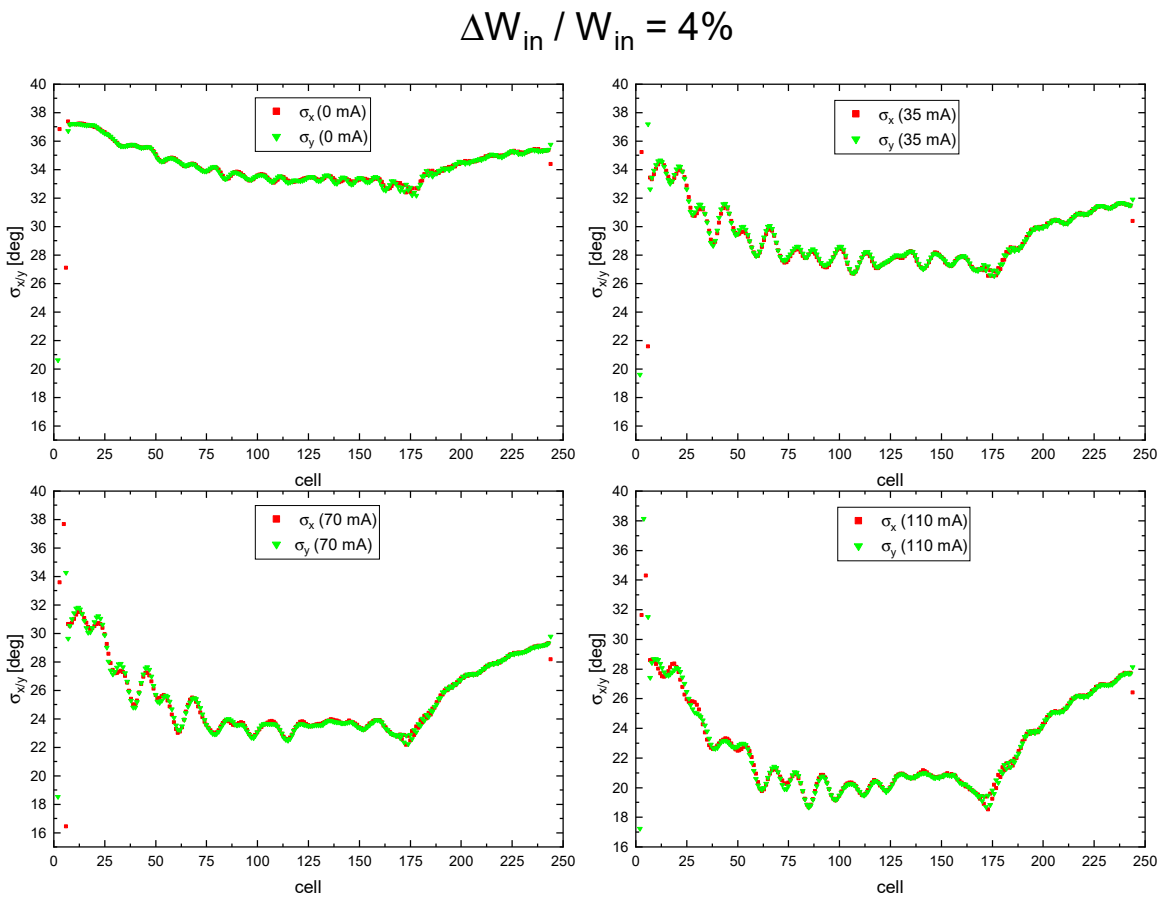

Figure 3.38: Curves of the transversal phase-advances along the RFQ for selected entrance current values between 0 and 100 mA with an entrance energy spread of $\Delta W_{in} = \pm 3.80\,\mathrm{keV}$ ($\frac{\Delta W_{in}}{W_{in}} = \pm 4.0\,\%$).

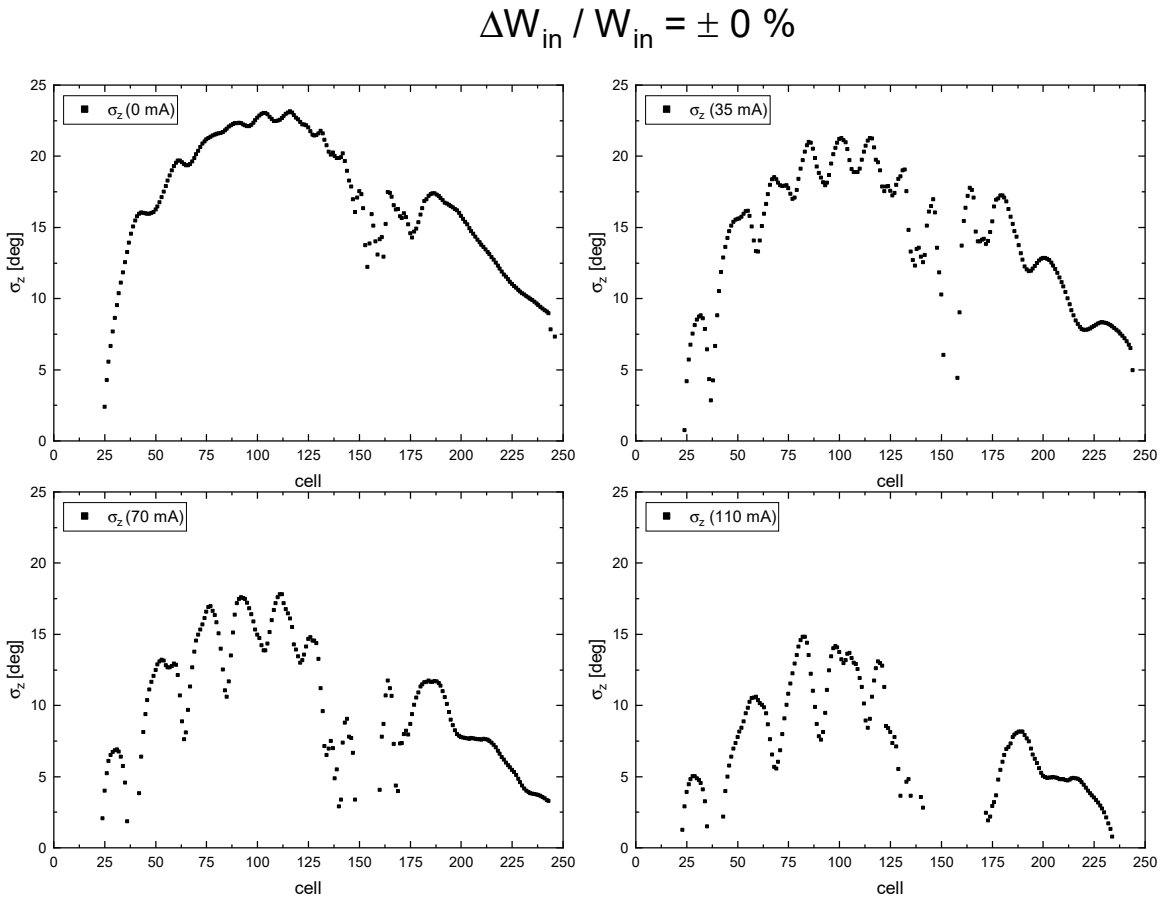

Figure 3.39: Curves of the longitudinal phase-advances along the p-Linac RFQ for selected entrance current values between 0 and 100 mA with an entrance energy spread of $\Delta W_{in} = \pm 0.00\,\mathrm{keV}$ ($\frac{\Delta W_{in}}{W_{in}} = \pm 0.0\,\%$).

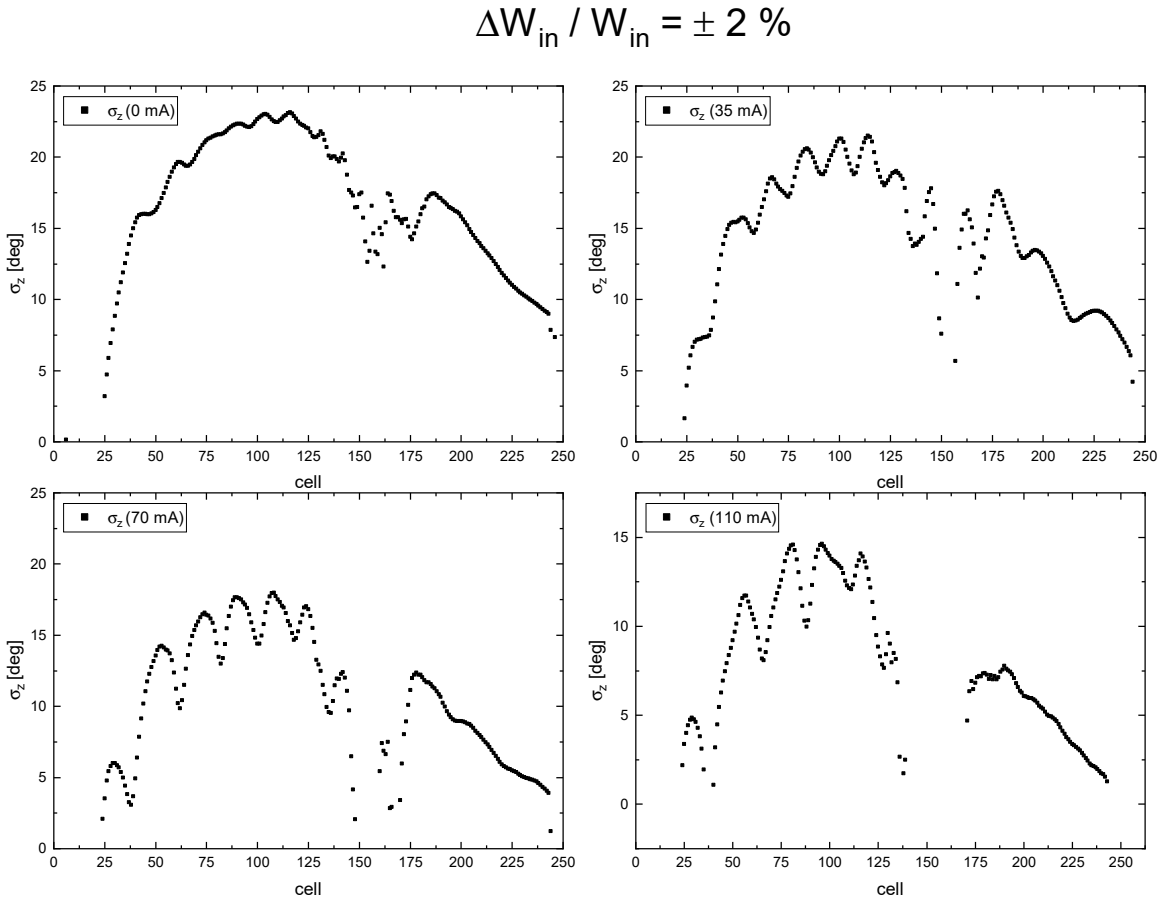

Figure 3.40: Curves of the longitudinal phase-advances along the RFQ for selected entrance current values between 0 and 100 mA with an entrance energy spread of $\Delta W_{in} = \pm 1.90\,\mathrm{keV}$ ($\frac{\Delta W_{in}}{W_{in}} = \pm 2.0\,\%$).

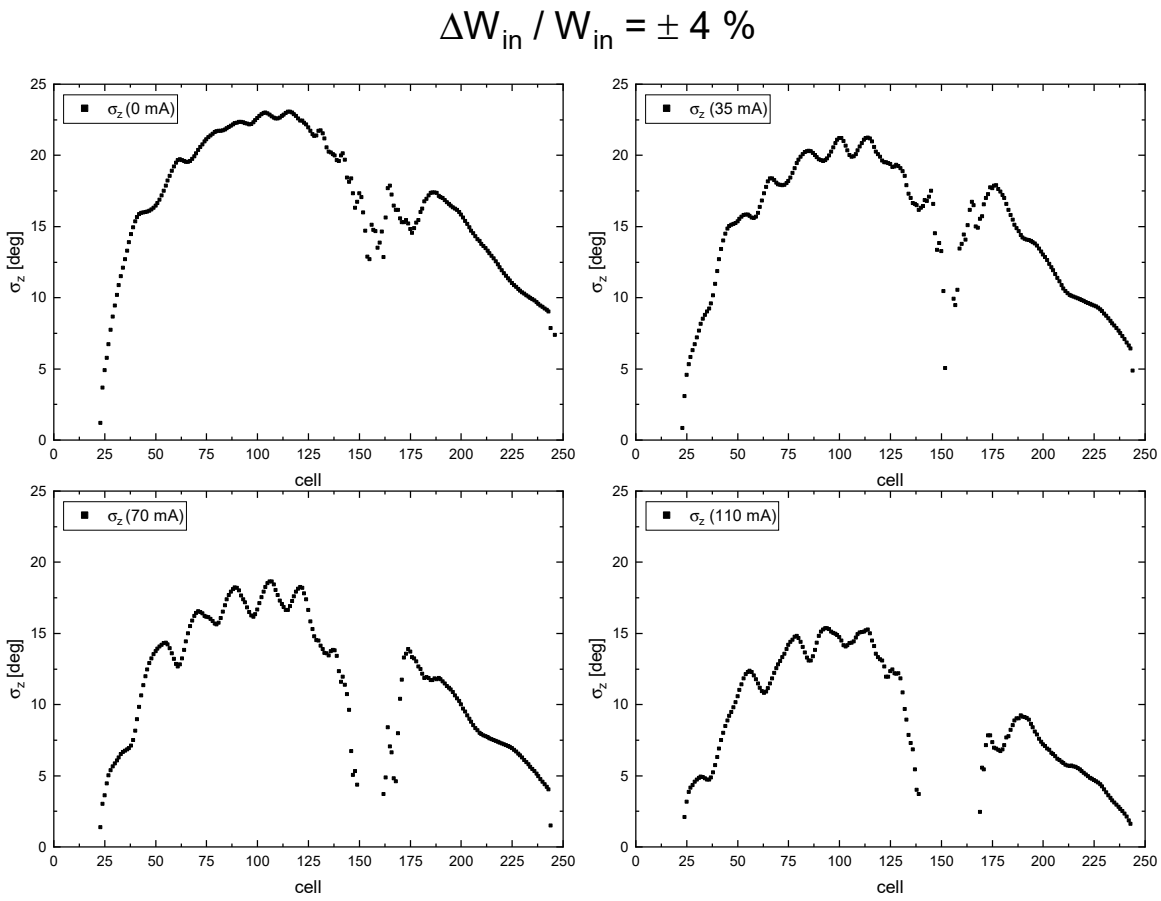

Figure 3.41: Curves of the longitudinal phase-advances along the RFQ for selected entrance current values between 0 and 100 mA with an entrance energy spread of $\Delta W_{in} = \pm 3.80\,\mathrm{keV}$ ($\frac{\Delta W_{in}}{W_{in}} = \pm 4.0\,\%$).

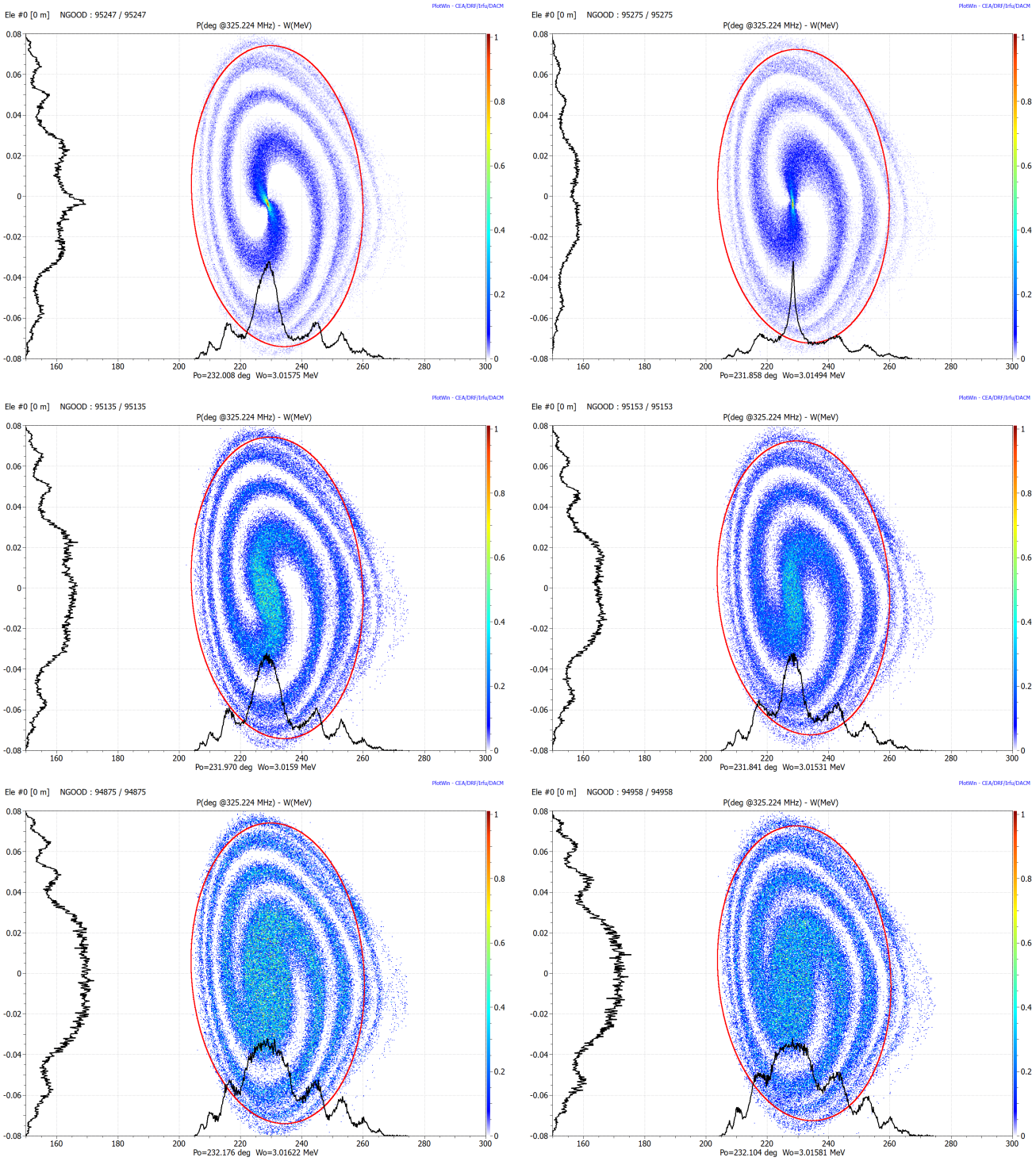

Figure 3.42: Long. phase space plots at the p-Linac RFQ exit in case of an entrance current of 0 mA (left) and 2 mA (right) with entrance energy spreads of $\Delta W_{in} = \pm 0.00$ keV ($\frac{\Delta W_{in}}{W_{in}} = \pm 0.0\,\%$), $\Delta W_{in} = \pm 1.90$ keV ($\frac{\Delta W_{in}}{W_{in}} = \pm 2.0\,\%$) and $\Delta W_{in} = \pm 3.80$ keV ($\frac{\Delta W_{in}}{W_{in}} = \pm 4.0\,\%$) (from top to bottom).

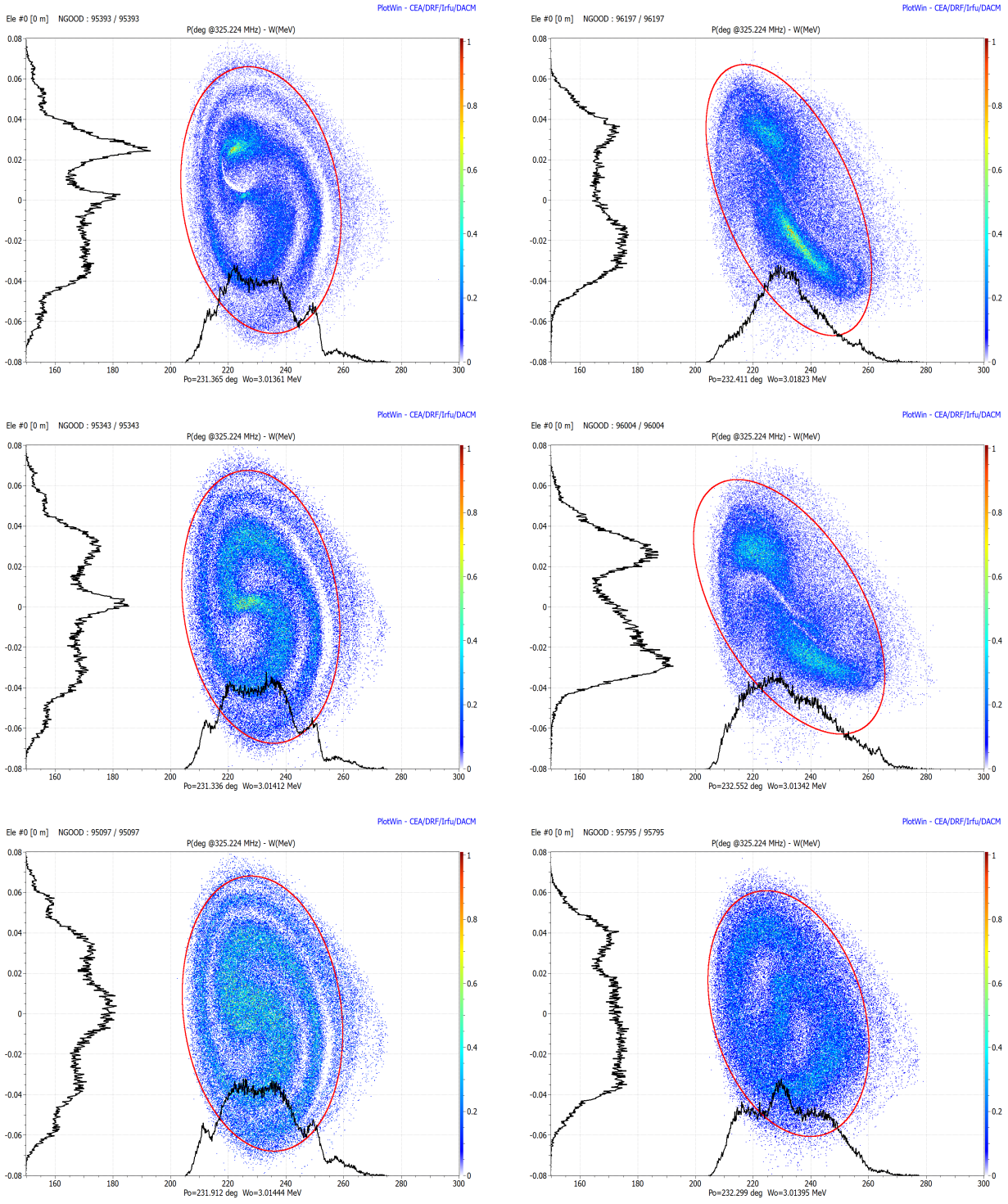

Figure 3.43: Long. phase space plots at the p-Linac RFQ exit in case of an entrance current of 10 mA (left) and 25 mA (right) with entrance energy spreads of $\Delta W_{in} = \pm 0.00$ keV ($\frac{\Delta W_{in}}{W_{in}} = \pm 0.0\,\%$), $\Delta W_{in} = \pm 1.90$ keV ($\frac{\Delta W_{in}}{W_{in}} = \pm 2.0\,\%$) and $\Delta W_{in} = \pm 3.80$ keV ($\frac{\Delta W_{in}}{W_{in}} = \pm 4.0\,\%$) (from top to bottom).

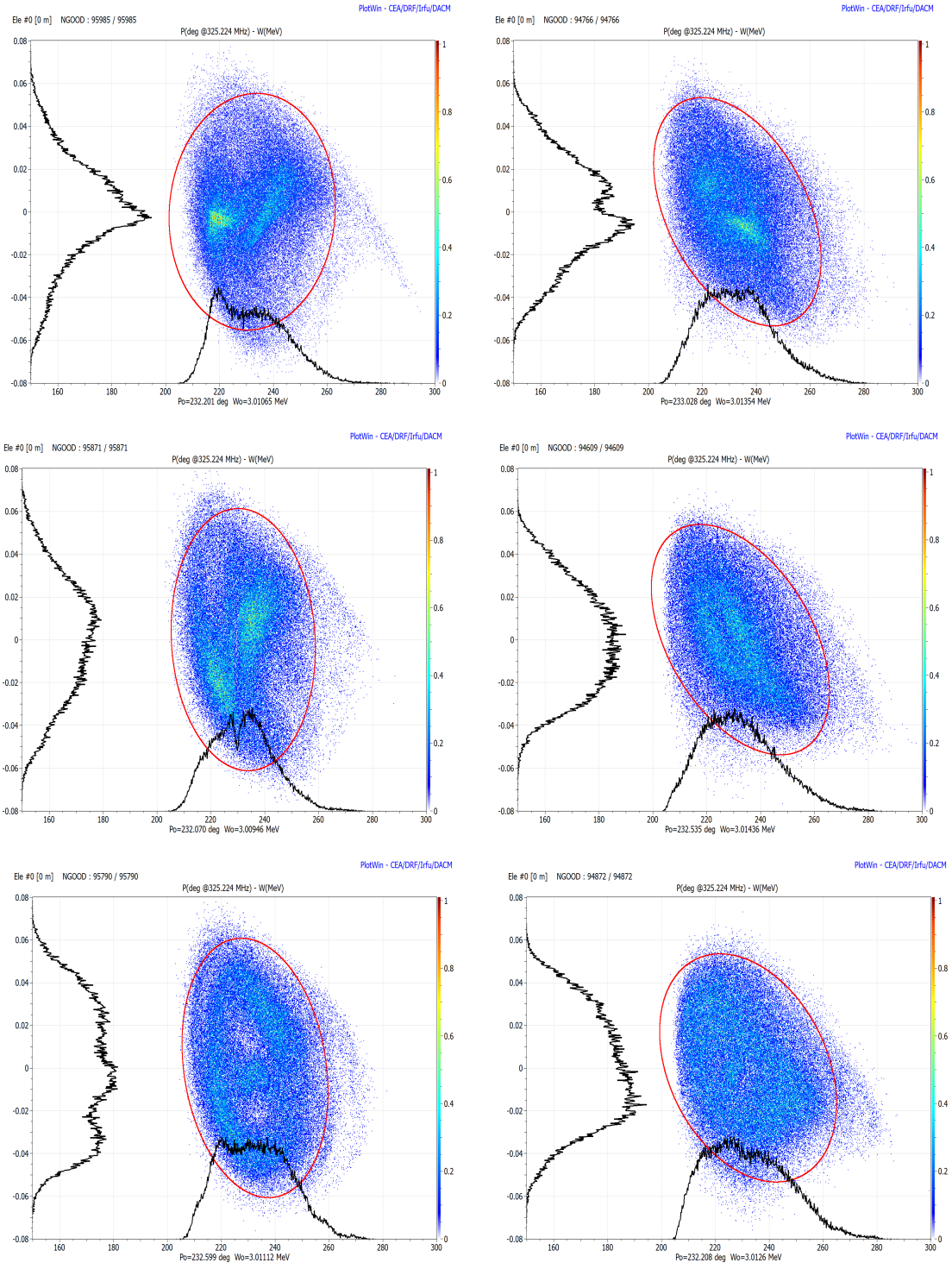

Figure 3.44: Long. phase space plots at the p-Linac RFQ exit in case of an entrance current of 35 mA (left) and 50 mA (right) with entrance energy spreads of $\Delta W_{in} = \pm 0.00\,\mathrm{keV}$ ($\frac{\Delta W_{in}}{W_{in}} = \pm 0.0\,\%$), $\Delta W_{in} = \pm 1.90\,\mathrm{keV}$ ($\frac{\Delta W_{in}}{W_{in}} = \pm 2.0\,\%$) and $\Delta W_{in} = \pm 3.80\,\mathrm{keV}$ ($\frac{\Delta W_{in}}{W_{in}} = \pm 4.0\,\%$) (from top to bottom).

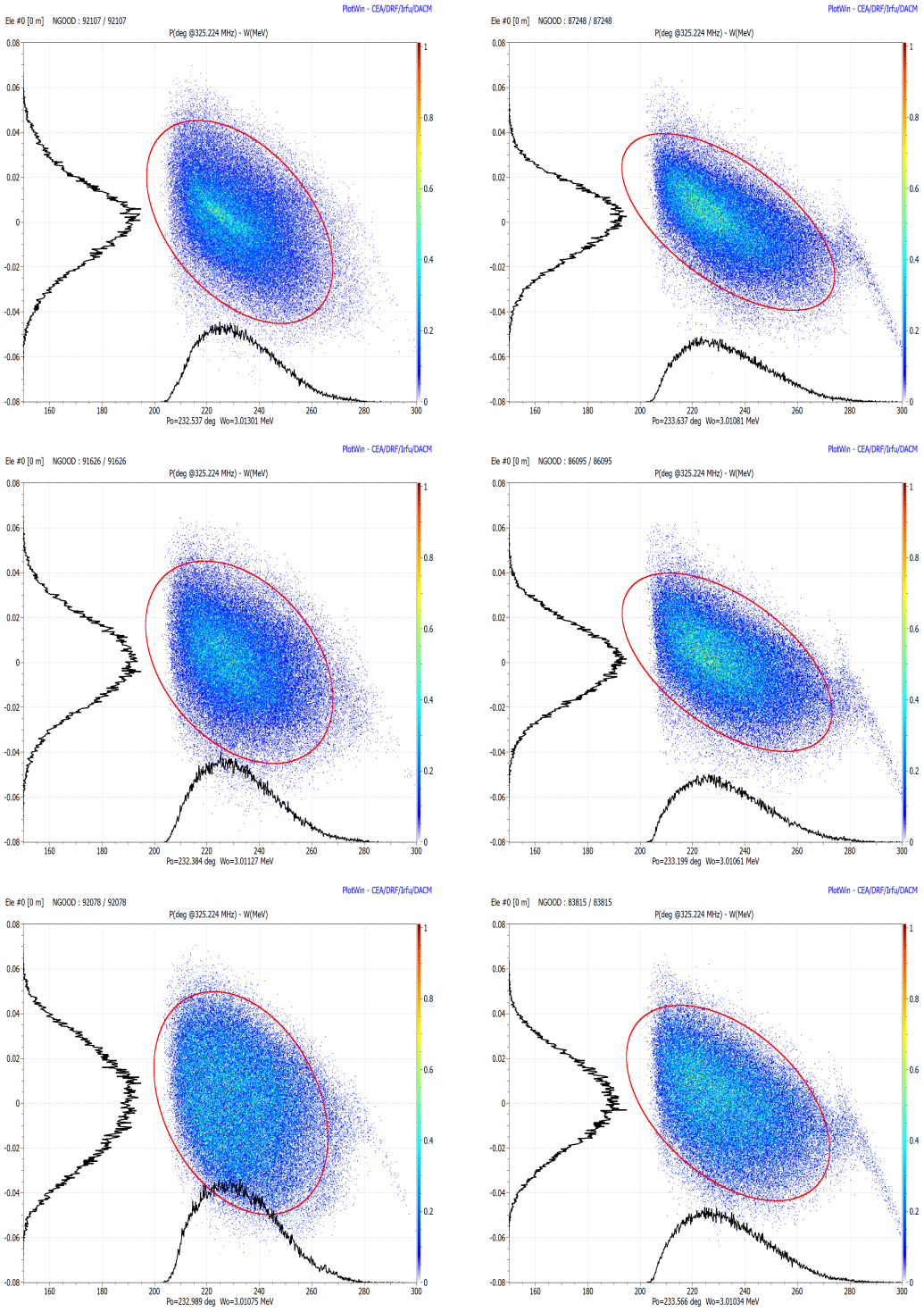

Figure 3.45: Long. phase space plots at the RFQ exit in case of an entrance current of 70 mA (left) and 110 mA (right) with entrance energy spreads of $\Delta W_{in} = \pm 0.00\,\mathrm{keV}$ ($\frac{\Delta W_{in}}{W_{in}} = \pm 0.0\,\%$), $\Delta W_{in} = \pm 1.90\,\mathrm{keV}$ ($\frac{\Delta W_{in}}{W_{in}} = \pm 2.0\,\%$) and $\Delta W_{in} = \pm 3.80\,\mathrm{keV}$ ($\frac{\Delta W_{in}}{W_{in}} = \pm 4.0\,\%$) (from top to bottom).

3.9 Effects of the Voltage Inhomogeneity on the Beam Dynamics

RFQ beam dynamics simulations usually assume a constant electrode voltage along the beam axis. For the FAIR p-Linac RFQ this requirement would be (sufficiently) met, if every RF-cell of its ladder structure were tuned to the same eigenfrequency, which is determined by the RF-cell's inductance and capacitance. These parameters are in turn specified by the geometric dimensions of each individual RF-cell. If they differed even slightly for a given cell, this cell's eigenfrequency and eigenmode would deviate from those of the overall RFQ. This would result in a local deviation of the voltage distribution. Due to imperfections in production as well as in the underlying CST Studio Suite[26] simulations, the actually manufactured RFQ varies from a perfect, symmetrical RFQ. Thus, the voltage distribution is not completely homogeneous or "flat" along the beam axis.

Furthermore, the first and last RF-cell are technically RF-"half" cells and originally would exhibit only half the inductance of inner RF-cells (cf. Fig. 4.8 (page 53) and Sec. 5.3 (pages 66-67) of Ref. [3]). Their eigen-frequencies are raised and so are the electrode voltages at these positions. The capacitance of the electrodes in the end cells varies in dependence of their "end-lengths", i.e. the electrode surplus before/after the first/last ring. Since adjusting the height of a specific ladder cell changes the length of the current path, its inductance can be corrected to match the desired frequency and voltage difference of the respective cell. (A thorough elaboration on the FAIR Proton-Linac RFQ's field-flatness as well as the associated CST MWS-Simulations and RF-tuning can be found in Ref. [3].)

In April 2019, the final machining step regarding the p-Linac RFQ's flatness and frequency was performed, which was followed by corresponding measurements [5]. Figure 3.46 shows the inhomogeneous distribution of the electric field along the RFQ before (red curve) and after tuning (black curve). Unfortunately, RFQGen does not offer to adjust the rather complex actually present voltage distribution along the RFQ for its beam dynamics simulations. However, RFQGen is able to assume simpler voltage distributions along the RFQ, so that one does not have to reside to simulating with a constant voltage along the RFQ equal to the design voltage (default). For this purpose two parameters exist. Although only the first one, i.e. v_{fac}, is of relevance for the voltage studies presented in this thesis, they are both introduced for the sake of completeness:

[26] https://www.3ds.com/products-services/simulia/products/cst-studio-suite/?utm_source=cst.com&utm_medium=301&utm_campaign=cst)

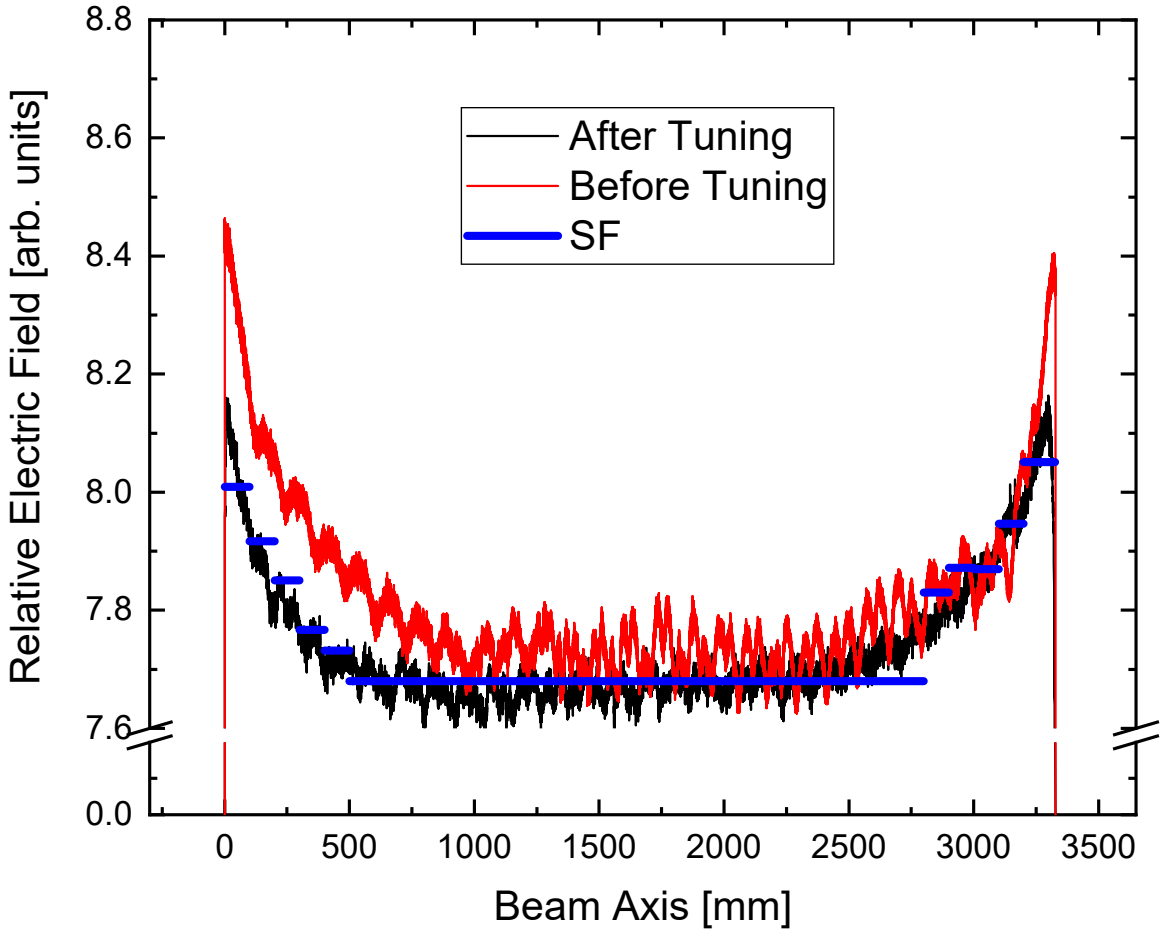

Figure 3.46: Field flatness along the RFQ before (red) and after tuning (black) (courtesy of M. Schuett; cf. Fig. 4 in Ref. [4]). The blue curve shows the average values in the respective intervals (step function). The only exception is the long middle interval: the field plotted here results directly from the design electrode voltage of 88.43 keV.

- v_{fac}: The v_{fac}-parameter specifies a multiplicative voltage factor for the electrode voltage; it is the quotient of the voltage used for the beam dynamics simulations and the design voltage[27]: $v_{fac} = \frac{V_{BD}}{V_{des}}$.
- tilt: the tilt-parameter t specifies an end-to-end slope for the electrode voltage. t is the percentage by which the voltage gets tilted. For example, $t = 10.0$ means that the voltage

[27] Among others, this parameter has further been proven especially useful to determine the minimum voltage required for a transmission greater than 0% and for establishing calibration curves for commissioning. Furthermore, it can be used for simulating the dynamics of different charge-stage ions present in the beam. Depending on the actual RFQ design, transmission might actually even increase by raising the applied voltage compared to the design voltage. If a sufficient RF power is provided and arcing can be avoided transmission might increase up to 10% (correspondence with L. M. Young).

at the RFQ entrance is 10 % lower than the design voltage and the voltage at the RFQ exit is 10% above the design voltage.

In order to approach the actual field distribution present in the tuned RFQ, the RFQGen model of the p-Linac-RFQ was segmented into 11 length intervals, whereby each interval had been assigned its average field value according to the tuned field distribution (cf. black curve in Fig. 3.46); they deviate up to almost 10.5 % from the actual electrode field. These average fields were converted to voltages as RFQGen requires this quantity instead of field values. Linearity between field- and voltage-values was assumed: i.e. $\frac{E_{int}}{E_{des}} = \frac{V_{int}}{V_{des}}$. Via $v_{fac} = \frac{V_{int}}{V_{des}}$ each interval then got assigned its specific v_{fac}-value (see Tab. 3.17).

The only exception to this scheme was the 6-th interval, which is furthermore an exception with regard to its length of 150 cm, i.e. slightly more than $\frac{2}{3}$ of the overall RFQ length. Not least in order to arrive at a maximum error estimate $V_{int=6}$ was set $V_{des} = 88.43\,kV$, whereby the actual average voltage value of this interval is slightly lower. This thus led to the average voltage

$$V_{ave} = \sum_{i=1}^{11} \frac{V_i\, l_i}{L_{RFQ}} = 89.18\,keV \tag{3.3}$$

slightly, i.e. by 0.84%, exceeding the design voltage $V_{des} = 88.43$ kV (cf. Tab. 3.18). (V_i and l_i are the interval voltages and lengths; respectively, and L_{RFQ} is the RFQ length.)

Most of the other intervals are instead approx. 10 cm long. Intervals 10 (ca. 7 cm) and 11 (ca. 16 cm) also stand out in terms of their lengths. The exit distribution behind the first interval was used as entrance distribution for the second interval and so forth, whereby the values of the start- and stop-cells as well as v_{fac}-entries were adjusted accordingly between simulations in the RFQGen-input file.

Int. number	Start of int. [mm] (cell number)	Re-scaled voltage [kV] (Perce. gain to nom. value [%])	v_{fac}
1	0 (0)	92.21 (4.27)	1.0427
2	100 (16)	91.16 (3.08)	1.0308
3	200 (31)	90.40 (2.23)	1.0223
4	300 (46)	89.43 (1.13)	1.0113
5	400 (61)	89.03 (0.68)	1.0068
6	500 (76)	88.43 (0.00)	1.0000
7	2800 (231)	90.16 (1.95)	1.0195
8	2900 (234)	90.64 (2.50)	1.0250
9	3000 (237)	90.61 (2.46)	1.0246
10	3100 (240)	91.50 (3.47)	1.0347
11	3200 (242)	92.70 (4.83)	1.0483

Table 3.17: Re-scaled electrode voltage of the defined intervals. The 4-th column shows the ratios of the re-scaled voltages to the design electrode voltage of 88.43 kV, i.e. the v_{fac}-values for each interval.

To further test the beam dynamics designs tolerance of electrode-voltage deviations the actual percentage deviations ranging from 0.0% to 4.8% were multiplied by several factors $f = (V_{int,f} - V_{des}) \setminus V_{int,f=1} - V_{des}$ between 1 and 10. $V_{int,f=1} - V_{des}$ is the difference between the respective average interval voltage based on the measured field distribution, i.e. in case of $f = 1$ (cf. Fig. 3.46), and the design voltage $V_{des} = 88.43\,kV$. Table 3.17 lists the interval numbers and the z-coordinates of their end-points as well as the number of the cells that mark the interval ends. Furthermore, the re-scaled interval voltages and their multiples as well as their percentage deviations from the design electrode voltage are shown. The same settings were used for these simulations as for the 100 mA entrance current matched case. Only the number of entrance macro-particles was adjusted from 100, 000 to 10, 000. This reduction was useful as these simulation series could not easily be automated by e.g. a python work-around. Instead, due to the many successive simulation runs a lot of manual adjustments and input were required. The reduction in input macro-particles cuts simulation duration significantly and thus benefits the work flow without limiting the validity of the voltage study. For all 11 intervals, the transmissions did not deviate more than 0.05% between the simulations with 10^4 and 10^5 entrance macro-particles for the homogeneous voltage/field-distribution cases (the $f = 0$-cases). Table 3.19 shows the transmissions, normalized rms-emittances and average energies at the RFQ exit for $f = 0, 1, 2, 3, 5, 7.5$ and 10, whereby the 2nd and 3rd columns

refer to both $f = 0$-cases. Whereas a factor of 2 could still fall within a pessimistic error estimation, the higher values of f are investigated only to study the (hypothetical) effects of the voltage on the beam dynamics. Scenarios with $f > 2$ are not realistic as – among others – field breakdown would occur (cf. Appx. C): in case of $f = 10$ the average voltage amounts to 108.42% ($V_{ave,f=10} = 95.88\,kV$; see Tab. 3.18) and the peak voltage to over 148% of the design voltage ($V_{int=11,f=10} = 131.16\,kV$; see Fig. 3.47).

Figure 3.48 shows the curves of the transmission and the normalized longitudinal rms-emittance for the different f-values. The deviations between the interval transmissions for the homogeneous voltage distribution case (10,000 macro-particles) and the cases $f \leq 5$ do not exceed 1.23%. For $f = 7.5$, the maximum deviation rises to 3.41% and for $f = 10$ to 5.36%. For $f \leq 7.5$ the transmission is still 100% up to the end of interval 5, but for $f = 10$ it has already dropped to 99.90%. For $f = 7.5$ and even more so for $f = 10$ the sharp drop in transmission due to cutting off longitudinal outliers (see next paragraph) is stronger causing significantly reduced RFQ exit transmissions: $T_{f=5} = 87.29\% < T_{f=7.5} = 85.11\% < T_{f=10} = 83.16\%$ (see Tab. 3.19).

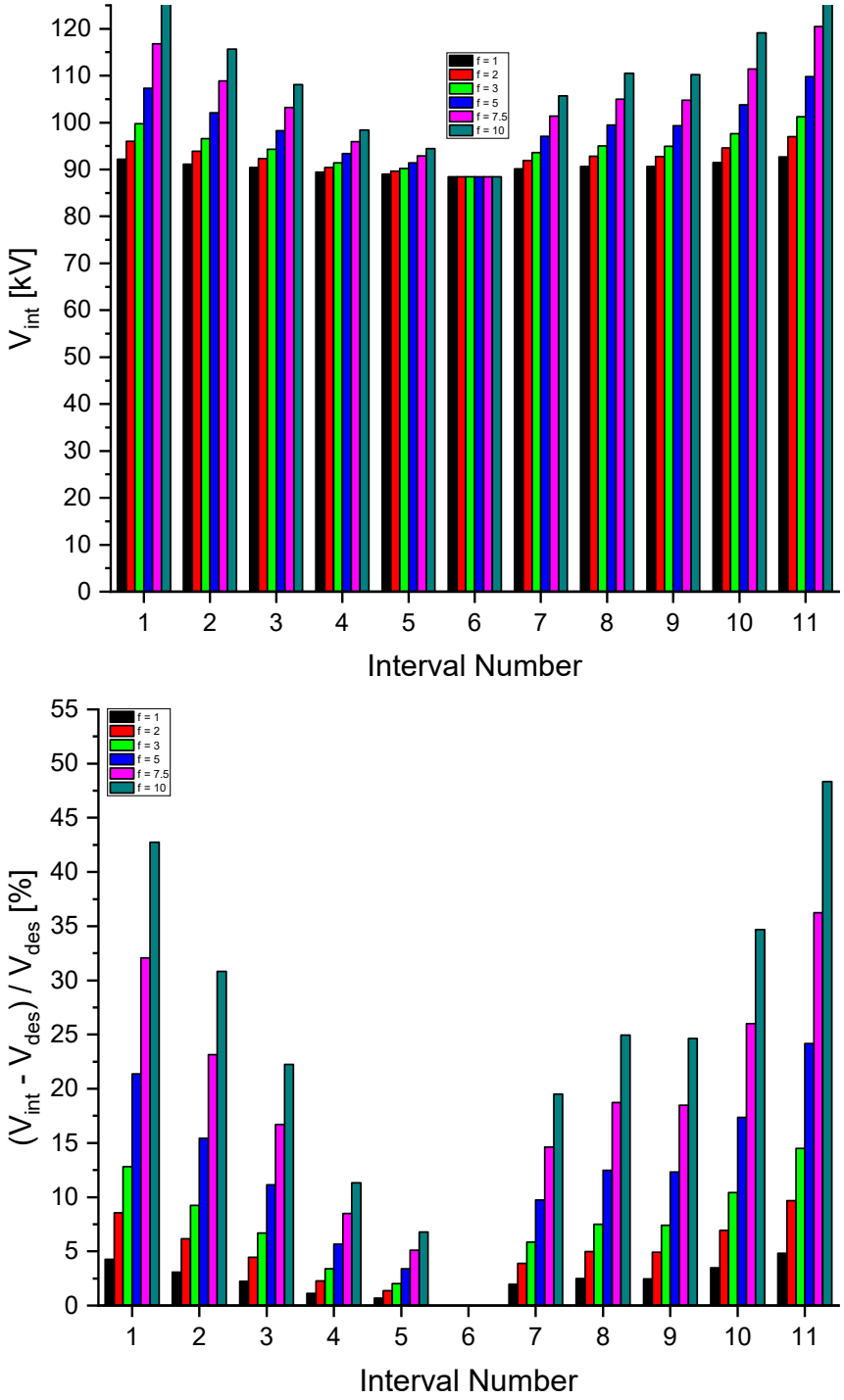

Figure 3.47: **Top:** All eleven interval voltages for different f-values.
Bottom: Relative difference $(V_{int,f} - V_{des}) / V_{des}$ between each interval voltage $V_{int,f}$ and the design voltage $V_{des} = 88.43\,kV$ for different f-values.

The longitudinal emittances exhibit a behavior expected from previous simulations (cf. Fig. 3.13 in Sec. 3.5), i.e. the characteristic co-evolution of this emittance and the transmission described in Sec. 3.5 is preserved. Like for the transmission, the curves run very similarly and even exhibit their peaks (main and minor) at the same positions. However, they also show certain idiosyncrasies that grow with f. For $f \leq 5$ the curves only exhibit minor deviations; even the maximum values only exceed that of the homogenous field case by $< 5\%$. For f = 7.5 and f = 10 more pronounced deviations arise from around cell 25 on. The maximum emittance exceeds the one of the homogeneous field distribution case by 28% for f = 7.5 and 45% for f = 10. This makes sense as the longitudinal emittance is most sensitive to voltage changes during beam shaping and bunching. At the falling edge of the main peak their curves run closer to the other curves again, but exhibit a slight rise at ca. cell 225 and onwards. Whereas this tendency also exists for the other cases with $f \neq 0$, it is much more pronounced due to longitudinal over-focusing in the acceleration section as a result of the much higher voltages.

f	V_{ave} [keV]	$V_{ave} \setminus V_{des}$ [%]
1	89.18	100.84%
2	89.92	101.69%
3	90.66	102.53
5	92.16	104.21
7.5	94.02	106.32
10	95.88	108.42

Table 3.18: Average voltages for different values of $f = (V_{int,f} - V_{des}) / (V_{int,f=1} - V_{des})$ with $V_{int,f=1} - V_{des}$ being the difference between the respective average interval voltage based on the measured field distribution, i.e. in case of $f = 1$ (cf. Fig. 3.46), and the design voltage $V_{des} = 88.43\,kV$. Note $V_{des} > 88.43\,kV$ for all values of f as the voltage value for the longest interval $V_{int=6,f}$ was set $V_{des} = 88.43\,kV$ for all values of f. This was also done to arrive at a maximum error estimate.

The transversal emittances depicted in Fig. 3.49 exhibit peaks mostly at the same positions for all f-values and their general evolutions remain roughly identical to that of the homogeneous field case ($f = 0$). However, deviations even for f-values as low as 2 are in some instances much larger than for the longitudinal emittances. Especially for $f = 7.5$ and $f = 10$, the peaks are amplified and even some of their positions shifted considerably. As the particle density gets modulated with z during beam shaping and bunching, lower space-charge forces are excreted on the lower charged sections of the beam. Hence, the transversal emittances within these beam sections are highly sensitive to changes in voltage/the electric field. Within the fringe-field region both

emittances experience a high jump for the two highest f-values. In case of the homogeneous field distribution ($f = 0$) this jump also occurs, albeit to a much lower extend. In case of $f = 7.5$, the x-emittance increases by 2.0% and the y-emittance by 8.7% compared to the homogeneous field case. For $f = 10$, these values are 9.8% (x-emittance) and 16.6% (y-emittance). However, for $f \leq 5$ the transversal exit emittances only differ by -4% (x-emittance) and -2% (y-emittance) from these of the homogeneous field case (see also Tab. 3.19); i.e. for $f = 1$, 2, 3 and 5 these exit emittances slightly decrease. This occurs also because their curves fall deeper after the main peak in the homogeneous field case. However, the main reason is that the emittances either do not jump sufficiently high or even drop slightly within the fringe field region.

From Fig. 3.20 it can be deduced that – perhaps counter-intuitively at first – the average particle energy rises only marginally with f despite V_{ave} increasing more significantly with f (cf. Tab.3.18). However, this linear, but weak growth is in accordance to the fact that only particles with sufficient synchronicity with the RF bucket contribute to W_{ave}. The geometric bucket length Z_Ψ is independent of the applied voltage: $Z_\Psi = \frac{\Psi \beta_s \lambda}{2\pi}$ with the bucket phase width Ψ only depending on ϕ_s (see Chap. A).

These simulation studies revealed that the FAIR p-Linac RFQ should be able to perform under the expected field inhomogeneity without the beam parameters behaving in a problematic fashion. Much larger inhomogeneities would be necessary to noticeably effect the performance. Furthermore, their influence over it might not always be detrimental, but could even lead to improvements for certain parameters.

Parameters at RFQ Exit	Hom. Vol. Dist. Sim. 1	Hom. Vol. Dist. Sim. 2	$f = 1$	$f = 2$	$f = 3$	$f = 5$	$f = 7.5$	$f = 10$
Transmission [%]	88.47 %	88.52%	88.50%	88.17%	88.07	87.29%	85.11	83.16%
$\varepsilon_{x,out,rms}$ $[\pi\, mm\, mrad]$	0.3230	0.3267	0.3169	0.3169	0.3136	0.3188	0.3333	0.3588
$\varepsilon_{y,out,rms}$ $[\pi\, mm\, mrad]$	0.3210	0.3193	0.3161	0.3132	0.3193	0.3190	0.3470	0.3722
$\varepsilon_{z,out,rms}$ $[\pi\, MeVdeg]$	0.20457	0.20290	0.21346	0.21598	0.21705	0.22576	0.24644	0.2602
$W_{ave}\,[MeV]$	3.012	3.012	3.025	3.036	3.046	3.068	3.092	3.117

Table 3.19: Transmissions, emittances and average energies at the p-Linac RFQ exit for selected values of $f = (V_{int,f} - V_{des}) \,/\, (V_{int,f=1} - V_{des})$.

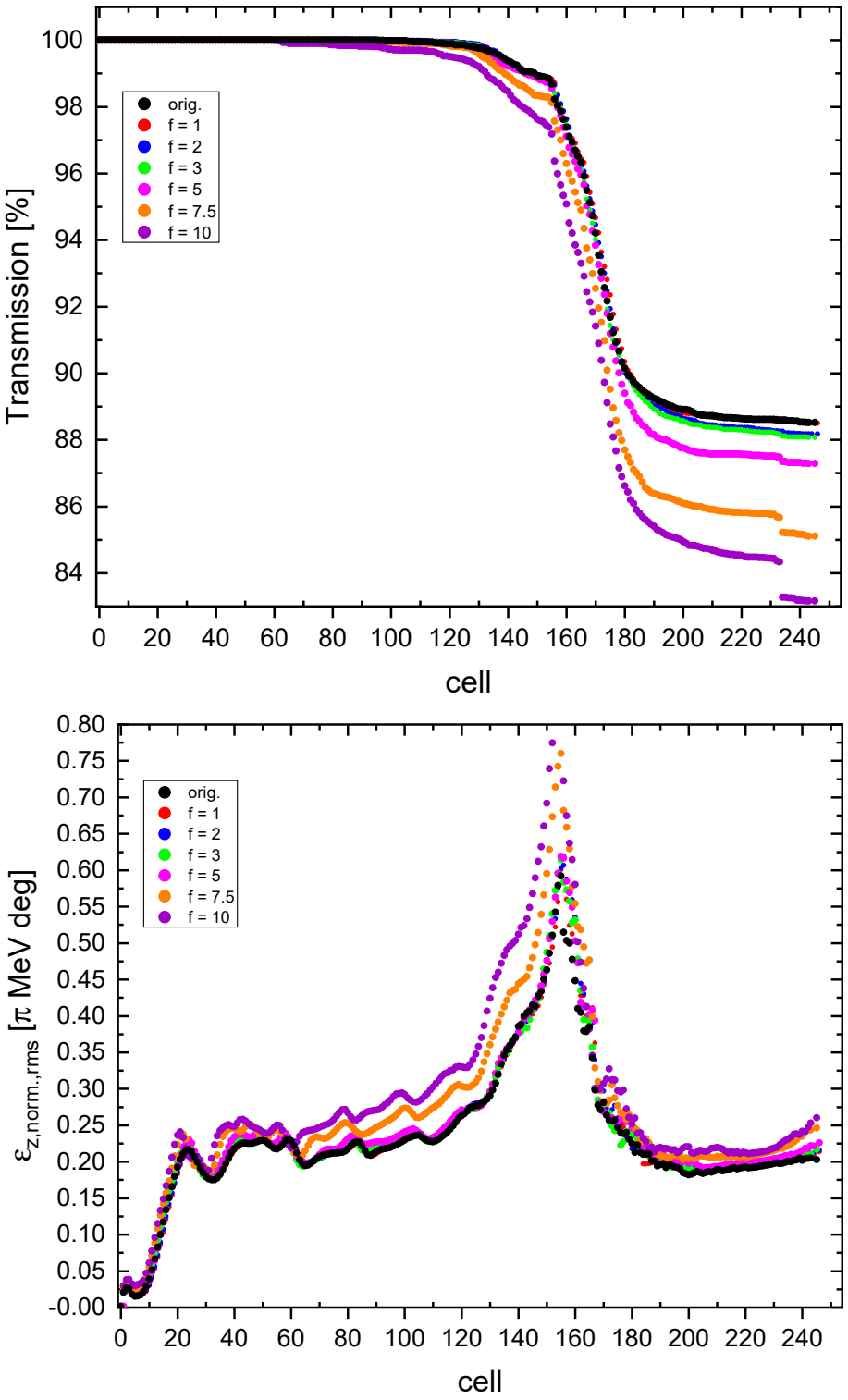

Figure 3.48: Transmissions (top) and normalized longitudinal rms-emittances (bottom) for different f-values along the RFQ.

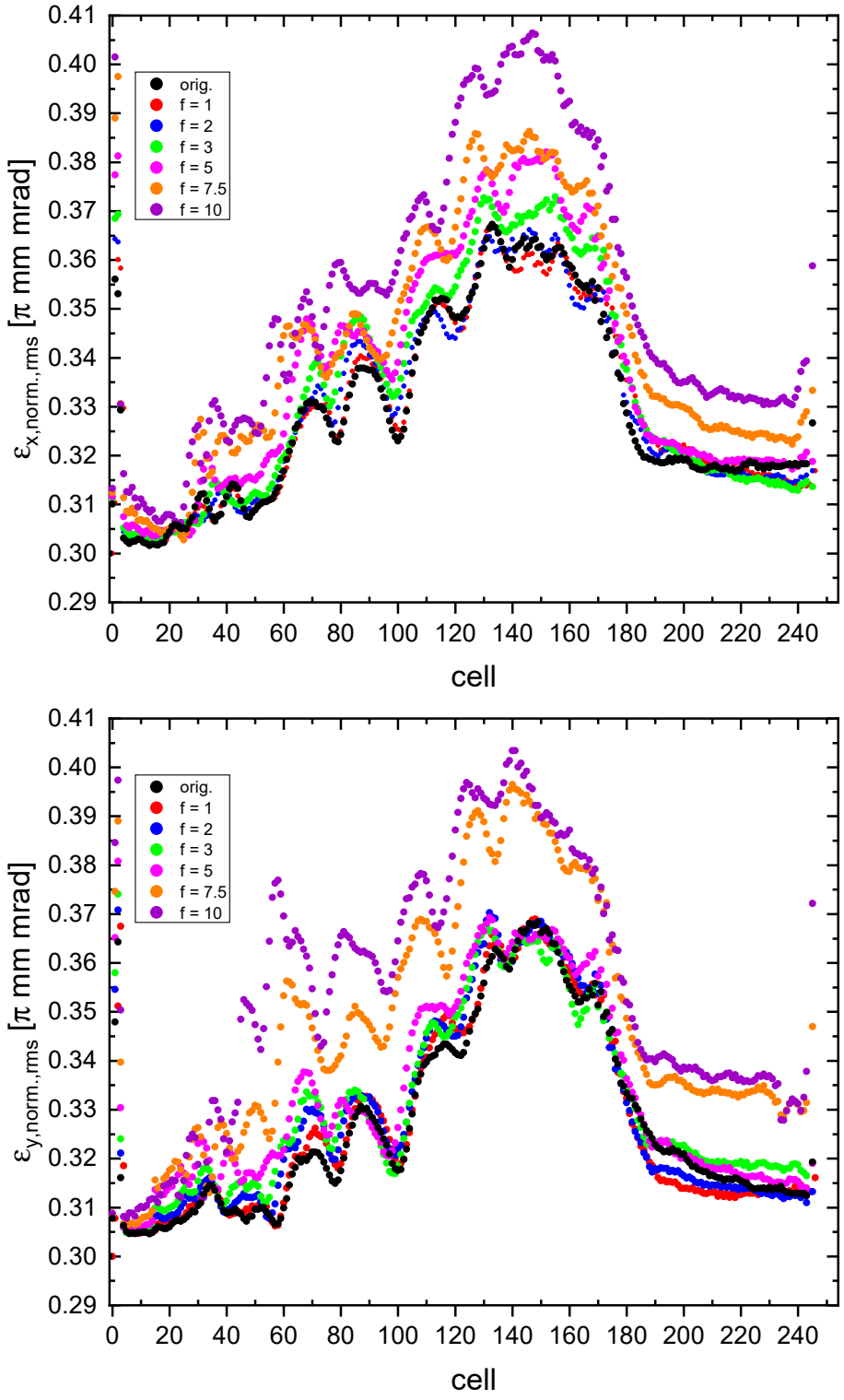

Figure 3.49: Transveral normalized rms-emittances for different f-values along the p-Linac RFQ: x- (top) and y-emittance (bottom).

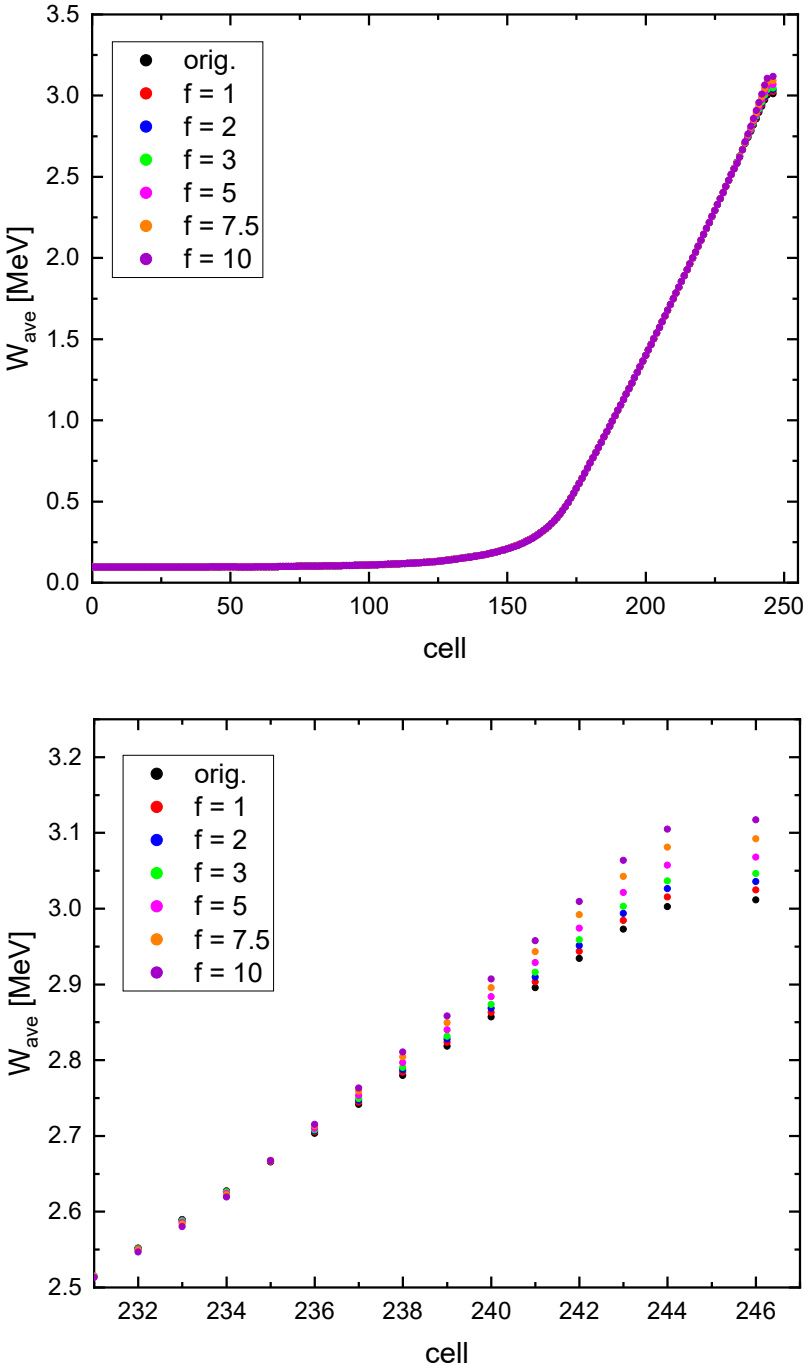

Table 3.20: **Top:** Average particle energies at cell center for different f-values along the RFQ. **Bottom:** Zoom at the last 16 cells. W_{ave} grows notably and lineally, but only very slowly with f. The energy discrepancies increase for later cells and higher f-values.

[4] Beam Dynamics Design of a New Compact RFQ

Compact RFQs play a crucial role in nuclear medicine and many industrial applications, for many of which portability and mobility of the devices are required and low RFQ exit energies and currents are sufficient. This chapter provides an overview of the main applications of compact RFQs in nuclear medicine (see Sec. 4.1) and of two new compact RFQs developed at CERN (see Sec. 4.2) followed by the introduction of the first beam dynamics draft of a new compact RFQ suited for the same applications (see Sec. 4.3). This design was developed with RFQGen, which was also used for successive RFQ entrance current studies (Sec. 4.4).

4.1 The Role of Compact RFQs in Nuclear Medicine

Within the framework of nuclear medicine open radioactive sources emitting ionizing radiation are employed tens of millions times each year with increasing tendency. These sources are introduced into patients for diagnostic and therapeutic purposes. The former comprise diagnostic procedures to detect or localize illnesses as well as to monitor their progression, among others to gain knowledge over crucial parameters for the choice of treatment options. The latter include therapeutic procedures, where radionuclides are employed – either in elemental form or bound to appropriate molecules – that selectively target the afflicted body regions. Related to this, but formally associated with the field of radiology rather than nuclear medicine is the area of brachytherapy, i.e. one or more sealed radiation sources being placed inside or next to the area requiring treatment [72].

Radionuclides are indispensable to all above mentioned medical applications. Most of the required radionuclides are not produced via natural decay chains and hence must be won by artificial transmutation driven by nuclear reactors or accelerators. For decades nuclear physics facilities, i.e. multi-purpose research reactors and accelerators, provided all medical radionuclides. Today production also takes place in dedicated medical cyclotrons. Additionally, the crucial role various types of particle accelerators play in radiation therapy should not go unmentioned. The energy of

heavy ion beams can be deposited very precisely, i.e. almost exclusively, into the afflicted tissue. This is due to the energy absorption profile of a given ion species depending on the ion velocity for a given target material. Thus, healthy surrounding tissue is largely spared. The Heidelberg Ionbeam-Therapy Center (HIT) is one of the worlds most known centers for such applications [34].

As of today, linear ion accelerators still contribute rather little to medical isotope production. The reasons why cyclotrons are still favored are [72]:

- For most of the required beam energies their design is very compact.
- For the majority of cases their beam current limitations pose no problems.
- Commercial manufacturers can look back on decades of designing and building these accelerators.
- Their low RF power requirements result in significantly reduced investment and operation costs.

However, the potential for linacs in this regard should not be underrated, since some proton-linacs at large accelerator facilities like BNL, the **L**os **A**lamos **N**eutron **S**cience **Ce**nter[1] (LANSCE) or the **M**oscow **M**eson **F**actory[2] (MMF) already generate medical isotopes requiring higher energy protons than available from standard medical cyclotrons. Although recent technical improvements in linac design could reduce the size and/or RF power requirement by a factor of 0.2 to 0.3, linacs still demand RF powers about an order of magnitude higher than these of cyclotrons. There are, however, a variety of cases, for which linacs are (or at the very least may turn out to be in the long run) the accelerator of choice [72]:

- Since Helium anions only occur in a metastable atomic state and the generation of He^--beams is very low in efficiency, negative ion cyclotrons are not ideally suited to produce alpha beams. However, beam losses on the septum commonly reduce the extracted beam currents of positive ion cyclotrons. Acceleration of intense beams of helium and heavier projectiles is more efficient in linacs.
- As the beam current increases, so does the plug power efficiency of a linac, which makes this accelerator type competitive for higher currents. Caveats are that such currents can be employed only in combination with the appropriate target technology and are only of

[1] `https://lansce.lanl.gov`

[2] The Moscow Meson Factory is located in Troitsk at the the **I**nstitute for **N**uclear **R**esearch (INR) of the **R**ussian **A**cademy of **S**ciences (RAS) (`http://www.inr.ru/english.html`).

interest for a certain sub-group of radioisotopes. These would be longer-lived ones that can be distributed over a wider region to many end-users from a centralized production facility.

- Mobile solutions as realized by AccSys Technology, Inc. for **P**ositron **E**mission **T**omography (PET) isotope production mounted on a truck pose a suitable alternative to very compact low-energy cyclotrons[3].
- Should further, drastic price reduction of solid state power amplifiers take place, the difference in investment could turn out more in favor of linacs.

Compact ion linacs have been designed and built for A/q ratios up to 3 in Europe and Japan, all driven by multi-cell cavities and delivering beams at a constant final beam velocity, i.e. at a constant energy per nucleon. The 7 A×MeV $12C^{4+}$ linac (217 MHz), which has been developed by IAP Frankfurt, Germany, and GSI Darmstadt acts as the injector at above mentioned HIT. This 21 MV injector consists of an ECR ion source, a 1 m 4-Rod RFQ and a 3.7 m IH-DTL and has since been reproduced for four other therapy centers. Since this design can be adapted to other end energies or max. A/q values, it might also become enticing for medical isotope production [72].

4.2 CERN's Compact PIXE and COMPASS RFQs

In recent years, CERN realized two compact RFQs based on the same (beam dynamics) design: the PIXE-and the COMPASS-RFQ, which are used in the fields of Cultural Heritage Studies and Proton Radiobiology, respectively. PIXE stands for **P**roton **I**nduced **X**-ray **E**mission: bombardment of a material with protons leads to ionization and hence to x-ray emission, which can be detected and analyzed. In this way, valuable information of the elemental constituents of materials or samples can be gained. As the proton beams used are low in current and energy (see Tab. 4.1), the PIXE method provides a powerful non-destructive elemental analysis technique frequently used by geologists, archaeologists and art conservators.

Table 4.1 shows the key parameters of the PIXE-RFQ, which was built at CERN in collaboration with INFN Florence within the MACHINA[4] Project [33]. Operated at a frequency of ca. 750 MHz and an electrode-voltage of only 35 kV, it accelerates protons from 20 keV to 2.0 MeV. The average entrance beam current is 5 nA, its peak value is 200 nA. The short total RFQ length of ca. 1.07 m, which makes it an easy transportable table-top device as required for many of its

[3] `https://www.accsys.com/pdf/pulsar_mob.pdf`
[4] **M**ovable **A**ccelerator for **C**ultural **H**eritage **I**n-situ **N**on-destructive **A**nalysis.

Parameter	Value
Syn. Entrance Energy $W_{syn}\,[keV]$	20
Syn. Exit Energy $W_{syn}\,[MeV]$	2.0
Operation Frequency $f\,[MHz]$	749.48
RFQ Length $[mm]$	1072.938
$V_{elec.}\,[kV]$	35
Min. Aperture $a_{min}\,[mm]$	0.7
Trans. Elec. Radius $[mm]$	1.439
Average / Peak Entr. Beam Cur. $I_{in}\,[nA]$	5/200
Transmission [%]	30
Max. duty cycle [%]	2.5

Table 4.1: Key parameters of the CERN PIXE-RFQ [32].

applications, as well as its remarkably small minimum aperture a_{min} of only 0.7 mm are not least made possible at the cost of a low, but still sufficient transmission of 30%.

The COMPASS[5]-RFQ is basically a vertically installed PIXE-RFQ, whose applications are in the field of Proton Radiobilogy. It was built in collaboration with the Amsterdam Medical Centre and Eindhoven University and radiates tissue samples with protons so that the resulting cell response (DNA damage and repair) can be observed. In this way, large amounts of data relevant for proton therapy can be collected and evaluated, which may hopefully lead to significant therapy improvements.

4.3 First Beam Dynamics Design Draft for a New Compact RFQ

Despite the already existent variety of compact RFQs today, there still exists a demand for a new compact, low duty cycle, low energy RFQ that accelerates protons beams of 5 to 10 mA from about 20 keV to about 2.0 MeV with transmissions of at least 70%.

[5] **CO**mmon **M**uon and **P**roton **A**pparatus for **S**tructure and **S**pectroscopy.

Parameter	p-Linac RFQ	Compact RFQ
Entrance Energy $W_{syn}\,[keV]$	95	25
Entrance Beam Current $I_{in}\,[mA]$	100	5
Electrode Length [mm]	3329.8	1561.2
Long. Electrode Profile	sinusoidal	sinusoidal
Electrode Voltage [kV]	88.43	88.00
Number of RFQ Cells*	245	124
ρ/r_0	0.85	0.85
$\rho\,[mm]$	3.2	3.2
$r_0\,[mm]$	3.8	3.8
$a_{min}\,[mm]$	2.4	2.3
m_{max}	2.02	1.98
Number of RM Cells	5	5
Acc. Sec. Exit Sync. Phase ϕ [deg]	-22.40	-30.03
$\varepsilon_{x/y,in,rms}\,[\pi\,mm\,mrad]$	0.30	0.15
$\Delta W_{in}\,[keV]$	0.0	0.1
$\varepsilon_{x,out,rms/95\%}\,[\pi\,mm\,mrad]$	0.32/1.69	0.22/1.40
$\varepsilon_{y,out,rms/95\%}\,[\pi\,mm\,mrad]$	0.32/1.69	0.22/1.35
$\varepsilon_{z,out,rms/95\%}\,[\pi\,MeV\,deg]$	0.20/1.24	0.13/0.81
$\varepsilon_{x-y,out,rms/95\%}\,[\pi\,mm^2]$	0.57/2.90	0.31/1.89
Synchronous Exit Energy $W_s\,[MeV]$	3.015	2.043
Average Exit Energy $W_{ave}\,[MeV]$	3.011	2.045
Transmission [%]	88.470	74.254

Table 4.2: Key parameter comparison between the FAIR p-Linac RFQ and the new compact RFQ. The beam parameters at the RFQ exits refer to 4.88 mm and 4.81 mm behind the end of the electrodes in case of the former and the latter, respectively. The beam parameters for the FAIR p-Linac RFQ refer to the matched case (cf. Tab. 3.8 in Sec. 3.2). (*Fringe-field "cell"/region not included.)

Table 4.2 shows the preliminary key (beam dynamics) design parameters of such an RFQ compared to those of the FAIR p-Linac RFQ, with whom it also shares its operation frequency of 325.224 MHz. Its electrode voltage is also nearly as high as that of the p-Linac RFQ (88.00 kV vs. 88.43 kV). Its electrode length[6] is 1561,2 mm and thus only amounts to about 47% of the

[6] The total length of this RFQ according to RFQGen is about 1573 mm. For comparison the total length of the p-Linac RFQ according to RFQGen is 3343.0 mm. RFQGen is of course ignorant of the actual distances at the RFQ ends (cf. Sec. 3.7).

p-Linac RFQ's electrode length (ca. 3330 mm). The RFQ exit energy of ca. 2.0 MeV is already sufficient for various medical and non-medical applications. The greater length (ca. +50%), electrode voltage (ca. +150%) and aperture (ca. +50%) of this RFQ compared to the more compact PIXE-RFQ enables a much higher exit current of approx. $0.75 \cdot 5\,mA = 3.75\,mA$. This corresponds to an increase by $3.75\,mA\,/\,(0.3 \cdot 200\,nA) = 6.25 \cdot 10^4$ and $3.75\,mA\,/\,(0.3 \cdot 5\,nA) = 2.5 \cdot 10^6$ compared to the PIXE RFQ's peak and average exit current, respectively. Note that the PIXE RFQ's peak current is not determined by the space-charge limit, i.e. the upper current limit for the onset of rapid emittance growth caused by interactions within the beam, but by the relatively low transversal emittances its small minimum aperture of only 0.7 mm requires (cf. Tab. 4.1).

Figure 4.2 shows the beam dynamics designs of the new compact RFQ, i.e. the curves of m, a and ϕ against the cell number (top) and the z-coordinate (bottom), respectively. The Gentle Bunching section ends at cell 49 ($z < 20\,cm$). This section is very short in order to reduce the overall RFQ / electrode length, but still sufficiently long for the beam dynamics to generate acceptable emittances and a transmission close to 75% at the RFQ exit.

The phase space plots of the new compact RFQ can be seen in Fig. 4.1: the distribution of the longitudinal sub-space exhibits some spiraling tendencies (as is the case for the low entrance current simulations performed on the FAIR p-Linac RFQ (cf. Sec. 4.4). The absence of potentially harmful peculiarities like the formation of multiple bunch centers gives rise to optimism.

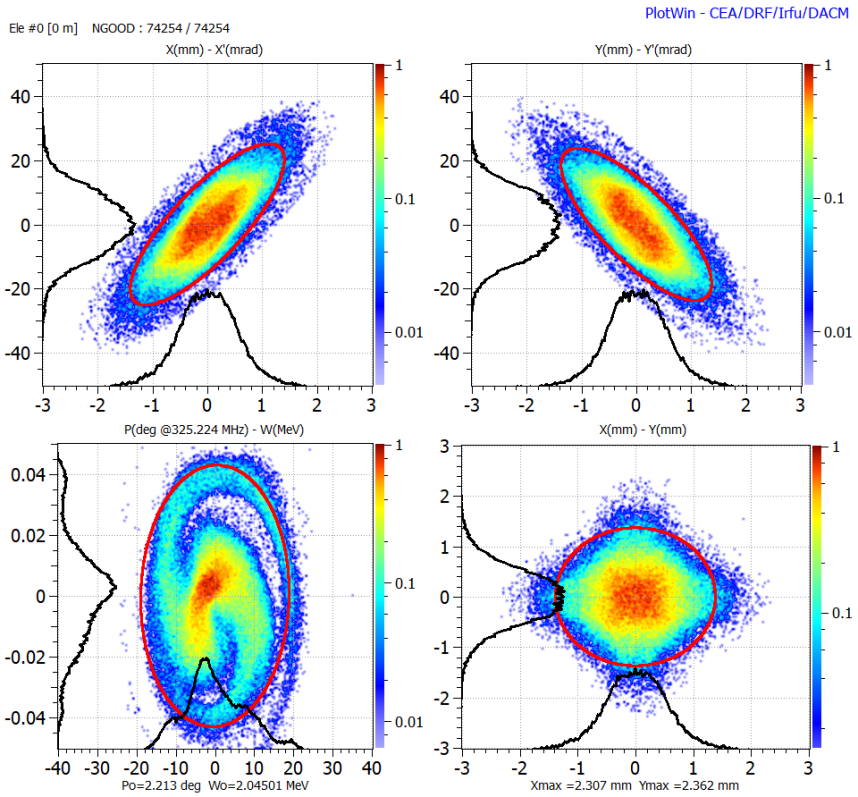

Figure 4.1: Phase space plots and distribution projections (black curves) at the RFQ exit, i.e. 4.81 mm behind the electrode ends (cf. Tab. 4.2). The entrance current was chosen to 5 mA represented by 10^5 macro-particles. The colors of the scatter plots refer to the normalized macro-particle density (cf. scales at the right frames of the plots). The red ellipses correspond to the normalized 95%-emittances (cf. Tab. 4.2).

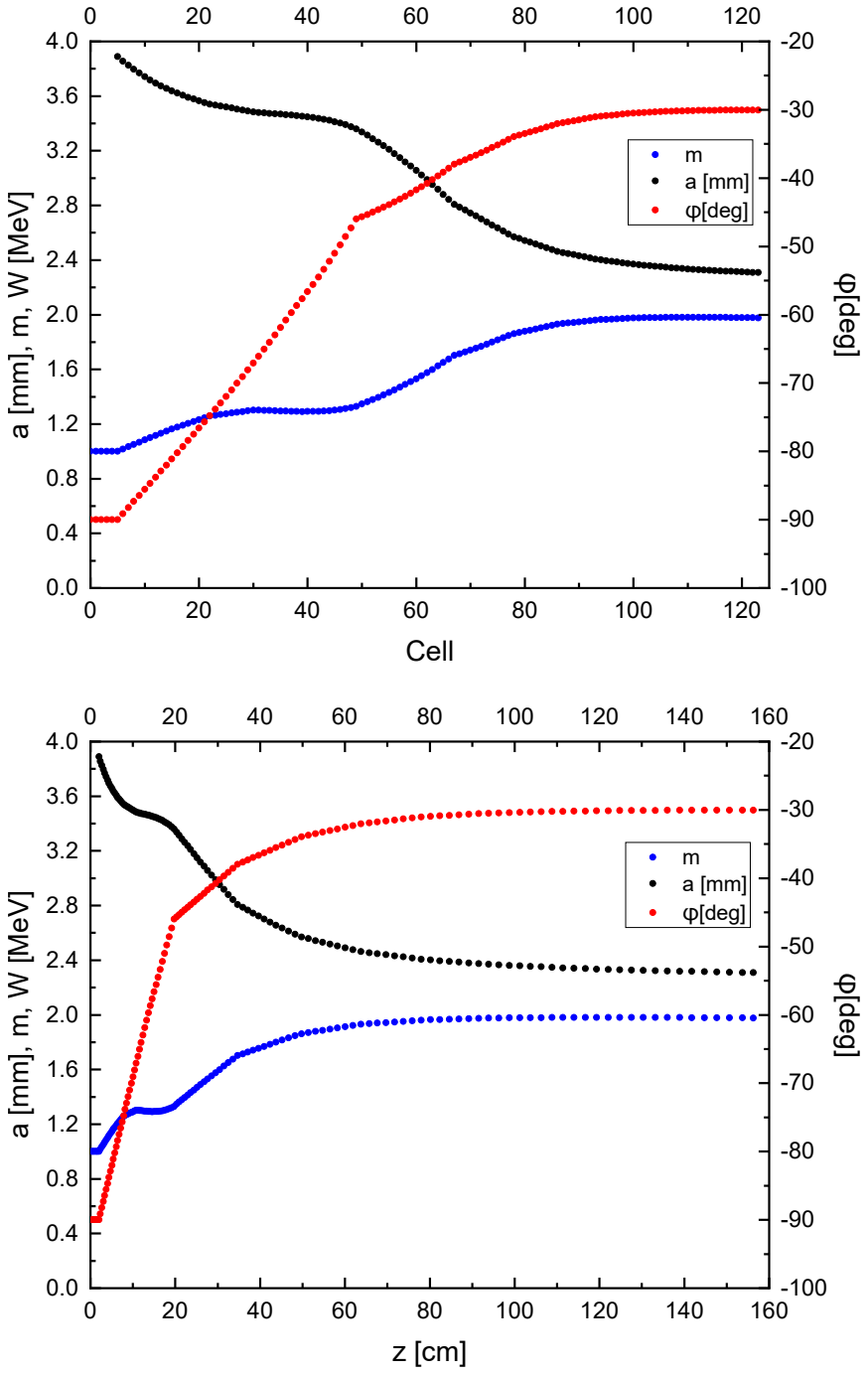

Figure 4.2: Beam dynamics design of the new compact RFQ. Shown are the modulation parameter m, aperture a and the synchronous phase ϕ against the cell number (top) and z-coordinate (bottom).

4.3.1 Particle Loss Profiles

The charts in the left column of Fig. 4.3 show the diagrams of the absolute particle loss percentage (100,000 initial macro-particles $\hat{=}100\,\%$) against the synchronous energy W_s within the cell, in which the respective losses occur. In total, 25,619 and of initially $100,000$ macro-particles are lost along the RFQ. A sharp peak of 9,819 macro-particles ($\hat{=}9.819\,\%$ of all initial macro-particles and $\hat{=}38.3\,\%$ of all losses) occurs for $W_{syn} = 270\,\mathrm{keV}$, i.e. at cell 67. Less than 100 macro-particles ($\hat{=}0.1\,\%$ of all initial macro-particles and $\hat{=}0.4\,\%$ of all losses) are lost in cells with synchronous energies above 0.5 MeV. Investigating this sharp peak revealed that cell 67 is the first cell for which longitudinal losses occur; the number of longitudinally lost particles within this cell is 9,593, whereas the number of radially lost particles here is only 586.

Albeit ΔW_{thr} was chosen according to $\Delta W_{thr} = 2\,W_{h-w}$ (with W_{h-w} chosen according to Eq. E.2 in Sub-Sec. E.1.6), this sudden onset in longitudinal losses might indicate a too low choice for ΔW_{thr}. Thus, as already performed in case of the FAIR Proton-Linac RFQ, a beam dynamics simulation with an adjusted ΔW_{thr}-value of nearly the synchronous energy at the RFQ exit, i.e. $\Delta W_{thr} = 1.99\,\mathrm{MeV}$, was run.

The respective particle loss diagrams are shown in the right column[7] of Fig. 4.3: 24,823 of $100,000$ macro-particles are lost along the RFQ. Even though the losses are distributed much more evenly along the RFQ than previously, they remain almost the same. No sharp peak occurs any longer, neither at cell 67 (i.e. at $W_{syn} = 270\,\mathrm{keV}$) nor for any other cells. The maximum number of lost particles per cell is much smaller in this than in the previous case (681 in cell 58 vs. 9,819 in cell 67). The loss profiles of both cases are very similar until cell 67, which was to be expected as in case of the adjusted simulation longitudinal losses are basically switched off; in total only 234 macro-particles are lost longitudinally with the first longitudinal loss particle[8] occurring in cell 92 ($W_s = 962.6\,\mathrm{keV}$). However, this leaves a growing number of particles increasingly off-phase to the synchronous particle along the RFQ. These are thus increasingly exposed to the "wrong" electric fields so that their trajectories eventually intersect with the RFQ (i.e. the electrodes or the cavity) and a second, much more wider peak forms around cell 99. These results are consistent with the corresponding ones in case of the FAIR p-Linac RFQ (see Sec. 3.5), where the peak of the losses per cell curve at the end of the gentle bunching section gets shifted towards the acceleration section.

[7] For each case two diagrams are provided: these of the upper row are scaled with regard to the original case, these of the lower ones with regard to the case of the adjusted ΔW_{thr}-value.

[8] Indeed, only one sole macro-particle is lost radially in (and hence up to) cell 92.

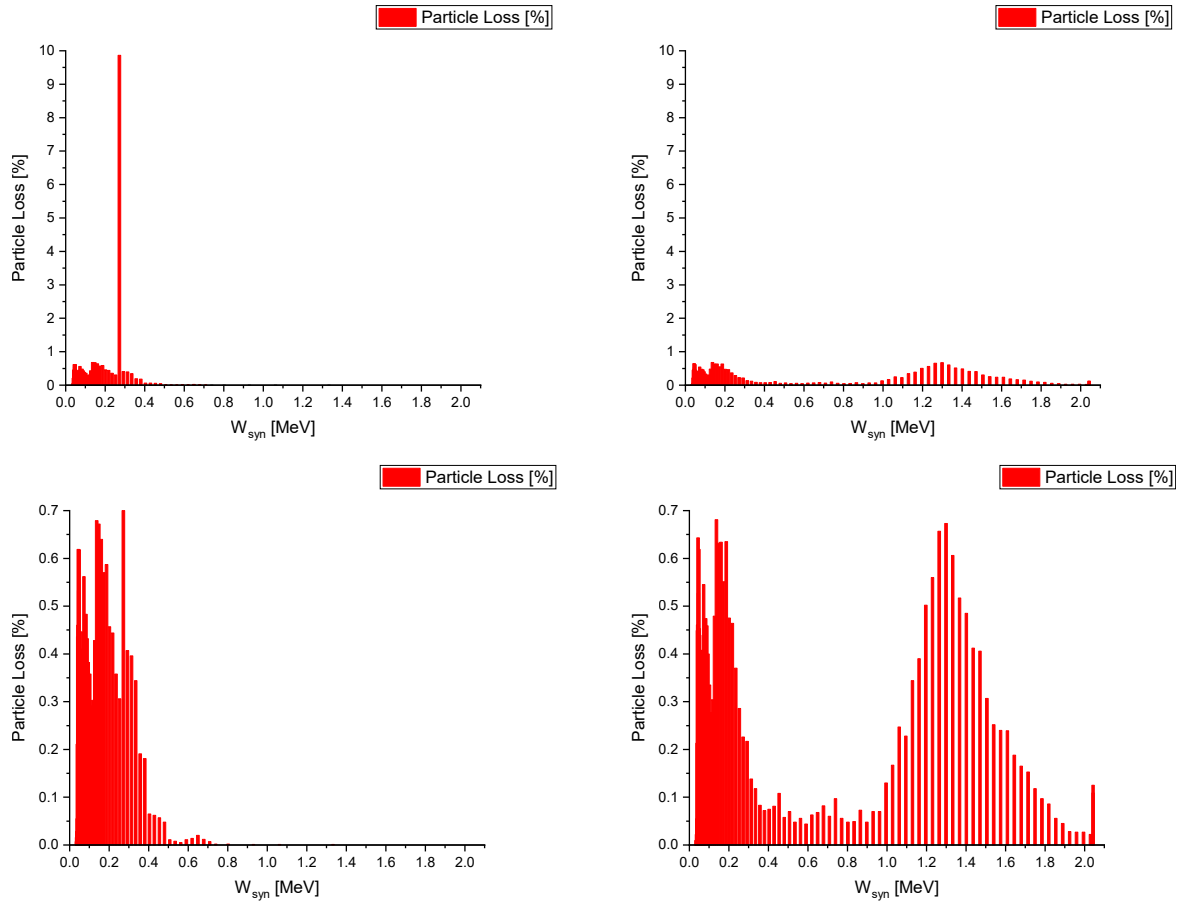

Figure 4.3: Particle losses per cell [%] against the synchronous energy W_{syn} for the new compact RFQ before (left column) and after the ΔW_{thr}-adjustment to a realistic value (right column). The ordinates of the graphs in the upper row are scaled according to the maximum particles losses per cell of the original simulation, these in the lower row according to the maximum of those from the simulation with the adjusted ΔW_{thr}-value.

Up to (including) cell 123, the last cell of the acceleration section, only 13 macro-particles are lost longitudinally. In the Δm-cell (cell 124; $W_{syn} = 2.043\,\text{MeV}$) about 110 macro-particles are lost, all of them longitudinally. This also holds true for "cell" 125 (the fringe-field "cell" / region; $W_{syn} = 2.043\,\text{MeV}$). As the threshold energy for the radioactivation of copper by proton collisions is about 2.0 MeV, radioactivation should not or only in a minor, tolerable fashion occur for this RFQ regardless how the actual particle loss profile might turn out. Nonetheless, an optimization of the gap and fringe-field effects at the RFQ ends should be undertaken according to Sec. 3.7 once the final beam dynamics design (or rather the corresponding RFQGen input-file)

will have been generated[9].

4.3.2 Intersection of the Phase Advance Curves

Figure 4.4 shows the curves of the longitudinal and transversal zero-current phase advances σ_{0l} and σ_{0t} against the cell number for the FAIR p-Linac RFQ (left) and the new compact RFQ (right). Within the "RFQ community" (or at least within a significant subset of it) a "rule of thumb" regarding these curves exists, which states that they should (at least within the gentle bunching and acceleration section) not intersect as this might result in so-called emittance transfer or exchange-related resonances during the beam bunching and acceleration process. These have been investigated thoroughly within the beam dynamics community for many decades with I. Hofmann playing a leading role ever since [36, 37]. More recent in-depth elaborations on these resonances with regard to RFQs specifically come from R. A. Jameson [38] as well as C. Zhang and H. Podlech [19].

Whereas for the FAIR p-Linac RFQ the $\sigma_{0l/t}$-curves do not intersect, in case of the new compact RFQ they intersect in two cells, i.e. at cell 17 and 74. However, such intersections also occur in case of CERN's Linac2 RFQ[10] and for the HIT[11]- and MedAustron[12]-RFQs [34, 35] (developed at IAP) without causing problems. Hence, it should be stated that while intersecting $\sigma_{0l/t}$-curves might result in an increased and sometimes fatal instability of an RFQ's performance and thus should if possible be avoided, it is not certain that they even slightly disturb an RFQ's beam dynamics per se. If and to what degree these kind of intersections cause problems ought to be investigated for each individual RFQ exhibiting them.

[9] The actual final beam dynamics design would of course include this optimization, albeit this is not mirrored in the RFQGen input-file, since the Code does as of yet not appropriately account for the effects of the longitudinal end gap-fields (cf. Sec. 3.7).

[10] Personal Correspondence with A. M. Lombardi.

[11] The Heidelberg Ion Beam Therapy Center (German: Heidelberger Ionenstrahl-Therapiezentrum (HIT)) is a German center for particle therapy of cancer patients with accelerated protons and carbon ions on the grounds of the Heidelberg University Hospital. The HIT was the first European therapy facility to also use heavy ions, and the first in the world to have a gantry, i.e. a movable beam delivery system that allows 360deg rotation of the beam around the patient (`https://www.klinikum.uni-heidelberg.de/interdisziplinaere-zentren/heidelberger-ionenstrahl-therapiezentrum-hit/` [German]).

[12] The MedAustron Center for Ion Therapy and Research is located in Wiener Neustadt in Wiener Neustadt in Lower Austria (`https://www.medaustron.at/en`).

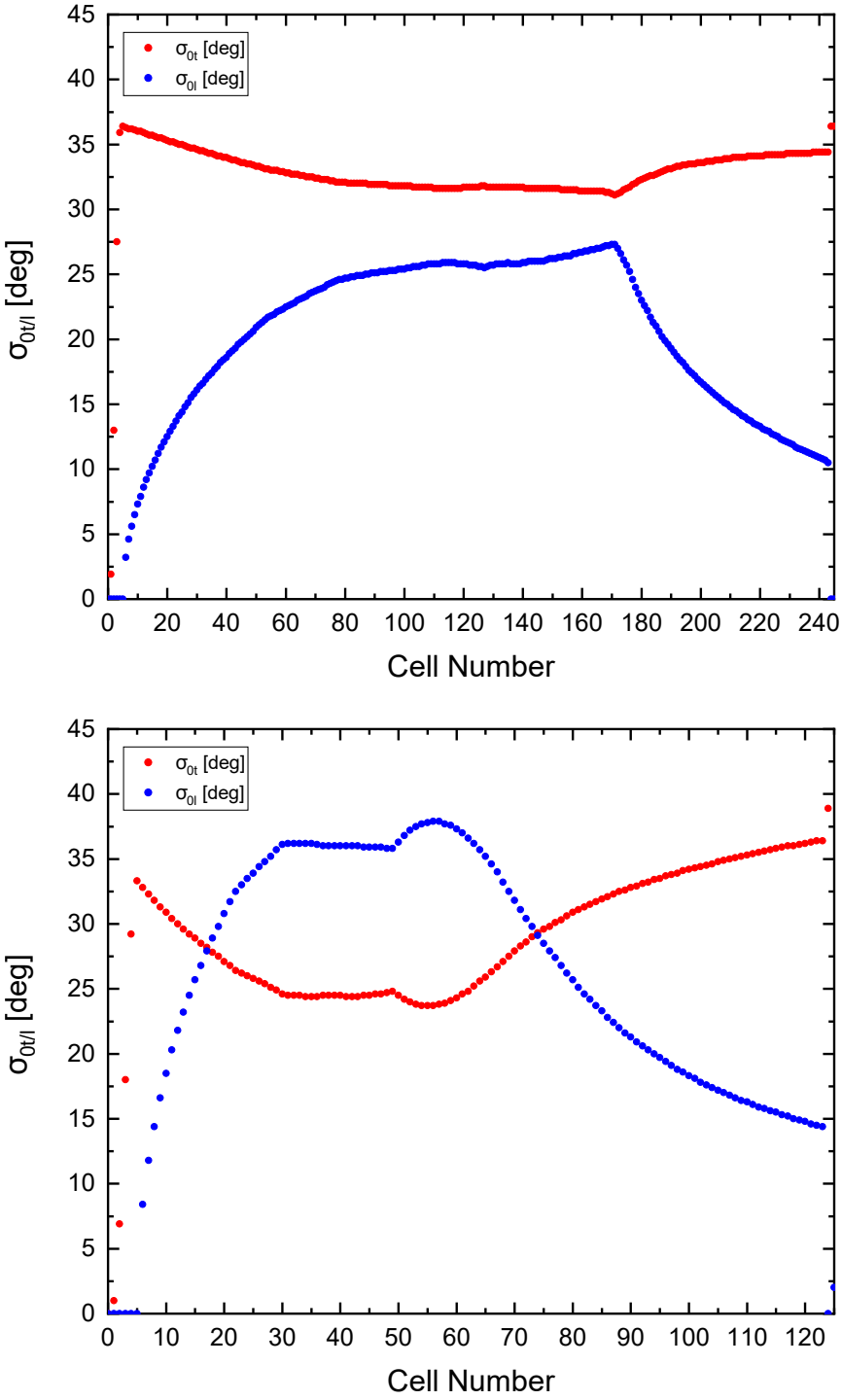

Figure 4.4: Curves of the longitudinal and transversal zero-current phase advances $\sigma_{0l/t}$ against the cell number in case of the FAIR p-Linac RFQ (top) and the new compact RFQ (bottom).

4.4 Current Studies with the New Compact RFQ

I_{in} $[mA]$	T [%]	I_{out} $[mA]$	$\varepsilon_{x,out,rms,n}$ $[\pi\, mm\, mrad]$	$\varepsilon_{y,out,rms,n}$ $[\pi\, mm\, mrad]$	$\varepsilon_{x,out,rms,n}$ $[\pi\, MeV\, deg]$
0.0	81.10	0.00	0.20	0.20	0.14
1.0	79.94	0.80	0.21	0.21	0.14
2.5	78.05	1.95	0.21	0.22	0.14
5.0	74.25	3.71	0.22	0.22	0.13
7.5	70.25	5.27	0.23	0.22	0.13
10.0	65.53	6.55	0.23	0.23	0.12

Table 4.3: Results of the entrance current studies for the new compact RFQ; except for the values of the first column, all values refer to the RFQ exit, i.e. 4.81 mm behind the electrodes (cf. Tab. 4.2).

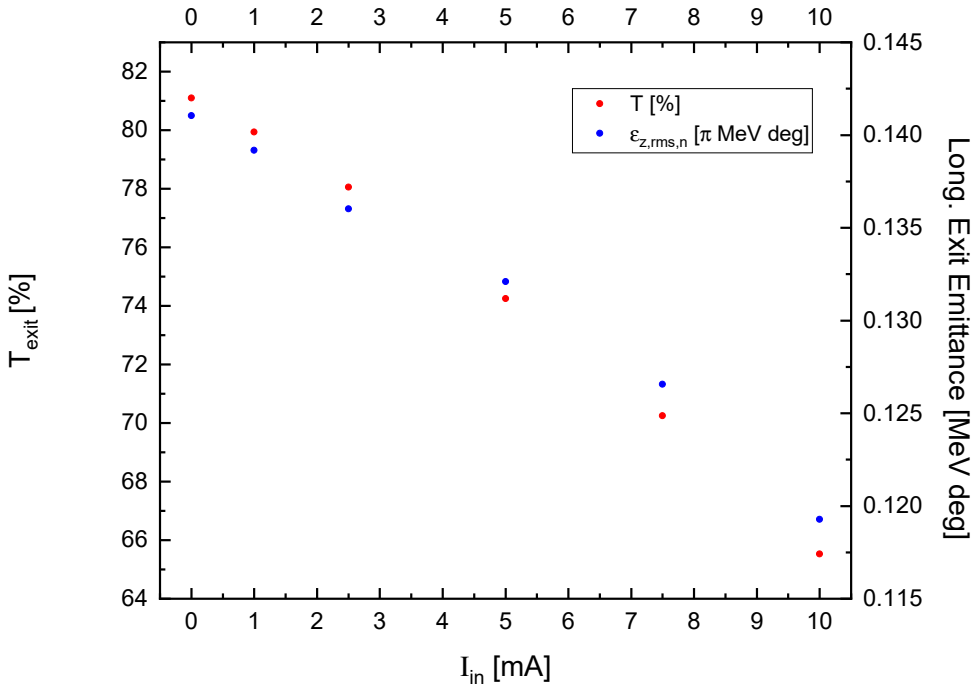

Figure 4.5: Transmission (red) and normalized longitudinal rms-emittance (blue) at the RFQ exit against the RFQ entrance current.

As mentioned above, the (output) currents needed for possible applications are rather low for this kind of RFQ, so that the maximum entrance current tested was only 10 mA. It can be seen in Tab. 4.3 that the exit emittances remain nearly constant for I between 0 mA and 10 mA. This beam dynamics design was generated for an entrance current of 5 mA. Transmission drops by

ca. 10% to about 65% if the entrance current is doubled. As can be seen from Fig. 4.5 both transmission and longitudinal normalized rms-emittance at the RFQ exit decrease with growing entrance current. This is a deviation form the behavior of these parameters in case of the FAIR p-Linac RFQ (cf. Sec. 3.8), where they exhibit an antagonistic behavior.

4.5 Further Steps

This first beam dynamics design for a possible future compact low energy, low duty factor RFQ has so far shown to be very promising. The results of the entrance current studies give further confidence that a feasible beam dynamics design might have already been found (or at least roughly outlined). However, the design could still be improved with regards to reducing the electrode length and/or voltage. This might come at the cost of reduced transmission and deteriorated exit emittances, though. Further considerations and investigations regarding the expected effects of the intersection of the $\sigma_{0l/t}$-curves should be undertaken. Insofar as considered appropriate or even necessary, it could then be investigated if and how "unknotting" these curves could be accomplished. (Achieving non-intersecting $\sigma_{0l/t}$-curves might probably require a completely new design approach, though.)

Another point on the agenda would be the optimization of the RFQ ends, especially the high energy end. Whereas the transition and fringe-field regions would have to be optimized in RFQGen itself, considering the longitudinal fields of the gap-fields requires a workaround as shown above for the p-Linac RFQ (cf. Sec. 3.7).

Although the beam profiles along the RFQ generated during the RFQGen-simulation exhibit smooth edges, which indicates good beam matching at the RFQ entrance, transversal entrance Twiss parameter studies analog to these for the FAIR p-Linac RFQ (see Sec. 3.2) should also be performed, both in regard to confirming / finding the optimal entrance Twiss parameters and testing the design's tolerance regarding these parameters. Their findings should then be checked in TOUTATIS (as was the case for the FAIR p-Linac RFQ).

Once a thus optimized beam dynamics design is gained, above current studies are to be undertaken. (The design entrance current remains $I_{in,des} = 5\,\mathrm{mA}$.) Furthermore, a study regarding voltage deviations is crucial. It can be done in RFQGen itself by adjusting the vfac-line (cf. Sec 3.9) accordingly. More sophisticated simulations in regard to the actual voltage distribution would only come into play at a much later stage in the RFQ development (or rather conditioning) process, i.e. after completed tuning. The afterward measured field / voltage distribution would be approximated by successive step functions as shown in case of the FAIR p-Linac RFQ in Sec. 3.9.

[5] Conclusions and Outlook

This dissertation presents the beam dynamics designs of two RFQs: that for the RFQ of the Proton-Linac of the FAIR project at GSI as well as a first design draft for a compact RFQ that could be used, besides other applications, to generate radioisotopes for medical purposes. The focus is put on the design of the FAIR p-Linac RFQ.

GSI's accelerator infrastructure currently is extended within the scope of the FAIR project. As the currently operating linear accelerator UNILAC is not able to generate a sufficient number of antiprotons, the FAIR project also includes a linac for proton acceleration (p-Linac; see Fig. 1.2) and subsequent injection into the synchrotron SIS18. The accelerating cavities as well as the MEBT-section located between the RFQ and these cavities were developed at IAP Frankfurt. Once completed, protons will be accelerated to 68 MeV at a beam current of up to 110 mA at a duty cycle of 0.08 % in the approximately 30 m long p-linac. The frequency of 325.224 MHz results from the choice of the klystrons (at a power of 2 MW per klystron).

The RF acceleration along the p-linac starts with the RFQ, which accelerates the beam from 95 keV to 3 MeV. Although this RFQ belongs to the high-current RFQs, it also accepts and accelerates significantly lower input currents down to the zero-current at convincing beam parameters (cf. Sec. 3.8).

Chapter [2] explains the main concepts needed to design an RFQ. Appendices A to D contain definitions and explanations of: the synchronous phase, the separatrix (Appx. A), space charge compensation (Appx. B), the "Bravery"- or "Kilpatrick"-factor (Appx. C) and the different classifications of beam emittances (Appx. D).

Both beam dynamics designs developed within the scope of this dissertation were generated using the RFQGen-code. This code is the successor to PARMTEQ(M). PARMTEQ was written to generate RFQ beam dynamics designs as well as to simulate the motion of particle beams and has been continuously refined and improved [22, 21]. RFQGen and TOUTATIS, another RFQ beam dynamics code relevant to this dissertation, are described in detail in Appx. E.

The beam dynamics design of the FAIR p-Linac RFQ as well as various test simulations with respect to input parameters such as beam current and transverse Twiss parameters are presented in chapter [3], the main chapter of the thesis: The design exhibits high tolerance regarding deviations from its design transversal entrance Twiss parameters (cf. Sec. D.3) and its design entrance current (cf. Sec. 3.8).

The design was finally fixed after many iterations taking into account the injection line measuring results (contributed by CEA, Paris, France) and the boundary conditions from RFQ cavity construction (performed at IAP Frankfurt).

Since the MEBT section behind the RFQ and the subsequent CH cavities had already been designed (IAP Frankfurt), the RFQ exit energy of 3 MeV as well as the desired values of the transverse and longitudinal emittances at the RFQ exit were already fixed [24]. The curves of aperture a, modulation m and the synchronous phase ϕ_s (see Fig. 0.3) are similar to those of the Linac4 RFQ at CERN. Except for the non-constant, but also linear progressions of the parameter curves within the last section (i.e. the acceleration section, where most of the total energy gain along the RFQ is obtained), this corresponds to a classical RFQ beam dynamics design according to the LANL FSP. However, these slight modifications can already result in a significant shortening of the RFQ and/or a lowering of the electrode voltage (cf. Sec. 2.11 and 3.1).

In Section 3.1, an alternative (hypothetical) electrode design for the FAIR p-Linac RFQ is presented that corresponds to a classical LANL design according to the FSP. While its key parameters and the exit distribution are very similar to those of the original design, its electrode length exceeds the maximum allowed value of 3335 mm by almost 190 mm.

On the other hand, the NFSP, which can be used to design particularly short, compact RFQs, would also not be able to generate a feasible "alternative" design for the FAIR p-Linac RFQ specifically due to its efficient parameter curves and the resulting shortening of the electrodes.
After the design of the FAIR p-Linac RFQ could be successfully fed into TOUTATIS, several simulations at this model were performed with the following objectives: determination/verification of the ideal transverse input Twiss parameters ("matched case") and reproducibility checks of the beam dynamics results of the RFQGen simulations for a wide range of input currents (0 - 110 mA). The results of all these studies give confidence in the validity and the reliability of the design.

Furthermore, the results of various other simulation series in RFQGen are also presented in this central chapter of the dissertation. These simulations are used to investigate the effects of the following factors on the beam dynamics: the threshold value for the energy difference between particle and synchronous energy for which RFQGen counts particles as lost, space-charge forces between neighboring beam bunches, image charge forces as well as the value of initial energy width. The results of these investigations reinforced confidence in this design.

As the FAIR p-Linac RFQ falls in the category of 4-Rod RFQs, non-negligible longitudinal electric fields remain along its end gaps [3, 28]. In June 2019, an article appeared in *Nuclear Inst. and Methods in Physics Research A* by M. Schuett, U. Ratzinger and M. Syha [28], which discusses the effects the longitudinal electric fields along the end gaps of the FAIR p-Linac RFQ have on its beam dynamics. This was the first time the effects of the longitudinal electric field along the entrance gap of a 4-Rod RFQ were investigated. Section 3.7 summarizes this article. The simulation results presented show that the longitudinal electric fields at the end gaps in general, and at the entrance gaps in particular, of 4-Rod RFQs can have quite severe effects on the beam dynamics and should thus be considered for the designs of 4-Rod RFQs.

Section 3.9 presents the voltage studies. The final step regarding the tuning of the operation frequency and flatness of the electric field distribution along the FAIR p-Linac RFQ took place in April 2019. It was immediately followed by corresponding measurements [5]. As RFQGen cannot be fed the relative complex voltage distribution actually present along the RFQ, this distribution was approximated through a sufficiently accurate step function (cf. Fig. 3.46).

The FAIR p-Linac RFQ arrived at the IAP experimental hall in early 2020. Due to the Covid19 lock down shortly thereafter, the planned measurements and tests had to be postponed. The next steps include:

- further tuning of frequency and improvement of flatness with dummy pistons made of aluminum (cf. Ref. [5])
- fabrication and assembly of the actual, water-cooled copper or stainless steel pistons, whose design results from the previous measurements
- conditioning at low power
- finishing of the entrance cone
- transportation of the RFQ to GSI's klystron RF testing rig for operation at the RF design power level.

[5] Conclusions and Outlook

At the time of this thesis' completion in September 2021, the ion source had already been installed and tested: the measured parameters fit the assumptions made when designing the RFQ[1].

Chapter [4] provides a study regarding the beam dynamics design of a compact RFQ, also with an operating frequency of 325.224 MHz, which would accelerate 5 to 10 mA proton beams from 20 keV to 2 MeV at transmissions above 70%. Its electrode lengths remains below 1.6 m. In addition to various industrial applications, this RFQ might be used in nuclear medicine or radiation therapy, for which the expected RFQ exit beam currents between ca. 3.75 mA and 7.5 mA are easily sufficient[2].

In summary, this initial beam dynamics design for a possible future compact low duty cycle, low energy RFQ has so far proven to be very promising. The results of the initial studies give further confidence that a viable beam dynamics design has already been found (or at least roughly outlined). Also the loss profiles along the RFQ give no reason to doubt the reliability of the design[3].

In addition to studies on the effect of the ρ/r_0 ratio, the optimization of the RFQ end gaps, especially the high-energy end gap with respect to the longitudinal electric fields should be carried out (as already done for the FAIR p-Linac RFQ (cf. Sec. 3.7)). Furthermore, dedicated studies regarding these Twiss parameters in RFQGen with subsequent cross-checking in TOUTATIS are to be performed here as well, once the actual design is fixed (cf. Secs. 3.2 and 3.4). After the "matched case" is determined and confirmed, input current studies should also be run for this design. Further investigations should also include a first tolerance study regarding voltage deviations (cf. Secs. 3.9).

Of no inconsiderable interest for future research would possibly also be the development of alternative electrode designs for both RFQs presented in this dissertation. Here, in addition to RFQGen, other software could be used to develop RFQ beam dynamics designs. For example, CEA only recently released its „RFQ designer"-code[4]; the design data can be directly fed into

[1] Personal correspondence with C. Kleffner (GSI)

[2] The seemingly high losses enable the desired emittance reduction. Furthermore, the loss particles will not result in radioactivation of the RFQ due to their low energies (cf. Fn. 3).

[3] Other than for the FAIR p-Linac RFQ, radioactivation within the compact RFQ itself was never really expected since copper's threshold energy for radioactivation is almost identical to its exit energy of 2 MeV. The aim of these studies was rather to identify possible critical positions along the RFQ in order to, if necessary, optimize its beam dynamics design. A further motivation was to generally check the reliability and validity of the beam dynamics simulations.

[4] `http://irfu.cea.fr/en/Phocea/Page/index.php?id=932`

TOUTATIS for subsequent beam dynamics simulations. In principle, these alternative designs would be subject to the same parameter and error studies as the designs of this dissertation. Each simulation of these studies should be repeated, if possible, with at least a second RFQ beam dynamics code, and thorough comparison of the simulation results should follow.

Bibliography

[1] O. Kester, P. Spiller, F. Becker, O. Dolinskyy, L. Groening, K. Knie, H. Reich-Sprenger, W. Vinzenz, M. Winkler, and D. Prasuhn. The Accelerator Facility of the Facility for Antiproton and Ion Research. In *Proceedings of IPAC2015, Richmond, VA, USA, pages 1343-1345*, 2015. URL https://doi.org/10.18429/JACoW-IPAC2015-TUBB2.

[2] C. Kleffner, S. Appel, R. Berezov, J. Fils, P. Forck, P. Gerhard, H. Hähnel, M. Kaiser, K. Knie, A. Kraemer, C. Muehle, S. Puetz, U. Ratzinger, A. Schnase, M. Schuett, Schreiber M., A. Seibel, T. Sieber, V. Srinivasan, M. Syha, J. Trueller, W. Vinzenz, M. Vossberg, and C. Will. Status of the FAIR Proton Linac. In *Proceedings of IPAC2019, Melbourne, Australia, pages 889-891*, 2019. URL http://accelconf.web.cern.ch/ipac2019/papers/mopts020.pdf.

[3] M. Schuett. *Design and Development of a 325 MHz Ladder RFQ*. PhD thesis, Goethe University Frankfurt, 2017. URL http://publikationen.ub.uni-frankfurt.de/frontdoor/index/index/docId/45748.

[4] M. Schuett, U. Ratzinger, and M. Syha. First RF Measurements of the 325 MHz Ladder-RFQ. In *Proceedings of LINAC2018, Beijing, China, pages 826-829*, 2018. URL https://doi.org/10.18429/JACoW-LINAC2018-THPO060.

[5] M. Schuett, U. Ratzinger, and M. Syha. RF Measurements and Tuning of the 325 MHz Ladder-RFQ. In *Proceedings of IPAC2019, Melbourne, Australia, pages 925-927*, 2019. URL https://doi.org/10.18429/JACoW-IPAC2019-MOPTS033.

[6] I. M. Kapchinsky and V. A. Teplyakov. A Linear Ion Accelerator with Spatially Uniform Hard Focusing. *Prib. Tekh. Eksp.*, 2(SLAC-TRANS-0099):19–22, 1969. URL http://inspirehep.net/record/54829/files/slac-trans-0099.pdf.

[7] Y.A. Budanov, O. Belyaev, S. Ivanov, A. Maltsev, I. Maltsev, V. Stepanov, S. Strekalovskyh, V. Teplyakov, and V. Zenin. RFQ Drift-Tube Proton Linacs in IHEP. In *Proceedings of LINAC2004, Lübeck, Germany, pages 285-287*, 2004. URL https://accelconf.web.cern.ch/l04/PAPERS/TUP01.PDF.

[8] A. M. Lombardi. The Radio Frequency Quadrupole (RFQ). In *Proceedings of the CERN Accelerator School 2005: Small Accelerators (CERN-2006-012), Zeegse, Netherlands, pages 201-207*, 2006. URL http://cds.cern.ch/record/813710/files/CERN-2006-012.pdf?version=1.

[9] K. R. Crandall, R. H. Stokes, and T. P. Wangler. RF Quadrupole Beam Dynamics Design Studies. In *Proceedings of LINAC79, Montauk, New York, USA, pages 205-216*. Los Alamos Scientific Lab., NM (USA), 1980. URL https://accelconf.web.cern.ch/l79/papers/s4-1.pdf.

[10] A. Schempp, H. Deitinghoff, M. Ferch, P. Junior, and H. Klein. Four-Rod- λ / 2-RFQ for Light Ion Acceleration. *Nucl. Instrum. Meth. B*, 10-11(2):831–834, 1985. URL https://doi.org/10.1016/0168-583X(85)90119-3.

[11] A. Schempp. Radio-Frequency Quadrupoles. *CERN Accelerator School, CERN 92-03*, 2: 522–537, 1992. URL http://doi.org/10.5170/CERN-1992-003.522.

[12] A. Schempp. RFQ Accelerators for Ion Implantation. *Nucl. Instrum. Meth. B*, 62:425–430, 1992. URL https://doi.org/10.1016/0168-583X(92)95270-2.

[13] A. Schempp. The Application of RFQs. In *Proceedings of LINAC92, Ottawa, Ontario, Canada, pages 545-549*, 1992. URL https://inis.iaea.org/search/search.aspx?orig_q=RN:28053372.

[14] A. Schempp. Design of Compact RFQs. In *Proceedings of LINAC96, Geneva, Switzerland, pages 53-54*, 1996. URL https://doi.org/10.5170/CERN-1996-007.53.

[15] A. Schempp. An Overview of Recent RFQ Projects. In *Proceedings of LINAC08, Victoria, BC, Canada, pages 41-45*, 2008. URL https://epaper.kek.jp/LINAC08/papers/mo302.pdf.

[16] C. Zhang and A. Schempp. Beam Dynamics Studies on a 200 mA Proton Radio Frequency Quadrupole Accelerator. *Nucl. Instrum. Methods Phys. Res., Sect. A*, 586(2):153–159, 2008. URL https://doi.org/10.1016/j.nima.2007.12.001.

[17] C. Zhang and A. Schempp. Design of an Upgradeable 45-100 mA RFQ Accelerator for FAIR. *Nucl. Instrum. Methods Phys. Res., Sect. A*, 609(2-3):95–101, 2009. URL https://doi.org/10.1016/j.nima.2009.08.051.

[18] C. Zhang. *Linac Design for Intense Hadron Beams.* PhD thesis, Goethe-University Frankfurt, 2009. URL http://publikationen.ub.uni-frankfurt.de/frontdoor/index/index/docId/7538.

[19] C. Zhang and H. Podlech. Design Approach for a 325 MHz, 3 MeV, 70-100 mA Proton Radio-Frequency Quadrupole Accelerator with Low Emittance Transfer. *Nucl. Instrum. Methods Phys. Res., Sect. A*, 947(162756), 2019. URL https://doi.org/10.1016/j.nima.2019.162756.

[20] F. Hinterberger. *Physik der Teilchenbeschleuniger und Ionenoptik.* Springer-Verlag, 2008.

[21] K. R. Crandall, T. P. Wangler, L. M. Young, J. H. Billen, G. H. Neuschaefer, and D. L. Schrage. RFQ Design Codes. Technical report, Los Alamos National Laboratory, 2005.

[22] L. Young and J. Stovall. RFQGen User Guide. Technical report, Los Alamos National Laboratory, 2021.

[23] R. Duperrier. *Intense Beam Dynamics in RFQs.* PhD thesis, Universite de PARIS-SUD U.F.R. Scientifique d'Orsay, 2000.

[24] N. Chauvin. Beam Dynamics Studies for the FAIR p-Linac LEBT (FPL-INJ-BeamDyn-2013-1). Technical report, CEA-Scalay French Alternative Energies and Atomic Energy Commission.

[25] R. Berezov, O. Delferriere, J. Fils, Y. Gauthier, R. Hollinger, K. Knie, C. Kleffner, and O. Tuske. Status of High Intensity Proton Injector for Facility for Antiproton and Ion Research. *Rev. Sci. Instrum.*, 90(123309), 2019. URL https://doi.org/10.1063/1.5127820.

[26] T. P. Wangler. *RF Linear Accelerators.* 2008 WILEY-VCH Verlag GmbH & Co. KGaA, Weinheim, 2 edition, 2008. URL https://onlinelibrary.wiley.com/doi/book/10.1002/9783527623426.

[27] H. Hähnel, C. M. Kleffner, U. Ratzinger, M. Syha, and R. Tiede. End to End Simulations and Error Studies of the FAIR Proton Linac. In *Proceedings of IPAC2019, Melbourne, Australia, pages 885-888*, 2019. URL https://doi.org/10.18429/JACoW-IPAC2019-MOPTS019.

[28] M. Schuett, M. Syha, and U. Ratzinger. Compensation of Longitudinal Entrance and Exit Gap Field Effects in RFQ's of the 4-ROD Type. *Nuclear Inst. and Methods in Physics Research, A*, 928:58–64, 2019. URL https://doi.org/10.1016/j.nima.2019.02.071.

[29] J. Schmidt, B. Koubek, and A. Schmepp. Simulations on the Boundary Fields of 4-Rod RFQ Electrodes. In *Proceedings of IPAC2013, Shanghai, China, pages 3803 - 3805*, 2013. URL https://accelconf.web.cern.ch/ipac2013/papers/thpwo020.pdf.

[30] S. S. Kurennoy, R. W. Garnett, and L. J. Rybarcyk. Electromagnetic and Multi-Particle Beam Dynamics Modeling of 4-Rod RFQs. In *Proceedings of IPAC2013, Shanghai, China, pages 3978-3980*, 2013. URL https://accelconf.web.cern.ch/ipac2013/papers/thpwo094.pdf.

[31] J. S. Schmidt, D. S. Bollinger, K. L. Duel, P. R. Karns, B. Koubek, S. S. Kurennoy, W. A. Pellico, V. E. Scarpine, A. Schempp, B. A. Schupbach, and C. Y. Tan. Investigations of the output energy deviation and other parameters duringcommissioning of the four-rod radio frequency quadrupoleat the fermi national accelerator laboratory. *Phys. Rev. ST Accel. Beams*, 17(030102), 2014. URL https://doi.org/10.1103/PhysRevSTAB.17.030102.

[32] H. W. Pommerenke. RF Design of a High-Frequency RFQ Linac for Pixeanalysis. In *Proceedings of LINAC2018, Beijing, China, pages 822-825*, 2018. URL http://doi.org/10.18429/JACoW-LINAC2018-THPO058.

[33] S. Mathot, G. Anelli, S. Atieh, F. Benetti, A. Bilton, B. Bulat, Th. Callamand, S. Calvo, L. Castelli, M. Chiari, C. Czelusniak, S. Falciano, G. Favre, M. Fedi, J.-M. Geisser, A. Gerardin, L. Giuntini, A. Grudiev, A. Lombardi, P. A. Mando, M. Manetti, E. Matacotta, C. Montesinos, F. Motschmann, H. Pommerenke, E. Previtali, P. Richerot, , C. Ruberto, K. Scibor, F. Taccetti, M. Timmins, V. Virgili, and M. Vretenar. The CERN PIXE-RFQ, a Transportable Proton Accelerator for the Machina Project. *Nucl. Instrum. Methods Phys. Res., Sect. B*, 459:153–157, 2019. URL https://doi.org/10.1016/j.nimb.2019.08.025.

[34] A. Bechtold. *Eine integrierte RFQ-Driftröhrenkombination für ein Medizin-Synchrotron.* PhD thesis, Goethe-University Frankfurt, 2003. URL https://hds.hebis.de/ubffm/Record/HEB118562967.

[35] B. Koubek, J. Haeuser, J. Schmidt, and A. Schempp. RF Setup of the MedAustron RFQ. In *Proceedings of LINAC2012, Tel-Aviv, Israel, pages 35-37*, 2012. URL https://accelconf.web.cern.ch/LINAC2012/papers/supb014.pdf.

[36] I. Hofmann. Emittance Growth of Beams Close to the Space Charge Limit. *IEEE Trans. Nucl. Sci.*, 28(3), 1981. URL https://accelconf.web.cern.ch/p81/PDF/PAC1981_2399.PDF.

[37] I. Hofmann. Stability of Anisotropic Beams with Space Charge. *Phys. Rev. E*, 57(4):4713–4724, 1998. URL https://doi.org/10.1103/PhysRevE.57.4713.

[38] R. A. Jameson. RFQ Designs and Beam-Loss Distributions for IFMIF. Technical report, Oak RidgeNational Laboratory, 2007. URL https://info.ornl.gov/sites/publications/files/Pub6207.pdf.

[39] U. Ratzinger. A Low Beta RF Linac-Structure of the IH-Type with Improved Radial Acceptance. In *Procedings of LINAC88, Williamsburg (Virginia), USA, pages 185-187*, 1988. URL https://accelconf.web.cern.ch/l88/papers/mo3-55.pdf.

[40] A. Schempp. 4 Rod RFQ Injector for GSI Linac. In *Proceedings of PAC89, Chicago, USA, pages 1093 - 1097*, 1989. URL https://accelconf.web.cern.ch/p89/PDF/PAC1989_1093.PDF.

[41] J. Klabunde. The High Charge State Injector for GSI. In *Proceedings of the 1992 Linear Accelerator Conference, Ottawa, Ontario, Canada, pages 570-574*, 1992. URL https://accelconf.web.cern.ch/l92/papers/th1-02.pdf.

[42] P. J. Spiller, W. Barth, O. Dolinskyy, F. Hagenbuck, O. Kester, K. Knie, R. Maier, D. Prasuhn, H. Reich-Sprenger, H. Simon, U. Weinrich, and M. Winkler. Status of the FAIR Accelerator Facility. In *Proceedings of IPAC2014, Dresden, Germany, pages 2084-2087*, 2014. URL https://doi.org/10.18429/JACoW-IPAC2014-WEPRO060.

[43] O. Kester. The FAIR Proton Linac. In *Proceedings of the Second International Workshop on Technology and Components of Accelerator-Driven Systems (TCADS-2), Nates, France, pages 325-328*, 2013. URL https://www.oecd-nea.org/jcms/pl_19606.

[44] M. Heilmann, A. Adonin, W. Barth, C.E. Düllmann, R. Hollinger, E. Jäger, P. Scharrer, W. Vinzenz, and H. Vormann. High Current Proton and Carbon Beam Operation via Stripping of a Molecular Beam at GSI UNILAC. In *Proceedings of IPAC2016, Busan, Korea, pages 1391-1393*, 2016. URL https://doi.org/10.18429/JACoW-IPAC2016-TUPMR057.

[45] M. Heilmann, A. Adonin, S. Appel, W. Barth, P. Gerhard, F. Heymach, R. Hollinger, W. Vinzenz, H. Vormann, and S. Yaramyshev. Unilac Proton Injector Operation for FAIR. In *Proceedings of IPAC2015, Richmond, VA, USA, pages 3709-3711*, 2015. URL https://doi.org/10.18429/JACoW-IPAC2015-THPF013.

[46] L. Groening, W. Barth, L. Dahl, R. Hollinger, P. Spädtke, W. Vinzenz, S. Yaramishev, B. Hofmann, Z. Li, U. Ratzinger, A. Schempp, and R. Tiede. A Dedicated 70 MeV Proton

Linac for the Antiproton Physics Program of the Future Facility for Antiproton and Ion Research (FAIR) at Darmstadt. In *Proceedings of LINAC 2004, Lübeck, Germany, pages 42-44*, 2004. URL https://accelconf.web.cern.ch/l04/PAPERS/MOP06.PDF.

[47] H. Bayle, O. Delferriére, R. Gobin, F. Harrault, J. Marroncle F. Senée, C. Simon, and O. Tuske. Effective Shielding to Measure Beam Current from an Ion Source. *Rev. Sci. Instrum.*, 85(02A713), 2014. URL https://doi.org/10.1063/1.4829736.

[48] U. Ratzinger. The New High Current Ion Accelerator at GSI and Perspectives for Linac Design Based on H-Mode Cavities. In *Proceedings of EPAC2000, Vienna, Austria, pages 98 - 102*, 2000. URL https://accelconf.web.cern.ch/e00/PAPERS/TUZF204.pdf.

[49] A. M. Almomani, M. Busch, F. Dziuba, C. M. Kleffner, U. Ratzinger, and R. Tiede. Updated Cavities Design for the FAIR p-Linac. In *Proceedings of IPAC2017, Copenhagen, Denmark, pages 2227-2229*, 2017. URL https://doi.org/10.18429/JACoW-IPAC2017-TUPVA064.

[50] M. Almalki, J. Balaguer, R. Brodhage, P. Fork, P. Girardot, W. Kaufmann, O. Kester, P. Kowina, T. Sieber, and C. Simon. The Mechanical Design of the BPM Inter-Tank Section for p-Linac at FAIR. In *Proceedings of IPAC2014, Dresden, Germany, pages 3474-3476*, 2014. URL https://doi.org/10.18429/JACoW-IPAC2014-THPME100.

[51] R. Brodhage, M. Kaiser, U. Ratzinger, W. Vinzenz, and M. Vossberg. Status of the FAIR Proton Linac. In *Proceedings of IPAC2015, Richmond, VA, USA, pages 3702-3704*, 2015. URL https://doi.org/10.18429/JACoW-IPAC2015-THPF011.

[52] D. Koser. *Development of a 108 MHz 4-Rod CW RFQ-Design for High Duty Cycle Acceleration of Heavy Ion Beams at the GSI-HLI.* PhD thesis, Goethe-University Frankfurt, 2020. URL http://publikationen.ub.uni-frankfurt.de/frontdoor/index/index/docId/59228.

[53] M. Vretenar. The Radio-Frequency Quadrupole. In *Proceedings of the CERN Accelerator School 2011: High Power Hadron Machines (CERN-2013-001), Bilbao, Spain, pages 207-223*, 2013. URL http://doi.org/10.5170/CERN-2013-001.207.

[54] D. Kleppner and R. J. Kolenkow. *An Introduction to Mechanics*, volume 2. Boston: McGraw-Hill, 1973. ISBN 0-07-035048-5. page 485.

[55] P. W. Hawkes. *Quadrupole Optics (The Electron Optical Properties of Rectilinear Orthogonal Systems).* Springer Tracts in Modern Physics, Volume 42, 1966.

[56] J. P. Blewett. Radial Focussing in the Linear Accelerator. *Phys. Rev.*, 88(5):1197–1199, 1952. URL https://journals.aps.org/pr/pdf/10.1103/PhysRev.88.1197.

[57] L. C. Teng. Alternating Gradient Electrostatic Focusing for Linear Accelerators. *Phys. Sci. Instrum.*, 25(3):264–268, 1953. URL https://doi.org/10.1063/1.1771038.

[58] P. Fischer. *Ein Hochleistungs-RFQ-Beschleuniger für Deuteronen.* PhD thesis, Johann Wolfgang Goethe-Universität, Frankfurt am Main, 2007. URL http://publikationen.ub.uni-frankfurt.de/frontdoor/index/index/docId/1548.

[59] W. Paul and M. Raether. Das elektrische Massenfilter. *Z. Physik*, 140:262–273, 1955. URL https://doi.org/10.1007/BF01328923.

[60] V. A. Tepliakov. RFQ Focusing in Linacs. In *Proceedings of LINAC92, Ottawa, Ontario, Canada, pages 21-24*, 1992. URL https://accelconf.web.cern.ch/l92/papers/mo2-01.pdf.

[61] J. Maus. *Development of RFQ Particle Dynamics Simulation Tools and Validation with Beam Tests.* PhD thesis, Goethe-University Frankfurt, Germany, 2010. URL http://publikationen.ub.uni-frankfurt.de/frontdoor/index/index/docId/20548.

[62] J. Maus. Untersuchungen zur Teilchendynamiksimulation in RFQs. Master's thesis, Goethe-University Frankfurt, Germany, 2008.

[63] P. Lapostolle. CERN Report AR/IntSG/65-15. Technical report, 1965.

[64] T. P. Wangler. Space-Charge Limits in Linear Accelerators (LA-8388 TRN: 81-001972). Technical report, 1980. URL http://www.osti.gov/scitech/biblio/6742291.

[65] L. M. Young. 25 Years of Technical Advances in RFQ Accelerators. In *Proceedings of the 2003 Particle Accelerator Conference, Portland, Oregon, USA, pages 60-64*, 2003. URL https://doi.org/10.1109/PAC.2003.1288841.

[66] P. Lapostolle and M. Weiss. Formulae and Procedures Useful for the Design of Linear Accelerators. Technical report, CERN Report No. CERN-PS-2000-001 (DR), 2000. URL https://cds.cern.ch/record/428133/files/ps-2000-001.pdf.

[67] H. Podlech, A. Bechtold, K. Kuempel, C. Lorey, N. Petry, A. Schempp, P. Schneider, and C. Zhang. The MYRRHA-RFQ - Status and First Measurements. In *Proceedings of IPAC2017, Copenhagen, Denmark, pages 2243-2245*, 2017. URL https://accelconf.web.cern.ch/ipac2017/papers/tupva071.pdf.

[68] C. Zhang and H. Podlech. New Reference Design of the European ADS RFQ Accelerator for MYRRHA. In *Proceedings of IPAC2014, Dresden, Germany, pages 3223-3225*, 2014. URL http://accelconf.web.cern.ch/AccelConf/IPAC2014/papers/thpme008.pdf.

[69] A. Lombardi. End-To-End Beam Dynamics for CERN Linac4. In *Proceedings of HB2006, Tsukuba, Japan, pages 365-371*, 2006. URL https://www.researchgate.net/publication/28611989_End-to-end_beam_dynamics_for_CERN_LINAC4.

[70] C. Rossi, P. Bourquin, S. Cazaux, O. Delferriere, M. Desmons, R. Duperrier, A. France, J.-B. Lallement, D. Leboeuf, A. M. Lombardi, S. Mathot, O. Piquet, M. Timmins, G .Vandoni, and M. Vretenar. The radiofrequency quadrupole accelerator for the linac4. In *Proceedings of LINAC08, Victoria, BC, Canada, pages 157-159*, 2008. URL http://accelconf.web.cern.ch/LINAC08/papers/mop040.pdf.

[71] K. R. Crandall. Ending RFQ Vane Tips with Quadrupole Symmetry. In *Proceedings of the 1994 International Linac Conference, Tsukuba, Japan, pages 227-229*, 1994. URL http://epaper.kek.jp/l94/papers/mo-69.pdf.

[72] Nuclear Physics for Medicine. Technical report, Nuclear Physics European Collaboration Committee (NuPECC), 2014. URL http://www.nupecc.org/pub/npmed2014.pdf.

[73] U. Ratzinger. Effiziente Hochfrequenz-Linearbeschleuniger für leichte und schwere Ionen, 1998. URL https://hds.hebis.de/ubffm/Record/HEB186810857.

[74] R. Tiede. *Simulationswerkzeuge für die Berechnung hochintensiver Ionenbeschleuniger*. PhD thesis, Goethe-University Frankfurt, 2009. URL http://publikationen.ub.uni-frankfurt.de/frontdoor/index/index/docId/6691.

[75] L. Bellan. *Beam Dynamics Characterization of the IFMIF/EVEDA RFQ Input Beam*. PhD thesis, University of Padova, 2017. URL http://paduaresearch.cab.unipd.it/10802/.

[76] W. D. Kilpatrick. Criterion for Vacuum Sparking Designed to Include both RF and DC. *Rev. Sci. Instr.*, 28:824–826, 1957. URL https://doi.org/10.1063/1.1715731.

[77] T. J. Boyd. Kilpatrick's Criterion. Technical report, Los Alamos Group AT-1 report AT-1:82-28, February 12, 1982.

[78] M. Baschke. Strahldiagnose mit neuer Matching-Sektion am Frankfurter Funneling Experiment. Master's thesis, Goethe-University Frankfurt, Germany, 2013.

[79] J.-P. Thibus. *Numerische Berechnungen zum Ionenstrahl-Funneling.* PhD thesis, Goethe-University Frankfurt, Germany, 2007. URL http://publikationen.ub.uni-frankfurt.de/frontdoor/index/index/year/2007/docId/721.

[80] H. Zimmermann. *Untersuchung zum Strahlfunneling.* PhD thesis, Goethe-University Frankfurt, Germany, 2004. URL http://publikationen.ub.uni-frankfurt.de/frontdoor/index/index/docId/4909.

[81] F. J. Sacherer. RMS Envelope Equations with Space Charge. *IEEE Trans. Nucl. Sci.*, 18 (3):1105–1107, 1971. URL https://doi.org/10.1109/TNS.1971.4326293.

[82] P. M. Lapostolle. Possible Emittance Increase through Filamentation due to Space Charge in Continuous Beams. *IEEE Trans. Nucl. Sci.*, 18(3):1101–1104, 1971. URL http://ieeexplore.ieee.org/xpl/freeabs_all.jsp?arnumber=4326292&abstractAccess=no&userType=inst.

[83] U.S. Particle Accelerator School. Introduction to Accelerators: Evolution of Accelerators and Modern Day Applications; Accelerator Structures III - RFQ. URL http://uspas.fnal.gov/materials/11ODU/Proton_7.pdf.

[84] R. Duperrier. TOUTATIS: A Radio Frequency Quadrupole Code. *Phys. Rev. ST Accel. Beams*, 3(124201), 2000. URL https://doi.org/10.1103/PhysRevSTAB.3.124201.

[85] A. Brandt. *Mathematics of Computation vol. 31, pp. 333-390.* 1977.

[86] P. Pierini. A Multigrid-Based Approach to Modeling a High Current Superconducting Linac for Waste Transmutation. 1998. URL https://www.researchgate.net/publication/241300783_A_Multigrid-Based_Approach_to_Modeling_a_High-Current_Superconducting_Linac_for_Waste_Transmutation.

Appendices

A The Synchronous Particle and the Separatrix

Multicell ion linacs generate a specific velocity gain in each accelerating cell. A particle that is a) injected into the linac with the correct initial (design) velocity and b) in synchronicity to the linac's RF field will gain the right amount of energy in each cell to maintain this synchronism with the field. It traverses each linac cell in the same time it takes the field to reverse its polarity, i.e. in half the RF period $T\,/\,2$, and the accelerating field it experiences is given by:

$$E_z(\vec{r},t) = E_0\,\cos(\phi_s)\,, \tag{A.1}$$

whereby E_0 is the longitudinal field amplitude, and ϕ_s is the so-called stable synchronous phase, i.e. the phase of the synchronous particle at cell center associated with stable cell-to-cell phase space motion (see below).

The velocity[1] of the synchronous particle (short: the synchronous velocity) $\beta_s = v_s/c$ increases with each passing cell. Hence, the cell lengths have to increase according to the synchronism condition, which states that the length of the linac's i-th cell[2] $l_{c,i}$ is the product of the synchronous velocity $v_{s,i}$ within this cell and half the RF period of the electric field oscillation $T\,/\,2 \;=\; \lambda/(2\,c)$:

$$l_{c,i} = v_{s,i}\,\frac{T}{2} = \frac{\beta_{s,i}\,\lambda}{2}\,. \tag{A.2}$$

For a given electric field amplitude E_0, the phase of the synchronous particle at cell center can take on two values, which ensure its synchronism with the field: the stable synchronous phase $\phi_{s,s} \;:=\; \phi_s < 0°$ and the unstable synchronous phase $\phi_{s,u} \;:=\; -\phi_s > 0°$. Within the scope of this thesis the term "synchronous phase" is synonymous to "stable synchronous phase" and – other than within this section – is occasionally simply labeled ϕ. (The unstable synchronous phase has no direct relevance for linac designs and is thus not addressed outside this section.)

[1] More accurately, β_s refers to the z-component of the synchronous relative velocity, i.e. the component along the beam axis.

[2] For RFQs, the cell length is half the electrode modulation period (cf. Sec. 2.5).

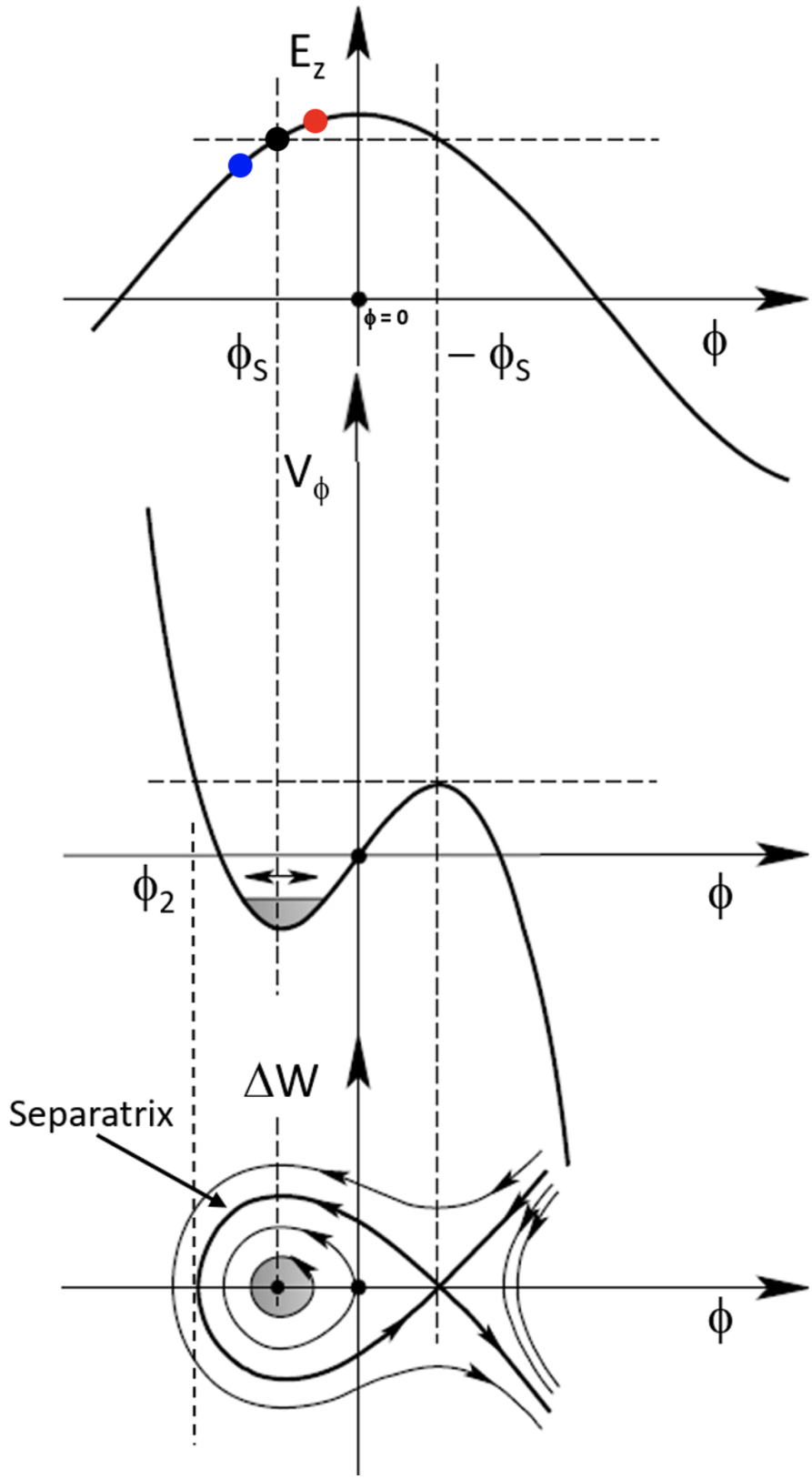

Figure A.1: **Top:** the accelerating field $E_z(\phi)$ as a cosine-function of ϕ. The black dot refers to the synchronous particle of stable synchronous phase ϕ_s, whereas the blue and the red dot refers to an "early" and a "late" particle, respectively.
Middle: potential $V_\phi(\phi)$; its local minimum (within the so-called bucket (see bottom graph)) occurs for $\phi = \phi_s$.
Bottom: particle trajectories and fixed points in phase space. Both the stable (left) and the unstable (right) fixed point occur at $\Delta W = 0$. Their ϕ-coordinates are ϕ_s and $-\phi_s$, respectively. The bold line is the separatrix, the trajectory, which encloses the so-called (beam) bucket. Trajectories within the bucket are stable, those outside the bucket are unstable. The ϕ-values for points within the bucket reach from ϕ_2 to $-\phi_s$.

All three graphs were adapted from Fig. 3.4 of Ref. [73] and refer to a stable synchronous phase $\phi_s = -90° < \phi_s < 0$ ($\phi_s \approx -30°$).

The attributes “stable” and “unstable” refer to the formation and preservation of stable beam bunches. As will be elaborated on in the following, the formation and acceleration of stable beam bunches require the phase of the synchronous particle to take on values ϕ_s with $-90° < \phi_s < 0°$. In this case, the bunch particles perform longitudinal oscillations around the synchronous particle. These oscillations are associated with the bunch particle positions ($\Delta\phi = \phi - \phi_s$, $\Delta W = W - W_s$) in phase space revolving around the so called-stable fixed point on closed trajectories.

The upper graph in Fig. A.1 shows the accelerating electric field E_z as a cosine function of particle phase ϕ. The (stable) synchronous phase $\phi_s < 0°$ lies on the rising edge of E_z. A particle with phase $\phi_s < \phi < -\phi_s$, i.e. a particle moderately faster than the synchronous particle reaches position z_* prior to it and is thus exposed to a lower accelerating field (cf. Eq. A.1). Therefore, the synchronous particle will eventually catch up with it and surpass it. A particle with phase $\phi_2 < \phi < \phi_s$ (see middle graph of Fig. A.1), whereby $\phi_2 \approx 2\,\phi_s$ [26], i.e. a particle moderately slower than the synchronous one reaches z_* after it and is hence exposed to stronger accelerating fields, so that it will eventually catch up with the synchronous particle and surpass it. In that way, particles both moderately faster and slower than the synchronous one oscillate around it and thereby contribute to a stable beam bunch. It can be demonstrated in analogy to this, that stable bunch formation around a synchronous particle of unstable synchronous phase $\phi_{s,u} = -\phi_s$ (whereby $-90° < \phi_s < 0\,°$) cannot be accomplished: particles slower than the synchronous particle are exposed to weaker accelerating fields and thus are even further slowed down, whereas faster particles experience higher fields and are thus further accelerated.

In a bunch around a synchronous particle with phase $\phi_s = 0°$ and maximum energy gain (cf. Eq. A.1), faster particles are also exposed to lower fields, which – as argued above – leads to bunch stability. Slower particles, however, are exposed to lower fields and thus will never be able to catch up. Such a bunch will therefore disperse.

The middle plot of Fig. A.1 shows the longitudinal potential $V_\phi(\phi)$, which reaches a local minimum at ϕ_s. The graph at the bottom shows four longitudinal phase space trajectories including the limiting stable trajectory known as the separatrix. The separatrix is also more casually referred to as “fish” or “golf club” among accelerator physicists as it – depending on the specific premises – resembles a stylized fish similar to the Christian “ichthys”-symbol or the

top of a golf club[3] (see Fig. A.2). Its name stems from the Latin word "separare" as this line separates the phase space into an inner area of stable and an outer area of unstable particle motion. The phase space area enclosed by the separatrix is called (beam) bucket. The separatrix passes through the unstable fixed point at $\Delta W = 0$ and $\phi = -\phi_s$. The coordinates of the stable fixed point are $\Delta W = 0$ and $\phi = \phi_s$. Only the trajectories inside the bucket are associated with stable particle motion in phase space, i.e. a revolution around the stable fixed point.

The bucket phase width[4] Ψ only depends on the synchronous phase ϕ_s:

$$\tan(\phi_s) = \frac{\sin(\Psi) - \Psi}{1 - \sin(\Psi)} . \tag{A.3}$$

For sufficiently small values of $|\phi_s|$ (for $|\phi_s|$ up to about 55°) this equation can be approximately solved for Ψ as[5]:

$$\Psi \approx 3 \cdot \phi_s . \tag{A.4}$$

The geometric bucket length Z_Ψ, sometimes also simply referred to as bunch length, is a function of ϕ_s:

$$Z_\Psi = \frac{|\Psi|, \beta_s \lambda}{2\pi} . \tag{A.5}$$

Kapchinsky and Teplyakov showed that Z_Ψ (and hence the bunch length) as well as as the so-called longitudinal small oscillation frequency are to be kept (nearly) constant during (quasi-)adiabatic beam bunching [26]. This requires ϕ_s to be varied along the RFQ in such a relation to β_s that $\Psi \times \beta_s$ remains constant.

The bucket area is maximum for $\phi_s = -90°$, and so is the phase acceptance: $\Psi = 360°$ (see Fig. A.2). However, the synchronous particle is not accelerated at all in this case (cf. Eq. A.1). In order to achieve acceleration of stable bunches, the synchronous particle's phase ϕ_s has to fulfill $-90° < \phi_s < 0°$. For drift-tube linacs, a synchronous phase ϕ_s of about $-30°$ is commonly chosen to ensure that acceleration is efficient and the bunches are furthermore sufficiently long [26]. The (final) phase of the (main) acceleration section of RFQs usually also takes on values around $-30°$.

[3] In this case one should actually speak of a quasi-separatrix rather than a separatrix as the latter per definition is a closed line, which is not the case for a "golf club" (see Fig. A.3).

[4] Not to be confused with the electric potential Ψ from App. E.

[5] The detailed derivations of Eqs. A.3 and A.4 are given in Sec. 6.4 of Ref. [26].

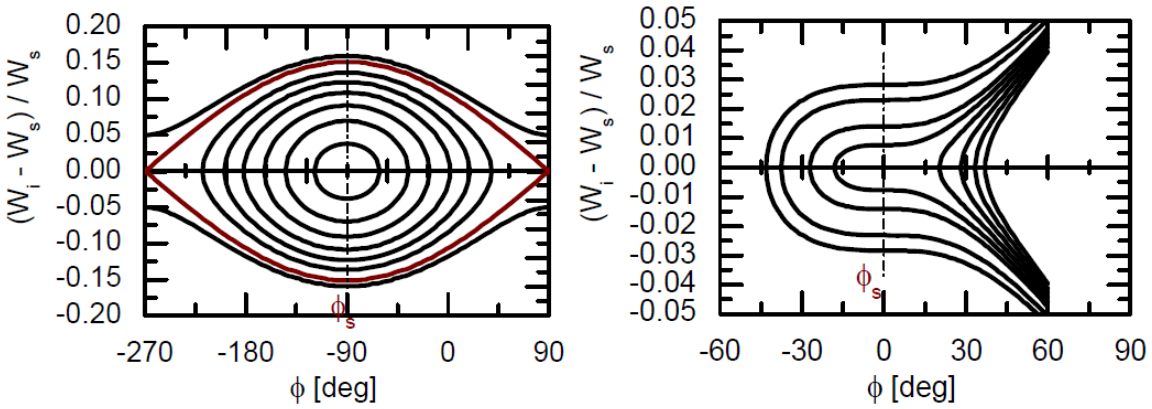

Figure A.2: Particle trajectories in phase space for the extreme-values of the synchronous phase $\phi_s = -90°$ (left) and $\phi_s = 0°$ (right) [74].
Left: For $\phi_s = -90°$ the bucket (enclosed by the separatrix drawn in brown), its phase width and geometric length are maximal: $\Psi = 360°$ and $Z_\Psi = \beta_s \lambda$. However, the synchronous particle is not accelerated in this case.
Right: For $\phi_s = 0°$ the synchronous particle is maximally accelerated, but no separatrix and thus no bucket exist as all trajectories are unstable.

The energy half width ΔW_{h-w} of the separatrix in the stable fixed point is (cf. Eq. 6.28 in Sec. 6.4 of Ref [26]):

$$\Delta W_{h-w} = \sqrt{\frac{2}{\pi} mc^2 qeE_0 T \beta_s^3 \gamma_s^3 \lambda (\phi \cos\phi_s - \sin\phi_s)}. \tag{A.6}$$

mc^2 and $q\,e$ are the particle rest energy and charge, respectively. Unfortunately, the so-called transit-time factor or transient-time factor T is designated the same symbol as the RF-period. Usually, $0.7 \leq T \leq 0.9$ holds true for linacs. The transient-time factor for RFQs is $T_{RFQ} = \frac{\pi}{4} \approx 0.79$ [26]. The relative velocity β_s, Lorentz factor γ_s and phase ϕ_s of the synchronous particle as well as the average axial electric field E_0 refer to the last acceleration cell [21] and are given in several tables of the RFQGen output-files.

A.1 Opening of the Bucket Under Acceleration

Above elaborations are not correct in a strict sense, but usually sufficiently accurate. However, in fact, the separatrix is a closed line only for constant values of β_s and γ_s, i.e. if the synchronous particle is not accelerated at all [26]. As β_s and γ_s increase along a linac, the bucket is expected to open; the separatrix is no closed line anymore (see Fig. A.2). For this reason, one should address

this trajectory and the area "enclosed" by it as quasi-separatrix and quasi-bucket, respectively. The quasi-bucket decreases with increasing particle energy. However, in case β_s, ϕ_s and field amplitude E_0 change adiabatically, it is possible to trap the particles oscillating within the quasi-bucket [74].

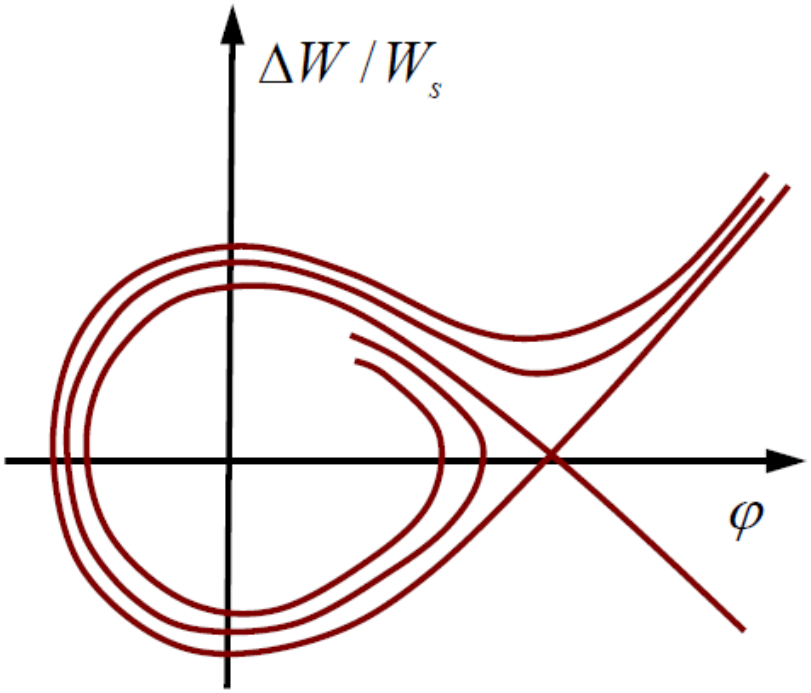

Figure A.3: The open quasi-bucket, which is "enclosed" by a "golf club"-shaped quasi-separatrix, forms as β_s and γ_s increase along the linac; particle trapping is still possible if these parameters change adiabatically [74].

B Space-Charge Compensation in the LEBT of the FAIR p-Linac

As the proton beam ionizes the residual Hydrogen-gas, electrons (as well as the contaminating ion-species H^{2+} and H^{3+}) are produced [75]. This electron generation is beneficial for the beam quality since these electrons are trapped by the proton beam; they stabilize its radial dimension since they compensate the repulsive space-charge forces between the protons. However, these electrons would experience strong acceleration by the RFQ electrodes even whilst they are still within the LEBT-section and the proton beam's space-charge compensation degree thus would rapidly decline. In order to keep the SCC-degree high along the LEBT-line, so-called repeller electrodes are placed at its end, as close to the RFQ entrance flange as possible. Although they generate an effective Coulomb barrier for the compensation electrons, the protons are not (significantly) accelerated/influenced by the repeller due to their much higher energies and masses [24]. (Reference [75] provides a detailed quantified description of these phenomena and principles in case of the IFMIF/EVEDA RFQ, which (among others) also can be operated with proton beams.)

As the repeller of the FAIR p-Linac RFQ works very efficient, the space-charge compensation degree for the RFQ entrance beam is considered 0%, albeit the beam was considered to be 90%

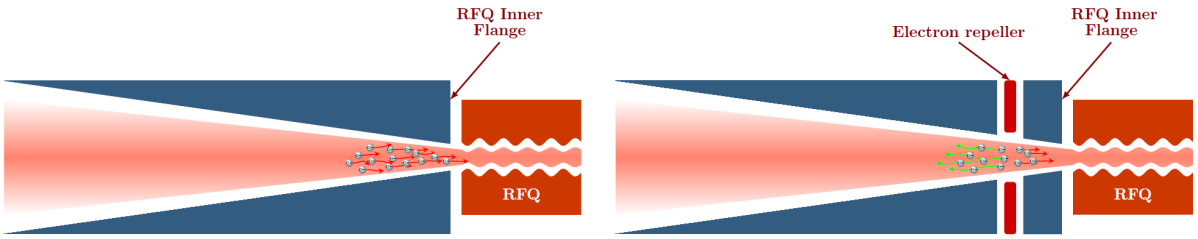

Figure B.1: RFQ injection cone without (left) and with an electron repeller (right) [24]. The repeller should be positioned as close to the RFQ entrance flange as possible so that a significant fraction of electrons do not pass the Coulomb barrier and thus still contribute to space-charge compensation along a maximal distance.

space-charge compensated for the LEBT-simulations[1].

Behind the repeller, the remaining electrons still trapped by the beam are rapidly "pulled" to the RFQ electrodes so that the beam's SCC-degree is basically 0% for the remaining drift into the RFQ and trough the RFQ entrance gap. To minimize this delicate distance without space-charge compensation, the repeller should be positioned as close to the RFQ entrance flange as possible and the RFQ entrance gap should be as short as the resulting gap-fields allow for (cf. Sub-Sec. 3.7.1).

[1] SCC-degree for LEBT beam dynamics simulations with TraceWin chosen in consultation with R. Berezov (GSI).

C The Bravery Factor

Room-temperature cavities with a copper surface will suffer from electric breakdown or sparking if their electric surface fields are sufficiently high. The mechanisms responsible for this are not fully understood yet, but electron field emission is suspected to initiate them. Furthermore, it has been suggested that protons originating on the surfaces or possibly from residual hydrogen gas take part in the discharge [26].

A large data set on RF breakdowns was evaluated during the 1950s by W. D. Kilpatrick in order to subsequently define conditions for breakdown-free operation of linacs [76]. Decades later, T. J. Boyd expressed these in the following concise formula:

$$\mathcal{F} = 1.64\,\mathcal{E}_\mathcal{K}{}^2\,e^{-\frac{8.5}{\mathcal{E}_\mathcal{K}}}, \tag{C.1}$$

whereby $\mathcal{F}$ is the numerical value of frequency f, if it is given in units of MHz, and $\mathcal{E}_\mathcal{K}$ is the numerical value of the so-called Kilpatrick (field) limit E_K, if it is given in units of MV / m.

The Kilpatrick limit E_K is the (hypothetical) maximal surface field, for which no breakdown occurs [77]. As can be seen, this limit increases with increasing frequency. For a given frequency $f = \mathcal{F}\,MHz$, Eq. C.1 requires to be solved iteratively for $\mathcal{E}_\mathcal{K}$[1].

As the underlying data were gained in an era before clean vacuum systems became standard, the Kilpatrick limit E_K is regarded as too conservative by today's standards, i.e. the actually present maximum surface field in a linac can exceed this limit significantly without field breakdown occurring. Nevertheless, E_K is still considered a key parameter for linac designs as the actually expected peak surface field $E_{S,max}$ is expressed through it:

$$E_{S,max} = b\,E_K, \tag{C.2}$$

[1] The LANL Code Collection "Poisson Superfish" includes a tool written for this specific purpose. More information about this package can be found at `https://laacg.lanl.gov/laacg/services/download_sf.phtml`, where it can also be downloaded from.

with b being the so-called bravery or Kilpatrick factor. b is usually chosen from 1.0 to 2.0 by accelerator designers [26], and the (maximum) electrode voltage and the minimum aperture along the RFQ have to be chosen in accordance with the resulting $E_{S,max}$.

For RFQs, b is usually kept below 1.8, although a value of 2.0 has been reached/surpassed in some cases without causing breakdown[2]. With $E_K = 17.8\,MV\,/\,m$ and $E_{S,max} = 31.5\,MV\,/\,m$, the bravery factor of the FAIR p-Linac RFQ takes on a rather conservative value of $b = 1.77$ (cf. Tab. 3.1 in Chap. [3]). (Detailed information on the calculation and/or simulation of the E_K- and $E_{S,max}$-values, respectively, of the FAIR p-Linac RFQ is given in Ref. [3].)

[2] Correspondence with L. M. Young and A. M. Lombardi.

D Beam Emittances

Each beam particle is associated with a point in the six dimensional phase space spanned by the three coordinate axes of the local domain (i.e. the x-, y- and z-axis) and the three axes of the momentum-space (i.e. the p_x-, p_y- and p_z-axis). In many cases its 2-dimensional sub-spaces $x-p_x$, $y-p_y$ and $z-p_z$ are more relevant and suited to describe beam dynamics and each beam particle can also be assigned to a point in each of these sub-spaces. The distributions of these points are associated with certain ellipses within these sub-spaces; this will be discussed more detailed below. For each sub-space, the so-called emittance ε is proportional to the area of the respective ellipse area F:

$$\varepsilon = \frac{F}{\pi}. \tag{D.1}$$

Emittances are (among others) classed as total or effective and as unnormalized or normalized emittances (see Sec. D.6). A further important emittance category is the rms-emittance. Three common definitions for the rms-emittance exist within the accelerator community. The rms-emittance is also determined by the specific particle distribution function (see Sub-Sec. D.4.1).

D.1 Transverse Emittances

The transversal components of the electric fields cause the particles to perform transversal oscillations around the beam axis, which define the contours in the x-p_x-sub-space. p_x and p_y are usually substituted by the divergences (or divergence angles) $x' = \frac{p_x}{p}$ and $y' = \frac{p_y}{p}$ [26]. If these forces are predominately linear, the angular frequencies of all particles are identical. This results in elliptical trajectories in phase space, also trajectory ellipses [26]. (The analogous holds true in the longitudinal phase space.) In this case concentric iso-(particle-)densities contours occur, which show significant geometric similarities to the trajectory ellipses, and so-called beam matching occurs. (Matching the input beam into an RFQ presents a non-trivial challenge, since it requires the transition of a beam exhibiting time-independent characteristics into one whose characteristics show an exactly suited time-dependence [26].)

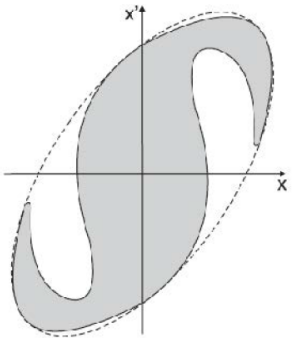

Figure D.1: The area in x-x'-phase space that actually is occupied by beam particle points (marked in gray) and framed by the continuous circumference, corresponds with the total emittance ε_{total}. The area enclosed by the dashed ellipse is associated with the effective emittance ε_{eff} [78].

D.2 Equation of an Ellipse and Percentage Emittances

Consider an ellipse in sub-space[1] x-x', its midpoint being congruent with the co-ordinate midpoint. Its main axes are x and $x\acute{}$ and the lengths of its semi-axes are a and b. This ellipse can be described by the general equation of an ellipse. If non-linear forces are present, the angular frequencies of particles further away from the beam axis exceed these of particles closer to the beam axis. After several oscillation periods the former will have outrun the latter [26]. Furthermore, particle trajectories get distorted and no longer resemble ellipses.

This leads to the total emittance ε_{total}, i.e. the emittance that corresponds to the actual area in the respective sub-space occupied by particles. This area in principle can take on virtually any imaginable form. The total emittance is almost impossible to measure, though this poses no real problem as this quantity has no direct relevance in the field of applied accelerator physics. However, it is necessary to define the effective emittance ε_{eff}. In accordance to Eq. D.9 this emittance corresponds with the smallest ellipse that includes all particle points in this sub-space (see Fig. D.1). Thus $\varepsilon_{eff} \geq \varepsilon_{total}$ always holds true.

As real beams usually do not exhibit well-defined boundaries single widespread particle points are often ignored, which leads to the concept of percentage emittances. They are defined by the ellipse-contour that refers to the respective percentage of the maximum particle density in

[1] The following considerations can of course also be applied to the y-y'- and the longitudinal $\Delta\phi$-ΔW-phase spaces.

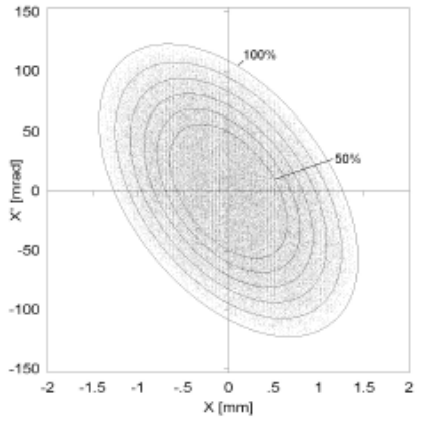

Figure D.2: Particle distribution in the x-x'-sub-space and the concentric ellipses associated with the 50 %-, 60 %-, 70 %-, 80 %-, 90 %- and 100 %-emittances (with $\varepsilon_{100\%} = \varepsilon_{eff}$) [79].

the respective sub-space (see Fig. D.2). Thus, the 50%-, 90%- and 95%-emittances refer to the contours of 50%, 90% and 95%, respectively, of the maximum density (to mention the most common percentages). In case that only condition (1) holds true the area occupied by beam particles will grow over time and hence the percentage emittances are not preserved.

Even though the percentage emittances (including the effective emittance, i.e. $\varepsilon_{100\%} = \varepsilon_{eff}$) are essential for the characterization of a beam, a beam emittance definition (largely) independent of the shape of the concrete area occupied by particle points would be of great use. Luckily, in form of the rms-emittance ε_{rms} this quantity actually exists. It will be addressed in greater depth in Sec. D.4 of App. D, but at first it is necessary to introduce the so-called Twiss parameters in order to derive at a more adequate, but also a more abstract ellipse equation.

D.3 The Twiss Parameters

Normally the x- and $x\,'$-axes[2] are not congruent to the principle axes of the emittance ellipse, but instead are rotated by an angle[3] $\psi \neq 0°$ against them (see Fig. D.3). It is possible to parametrically express the spacial co-ordinate $\tilde{x}$ and the angular co-ordinate $\tilde{x'}$ on the principle axes of such an ellipse by:

[2] For convenience the following considerations only address the x-x'-phase space. However, they can easily be applied to the other two planes, i.e. the y-y'- and the $\Delta\phi$-ΔW-sub-spaces (see Sec. D.6).
[3] Not to be confused with the bucket phase width Ψ from Chap. A.

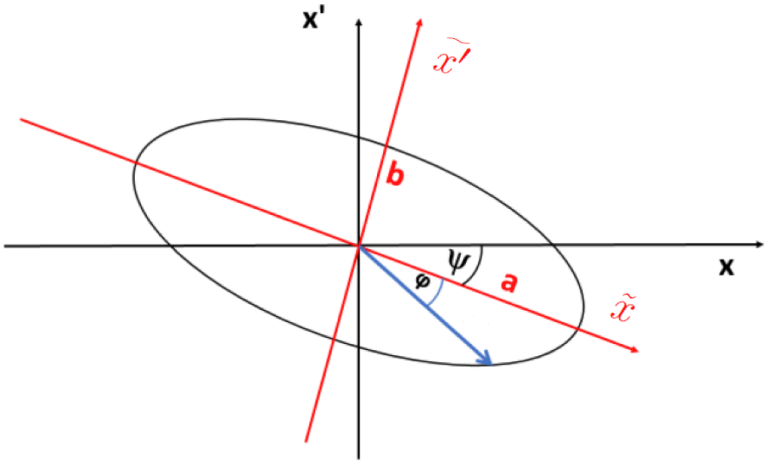

Figure D.3: Shown is an ellipse in the x-x'-plane that is rotated by angle ψ against the main axes. Vector $\vec{o} = \begin{pmatrix} \tilde{x} \\ \tilde{x'} \end{pmatrix}$ connects the co-ordinate origin with the point on the ellipse circumference representing this particle. φ is the acute angle spanned between $\vec{o}$ and the $\tilde{x}$-axis.

$$\tilde{x} = a \cos\varphi \tag{D.2}$$

and

$$\tilde{x'} = b \sin\varphi, \tag{D.3}$$

whereby $\varphi \in [0; 2\pi]$ is the internal rotation angle between vector $\vec{o} = \begin{pmatrix} \tilde{x} \\ \tilde{x'} \end{pmatrix}$ of the respective beam particle and the $\tilde{x}$-axis (see Fig. D.3). Via a rotational matrix the principle co-ordinates $(\tilde{x}, \tilde{x'})$ can be transferred to (x, x') [80]:

$$\begin{pmatrix} x \\ x' \end{pmatrix} = \begin{pmatrix} \cos\psi & \sin\psi \\ -\sin\psi & \cos\psi \end{pmatrix} \begin{pmatrix} \tilde{x} \\ \tilde{x'} \end{pmatrix}. \tag{D.4}$$

Via Eq. D.2 - Eq. D.4 the lengths of the semi-axes a and b get [26]:

$$a = \frac{x \cos\psi - x' \sin\psi}{\cos\varphi} \tag{D.5}$$

$$b = \frac{x \sin\psi - x' \cos\psi}{\sin\varphi}. \tag{D.6}$$

The area F of an ellipse simply being

$$F = \pi\, a\, b, \tag{D.7}$$

emittance ε can thus by applying Eq. D.1 and Eq. D.7 be written as:

$$\varepsilon = \frac{F}{\pi} = a\, b, \tag{D.8}$$

i.e. as the product of the lengths of the semi-axes. In accordance to Eq. D.4 it can also be expressed by [26]:

$$\varepsilon = a\, b = x^2 \left(\frac{a}{b} \sin^2\psi + \frac{b}{a} \cos^2\psi\right) + 2\, x\, x' \sin\psi \cos\psi \left(\frac{a}{b} - \frac{b}{a}\right) + x'^2 \left(\frac{a}{b} \cos^2\psi + \frac{b}{a} \sin^2\psi\right). \tag{D.9}$$

In the above discussion the x- and $x\,'$-axes were treated as if they were dimensionless (or at least at if they were of the same dimension). However, this is not the case since x defines a length and $x\,'$ defines an angle. Accordingly the dimensions of x and $x\,'$ are m (usually cm or mm instead) and rad (usually mrad instead), respectively. Emittance ε is therefore of dimension m rad (usually cm mrad or mm mrad instead). From this follows that the semi-axes of an ellipse tilted by $\psi \neq 0°$ ($\psi \in [0, 360°)$) against the x- and the $x\,'$-axis, respectively, are generally of undefined dimensions. It is important to note, that the rotation angle ψ usually depends on the scaling of the axes and therefore lacks physical meaning. However, for four values of ψ the principal axes $\tilde{x}$ and $\tilde{x}'$ are "congruent"[4] to co-ordinate axes x and x'. Theses values are 0°, 90°, 180° and 270°. Here, the principal axes are of defined dimensions and ψ is independent on the axes' scaling. All this implies that characterization of ellipses by their semi-axis lengths a and b and rotation angle ψ as in Eq. D.9 is inapplicable in most cases, as these parameters usually depend on the chosen co-ordinate axes [62].

By introducing the Twiss[5] parameters α, β and γ via

$$\alpha := \left(\frac{a}{b} - \frac{b}{a}\right) \sin\psi \cos\psi, \tag{D.10}$$

[4] The principal axes are congruent in that sense, that spacial co-ordinate axes x and $\tilde{x}$ as well as angular axes x' and $\tilde{x}'$, respectively, are congruent to each other also in regard to their orientation. In the case of $\psi = 0°$ one refers to it as an upright ellipse.

[5] Twiss parameters β and γ are not to be confused with the relative longitudinal velocity $\beta = \frac{v}{c}$ and the Lorentz factor γ, respectively (cf. Sec. D.6).

$$\beta := \frac{b}{a}\,\sin^2\psi \,+\, \frac{a}{b}\,\cos^2\psi \tag{D.11}$$

and

$$\gamma := \frac{a}{b}\,\sin^2\psi \,+\, \frac{b}{a}\,\cos^2\psi \tag{D.12}$$

emittance ε can be expressed much more comprehensively according to Eq. D.9:

$$\varepsilon = a\,b = \gamma\,x^2 \,+\, 2\,\alpha\,x\,x' \,+\, \beta\,x'^2. \tag{D.13}$$

Other than a, b and ψ the Twiss parameters are independent of the axes' scaling and are coupled to each other by [62]:

$$\gamma = \frac{1+\alpha^2}{\beta}. \tag{D.14}$$

Thus, if the values of two Twiss parameters are given, the third is then automatically determined, i.e. only two Twiss parameters can be chosen independently. As $1 + \alpha^2 > 0$ it further follows that β and γ have to exhibit the same sign. Whereas α is dimensionless, β has the dimensions $\frac{m}{rad}$ (often $\frac{cm}{mrad}$ or $\frac{mm}{mrad}$ instead) and γ the dimensions $\frac{rad}{m}$ (often $\frac{mrad}{cm}$ or $\frac{mrad}{mm}$ instead).

The sign of α also determines the ellipse orientation in the considered sub-space (see Fig. D.4) [80]:

- $\alpha = 0$: the ellipse is in its principal axis position (upright ellipse)
- $\alpha < 0$: divergent particle beam
- $\alpha > 0$: convergent particle beam.

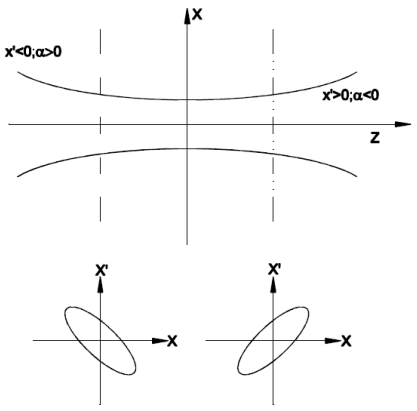

Figure D.4: Twiss parameter α determines the ellipse orientation [80].

D.4 RMS-Emittance

Analogously to Eq. D.13, the following formula describes the rms-emittance ε_r:

$$\varepsilon_r = \gamma_r \overline{x^2} + 2\,\alpha_r \overline{x\,x'} + \beta_r \overline{x'^2} = \sqrt{\overline{x^2}\,\overline{x'^2} - \overline{xx'}^2}. \tag{D.15}$$

α_r, β_r and γ_r[6] are the Twiss parameters belonging to the rms-emittance. They are also referred to as Courant-Snyder parameters. In analogy to Eq. D.14

$$\gamma_r = \frac{1+\alpha_r^2}{\beta_r} \tag{D.16}$$

holds true. $\overline{x^2}$, $\overline{x'^2}$ and $\overline{xx'}$ represent the second moments of the particle distribution. For N particles they are:

$$\overline{x^2} = \frac{1}{N}\sum_{i=1}^{N}(x_i - \overline{x})^2, \tag{D.17}$$

$$\overline{x'^2} = \frac{1}{N}\sum_{i=1}^{N}(x_i' - \overline{x'})^2 \tag{D.18}$$

and

$$\overline{xx'} = \frac{1}{N}\sum_{i=1}^{N}(x_i - \overline{x})\cdot(x_i' - \overline{x'}), \tag{D.19}$$

with $\overline{x}$ and $\overline{x'}$ being the rms-values of the x- and x'-co-ordinate, respectively, that give the rms-emittance its name:

$$\overline{x} = \sqrt{\frac{1}{N}\sum_{i=1}^{N} x_i^2} = \sqrt{\frac{x_1^2 + x_2^2 + ... + x_N^2}{N}} \tag{D.20}$$

and

$$\overline{x'} = \sqrt{\frac{1}{N}\sum_{i=1}^{N} {x_i'}^2} = \sqrt{\frac{{x_1'}^2 + {x_\prime}_2{}^2 + ... + {x_N'}^2}{N}}. \tag{D.21}$$

Under the assumption that the projections of the ellipse corresponding to the rms-emittance on the x- and x'-axes equal the rms-values of the co-ordinate distributions, one obtains [26]:

[6] Strictly speaking $\alpha_{r,x}$ etc.

$$\overline{x^2} = \beta_r \varepsilon_r \Rightarrow \beta_r = \frac{\overline{x^2}}{\varepsilon_r} \tag{D.22}$$

and

$$\overline{x'^2} = \gamma_r \varepsilon_r \Rightarrow \gamma_r = \frac{\overline{x'^2}}{\varepsilon_r}. \tag{D.23}$$

It further follows from Eq. D.16:

$$\alpha_r^2 = \beta_r \gamma_r - 1 = \frac{\overline{x^2}\,\overline{x'^2}}{\varepsilon_r^2} - 1 = \frac{\overline{x^2}\,\overline{x'^2} - \varepsilon_r^2}{\varepsilon_r^2}, \tag{D.24}$$

so that via Eq. D.15 one arrives at:

$$\alpha_r = -\frac{\overline{xx'}}{\varepsilon_r}. \tag{D.25}$$

D.4.1 RMS-Emittance Conventions

Unfortunately, there exists no universally acknowledged definition of the rms-emittance ε_r. Therefore, it is necessary to consider which definition applies for a given emittance discussion [26]. The rms-emittance definition above is the most common one and stems from F. J. Sacherer [81]. According to another convention introduced by P. M. Lapostolle [82] the rms-emittance is the Sacherer rms-emittance times four. It is, however, mostly referred to as 4-rms-emittance (in accordance with the Sacherer convention being the more popular one). The 4-rms-emittance of a DC beam is equal to the total emittance ε_{total} of an equivalent Kapchinsky–Vladimirsky-distribution (see below) with homogeneous particle distributions in all 2-dimensional projections. For almost all other real beams, this 4-rms-emittance contains about 90 % of the particles [26].

$\overline{x}$ and $\overline{x'}$ depend on the particle distribution in phase space with its characteristic distribution function. From Eq. D.17 – Eq. D.19 follows that also the second moments depend on the particle distribution in phase space and therefore also on the concrete distribution function. Beam dynamics simulation codes like RFQGen often operate with the total emittance $\varepsilon_{total,sim}$ of a simulated distribution and the associated rms-emittance $\varepsilon_{r,n}$ for uniform hyper-ellipsoids in the n-dimensional phase spaces, respectively[7]:

$$\varepsilon_{r,n} = \frac{\varepsilon_{total,sim}}{n+2}. \tag{D.26}$$

[7] Equation D.27 formulated by M. Weiss [26].

Important cases of these n-dimensional phase spaces are:

- $n = 6$, i.e. uniform density distribution in $6D$-phase space, known as $6D$ Waterbag distribution: $\varepsilon_{r,6} = \frac{\varepsilon_{total,sim}}{8}$
- $n = 4$, i.e. uniform density distribution in $4D$-phase space, known as $4D$ Waterbag distribution: $\varepsilon_{r,4} = \frac{\varepsilon_{total,sim}}{6}$
- $n = 3$, i.e. an in all three-dimensional projections uniform density distribution: $\varepsilon_{r,3} = \frac{\varepsilon_{total,sim}}{5}$
- $n = 2$, i.e. an in all two-dimensional projections uniform density distribution, known as Kapchinsky–Vladimirsky (KV) distribution: $\varepsilon_{r,2} = \frac{\varepsilon_{total,sim}}{4}$.

Most RFQGen and all TOUTATIS beam dynamics simulations presented in this thesis were carried out on $4D$ Waterbag distributed entrance beams. (Some RFQGen simulations were performed with input distributions generated by preceding LEBT simulations with TraceWin (cf. Secs. 3.3 and 3.7)). Unless stated otherwise all emittances presented in this thesis are normalized rms-emittances (see Sec. D.6).

D.5 A Brief Remark on Emittance Definition

In this thesis, the transversal emittances are given in units of π mm mrad, and the longitudinal are given in units of π MeV deg. For example, a normalized transversal rms-emittance shall be given as $0.3\,\pi$ mm mrad. Here, the factor π seems inconsistent according to the most common emittance definition as given above: $\varepsilon = A\,/\,\pi$; the expression $\varepsilon_{trans.,rms,n} = 0.3\,\pi\,mm\,mrad$ seems to suggest that the emittance is the phase space area A occupied by beam particles itself. This is indeed also a valid definition of the emittance, albeit a much less common one. However, expressions such as $\varepsilon_{trans.,rms,n} = 0.3\,\pi\,mm\,mrad$ are widely used, even in case $\varepsilon = A\,/\,\pi$ applies.

Here, the factor π is actually added precisely to avoid confusion: in case the emittance is defined as $\varepsilon = A\,/\,\pi$ (which is the case for the emittance values presented in this thesis), π is to be ignored and the emittance is given by the numerical value in the respective units, i.e. above example $0.3\,\pi$ mm mrad is to be read as:

$$\varepsilon = A\,/\,\pi \;\Rightarrow\; \varepsilon_{trans.,rms,n} = 0.3\,mm\,mrad\,.$$

For the less likely case, that the emittance is defined as the area itself, the numerical value is to be multiplied with π to derive at the emittance in mm mrad, i.e. in case of above example:
$\varepsilon = A \Rightarrow \varepsilon_{trans.,rms,n} = 0.3\,\pi\,mm\,mrad \approx 0.942\,mm\,mrad$.

Independently of the actual emittance definition, a notation such as $\varepsilon_{trans.,rms,n} = 0.3\,\pi\,mm\,mrad$ is a valid expression for the respective phase space area. If π was omitted (and no further information given), this unambiguity would disappear. For example, without further information the expression

$$\varepsilon_{trans.,rms,n} = 0.3\,mm\,mrad \tag{D.27}$$

could either state that the occupied area A in phase space is $0.3\,\pi\,mm\,mrad \approx 0.942\,mm\,mrad$ in case $\varepsilon = A\,/\,\pi$ applies, or it could state that this area is 0.3 mm mrad, in case $\varepsilon = A$ applies.

D.6 Normalized Beam Emittances

The divergence angles x' and y' are defined as $\frac{v_x}{v_z}$ resp. $\frac{v_y}{v_z}$, i.e. the ratios of the respective transversal velocity to longitudinal velocity. From this definition and from Eq. D.13 follows that the transversal emittances ε_x and ε_y depend on the longitudinal particle velocity v and thus are not directly comparable for different particles and beams, respectively. For this reason the transversal emittances are normalized with respect to the relative longitudinal velocity[8],[9] $\beta = \frac{v}{c}$ and the Lorentz factor[10] $\gamma = \frac{1}{\sqrt{1-\beta^2}}$:

$$\varepsilon_{x,n} = \beta\,\gamma\,\varepsilon_x \tag{D.28}$$

and

$$\varepsilon_{y,n} = \beta\,\gamma\,\varepsilon_y. \tag{D.29}$$

Transverse emittances, that are not velocity-normalized (as the ones discussed in the previous sections), usually are marked with the index u, i.e. $\varepsilon_{x,u}$ and $\varepsilon_{y,u}$. Therefore Eq. D.28 and Eq. D.29 can also be expressed as:

[8] Assuming all beam particles are of the same ion species, i.e. of the same mass. Otherwise the emittances are normalized in regard to the particle momenta.
[9] $v_x \ll v_z$ and $v_y \ll v_z \Longrightarrow v_z \approx v$ and $\beta_z \approx \beta$.
[10] β and γ are not to be confused with the Twiss parameters represented by the same symbols (cf. Fn. [5]).

$$\varepsilon_{x,n} = \beta\,\gamma\,\varepsilon_{x,u} \tag{D.30}$$

and

$$\varepsilon_{y,n} = \beta\,\gamma\,\varepsilon_{y,u}. \tag{D.31}$$

As $\beta\,\gamma$ is dimensionless normalized and unnormalized transversal emittances are of the same units. The normalized longitudinal emittance $\varepsilon_{z,n}$ generally is expressed in one of the following ways [26]:

$$\varepsilon_{z,n} = \frac{\Delta z\,\Delta p_z}{mc} = \frac{\Delta t\,\Delta W}{mc} = \frac{\Delta\phi\,\Delta W}{\omega mc}, \tag{D.32}$$

with $v\,\Delta p_z = \Delta W$, $\Delta z = v\,\Delta t$ and $\Delta\phi = \omega\,\Delta t$ [26]. This emittance originally has the same units as the transversal emittances, i.e. mm mrad. However, the longitudinal emittance is often re-defined as:

$$\varepsilon_z = \Delta W\,\Delta\phi \tag{D.33}$$

or as

$$\varepsilon_{z,n} = \Delta W\,\Delta t. \tag{D.34}$$

Hence, the longitudinal emittance is often times expressed in units of either MeV deg or keV ns. Both definitions do not depend on the beam energy, but the first definition depends on the frequency. Therefore, the latter is to be preferred in case of a linac undergoing one or more frequency transitions.

E Two RFQ Beam Dynamics Codes

In the following the RFQGen-code, its predecessor PARMTEQ(M)[1] and further associated LANL RFQ codes (cf. Sec. E.1) as well the TOUTATIS RFQ beam transport code from CEA Saclay (cf. Sec. E.2) are introduced. Whereas PARMTEQ(M)/RFQGen[2] is suited to generate an RFQ beam dynamics design from scratch, TOUTATIS is a mere transport code, i.e. it requires to be fed an already fleshed out RFQ beam dynamics design, on which it can then perform beam dynamics simulations. It was partly written as a tool to cross check PARMTEQ simulations and to allow for more accurate simulations regarding high current RFQs by disregarding certain approximations, whereby the authors of TOUTATIS and RFQGen were actually in close correspondence [23].

E.1 The LANL RFQ Design Codes and RFQGen

Like several other RFQ design codes PARMTEQ was developed by members of the accelerator-design group[3] of the Los Alamos National Laboratory. It was written in order to design high-performance RFQs. For this thesis the RFQ Design Codes package[4] was used, containing all LANL Codes necessary to design the RFQ electrode profile and to subsequently perform beam dynamics simulations on the design [21]. The package comprises:

- CURLI (**Cur**rent **Li**mits): for a given RFQ design problem CURLI calculates the current limit at the end of the gentle buncher, the most critical spot of the RFQ. The most common procedure is variation of aperture. For each aperture value, the modulation at which the longitudinal current limit equals the transversal current limit is determined. If a parameter

[1] **P**hase **a**nd **R**adial **M**otion in a **T**ransverse **E**lectric **Q**uadrupoles. "M" refers to the six additional multipole terms that extend the two term potential to the eight-term potential (cf. Sec. 2.6). Other than for the older PARMTEQ versions these terms can (and usually should be) activated by PARMTEQM; each can be switched off independently, though.

[2] Since PARMTEQ(M) and RFQGen do not differ fundamentally, but mainly regarding certain rather minor details, they are treated as basically one single code in many instances throughout this appendix.

[3] An overview of the design codes provided by the **L**os **A**lamos **A**ccelerator **C**ode **G**roup (LAACG) is given at `https://laacg.lanl.gov/laacg/services/serv_codes.phtml`.

[4] There also exists the RFQ Manufacturing Codes Package. It includes the code "Vanes", which generates and investigates machine instructions for numerically controlled machining of the vanes or electrodes. (This is mentioned only for completeness as this package is of no relevance to this thesis.)

set is selected, CURLI generates a short file of calculated parameters for the following RFQuick code [21, 22].

- RFQuick: for a series of shaper energies, the RFQuick code quickly (hence its name) generates first RFQ designs based on the parameters previously determined by CURLI. As a specific shaper energy is chosen, the associated PARMTEQ input file is written [21, 22]. It happens quite frequently, that the RFQ designer afterward takes great freedom in manually modifying this file in order to find a more promising approach better suited to the peculiarities of the given problem[5].

- PARI: PARI determines the electrode modulation needed to generate the accelerating and focusing forces assumed by the 2-term potential function. It also considers the effects of a circular pole tip geometry [21].

- PARMTEQ(M): this code generates the detailed, final RFQ design and performs the beam dynamics simulations through this RFQ model. This code uses a two-dimensional space-charge calculation. PRAMTEQM includes the effects of higher order multipole[6] components (cf. Sec. 2.6) originating from the application of circular vane tips [21]. Its foundations will be described more detailed in the next section.

- Lingraf: Lingraf plots the beam dynamics simulated by PARMTEQM. It generates output in form of several graphic files as well text files containing tables [21]. The new LANL Codes distribution by L. M. Young and J. Stovall containing RFQGen also comprises a modified version of this code renamed Pargraf [22].

E.1.1 PARMTEQ(M) and RFQGen

The RFQGen[7] code, which merges PARI with PARMTEQM, designs the RFQ cells including those of the matching sections at both ends of the RFQ. In order to produce the fields associated with the respective two-term potential RFQGen slightly modifies the geometry of the cells as given by RFQuick. For this purpose, RFQGen in a first step alters the modulation to arrive at

[5] Ultimately, CURLI and RFQuick are not needed to generate an RFQ beam dynamics design at all. Experienced RFQ beam dynamics designers can write a sufficiently well running initial RFQGen input file more or less from scratch. However, more often than not, the RFQuick generated input file serves as a good base to start the actual design process if only it serves as a template saving time and eliminating potential sources of error. To this end, one can alternatively resort to the input file of an already sufficiently validated beam dynamics design from an earlier project (at best with at least roughly similar requirements to the one at hand).

[6] The "M" in PARMTEQM refers to these multipole contributions.

[7] The corresponding software package is provided by LMY Technology and comes with three additional codes (`https://lmytechnology.com`).

the required longitudinal field. As a next step, the mid-cell radial aperture r_0 is modified to produce the required transversal field [22].

Although both programs have been improved and (slightly) extended, the physical models constituting the basis for RFQGen have remained nearly unchanged [26, 21, 22]. The following explanations regarding PARMTEQ(M) therefore also hold true for RFQGen.

The approximations underlying PARMTEQM are based on certain simplifications of RFQ beam dynamics. This is mainly due to the fact, that the first PARMTEQ version was published as early as 1977, when computational possibilities were far more restricted than they are today. Nonetheless, the newer versions of PARMTEQ(M) and of its successor RFQ-Gen generate realistic and reliable results and still are essential tools for many RFQ designers [23].

PARMTEQM's beam dynamics computing considers a particle distribution in the 6D-phase space x, x', y, y', ϕ, W. The phase-coordinate φ is the difference between a particle's phase and the synchronous phase: $\varphi = \phi - \phi_s$. These φ-coordinates are used to estimate the longitudinal distribution of the beam bunch. This knowledge is required to calculate the resulting image and space-charge forces. They are calculated for each individual particle using analytical expressions containing tabulated external field coefficients.

E.1.2 PARMTEQ's Equation of Motion Algorithm

Finding an analytical solution of the equation of motion (EOM) in an RFQ is not possible due to the complexity of the electric field expression (which also includes Bessel functions). Therefore, one has to resort to one of the many incremental integration algorithms. Within the accelerator beam dynamics community, the Runge-Kutta algorithm and the field of Lie algebra provide very popular remedies for this problem [23].

Written in an era of far less available computing power, PARMTEQ(M) instead uses a so-called leap-frog approach. This algorithm is based on the linear discretization of the particle trajectories with regard to an independent parameter. The algorithm's accuracy only depends on the increment size, and no other approximations are introduced.

For historical reasons, in PARMTEQ(M) the longitudinal position z was selected as this independent parameter. Therefore, PARMTEQ(M) – along with most drift tube-codes – falls

under the category of so-called z-codes, whose simulation results can be compared with beam diagnostic measurements in a simple fashion. (Codes for which the independent parameter is time t are accordingly referred to as t-codes. TOUTATIS classifies as such a code (see Sec. E.2).)

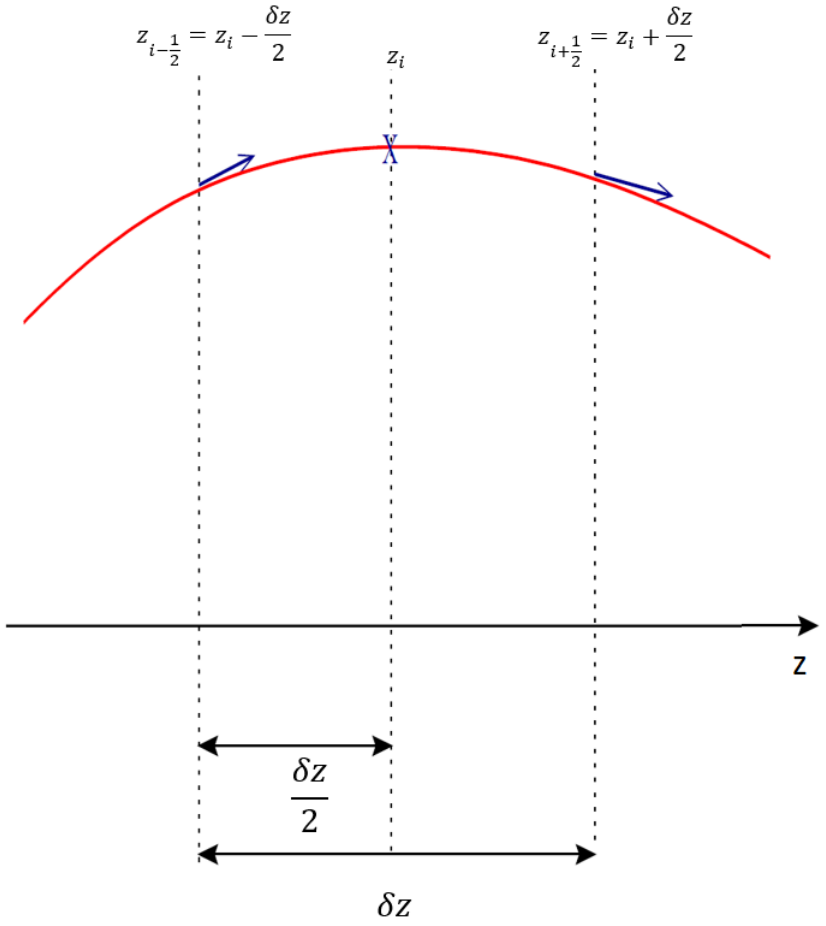

Figure E.1: PARMTEQ's leap-frog algorithm evaluates the accelerating force exerted on a particle at an intermediate position $z = z_i$ (cf. blue cross) between those positions $z = z_{i-\frac{1}{2}} = z_i - \frac{\delta z}{2}$ and $z = z_{i+\frac{1}{2}} = z_i + \frac{\delta z}{2}$, for which the normalized momentum $(\gamma\,\vec{\beta})$ (cf. blue arrows) is evaluated, whereby δz is the discretization increment. (Figure adjusted from Ref. [23].)

PARMTEQ's leap-frog algorithm evaluates the momentum[8] accelerating force exerted on a particle at an intermediate position $z = z_i$ between those positions $z = z_{i-\frac{1}{2}} = z_i - \frac{\delta z}{2}$ and

[8] $\vec{p} = \gamma\, m_0\, c\, \vec{\beta} \Rightarrow \gamma\,\vec{\beta} = \frac{\vec{p}}{m_0\, c}$

$z = z_{i+\frac{1}{2}} = z_i + \frac{\delta z}{2}$, for which the normalized momentum $(\gamma\,\vec{\beta})$ is evaluated (see Fig. E.1). (Reference [23] offers a more in-depth discussion of this algorithm and its equations of motion.) Thus, the normalized momentum at $z = z_{i+\frac{1}{2}} = z_i + \frac{\delta z}{2}$ is:

$$(\gamma\,\vec{\beta})_{i+\frac{1}{2}} = (\gamma\,\vec{\beta})_{i-\frac{1}{2}} + \frac{Ze}{\beta_z\,E_0}\,\vec{E}(z_i)\,\sin(\phi_i)\,\delta z, \tag{E.1}$$

with Ze and E_0 being the respective ion-species' charge and norm. rest-energy, and β_z its longitudinal relative velocity component at $z = z_{i-\frac{1}{2}} = z_i - \frac{\delta z}{2}$. Note that the electric field vector $\vec{E}$ and the particle phase ϕ in this equation refer to the values at intermediate position z_i [23].

As concessions to the rather low computing power available in the first days of PARMTEQ γ is set to $\gamma = 1$. Furthermore, paraxiality is assumed for PARMTEQ(M), i.e. it is assumed that the particle trajectories are virtually parallel to the beam axis, i.e. $\beta = \sqrt{\beta_x^2 + \beta_y^2 + \beta_z^2} \approx \beta_z$ with $\beta_z \gg \beta_x$ and $\beta_z \gg \beta_y$. Thus, PARMTEQ(M) treats the transversal particle co-ordinates x and y as constants during the longitudinal shift of δz, whereby the low value of that increment serves as justification for the validity of this approach. However, for steep divergence angles $x' = \frac{p_x}{p}$ and $y' = \frac{p_y}{p}$ (cf. Sec. D.1 in App. D) this might be questionable. Since the computation power available to the typical PARMTEQ-user has grown immensely since both PARMTEQ and PARMTEQ(M) were first released, these assumptions should be eventually discarded even though they might mostly result in rather minor errors. More realistic models are now possible to be implemented at acceptable conditions such as only minor increase of simulation run times etc.

E.1.3 Space-Charge Force Considerations in PARMTEQ(M)

Space-charge calculations require particle tracking in order to describe the evolution of the beam distribution and to include space-charge emittance growth effects. The simulation particles are commonly referred to as macro-particles. They function as individual sources of the space-charge field, whereby each macro-particle represents the total charge of many (usually 10^4 to 10^5) actual beam particles. A popular macro-particle tracking approach is the **P**article-**I**n-**C**ell (PIC) method, where a mesh is superimposed on the bunch at each step. This enables smoothing of the fields to reduce the effects of artificially large forces that would otherwise be caused by binary encounters between macro-particles. The number of particles within each cell is counted, and the smoothed space-charge force exerted on each particle is calculated by summation over the fields of all charges within each cell. Eventually, each macro-particle is given an impulse according to these forces. The required calculation time is a function of the number of macro-particles

as well as the mesh-cell number. Since a three-dimensional calculation would require a high number of mesh-cells, usually at least one assumption of symmetry is introduced to decrease the run-time [26].

PARMTEQ(M)/RFQGen handles space-charge effects with the the so-called SCHEFF (**S**pace **Ch**arge **Eff**ects) sub-routine written by K. R. Crandall, for which the space-charge calculation takes place in two dimensions and the charge of each (macro-)particle is distributed in a ring, whereby radial symmetry is assumed. Hence, *scheff*-subroutine is categorized as a r-z-PIC [26]. The *scheff*-line of the RFQGen input file requires the specification of the following parameters [22]:

- $I_T\,[mA]$: the beam current[9]. More precise, I_T is the current averaged over one RF period. A current of e.g. 1 mA corresponds to a charge of 1 pC per bunch, if a frequency of 1000 MHz is chosen.
- $\delta R_{SC}\,[cm]$: the initial radial mesh interval length, i.e. the initial ring width (cf. Fig. E.2 (left))
- $\delta Z_{SC}\,[cm]$: the initial longitudinal mesh interval lengths, i.e. the initial slice length (cf. Fig. E.2 (left))
- N_R: number of radial mesh intervals with the maximum value being 40 and the radial dimension of the mesh region being $N_R\,\delta R_{SC}$ (cf. Fig. E.2 (left)); for all simulation within this thesis N_R was set to its maximum value of 40 in order to guarantee simulations of high accuracy
- N_Z: number of longitudinal mesh intervals with the maximum value being 80 and the longitudinal dimension of the mesh region being[10] $N_Z\,\delta Z_{SC}$; for all simulation within this thesis N_Z was set to its maximum value of 80 in order to guarantee simulations of high accuracy
- N_{Bunch}: number of adjacent longitudinal bunches included in the calculation, both ahead and behind the considered bunch; for all simulations presented within this thesis except

[9] Previous to version RFQGen 5.10.0, I_T was still calculated as if each particle had the charge number of 1. Thus, if an ion has a charge of 10, the user had to enter one tenth of the actual electric current as value for I_T. This is only mentioned for completeness and was of no relevance to the beams considered in this thesis, since they were all proton beams ($q = 1$). This was eventually adjusted by L. M. Young so that I_T now refers to the actual electric current of the beam [22]

[10] If a negative number is entered for N_Z, RFQGen sets up N_Z mesh intervals as the maximum of $N_Z\,\delta Z_{SC}$ and the separatrix (cf. Fig. E.2 (left)) size.

for cases 1 and 3 in Sec. 3.6 N_{Bunch} was set to 5. These two simulations were performed with $N_{Bunch} = 0$ to investigate the influence of neighboring bunch interactions on the beam dynamics of the FAIR p-Linac RFQ, both separately and in relation to the influence of image-charge effects. (Also presented in this section is the separate investigation of the influence of image-charge effects on the beam dynamics of the FAIR p-Linac RFQ (cf. Sub-Sec. E.1.4).)

- N_{RM}: number of cells within the radial matching section
- $L_{Bunch}\,[cm]$: distance between two adjacent bunches; for all simulation within this thesis the according entry was set to zero. Thus, the code sets this length to the default value of $\beta_s\,\lambda_s$, i.e. two RFQ cell lengths or one modulation period.
- $Mesh\,Interval$: number of cells after which the space-charge mesh is re-adjusted; for all simulation within this thesis this value was set to 10, which assures both high accuracy and performance speed.

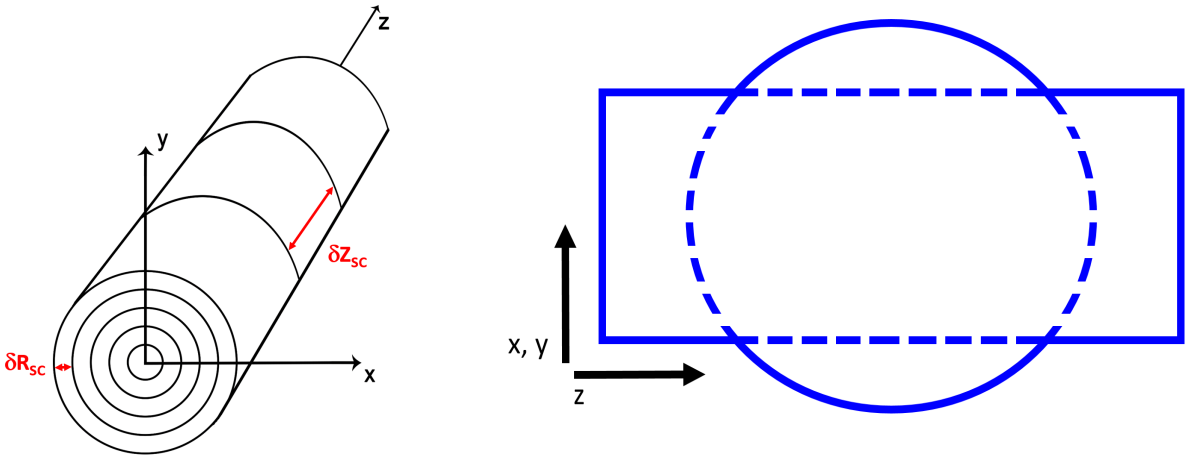

Figure E.2: **Left:** Cylindric mesh of a schematic beam bunch as calculated by RFQGen's *scheff*-subroutine: this bunch's mesh is divided into four rings ($N_R = 4$) with ring diameter δR_{SC} and three slices ($N_Z = 3$) of length δZ_{SC}. (Fig. adjusted from Ref. [83]).
Right: Cross-sections in the x-z- and y-z-planes of a beam bunch as approximated in PARMTEQ(M)/RFQGen by superposing a cylinder and a sphere of equal space-charge density. The dimensions of both geometric bodies as well as their superposition weighting factors depend on the degree to which the beam package is bunched [23]; the weighting factor of the sphere grows with the degree of "bunchedness".

The values for these entries have to be chosen in a fashion that allows for a compromise between a sufficiently high accuracy of the mesh and optimized simulation run times. The latter are especially relevant for high numbers of input macro-particles and when performing extensive

RFQ beam dynamics studies regarding parameters such as the entrance current or the transversal entrance Twiss parameters.

The *scheff*- and *image*-line (cf. Sub-Sec. E.1.4) entries, whose values are fixed for each of the two RFQs are also listed in this table; the two exceptions regarding each the N_{Bunch}- and the image-charge entry are highlighted.

E.1.4 Image-Charge Effects in PARMTEQ(M)

If a charged particle beam moves sufficiently close to a conducting surface, image-charge effects should generally be included into the beam dynamics description. As the electrode tips in an RFQ are relatively close to the beam axis, the influence of image-charges on the beam dynamics often becomes significant even for relatively low beam currents[11]. The code considers this influence by interpolation of data from a series of calculations by the CHARGE 3D code for point-charges and line-charges in cells of various shapes [21].

These calculation are based on the type of selected longitudinal electrode surface geometry. In so-called geometry files the electrode data for already existing RFQs is stored, whereby the data of electrodes with a common longitudinal profile are contained within the respective file. Table E.1 shows the names of these files as well as the associated electrode profiles [21]. Each geometry file contains the results of CHARGE 3D calculations and subsequent harmonic analysis of the fields for a range of electrode-tip modulation m, and the ratios L_z/r_0 and ρ/r_0; L_z is the cell length, ρ is the vane-tip transverse radius of curvature, and r_0 is the mid-cell radial aperture. The code interpolates between the values stored in the file, whereby each line in the file has 12 entries: the cell length to aperture ratio L_z/r_0, modulation m, the so-called field enhancement factor[12], the multipole-coefficients of the eight-term potential (cf. Sec. 2.6) and the specific capacitance C_l per unit length in pF/m. The numerical solution of the calculation is projected on a base of cylindrical harmonics. The CHARGE 3D algorithm and the respective formulas are described in great detail in Ref. [23].

[11] It might, however, turn out to be rather insignificant even for high beam currents as shown in Sec. 3.6. Cases 2 and 3 presented in this section represent the only two RFQGen beam dynamics simulations within the scope of this thesis, for which the image-charge effects were switched off. This was done specifically to investigate their influence on the beam dynamics of the FAIR p-Linac RFQ both separately and in relation to above mentioned neighboring beam interactions.

[12] The field enhancement factor β is often introduced in the Fowler-Nordheim law for the emitted current density j. More information on this is provided in Sec. 5.10 of Ref. [26].

Geometry File Name	Data for
V2TERM.txt	vanes with a longitudinal profile determined by the 2-term potential
VSINE.txt	vanes with a sinusoidal longitudinal profile
R2TERM.txt	rods with a longitudinal profile determined by the 2-term potential
RSINE.txt	rods with a sinusoidal longitudinal profile
RCIRCLE.txt	rods with a circular longitudinal profile

Table E.1: Electrode geometry files for CHARGE 3D and PARMTEQ(M)/RFQGen [21].

The most common choice for 4-vane RFQs is V2term.txt file [21]. For files V2term.txt and R2term.txt (for 4-rod RFQs), the longitudinal profile over a cell comes from the 2-term potential, i.e. the longitudinal electrode profiles follows the longitudinal profiles of the equipotential surfaces as given by the two-term potential. Note that in this case the transverse profiles of the electrodes do not adhere to the shape of the two-term potential equipotential surfaces. (This also holds true, if R2TERM.txt is chosen.) All other multipole terms would vanish, if that was the case. For the FAIR p-Linac RFQ the choice fell to VSINE.txt, i.e. vane-shape electrodes exhibiting a sinusoidal longitudinal surface profile.

The deviation of m from its course according to the two-term potential associated with this choice might potentially affect frequency f to such a degree that sufficient tuning becomes impossible[13]. This can, however, be avoided if a constant ratio between the transversal electrode radius to mid-cell-radius ρ/r_0 is chosen along (most of) the RFQ length[14].

Furthermore, regardless of the choice of geometry file, RFQGen per default offers a prompt-option to specifically adjust m to generate the same acceleration coefficient A as given by the two-term potential. This default option was also made use of for the generation of the beam dynamics design of the p-Linac as not taking it would lead to sub-par values of A and thus to insufficient longitudinal focusing resulting in a significant RFQ exit transmission drop of about 10%. Indeed, CST MWS simulations [3] performed and successive measurements [4, 5] on the assembled RFQ hinted at and proved, respectively, the sufficient tunability of the FAIR p-Linac RFQ (see Sec. 3.9).

The effects of image-charges are estimated for the start and center of an RFQ cell. This is done by making use of analytical expressions with tabulated coefficients. Hereby, the forces are

[13] Correspondence with J. E. Stovall and L. M. Young.
[14] Correspondence with A. M. Lombardi.

integrated over half the RFQ-cell, i.e. over $\frac{l_c}{2} = \frac{\beta_s \lambda}{4}$. As a continuous beam is prebunched and eventually bunched (and its charge/particle density is modified accordingly), it is represented by the superposition of a cylindrical beam and a sphere, both charged evenly (see Fig. E.2 (right)).

With the exception of cases 2 and 4 in Sec. 3.6, the image-charge effects were activated for all RFQGen beam dynamics simulations presented within this thesis.

E.1.5 Input Macro-Particle Distributions for PARMTEQ(M)

An input-line defines the properties of all or a fraction of some particles in the input beam. An input file can contain one or multiple input lines, whereby each such line specifies a certain number of macro-particles. Also specified in the input-line is the distribution type, which also defines the format of the corresponding input-line.

No simulations presented in this thesis were run on input-files containing multiple input-lines. For most simulations, exactly one input-line was used. The exceptions to this are shown in Secs. 3.3 and 3.7, where the input-line was commented out (and thus de facto deleted) and replaced by an "adjust"-line (only consisting of an entry of the same name), which tells the code to input distribution files. This was done to run these RFQGen simulations with input distribution files generated through preceding LEBT simulations with TraceWin[15].

In all cases containing an active input-line, the entered distribution type was always type 6, which refers to a so-called 4D water bag distribution, a commonly used distribution that leads to realistic and reliable simulation results. It is characterized by a uniform phase and a random energy distribution. As most distribution types[16], this type requires an input-line of the following format:

input type, N_A, α_x, β_x, ε_x, α_y, β_y, ε_y, $\Delta\phi$, ΔW, δx, $\delta x'$, δy, $\delta y'$, $\delta\phi$, δW.
The further entries are:

- N_A: number of macro-particles specified according to the respective input-line, whereby 10^6 is the upper limit. In most cases $10^4 \leq N_A \leq 10^5$ represents a good compromise between high accuracy and short duration of the simulation. As already mentioned, all simulations

[15] The TraceWin output distribution files first had to be converted to a format readable by RFQGen. This conversion was automated with a tool written in Visual Basic by R. Tiede.

[16] It is also possible to enter a negative value for this entry: then the code will adjust the randomly chosen particle distribution to achieve the exact values of the parameters as specified in the input line. Comprehensive information on the available distribution types (and the deviating line-formats some of them require) is provided in Refs. [21] and [22].

presented in this thesis, which made use of input simulations directly generated by RFQGen itself, were run on an input-file containing only one input-line. N_A was set to 10,000 for the Entrance Current and Transversal Twiss Parameter[17] studies as those contained hundreds of simulations.

- $\varepsilon_{x/y}$: the unnormalized x/y-emittance in units[18] of (π) cm rad
- $\alpha_{x/y}$ and $\beta_{x/y}$: the associated x/y-Twiss parameters, $\alpha_{x/y}$ is dimensionless, the units of $\beta_{x/y}$ are cm/(π) rad
- $\Delta\phi$ and ΔW: the distributions phase and energy spreads in degrees and MeV, respectively
- $\delta x/y$ and $\delta x'/y'$: the respective displacements of the actual beam axis with regard to the z-axis in the spatial positions and divergences given in units of cm and mrad, respectively
- $\delta\phi$ and δW: displacements of the average particle phase and energy to those of the synchronous particle in degrees and MeV, respectively[19].

E.1.6 Longitudinal Particle Losses in PARMTEQ(M)

Transversal or radial losses refer to particles hitting the RFQ electrodes. Accordingly, a macro-particle is classified as radially lost by PARMTEQ(M)/RFQGen if and when its trajectory intersects with the electrode surface. These macro-particles are then taken out of the further simulation.

However, longitudinally lost macro-particles are classified in a less straightforward and in a more arbitrary fashion, though, that – as will be explained within this subsection – indirectly also influences the spectrum of radial losses along the RFQ. Longitudinal loss particles are determined by the so-called *elimit*-parameter, which is to be entered in the corresponding line of the PARMTEQ(M)/RFQGen input file. It refers to the threshold ΔW_{thr} for the energy difference $|W_s - W_i|$, i.e. the difference between the synchronous energy W_s and a given

[17] The simulation regarding the matched case was re-done with $N_A = 10^5$. No significant deviations to the prior results were found. This finding was validated by several random checks for other simulations. Analogously, random simulations with $N_A = 10^5$ were re-done with $N_A = 10^6$; the much longer simulation duration for $N_A = 10^6$ seemed not justified by the non-noticeable gain in accuracy.

[18] The meaningfulness or superfluity of factor π when specifying ε- or β-values is discussed in Sub-Sec. D.5 in Appx. D

[19] These two and all of the above four displacements were set zero for all simulations shown in this thesis as RFQs are generally not prone to exhibit such displacements and furthermore not notably sensitive to them. The influence of these displacements on the new RFQ beam dynamics designs presented in this thesis should still be investigated within the scope of comprehensive error studies at some point (see Chap. [5]).

particle's energy W_i. The *elimit*-parameter is the numeric value of this threshold given in MeV: $\Delta W_{thr} = elimit\, MeV$. A macro-particle is classified as longitudinally lost by the code, if its energy W_i deviates more than this threshold value from the synchronous energy.

One practicable, wide-spread definition of this accepted energy window ΔW_{thr} is two times the energy half width ΔW_{h-w} of the separatrix in the so-called stable fix point (cf. Appx. A):

$$\Delta W_{h-w} = \sqrt{\frac{2}{\pi}\, mc^2\, qe\, E_0 T\, \beta_s^3 \gamma_s^3\, \lambda\, (\phi \cos\phi_s \, - \, \sin\phi_s)}\,. \tag{E.2}$$

mc^2 is the particle rest energy, and qe is its charge. T is the so-called transit-time factor or transient-time factor (not to be confused with the RF period), which takes on the value $T_{RFQ} = \frac{\pi}{4} \approx 0.79$ for RFQs [26]. The synchronous particle velocity β_s and the associated Lorentz factor γ_s as well as the synchronous phase ϕ_s and the average axial electric field E_0 refer to the last acceleration cell [21]. They can be found in various tables of the RFQGen output-files.

Per default, RFQuick also writes the value of ΔW_{thr} according to $\Delta W_{thr} = 2.0\, \Delta W_{h-w}$ in the initial PARMTEQ(M)/RFQGen[20] input file. This default value can be adjusted by the user [21]. As this initial input file often (drastically) differs from the adjusted and honed one the finalized RFQ beam dynamics design is based on (especially if it does not adhere to the LANL Four Section Procedure), so should the values of β_s, γ_s, ϕ_s and E_0 in Eq. E.2. Thus, ΔW_{h-w} and hence ΔW_{thr} must be checked and possibly re-adjusted in order to run meaningful beam dynamics simulations.

PARMTEQ(M)/RFQGen does not track how many of the longitudinally lost particles actually still traverse the RFQ. (TOUTATIS on the other hand offers such a feature (cf. Sec. 3.4)). Such particles nonetheless might "survive" the transport trough the RFQ (much) longer than implicit by their sudden deletion by RFQGen due to the given setting of the *elimit*-parameter. Hence, they actually should be considered with regards to space- and image-charge effects. Some of them should even reach the RFQ exit, where they exhibit lower energies than those exit particles that have been (sufficiently) "in phase" towards their transport through the RFQ and thus have been properly accelerated. These low-energy exit particles get lost in the LEBT-line and hence do not tribute to the entrance current of the p-Linac.

RFQGen offers a simple method to take into account the effects of particles that are usually

[20] Actually, other than for RFQGen, $\Delta W_{thr} = 1.5\, \Delta W_{h-w}$ applies for PARMTEQ-M [21].

disregarded too soon due to an ΔW_{thr}-value chosen to $\Delta W_{thr} = 2.0\,\Delta W_{h-w}$. It consists in switching off the longitudinal losses or rather: de facto disabling (almost) all macro-particles to get classified as longitudinally lost by RFQGen. This is done by re-adjusting the ΔW_{thr}-value to an unreasonably high value, i.e. almost[21] the value of the desired final synchronous energy, so that the resulting threshold is never surpassed for most macro-particles. As the settings of this new simulation differ from those of the reference case only regarding the *elimit*-parameter, one might at first naively assume that the number of RFQ exit macro-particles $N_{exit,new}$ in this simulation is given by the sum of the number of RFQ exit macro-particles in the reference simulation $N_{exit,old}$ and the number of lost macro-particles along the RFQ for the reference case $N_{L,old}$: $N_{exit,new} = N_{exit,old} + N_{L,old}$. However, as will be shown in Sec. 3.5, the matter is more complex since particles that get too much out of phase, i.e. whose phase ϕ_i deviates too much form the synchronous phase ϕ_s, will eventually be exposed to radial fields that cause their collision with the electrodes. Thus, a certain fraction of these particles, that no longer get lost longitudinally due to the adjustment in the *elimit*-line, will later on still get lost radially and above naive summation does not hold true.

The difference $N_{exit,new} - N_{exit,old}$ gives a good estimation of the number of improperly accelerated particles to be expected at the RFQ exit. Furthermore, the simulation performed with the high *elimit*-value might even be closer to reality, since it takes into account the space-and image-charge force contributions of macro-particles, which are already disregard as longitudinally lost in the reference simulation. Therefore, the loss profile along the RFQ in case of the high *elimit*-value simulation is closer to reality and provides more relevant information about the expected RFQ radioactivation than the loss profile of the reference case (cf. Sec. 3.5).

E.2 The TOUTATIS-Code

The TOUTATIS code was written by R. Duperrier over two decades ago to simulate the transport of particle beams through (high intensity) RFQs[22]. TOUTATIS is a time-based code, i.e. its independent parameter of motion is time t. Each particle is transported for a certain period of time, i.e. until the moment $t = t_0$ is reached. This provides more exact space co-ordinates for evaluating the space-charge distribution. However, the exact phase co-ordinates φ cannot be determined simultaneously.

[21] Entries too close to the final synchronous energy or even higher than it are not accepted by the code.
[22] The code and more information on it are provided at `http://irfu.cea.fr/en/Phocea/Page/index.php?id=781`.

TOUTATIS uses multigrids and adaptive mesh methods for a fine representation of the forces. Calculation of the fields is performed with a Poisson solver of high accuracy. References [84] and [23] provide a more detailed look at this code.

Note that TOUTATIS is not suited to develop new RFQ beam dynamics. Instead it was written as a code enabling cross-checking the results of other RFQ beam dynamics codes[23]. Further goals were a more reliable description of the electric fields and an improved user friendliness. Regarding this thesis it provides a great advantage that the PARMTEQ(M)/RFQGen input file can also serve as an input file for TOUTATIS directly.

E.2.1 The TOUTATIS Algorithm

Albeight TOUTATIS still uses a simple beam dynamics concept, it discards several simplifications and approximations made by PARMTEQ(M) such as paraxiality. Among others, this was done to achive more accurate predictions regarding the particle losses along the RFQ in order to predict and (via corresponding design adjustments) eventually prevent/limit radioactivation of high intensity RFQs [23]. The simulation process begins with setting an initial distribution of macro-particles in the 6D-phase space. In order to determine the longitudinal position of the bunch within the RFQ the centroid of the particle positions is calculated. As soon as the centroid position is know TOUTATIS generates a mesh onto the electrodes close to the particle distribution. Charge distribution ρ is discretized in a 3D mesh with a so-called **C**loud-**I**n-**C**ell (CIC)-scheme: the electrode geometry is mapped onto the same grid, which then also is used to solve the Poisson equation. The forces are derived from a potential found by this procedure. This concepts takes into account external fields as well as space-charge and image-charge effects. The macro-particles are exerted to these forces via the following step by step scheme [84, 23]:

$$\vec{r}_{n+1} = \vec{r}_n + \vec{\beta}_n c\delta t + \frac{\delta t^2}{2}\vec{a}_n, \tag{E.3}$$

$$(\gamma\vec{a})_{n+1} = \frac{q}{m}\,\vec{E}(\vec{r}_{n+1}), \tag{E.4}$$

$$(\gamma\vec{\beta})_{n+1} = (\gamma\vec{\beta})_n + \frac{\delta t}{2c}\,[(\gamma\vec{a})_{n+1} + (\gamma\vec{a})_n], \tag{E.5}$$

[23] During finalization of this thesis in summer of 2021 attention was brought to the "RFQ Designer" code published a few months prior by CEA. As its name suggests it functions as a stand alone RFQ (beam dynamics) designing code. Successive beam dynamics simulations on the so developed design can be performed in – among others – TOUTATIS. Further information as as well as the download link are found at `http://irfu.cea.fr/en/Phocea/Page/index.php?id=932`.

with position vector $\vec{r}$, velocity vector $\vec{\beta}c$, temporal step-width δt, acceleration vector $\vec{a}$, Lorentz-factor γ, electric charge q, particle mass m and electric field vector $\vec{E}$. Since the Jacobian of this scheme is equal to 1, TOUTATIS is immune to emittance damping which might be brought forth by the "leap frog" scheme. By looping of this algorithm any longitudinal position in the RFQ can be reached.

E.2.2 The Finite Difference Method

The Poisson equation is solved by the so-called finite difference method. Figure E.3 shows a mesh of seven nodes. Node n_0 depends on its neighbors, nodes n_1 to n_6, by a finite equation. This equation entails a function f of the charge density ρ_0 on the considered node n_0, the electric potential Ψ_i at each node and the corresponding weighting coefficients α_i:

$$\Psi_0 = f(\rho_0, \sum_{i=0}^{6} \alpha_i \, \Psi_i). \tag{E.6}$$

α_i depends on distance h_i between node n_0 and node n_i (cf. Figure E.3).

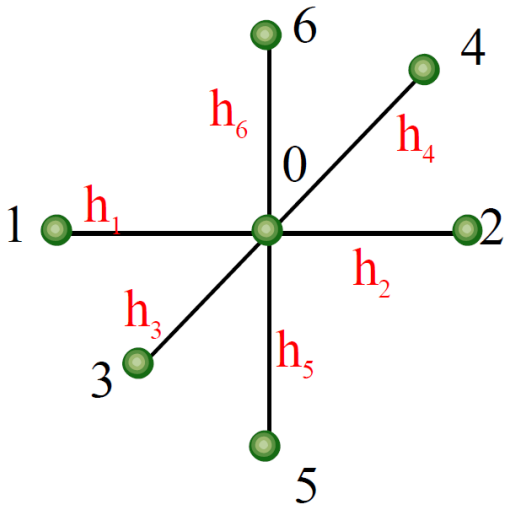

Figure E.3: Finite Difference Method: nodes n_0 to n_6 (green balls) and the distances h_i of the outer nodes n_1 to n_6 to the central node n_0 [84].

This kind of weighting enables the code to consider the specific electrode shape with high accuracy. The popular, but less efficient and accurate stairs discretization is thereby avoided. While computing each node of the grid the respective equation considers the new values calculated for the previous nodes. After all nodes of the mesh have been computed in this

way, this procedure is iterated until convergence is obtained, i.e. until the values of the electric potential do not undergo any further changes. This approach to use finite difference equations is referred to as Gauss-Seidel relaxation. Its accuracy solely depends on h_i; for $h \to 0$ the solution becomes exact. However, for practical considerations this convergence takes place too slowly in real life examples. Various methods have been developed to accelerate this relaxation process such as the Chebyshev acceleration and the Frankel-Young acceleration.

In the case of TOUTATIS the associated computation time could been reduced from one week to five hours, i.e. reduced to 0.3 ‰ of its initial value, with the multigrid method described in the next subsection.

E.2.3 TOUTATIS' Multigrid Method

Applicable multigrid methods were first introduced by Brandt in the 1970s [85]. They are used to solve equations of the form:

$$\Delta\Psi = \rho, \tag{E.7}$$

with Δ being the the Laplacian, Ψ the unknown scalar potential and ρ the source term. The latter is discretized within a fine grid. A gross estimation Ψ_i of Ψ is achieved by performing the Gauss-Seidel cycle i times on this grid. The Laplacian of Ψ_i does not equal ρ; the difference is referred to as residual or defect $\widetilde{\rho_i}$:

$$\widetilde{\rho_i} = \Delta\Psi_i - \rho. \tag{E.8}$$

The residual solves a second Poisson equation concerning the potential error $\widetilde{\Psi_i}$:

$$\Delta\widetilde{\Psi_i} = \widetilde{\rho_i}. \tag{E.9}$$

$\widetilde{\Psi_i}$ is also referred to as scalar correction. With it, Ψ can be obtained:

$$\Psi = \Psi_i - \widetilde{\Psi_i}. \tag{E.10}$$

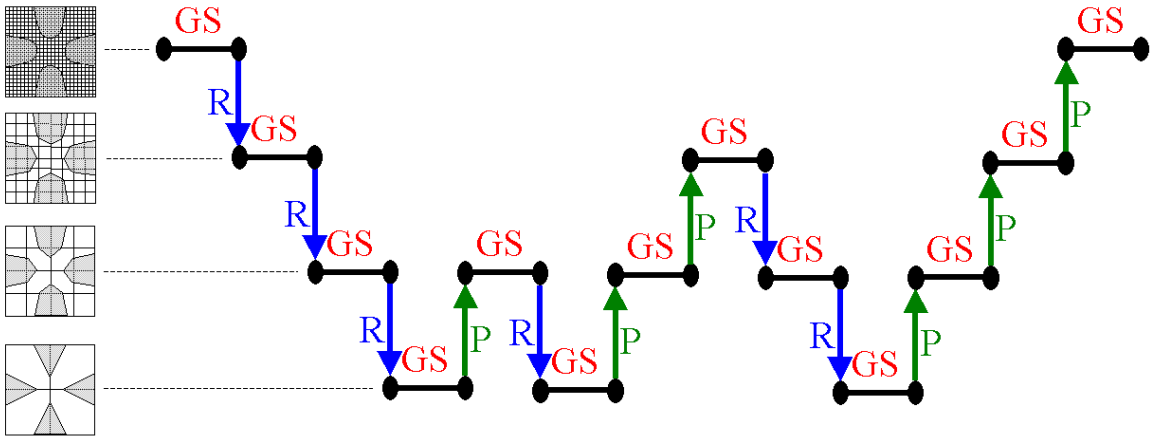

Figure E.4: Schematic of the TOUTATIS cycle; GS: 3 Gauss-Seidel relaxations, R: restriction and P: prolongation [84].

A crucial concept in multigrid methods is to estimate the error after a few relaxation cycles rather than the final solution Ψ for the potential itself. Equation E.9 is solved performing a relaxation process with a coarser grid, whereby the residual has been first discretized in this new mesh (restriction), in order to arrive at a sufficient estimation of this error rapidly. This coarser grid for its part is impaired by errors, which are also estimated by the same procedure. In order to correct one fine grid using a coarser grid, an interpolation process referred to as prolongation is executed. This forms the main principle underlying multigrid methods: the different stages have to be combined by the user himself with regard to his specific problem. From here many possible cycle architectures emerge, e.g. the popular V-cycle architecture [86]. Figure E.4 shows the cycle architecture used by TOUTATIS.

E.2.4 Adaptive Mesh Refinement in TOUTATIS

For neighboring bunches to be considered for the calculation the longitudinal dimension of the grid is set to $\beta\lambda$. Also for the same purpose a longitudinal periodicity is built in the relaxation process. The main disadvantage of this method effects the acceleration of a beam bunch: During the decrease in phase spread the resolution of the grid covering the bunch also declines. As a simple solution to this problem TOUTATIS applies a second mesh embedded within the main grid (see Figure E.5). While the big grid dimensions depend on the electrode geometry, the dimensions of this second mesh are determined by the rms-sizes of the bunch.

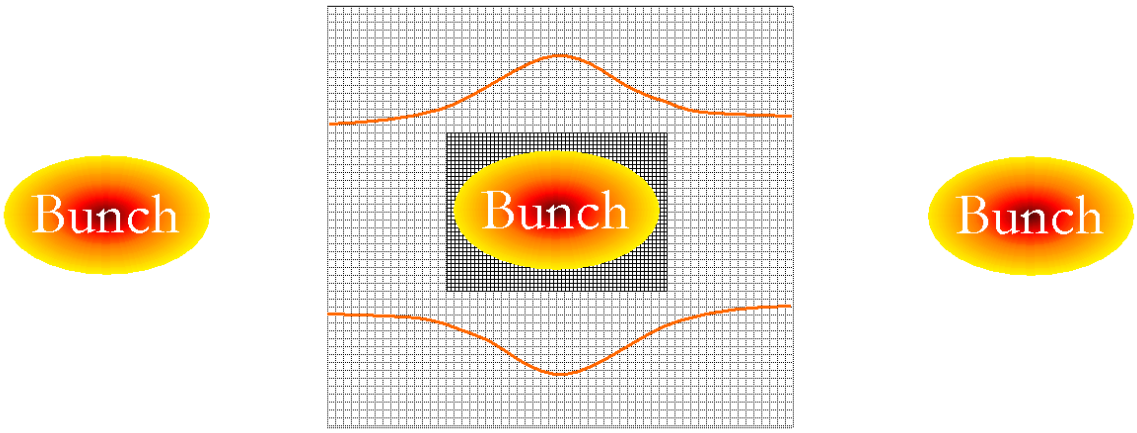

Figure E.5: TOUTATIS' adaptive mesh refinement illustrated [84].

F Lists of Figures and Tables

List of Figures

0.1 Übersicht über die GSI-Anlagen und jene des FAIR-Projekts II
0.2 Layout des FAIR Protonen-Linacs. III
0.3 Strahldynamik-Design des FAIR Protonen-Linac RFQ. VIII
0.4 Feldebenheit des FAIR p-Linac RFQ und Spanungsstufenfunktion. XIV
0.5 Strahldynamik-Design des neuen kompakten RFQ. XVIII
0.6 Phasenraumplots und die Projektionen der Verteilungen am Ausgang des neuen, kompakten RFQ. XIX
0.7 $\sigma_{0l/t}$-Kurven des FAIR p-Linac RFQ und des neuen kompakten RFQ. XXI

1.1 Overview of the GSI and FAIR project. 4
1.2 Layout of the FAIR Proton-Linac. 6
1.3 Digital mock-up of the p-linac building viewed at from south. 8
1.4 Isometric view of the LEBT for the FAIR p-Linac RFQ. 9
1.5 Schematic layout of the p-linac and isometric view of the coupled CH prototype of the p-linac. 10

2.1 Basic structure of a 4-vane RFQ. 11
2.2 The 750 kV Cockcroft-Walton generator for CERN's Linac2. 13
2.3 Geometric development of quadrupole/RFQ electrodes and the electrodes of the p-Linac RFQ. 15
2.4 RFQ electrodes cross sections. 19
2.5 Ideal vs. real trans. RFQ-electrode profiles in case of rod-shaped electrodes. . . 21
2.6 Alternating gradient focusing of an ion beam in a FODO-channel. 25
2.7 Design parameter curves for a LANL FSP 425-MHz test design. 30
2.8 Sketch of the electrode tip profile along an arbitrarily chosen hypothetical RFQ. 31
2.9 Design parameter curves of a NFSP design. 36
2.10 Beam dynamics design of CERN's Linac4 RFQ by A. Lombardi. 38

3.1 Beam dynamics design of the FAIR Proton-Linac RFQ. 41
3.2 Detailed sketch of the electrode profiles at the RFQ exit. 46
3.3 Beam dynamics design of the FAIR Proton-Linac RFQ and CERN's Linac4 RFQ. 47
3.4 Phase space plots and distribution projections for the design beam at the FAIR p-Linac RFQ's exit. 48
3.5 Beam dynamics design of the FAIR Proton-Linac RFQ as built and the alternative design according to the LANL scheme. 51
3.6 Phase space plots and distribution projections at the FAIR p-Linac RFQ exit for RFQGen simulations run with the optimal set of trans. input Twiss parameters. 52
3.7 Matrix providing an overview over the combinations of the initial trans. Twiss parameters. 53
3.9 TraceWin simulated beam density plots in the LEBT-line of the FAIR-p-Linac RFQ. 55
3.8 Phase space plots and distribution projections at the entrance and exit of the FAIR p-Linac RFQ. 56
3.10 Sketch of the LEBT-line for the FAIR p-Linac RFQ. 57
3.11 Comparison of the RFQ exit distributions from measured vs. generic input distributions. 58
3.12 Comparison of the exit phase space plots for the RFQGen and TOUTATIS simulations (on 100 mA matched beam). 61
3.13 Norm. rms-emittances and transmission of the matched beam. 63
3.14 Particle losses per cell against the synchronous energy W_s for two cases. 65
3.15 Long. phase space plots and distribution curves at the RFQ exit for different ICE- and NNB-settings. 68
3.16 Phase space plots and distribution curves at the RFQ exit for different ICE- and NNB-settings. 69
3.17 Long. phase space plots and distribution curves at the RFQ exit for case 1. . . 70
3.18 Phase space plots and distribution curves at the RFQ exit for case 2. 71
3.19 Phase space plots and distribution curves at the RFQ exit for case 3. 72
3.20 Particle losses against the synchronous energy for cases 0-3. 73
3.21 Long. electric field distribution along the p-Linac RFQ. 75
3.22 Curve of the long. electric field at the p-Linac RFQ entrance. 77
3.23 Voltage amplitude at the entrance of the p-Linac RFQ against gap distance d. 78
3.24 Effective energy gain ΔW_{eff} against the entrance phase ϕ_0 and particle position, respectively. 79

3.25 On-axis gap fields at the p-Linac RFQ entrance. 81
3.26 Detailed sketch of the electrode profiles at the p-Linac RFQ exit. 82
3.27 Norma. particle density plot between the entrance flange and the radial matcher. 84
3.28 Two RFQ entrance distributions in long. phase space. 85
3.29 Various beam parameters for different entrance energy spreads. 90
3.30 Beam parameters at the p-Linac RFQ exit for the RFQGen and TOUTATIS current studies with $\Delta W_{in} = \pm 0.00\,\mathrm{keV}$. 91
3.31 Transmissions and the norm. long. rms-emittances along the p-Linac RFQ for selected entrance current values and different entrance energy spreads. 92
3.32 Transmissions and loss particles along the p-Linac RFQ for selected entrance current values and different entrance energy spreads. 93
3.33 Norm. trans. rms-emittances along the p-Linac RFQ for selected entrance current values at an entrance energy spread of $\Delta W_{in} = \pm 0.00\,\mathrm{keV}$. 94
3.34 Norm. trans. rms-emittances along the p-Linac RFQ for selected entrance current values at an entrance energy spread of $\Delta W_{in} = \pm 1.90\,\mathrm{keV}$. 95
3.35 Norm. trans. rms-emittances along the p-Linac RFQ for selected entrance current values at an entrance energy spread of $\Delta W_{in} = \pm 3.80\,\mathrm{keV}$. 96
3.36 Trans. phase-advances along the p-Linac RFQ for selected entrance current values at an entrance energy spread of $\Delta W_{in} = \pm 0.00\,\mathrm{keV}$. 97
3.37 Trans. phase-advances along the p-Linac RFQ for selected entrance current values at an entrance energy spread of $\Delta W_{in} = \pm 1.90\,\mathrm{keV}$. 98
3.38 Trans. phase-advances along the p-Linac RFQ for selected entrance current values at an entrance energy spread of $\Delta W_{in} = \pm 3.80\,\mathrm{keV}$. 99
3.39 Long. phase-advances along the p-Linac RFQ for selected entrance current values at an entrance energy spread of $\Delta W_{in} = \pm 0.00\,\mathrm{keV}$. 100
3.40 Long. phase-advances along the p-Linac RFQ for selected entrance current values at an entrance energy spread of $\Delta W_{in} = \pm 1.90\,\mathrm{keV}$. 101
3.41 Long. phase-advances along the p-Linac RFQ for selected entrance current values at an entrance energy spread of $\Delta W_{in} = \pm 3.80\,\mathrm{keV}$. 102
3.42 Long. phase space plots at the p-Linac RFQ exit for entrance currents of 0 mA and 2 mA at different ΔW_{in}-values. 103
3.43 Long. phase space plots at the p-Linac RFQ exit for entrance currents of 10 mA and 25 mA at different ΔW_{in}-values. 104
3.44 Long. phase space plots at the p-Linac RFQ exit for entrance currents of 35 mA and 50 mA at different ΔW_{in}-values. 105

3.45 Long. phase space plots at the p-Linac RFQ exit for entrance currents of 0 mA and 2 mA at different ΔW_{in}-values. . . . 106
3.46 Field flatness along the RFQ before and after tuning as well as voltage step-function. . . . 108
3.47 All eleven interval voltages and voltage differences for different f-values. . . . 112
3.48 Transmissions and norm. long. rms-emittances along the p-Linac RFQ for different f-values. . . . 115
3.49 Trans. norm. rms-emittances along the p-Linac RFQ for different f-values. . . . 116

4.1 Phase space plots and distribution projections at the new compact RFQ exit. . 124
4.2 Beam dynamics design of the new compact RFQ. . . . 125
4.3 Particle losses per cell [%] against the synchronous energy W_{syn} for the new compact RFQ for two ΔW_{thr}-settings. . . . 127
4.4 $\sigma_{0l/t}$-curves against along the p-Linac RFQ and the new compact RFQ. . . . 129
4.5 Transmission and norm. long. rms-emittance at the new compact RFQ exit against the entrance current. . . . 130

A.1 Acc. field $E_z(\phi)$, potential $V_\phi(\phi)$ and particle trajectories in phase space. . . . 152
A.2 Particle trajectories and bucket in phase space. . . . 155
A.3 The open quasi-bucket "enclosed" by a "golf club"-shaped quasi-separatrix. . . 156

B.1 RFQ injection cone without and with an electron repeller. . . . 157

D.1 Total and effective emittance areas in x-x'-phase space. . . . 162
D.2 Particle distribution and concentric emittance-ellipses in x-x'-phase space. . . . 163
D.3 Emittance ellipse in the x-x'-plane rotated by angle ψ against the main axes . 164
D.4 Twiss parameter α determines the ellipse orientation [80]. . . . 166

E.1 PARMTEQ's leap-frog algorithm. . . . 176
E.2 Cylindric mesh of a schematic beam bunch as calculated by RFQGen's $scheff$-subroutine . . . 179
E.3 Finite Difference Method Grid. . . . 187
E.4 Schematic of the TOUTATIS cycle. . . . 189
E.5 TOUTATIS' adaptive mesh refinement illustrated. . . . 190

List of Tables

0.1 Parameter des Designstrahls am Eingang des FAIR p-Linac RFQ. IX
0.2 Parameter des Designstrahls am Ausgang des FAIR p-Linac RFQ (4.88 mm hinter dem Ende der Elektroden). IX
0.3 Trans. Elektrodenradius ρ, Radius der RFQ-Zellenmitte (mittlere Apertur) r_0 und ihr Verhältnis $\rho\,/\,r_0$ sowie Bravery-Faktor für den FAIR p-Linac RFQ. . . X
0.4 Vergleich der Schlüsselparameter zwischen dem FAIR p-Linac RFQ und dem neuen kompakten RFQ. XVII

2.1 Key design and beam parameters of the Linac4 RFQ at CERN. 37

3.1 Parameter comparison between the Linac4 RFQ and the FAIR p-Linac RFQ. . 43
3.2 Lengths of various RFQ sections and regions given by the RFQGen-output files. 45
3.3 Values of the trans. electrode radius ρ, the mid-cell aperture / mid-cell radius r_0 and their ratio $\rho\,/\,r_0$. 45
3.4 Design and entrance beam parameters of the FAIR p-Linac RFQ. 46
3.5 Parameters of the design beam at the exit of the FAIR p-Linac RFQ. 48
3.6 Comparison between the parameters of the Linac4 RFQ's and the FAIR p-Linac RFQ's acceleration sections. 49
3.7 Comparison of the design parameter for the p-Linac RFQ as built (left) and an alternative design according to the LANL scheme (right). 50
3.8 Comparison of the cases run with the original design entrance trans. Twiss parameters and the matched ones. 54
3.9 Comparison of simulation results based on measurements and generic entrance distributions. 59
3.10 Comparison of the exit beam parameters for the RFQGen and TOUTATIS simulations performed on the matched beam. 60
3.11 Comparison of the transmissions at the FAIR p-Linac RFQ exit and the total long. and radial losses along the RFQ for the reference case and the $\Delta W_{thr} = 2.99\,MeV$ case. 64
3.12 Comparison of the RFQ exit beam parameters for cases 0-3. 67
3.13 Characteristic lengths at the RFQ entrance. 78
3.14 Sketch of the p-Linac RFQ entrance. 79
3.15 Characteristic lengths at the p-Linac RFQ exit. 83
3.16 Transmissions and norm. rms-emittances at the p-Linac RFQ exit. 86
3.17 Re-scaled electrode voltage of the defined intervals. 110

3.18 Average voltages for different f-values. 113
3.19 Transmissions, emittances and average energies at the p-Linac RFQ exit for different f-values. 114
3.20 Average particle energies at cell center for different f-values along the RFQ. . 117

4.1 Key parameters of the CERN PIXE-RFQ. 122
4.2 Key parameters comparison between the p-Linac RFQ and new compact RFQ. 123
4.3 Results of the entrance current studies for the new compact RFQ. 130

E.1 Electrode geometry files for CHARGE 3D and PARMTEQ(M)/RFQGen. . . . 181

G List of Abbreviations and Acronyms

2/3/4/6D two/three/four/six-dimensional or two/three/four/six dimensions

AC **A**lternating **C**urrent

ACCT **AC** **C**urrent **T**ransformer

AGF **A**lternating **G**radient **F**ocusing

BNL **B**rookhaven **N**ational **L**aboratory in New York, USA

CEA French Alternative Energies and Atomic Energy Commission (**C**ommissariat à l' **É**nergie **A**tomique)

CERN European Organization for Nuclear Research (**C**onseil **E**uropéen pour la **R**echerche **N**ucléaire) in Geneva, Switzerland

CH **C**rossbar **H**-Mode

CST MWS **M**icro**W**ave **S**tudio (Software) formerly distributed by **C**omputer **S**imulation **T**echnology (Darmstadt, Germany)

CURLI **Cur**rent **Li**mits (Software)

DACM CEA's **D**epartment of **A**ccelerators, **C**ryogenics and **M**agnetism (Département des Accélérateurs, de Cryogénie et de Magnétisme)

DTL **D**rift **T**ube **L**inac

elimit **E**nergy **Limit** (threshold parameter for long. loss particles in RFQGen/PARMTEQ: $\Delta W_{thr} = elimit\, MeV$)

ECR **E**lectron **C**yclotron **R**esonance

ESR **E**xperimental **S**torage **R**ing

FAIR **F**acility for **A**ntiproton and **I**on **R**esearch at GSI Darmstadt, Germany

FNAL **F**ermi **N**ational **A**ccelerator **L**aboratory (Fermilab) in Bataiva/Illinois, USA

FSP **F**our **S**ection **P**rocedure (also: LANL FSP)

GB **G**entle **B**uncher/**B**unching

GSI GSI (**G**esellschaft für **S**chwer**i**onenforschung) Helmholtz Center for Heavy Ion Research in Darmstadt, Germany

HESR **H**igh-**E**nergy **S**torage **R**ing

HLI High Charge Injector (**H**och**l**adungs**i**njektor) at GSI Darmstadt, Germany

HSI High Current Injector (**H**och**s**trom**i**njektor) at GSI Darmstadt, Germany

IAP **I**nstitute for **A**pplied **P**hysics in Frankfurt/Main, Germany

ICE **I**mage **C**harge **E**ffects

IH **I**nterdigital **H**-mode

LANL **L**os **A**lamos **N**ational **L**aboratory

LEBT **L**ow **E**nergy **B**eam **T**ransport

linac (RF) **lin**ear **ac**celerator

long. **long**itudinal

MEBT **M**edium **E**nergy **B**eam **T**ransport

NFSP **N**ew **F**our **S**ection **P**rocedure

NNB **N**ext **N**eighbor **B**unch(es)

norm. **norm**alized

PARMTEQ **P**hase **A**nd **R**adial **M**otion in **T**ransverse **E**lectric **Q**uadrupoles (Software)

PIC **P**article-**i**n-**C**ell

PIXE **P**roton **I**nduced **X**-ray **E**mission

p-linac **A**roton (RF) **lin**ear **ac**celerator

RF **R**adio **F**requency

RFQ **R**adio **F**requency **Q**uadrupole

RFQGen **R**adio **F**requency **Q**uadrupole **Gen**erator (Software)

RM(S) **R**adial **M**atcher/**M**atching(**S**ection)

RMS **R**oot **M**ean **S**quare

SCC **S**pace **C**harge **C**ompensation

SCHEFF **S**pace **Ch**arge **Eff**ects (sub-routine used by RFQGen/PARMTEQ)

SIS18/100 heavy ion synchrotron (**S**chwer**i**onen-**S**ynchrotron) at GSI Darmstadt, Germany; the respective numbers refer to the respective maximum magnetic rigidity in T/m

trans. **trans**versal

UNILAC **Uni**versal **L**inear **Ac**celerator at GSI Darmstadt, Germany